Femtosecond Electron Dynamics in Hot Solid-Density Plasmas

Quincy Y. van den Berg

Keble College

University of Oxford

A thesis submitted for the degree of

Doctor of Philosophy

Hillary Term 2021

Abstract

X-ray Free Electron Lasers (XFELs) have shown to be an extremely versatile tool for the experimental study of warm and hot dense matter. Their femtosecond pulse length, high peak brightness and tunable wavelength open up an immense window of opportunity to study solid-density plasmas that are created in a well-controlled manner. At these high densities, the light-matter interaction can be modelled with a collisional-radiative code that describes the ion charge state populations, electron distribution function (EDF) and radiative properties.

In this thesis I will outline a numerical scheme based on the inhomogeneous, isotropic Fokker-Planck equation that describes the non-equilibrium evolution of the EDF in a warm dense system. The scheme encompasses a variety of collisional and radiative interactions between electrons, ions and photons in the system and implicitly conserves density and energy. The Fokker-Planck scheme has been integrated into a non-Local Thermodynamic Equilibrium (LTE) collisional-radiative code that computes the ion charge state populations of a warm dense system under irradiation of an XFEL. The two schemes together constitute a self-consistent method to compute the population dynamics, energy- and density balance of the combined electron and ion system.

The experimental section of this thesis describes a measurement of the collisional ionisation frequencies in a solid-density magnesium plasma. These rates are of great interest as they relate to the optical and electrical properties of high energy-density materials. The experiment relies on the use of an XFEL both to produce and probe the sample, and obtain a spectroscopic measurement of the rate and plasma conditions. This is the first direct measurement of the ionisation rate in the strongly-coupled regime where the rates are significantly enhanced by density effects such as ionisation potential depression.

Contents

List of Acronyms

Abbreviation	Description
3BR	Three-Body Recombination
BC	Burgess and Chidichimo
CAM	Clark, Abdallah and Mann
CCFLY	Radiative-collisional atomic physics code (C++)
CDE	Collisional De-Excitation
CE	Collisional Excitation
CF	Clark and Fontes
CI	Collisional Ionisation
CVODE	Ordinary Differential Equation solver from the Sundials suite
DR	Dielectronic Recombination
EK	Ecker and Kröll
ELFIE	ELFIE laser at École Polytechnique
European XFEL	European X-ray Free Electron Laser
FEL	Free Electron Laser
FLYCHK	Atomic Kinetics code
FWHM	Full Width at Half Maximum
GF	Gaunt Factor
HDM	Hot Dense Matter
HED	High Energy Density
IB	Inverse Bremsstrahlung
ICF	Inertial Confinement Fusion
IPD	Ionisation Potential Depression
KLL	KLL Auger Decay

Abbreviation	Description
LCLS	Linac Coherent Light Source
LHS	Left Hand Side
LLNL	Lawrence Livermore National Laboratory
LTE	Local Thermodynamic Equilibrium
MB	Maxwell-Boltzmann
mEK	Modified Ecker-Kröll
ODE	Ordinary Differential Equation
PAL-XFEL	Pohang Accelerator Laboratory X-ray Free Electron Laser
PI	Photo-Ionisation
RDE	Radiative De-Excitation
RE	Radiative Excitation
RHS	Right Hand Side
RR	Radiative Recombination
SACLA	SPring-8 Angstrom Compact free electron LAser
SASE	Self Amplified Spontaneous Emission
SCFLY	Radiative-collisional atomic physics code (Fortran-77)
SE	Spontaneous Emission
SH	Scaled Hydrogenic
SLAC	Stanford Linear Accelerator Centre
SP	Stewart and Pyatt
SwissFEL	Swiss X-ray Free Electron Laser
SXR	Soft X-ray beamline at LCLS
WDM	Warm Dense Matter
XFEL	X-ray Free Electron Laser

List of Symbols

Symbol	Unit/value	Description
D	$\mathrm{eV}^2\ \mathrm{s}^{-1}$	diffusion coefficient
E	eV	Energy
I_H	13.6 eV	Rydberg constant
α	$\approx 1/137$	Fine structure constant
ξ	-	number of electrons in shell
a	$\mathrm{eV}\ \mathrm{s}^{-1}$	drift coefficient
a_0	5.29-10-9 cm	Bohr radius
m_e	9.1093×10^{-28} g	Electron mass
q_e	1.602176×10^{-19} C	Electron charge
(x, y)		Functional inner product
E_{kin}	eV or J	Kinetic energy
F_{ij}	-	Oscillator strength
G	-	Gaunt factor
H	eV	Hamiltonian
I_0, J	Wcm^{-2}	Radiation intensity
K, L, M	-	Atomic shells
L, s	cm	Path length
N	-	Number of particles
P, E_{-+}	eV	threshold potential
S/V	$\mathrm{cm}^{-3}\ \mathrm{s}^{-1}$	Volumetric rate coefficient
S	s^{-1}	Rate coefficient
T, T_e	eV	Temperature
V, U, E_{pot}	eV or J	Potential energy
V	cm^3	Volume
Z	-	charge number
Γ	-	Coupling parameter
ϵ_0	$8.854 \times 10^{-12}\ \mathrm{Fm}^{-1}\mathrm{s}$	Vacuum permittivity constant
$\hat{A}$	-	Operator
$\hbar = \frac{h}{2\pi}$	1.05457×10^{-27} erg·s	Reduced Planck constant
κ	cm^{-1}	Opacity
λ_D	cm	Debye length
λ	cm	Wavelength

Symbol	Unit/value	Description
$\langle \cdots \rangle$		Ensemble average
$\ln \Lambda = ln(\lambda_D/r_0)$	-	Coulomb logarithm
ν, ω	s^{-1}	Frequency
ϕ, φ	[-]	Line shape
σ	cm^2	Reaction cross-section
ε	Wcm^{-3} or $eVcm^{-3}s^{-1}$	Emissivity
$\vec{p}$	$cm{\cdot}g{\cdot}s^{-1}$	Momentum vector
$\vec{r}$	cm	Position vector
$\vec{v}$	cm/s	velocity vector
c	$2.9979 \times 10^8 m\,s^{-1}$	Speed of light
f_1	$[f]$	One-particle distribution function
f_E	$eV^{-1}{\cdot}cm^{-3}$	Distribution function in energy space
f_v	$cm^{-6}{\cdot}s^3$	Distribution function in velocity space
g	-	Statistical weight of a state
h	6.626068×10^{-27} erg·s	Planck constant
i, j, k	-	indices
k_B	8.6173×10^{-5} eV/ K	Boltzmann constant
n_a	cm^{-3}	Density of particle species a
$r_0 = Zq_e^2/k_BT$	cm	Landau length
t	s	Time
x^{eq}, x^{LTE}	[x]	Equilibrium quantity x
x_e	[x]	Electron quantity
x_i	[x]	Ion quantity
z	-	charge

List of Figures

List of Tables

Chapter 1

Introduction

Contents

The study of high energy density science has seen a recent increase in research interest since the advent of powerful X-ray free electron lasers that can be used to experimentally produce high energy density systems. A high energy density system is loosely defined as having an energy density exceeding $10^5\,\mathrm{J}\cdot cm^{-3}$, and they are prevalent in nature in many forms. Examples of such Warm Dense Matter (WDM) are the interior of large planets such as Jupiter, lightning discharges, and the matter that all types of stars are built out of. Our understanding of the warm dense systems in the universe around us hinges on our ability to model and measure their electrical, thermal and radiative properties.

The type of WDM that this work focuses on has a charge carrier density comparable to that of a solid metal, and an electron temperature that can be associated with the plasma state. Whereas this type of matter can be found in a stable state in nature, it requires significant effort to recreate these systems in a laboratory environment. The high energy density causes the systems to rapidly expand in the absence of the strong gravitational confinement of an astrophysical body. The theoretical study of WDM is severely complicated by the fact that free electrons carry a similar amount of electrostatic- V_{pot} and kinetic (thermal) energy E_{kin}. This is expressed in the form

of a coupling constant Γ for the system:

$$\Gamma = \frac{V_{\text{pot}}}{E_{\text{kin}}}. \tag{1.1}$$

Classical plasmas for which a well-developed theory exists, live in the weakly coupled regime ($\Gamma \ll 1$). In this case, the electrons move as if they were a weakly-interacting gas apart from possible electron-ion interactions. Any interaction that electrons have with each other or with an ion can be described as a binary event; an interaction between two or three particles depending on the atomic process of interest. Solid state materials, on the other hand, are strongly coupled ($\Gamma \gg 1$) and the electrons have a larger binding potential than kinetic energy. WDM is a state of matter that lies in the transition range where electron-electron and electron-ion interactions become many-body events.

When creating high energy density systems experimentally, there are two classes of methods to contain the particles in the system and substitute the role of the gravitational confinement that cannot be replicated in a laboratory: either through an externally-applied magnetic field, or through the inertia of the particles themselves. Inertial confinement methods rely on having a rapid discharge of energy into the system during which the system heats up before eventually expanding. In this thesis, the heating mechanism comes in the form of photo-absorption from a powerful X-ray source. The use of a X-ray-driven heating mechanism provides a way to create warm dense systems with near-homogeneous conditions in a reproducible manner.

The advent of fourth generation of X-ray Free Electron Laser (XFEL) sources plays a central role in the research underpinning this thesis. Free Electron Lasers (FELs) had already been built for higher wavelengths in the visible and infra-red range in the 1970s [1]. From the moment X-ray FEL were proposed in 1992, it took almost two decades for the first XFEL to be taken into commissioning at the Linac Coherent Light Source (LCLS) facility [2]. As these experimental efforts and investments would suggest, XFELs are extremely versatile machines that have a great potential to contribute towards many branches of science.

They can be deployed both as a diagnostic tool used to probe matter with a femtosecond temporal resolution, as well as a photo-pump used for X-ray heating. Furthermore, XFELs are uniquely tunable and the peak power, frequency and pulse duration can be set independently (within some limits of the experimental facility). Owing to the small bandwidth in frequency, XFELs can be tuned to pump or probe specific atomic transitions for the study of physical, biological and chemical dynamics of matter at a time scale that was previously inaccessible.

This work will explore the collisional dynamics of warm dense systems both experimentally and computationally. Dense plasmas are heavily transient systems with a complex balance of atomic transitions. I will address the question on how to model the light-matter interaction in a non-equilibrium warm dense system that is irradiated by an XFEL. This computational model includes a description of the non-equilibrium evolution of both the free-electron population as well as the ion system.

Subsequently, an experimental study will be presented on the collisional ionisation and recombination dynamics in warm dense magnesium. The nature of collisional dynamics in a dense, strongly-coupled system is that of a quantum many-body interaction. The main results of this work are a measurement of the collisional frequencies for a strongly-coupled magnesium plasma, as well as a cross-section model that can be readily implemented in atomic-kinetics simulations. All experiments discussed make extensive use of the capabilities of XFELs and at present could not have been performed without them.

1.1 Relevant concepts

The work presented in this thesis will focus on the non-equilibrium collisional dynamics of a solid-density plasma. Understanding the modelling approaches and constraints requires some background knowledge on the subjects of local thermodynamic equilibrium and detailed balance. Although the systems studied in this work are often not in equilibrium, most of the computational models used here are benchmarked and validated in equilibrium conditions.

Closely connected to the concept of local thermodynamic equilibrium is that of detailed balance. Detailed balance provides a framework to relate the transition rates of counter-directional atomic transitions to each other. Being able to relate the rate of every atomic process to its inverse reaction allows for a reduction in the number of models required to describe a warm dense system. It is essential that detailed balance is applied when constructing ion transition rate models in order to correctly describe their behaviour near local thermodynamic equilibrium.

In the penultimate subsection, the operating mechanism and the properties of X-ray free electron lasers will be discussed. Finally, I will introduce the concept of modelling warm dense systems with radiative-collisional codes.

1.1.1 Local Thermodynamic Equilibrium

Laboratory-created plasmas are often created on short time-scales through a rapid discharge of energy, or by exposing a solid to a powerful laser. The method of creation of a warm dense system intrinsically leads to a system that is unstable and rapidly evolves. Nevertheless, it is still possible for warm dense systems to be close to a state of Local Thermodynamic Equilibrium (LTE) while they evolve, even if this is on the femtosecond time scale. The concept of LTE therefore warrants special attention, and it plays an important role in deriving and benchmarking the ion transition rates, as well as verifying conservation laws for the electron density and energy.

Thermodynamic equilibrium is an internal state of a system that maximises the entropy, while minimising some thermodynamic potential[1]. Thermodynamic equilibrium is a unique state that any isolated system will naturally evolve towards, if given enough time to do so. A classic example is an isolated gas held at a constant volume. Through inter-particle collisions, the gas particles will redistribute their energy until they reach an energy distribution that maximises the entropy, the Maxwell-Boltzmann (MB) distribution given by Eq. 1.2:

$$f_{MB}(E) = 2n\sqrt{\frac{E}{\pi}}(k_B T)^{-3/2} \exp\left(-E/k_B T\right), \tag{1.2}$$

where E is the particle's kinetic energy, k_B the Boltzmann constant, n the particle density, and T denotes the temperature. In a global state of equilibrium, there is a clear relation between the gas properties such as the pressure, density and temperature. Each of these quantities will be uniform across the system, and they are uniquely connected through an equation of state. When applied to a gas of non-interacting particles, this well-known result from the kinetic theory of gases leads to the ideal gas law. In plasma physics, this distribution carries significance as it is the equilibrium distribution for a hot electron gas. The interaction processes in an electron gas are of an entirely different nature, but lead to the same distribution.

A state of equilibrium can also exist locally. It is possible for a warm dense system to have a number density, and also an energy density, that varies (slowly) over space, all while the system has equilibrated locally. For this to occur, the time scale on which collisions take place that redistribute energy, must be much smaller than the time scales associated with the system's time evolution or macroscopic transport properties. This loose definition enables us to speak of a local temperature and

[1]Depending on the conditions, this can be the Helmholtz or Gibbs free energy.

density, even in a dynamic system with spatial and temporal gradients. A warm dense system in LTE has three properties:

- All free particle species present have a MB distribution function (thermal distribution) at the same temperature
- The occupation numbers of bound atomic levels follow a Boltzmann distribution
- The ionisation degrees of the ions are given by the Saha distribution

Though seemingly different, these properties are all established by collisional interactions of the species in the system. When allowed to equilibrate, these collisions will re-arrange the energy distribution and ion states in a way that they observe equilibrium relations. For this reason, the LTE state is unique as the ion population dynamics, as well as the plasma conditions (temperature and density), are prescribed by the same physics. There exists a distribution for the radiation field that maintains the equilibrium relations of all radiation-induced transition rates, the Planck radiation field or black-body radiation. An external field from an XFEL generally does not have this profile due to its narrow frequency bandwidth. However, the black-body field can be used to derive the reaction cross-sections of radiation-induced ion transitions.

Due to the connection between the ion state occupations and the electron distribution, there exists a unique temperature-density relation for each plasma. When a system of some given density has an excess of thermal energy (higher temperature) than this relation prescribes, more ions will be ionised to bring the system back to LTE. Any plasma state created through electron collisions takes the system closer to LTE.

The XFEL laser field is therefore a perturbation to the state of LTE. The laser has the ability to independently alter bound state occupation levels of the ions, and in particular the degree of ionisation, without involving the free electrons. A laser-created plasma is by definition not in LTE, but if the collisions are fast enough compared to the plasma evolution, LTE can be restored. In much of this work, that is the case and we still have all the benefits of being in a state of LTE despite having a laser-created plasma.

The fundamental parameters that determine whether this is true are the electron-ion collision frequencies, particularly for ion transitions that rearrange the bound occupation levels or the degree of ionisation. This notion explains the significance of measuring these collisional rates, more of which will be discussed in Chapter. 4.

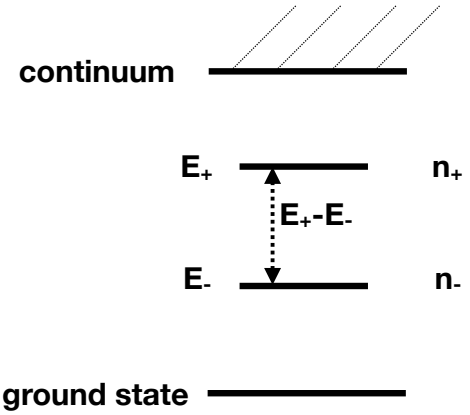

Figure 1.1: Two ion states, $|-\rangle$ and its excited state $|+\rangle$ separated by an energy $E_+ - E_-$. Each state has an occupation level given by n.

As mentioned before, LTE implies that there is a unique relationship between bound occupation levels and the ionisation degree of the ions. There are two distributions that govern this, the Boltzmann distribution for bound states and the Saha distribution for ionisation.

The Boltzmann distribution is best explained when considering two bound ionic states where state $|-\rangle$ is the lower state, and state $|+\rangle$ the excited state as depicted in Fig. 1.1. State $|-\rangle$ with occupation n_- and $|+\rangle$ with occupation n_+ are linked through each other by an excitation event induced by free electrons, collisional excitation[2]. When there is LTE, these occupation levels relate to each other through the Boltzmann distribution as:

$$\frac{n_+}{n_-} = \frac{g_+}{g_-} \exp\left(-\frac{E_+ - E_-}{k_B T}\right). \tag{1.3}$$

The ratio of ion state number densities is proportional to the ratio of their statistical weights g (also called multiplicities), and the Boltzmann factor. For increasing temperatures, the occupation levels more closely resemble the states' multiplicities as electrons can more easily excite. Naturally, at low temperatures the system resides in the lower accessible state. This relation is only valid for bound-bound transitions, where the number of bound electrons is the same for both states.

For bound-free transitions in WDM, as is the case for ionisation events, the Saha distribution is valid instead [3,4]. For states separated by an ionisation event, following the same notation as in Eq. 1.3 , the ratio of occupations is given as:

$$\frac{n_e n_+}{n_-} = \frac{2}{\lambda_e^3} \frac{g_+}{g_-} \exp\left(-\frac{E_+ - E_-}{k_B T}\right), \tag{1.4}$$

[2]See Subsection 3.5.2.

where a dependency on the electron density enters the equation. The wavelength in Eq. 1.4 is the thermal De Broglie wavelength for electrons, given as:

$$\lambda_e = \frac{h}{\sqrt{2\pi m_e k_B T}}. \tag{1.5}$$

Formally speaking, a better expression for the De Broglie wavelength would use the reduced mass of the electron and ion, but in this work the ions are always at room temperature and can be considered motionless compared to the electrons.

Similarly to excitation, a higher temperature implies a higher degree of ionisation. For a warm dense system of a known charge number, there is then a unique relation between electron density and temperature. By examining how close a system lies to this prescribed temperature-density curve, it can be quantified how close or distant a system is from the state of LTE.

1.1.2 Detailed Balance

A concept very closely tied to LTE is that of microscopic reversibility or detailed balance. This reversibility lays a connection between a forward transition rate and its inverse, for instance collisional excitation and de-excitation. If one rate is known for a given distribution function, the other can be constructed through microscopic reversibility.

These terms are often used interchangeably, although here the author will refer to microscopic reversibility for discussing reaction cross-sections and rates in non-LTE circumstances. Detailed balance will be reserved for volumetric transition rates in LTE. The form of the Maxwell-Boltzmann, Saha and Boltzmann distributions can all be derived from the principles of detailed balance alone [5]. Its main application in this thesis, is to be able to relate forward to inverse transition rates and describe both processes with a single reaction cross-section. Appendix B contains an introduction to reaction cross-sections.

The notion of microscopic reversibility relies on the fact that in an LTE state of a WDM system, the occupation levels of ion states are determined by the electron distribution and radiation field. The occupation levels of bound states, as well as the degree of ionisation, are fixed depending on the electron temperature and density. Despite this, there will be forward and inverse transitions taking place. In order for the ion occupations to be constant, the forward and inverse reactions must be in balance and this creates a natural connection between forward and inverse cross-sections.

It is not merely a convenience that one cross-section can be derived from the other. It is in fact a condition for a collisional-radiative code to be able to describe an

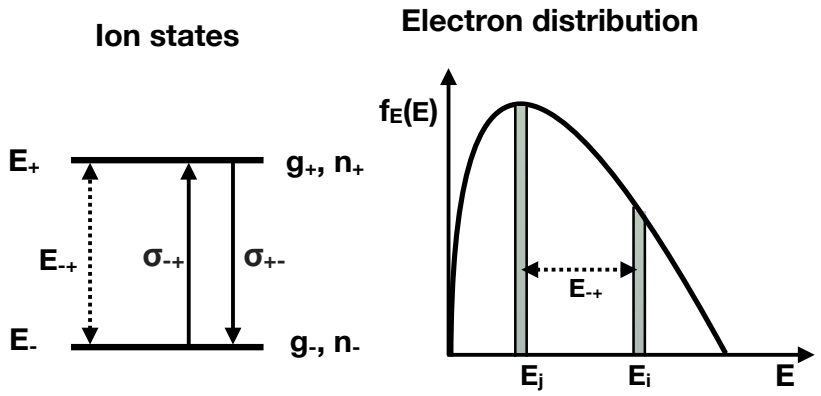

Figure 1.2: Energy diagram for collisional excitation and de-excitation of an ion from energy E_- to E_+ due to collisions with free electrons. Upon a reaction, an electron from a region in the distribution is relocated to another energy due to giving or receiving energy from the ion transition.

equilibrium situation accurately, that all cross-sections satisfy microscopic reversibility relations. Simply taking two cross-sections from independent research efforts may result in a validation of this principle, which is why microscopic reversibility will be applied to every cross-section in this section on ion transition rates.

Taking as an example the bound-bound transitions induced by electron impact, collisional excitation and de-excitation, the atomic transitions are:

$$z + e^- \leftrightharpoons z^* + e^- \tag{1.6}$$

where the incident electron loses energy to excite an ion into an excited state z^*. For a given incident electron energy, we examine this process in Fig. 1.2. In this figure, we see the bound ion states that are separated by an energy $E_{-+} = E_+ - E_-$. In this example, we let the electrons from the distribution function with energies between E_i and $E_i + dE$ collide with the ion population in the lower state. This can produce a collisional excitation event with probability σ_{-+}. The forward rate is then proportional to:

$$S^{CE}(t)/V = n_-(2E_i/m_e)^{1/2}\sigma_{-+}(E_i)f_E(E_i,t)dE. \tag{1.7}$$

After the excitation, the electrons involved will have lost energy and have relocated in phase space to energies between $[E_j, E_j+dE]$. As energy conservation applies, it must hold that $E_{-+} = E_i - E_j$. When these electrons collide with the ion population in the upper state, they can induce a collisional de-excitation reaction whereby they gain energy and end up with energy E_i that they had initially. The collisional de-excitation

rate is proportional to:

$$S^{CDE}(t)/V = n_+(2E_j/m_e)^{1/2}\sigma_{+-}(E_j)f_E(E_j,t)dE. \tag{1.8}$$

In equilibrium, the ion populations are fixed and the forward and inverse rates must be equal. Due to this statement, the cross-sections become linked to each other. In equilibrium, the relation

$$\left(n_-\sqrt{E_i}\sigma_{-+}(E_i)f_E(E_i)\right)^{eq} = \left(n_+\sqrt{E_j}\sigma_{+-}(E_j)f_E(E_j)\right)^{eq} \tag{1.9}$$

yields an explicit form for the cross-sections. Eq. 1.9 is not only valid for bound-bound, but also for bound-free processes involving multiple electrons and possibly photons. This form of microscopic reversibility is far more general than it appears to be. Although it is constructed from equilibrium principles, it holds also for distribution functions that are non-thermal and for ion occupations that don't satisfy LTE relations.

This becomes clear by substituting equilibrium expressions for the population ratio n_-/n_+. For bound-bound transitions, we can substitute the Boltzmann distribution Eq. 1.3 into Eq. 1.9 which gives:

$$\sigma_{+-}(E) = \frac{g_-}{g_+}\frac{E+E_{-+}}{E}\sigma_{-+}(E+E_{-+}), \tag{1.10}$$

where this expression has been generalised across all electron energies and energy conservation links the incoming and outgoing electron. The dependencies on electron temperature and density disappear from the cross-section, making this a generally applicable formula regardless of the equilibration status of the WDM sample. When using double differential cross-sections, Eq. 1.10 sometimes contains a delta function term $\delta(E_i - E_j - E_{-+})$ to express energy conservation as is used in Appendix B, Eq. B.4. This removes the need to integrate cross-section integrals over both the incoming and outgoing energies, as there is a one-to-one relation between them.

When bound-free transitions are involved, the Saha equation Eq. 1.4 should be used. Its exact form will depend on the reaction products involved.

1.1.3 X-Ray Free Electron Lasers

History

First invented in 1971 by John Madey for generating infrared light [1], FELs are machines to generate stimulated emission from electrons moving through a periodic magnetic field. There is no optical resonator cavity which has distinct benefits, and

the laser parameters are entirely determined by the external electromagnetic fields applied to the electrons.

Due to there not being an optical cavity[3], it is possible to obtain pulses of order femtosecond duration, that are near monochromatic. FELs can be tuned for a wide range of emitted wavelengths, from infra-red to hard X-rays. They also come with peak powers beyond $10^{19}\,\mathrm{W/cm^2}$ in a narrow wavelength band, 8-10 orders of magnitude higher than what can be accomplished with synchrotron radiation sources [6].

Claudio Pellegrini proposed to build a FEL for X-rays in the 1990s [7] and it took until 2009 before it was indeed commissioned and made available for experiments at the Stanford Linear Accelerator Centre (SLAC) in California [2]. Driven by the scientific success of this facility, more XFELs have been built around the globe, amongst them Swiss X-ray Free Electron Laser (SwissFEL) in Switzerland [8, 9], SPring-8 Angstrom Compact free electron LAser (SACLA) in Japan [10], Pohang Accelerator Laboratory X-ray Free Electron Laser (PAL-XFEL) in South Korea [11] and at the time of writing, most recently the European X-ray Free Electron Laser (European XFEL) in Germany [12].

Operating principle

An XFEL consists of an electron accelerator that fires electron bunches into an undulator, a series of magnets with alternating poles that cause the electrons to oscillate along their trajectory. When the electrons are accelerated by the magnetic field to move in a sinusoidal trajectory, they emit radiation in the direction normal to the acceleration vector, which is the longitudinal direction along the beam path. This mechanism is the source of light that is generated.

The radiation emitted due to the electrons' acceleration comes at random points in time and would therefore naturally be incoherent. Although the intensity can still be increased by providing a larger electron current, this is sub-optimal as the radiation intensity will only scale linearly with the number of electrons. What makes XFELs so powerful is that the electrons are collected in bunches and made to emit light coherently, thereby making the intensity proportional to the square of the electron current. This is what causes the significant increase in peak brightness when compared to previous generations of light sources, such as synchrotrons [13].

[3]There are also no known materials that reflect X-rays sufficiently well to even consider building a resonator cavity where the light needs to be reflected many times in order to achieve the required gain.

Hans Motz laid out the foundation to create this near-monochromatic, short pulse of coherent emission by applying periodic magnetic fields along the electron trajectory [14]. He expressed the wavelength of the emitted radiation in terms of the undulator spatial period, magnetic field strength and the electron kinetic energy, setting the basis to tune the wavelength. For an electron bunch, the wavelength λ_r observed on the longitudinal axis (the axis the beam moves along) is seen as:

$$\lambda_r = \frac{\lambda_u}{2\gamma^2}\left(1 + \frac{K^2}{2}\right), \tag{1.11}$$

where λ_u is the spatial period of the undulator's magnetic field, γ being the relativistic Lorentz factor, and K the undulator parameter defined as:

$$K = \frac{q_e B_0 \lambda_u}{2\pi m_e c}. \tag{1.12}$$

Here, B_0 denotes the magnetic field amplitude. With this knowledge, the wave length can be easily tuned by changing the magnetic field strength. Eq. 1.11 can be understood by considering the relativistic effects taking place on an electron bunch as it moves through the undulator. From a frame of reference of the electrons, Lorentz contraction takes place and the magnetic field's period is reduced by a factor γ. Secondly, upon emission the relativistic Doppler effect reduces the wavelength further by another factor γ.

The only condition for the tunability is that the electrons are grouped into bunches that are shorter than the emitted wavelength. Previously, this was a restriction for the emitted wavelength, as higher energies (or shorter wavelengths) require the electron bunches to be more closely packed. Pellegrini's proposal in 1992 was therefore to propose a Self Amplified Spontaneous Emission (SASE) XFEL, to get the electron bunches to self-organise. Fortunately, this self-assembly process happens naturally due to the interaction of the electron bunch and its emitted radiation [15].

As depicted in Fig. 1.3, the radiation then interferes constructively, leading to the high gains observed in XFELs despite the beam only making a single pass through the undulator system. When the radiation fields from individual electrons (P_1) add up randomly, the total emitted power scales linearly with the number of electrons N. For the case where the emitted radiation adds up constructively, as the electromagnetic waves are spaced by a regular length λ, the total emitted power scales quadratically with the number of electrons. As it has been developed over the course of over 50 years, the theory of XFELs is much more extensive than what has been discussed here. For more details, I refer the interested reader to publications from Pellegrini

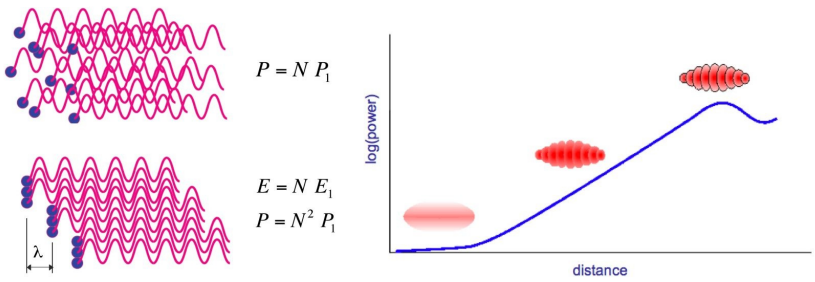

Figure 1.3: The effect of SASE in an XFEL is demonstrated here. When the electrons emit radiation at random times, the total power scales linearly with the number of electrons N. Under the SASE scheme, the interaction between electrons and their emitted radiation enforces a regular spacing λ between the emitted radiation waves, causing them to interfere constructively and raising the power by a factor N^2.

et al. where he gives a historical review of both the experimental and theoretical development of the XFEL in Ref. [16].

Life cycle of X-ray irradiated foil

Irradiating a thin foil target is an attractive way to generate HED systems that are reasonably uniform in electron conditions. When the target thickness is comparable to an absorption length of the X-rays, the front and back of the target are heated to similar conditions [17]. This effect is strengthened by using increasingly intense X-rays, as saturable absorption starts to occur when the front of the target eventually becomes fully ionised, causing the X-rays to penetrate deeper and thus reducing longitudinal energy density gradients [18]. As a result, volumetric heating can be achieved where a small volume of dense plasma lives in similar conditions as it evolves over time.

When a pulse of X-ray photons hits the foil, the most likely process to occur is K-shell Photo-Ionisation (PI). This produces a large fraction of core-hole ionised ions and ensures that the energy density in the system rapidly increases. The core-hole ions primarily decay in two ways, both of which processes involve in an electron from a higher shell dropping down into the K-shell. This can be done by emitting a photon through Spontaneous Emission (SE), or by ejecting another electron through Auger decay. The latter process is far more likely to occur, accounting for roughly 96 % of all decay processes [19]. Auger decay is a process that further increases the degree of ionisation, and it also distributes energy from the ions into the free electron

population. It is therefore the most important heating process taking place in an X-ray created plasma.

After the highly energetic Auger electrons are created, they go on to collide with the remaining ions, causing Collisional Excitation (CE) and Collisional Ionisation (CI) , as well as the inverse processes collisional Collisional De-Excitation (CDE) and Three-Body Recombination (3BR). These collisional processes occur on the femtosecond time scale and act primarily as the driver towards LTE. If it were not for the frequent collisional events, the free electron population would be a dual distribution with cold and hot electrons living in separate regimes. It is not, and this is owed to the collisional redistribution of the free electron kinetic energy.

As the plasma becomes hotter and denser, the remainder of atomic processes begins to take effect. Continuum lowering is an effect that only affects the plasma at a high electron density, and it changes the electronic structure of the ions by lowering the ionisation thresholds. This effect has been measured directly in LCLS-produced plasmas and we will discuss two models to describe the continuum lowering.

Possible experiments

The XFEL has unique properties that enable us to probe materials on the length[4] and time[5] scales of atomic and molecular dynamics [13]. It comes as no surprise that the XFEL revolutionised many branches of material science, biology, chemistry and physics [20, 21].

Of special importance to this thesis is the XFEL's ability to create a solid-density plasma that is isochorically heated with radiation intensities up to $10^{18}\,\mathrm{W/cm^2}$, with small longitudinal temperature gradients in the target [22]. This opens up the possibility to create WDM that can be well characterised, making it suitable for experiments related to WDM.

A large variety of phenomena can be studied with XFELs, ranging from the evolution of the charge state distribution of ions [23], transport properties such as the electrical and thermal conductivity [24–26], optical properties such as the opacity [27,28], collisional rates [29,30], lifetimes of atomic core-hole[6] states [31], and probing the electronic structure as it changes due to the influence of a high electron density [32, 33], and equilibration behaviour for non-equilibrium electron distributions [34].

[4]Due to the photon wavelength being on the order of the Bohr radius.

[5]The femtosecond pulse duration is comparable to the classical orbital period of a valence electron around a nucleus.

[6]These are states with an electron vacancy in an inner shell; generally this refers to the n=1 shell.

All these experiments typically start by first producing a hot, dense plasma with conditions where it is possible to observe a characteristic feature of an atomic transition. The appropriate diagnostic tools, most often emission and transmission spectroscopy, can then shed light on the underlying physics.

1.1.4 Modelling Warm Dense Systems

At the macroscopic level, a transient warm dense system can be characterised by its energy density, equation of state, particle density and transport properties. In order to obtain the macroscopic properties, some knowledge is required of the internal state of the system at a more microscopic level. In this thesis, this amounts to having knowledge of the material's charge state distribution as a function of time. Whereas a solid metal at room temperature has a fixed number of conduction electrons that obey Fermi-Dirac statistics, a transient warm dense system has more degrees of freedom to evolve. The number- and energy density of the free electron population can be much higher than in the solid state. Additionally, the ion states can have a wide variety of vacancies in the electron shell structure. The complete electron-ion system still obeys the quasi-neutrality principle as a rapidly heated or shocked system is confined by the inertia of the ions.

Due to the high kinetic energy of the free electrons, they can collisionally induce excitations or ionisations in the bound ion states. In solid-density plasmas, this leads to a large collection of possible charge state configurations that can occur. The state of the system can be expressed by the population of each configuration, having defined what these configurations look like. In this work, the super-configuration construct is used to express the occupation numbers of bound electron shells. Only the principal quantum number n is used to denote a state, and super-configurations simply count how many electrons are bound with each quantum number. States are denoted in the $K^aL^bM^c$ notation which means that there are a electrons in the K-shell ($n = 1$), b electrons in the L-shell ($n = 2$), and c electrons in the M-shell ($n = 3$). When more bound shells are occupied, the notation can be extended. This is a simplified description when compared to the full relativistic quantum mechanical characterisation of an ion state that includes spin and angular momentum (referred to later as detailed configurations). The advantage is that there are far fewer super-configurations to keep track of, rather than the intractably large number of detailed configurations.

The warm dense system evolution can be computed with radiative-collisional codes that make use of the super-configuration framework, or possibly hybrids of super- and

detailed configurations. Each of them account for the population dynamics by linking ion states to each other through their atomic transition rates. Ion states can evolve into other states through atomic transitions, some of which occur spontaneously, or under the influence of a collisional or radiative stimulus. Computing the transition rates for each ion population, a coupled system of equations in the form of the Master equation arises for the ion populations. From the time-dependent population, other material properties such as the opacity, emissivity, electron- density and energy can be derived. One of the most valuable diagnostic tools is the ability to compute an emission spectrum that can be compared to experimental results.

The non-LTE radiative-collisional codes used in our group are CCFLY and its predecessor SCFLY. The codes are designed to be consistent with each other and lean on the same experimental benchmarks. SCFLY has been verified experimentally on low-Z systems with high pressure ionisation (fewer states), created by > 1 keV X-rays. Examples include verifying the population evolution of XFEL-irradiated neon, measured by Young *et al.* [35] and modelled by Orlando Ciricosta [36]. Further benchmarks include modelling the aluminium K-α emission spectra [22,37], measurements of IPD in Al, Si, Mg and oxide mixtures [32, 38]. Finally, SCFLY was also benchmarked on optical properties with a series of absorption [17], opacity [28] and energy density [39] measurements.

The combination of these experiments led to the development of an atomic-kinetics module where the rates, continuum lowering, radiation transport and emission spectra were all experimentally verified. A review paper by Orlando Ciricosta discusses the experimental validation, as well as model approaches used in SCFLY [40]. The equations of motion for a warm dense system are formulated in Section 3.2.

1.2 Author contribution

It must be stated that the research conducted in the process of writing this thesis is largely a collaborative effort. The experimental work involved contributions from research groups in Spain, South Korea, California, Germany, the Czech Republic and of course the UK where this work was written. Various arrangements of people took part in experiments before and during my DPhil time, and they made it possible for me to make a modest contribution to the field of research.

The research presented is not an exhaustive list of all the activities undertaken during my DPhil. I composed the chapters in a way that only highlights the areas where my contribution has been instrumental. The research can be divided between

computational and experimental work, with the computational part directed towards expanding our group's atomic-kinetics modelling suite CCFLY by writing a module that can describe non-equilibrium electron behaviour. CCFLY and its predecessor SCFLY are amongst the most-used research tools in our group, and they have been used in numerous high-profile publications.

All earlier code versions operated on the assumption that the electron population lives in an equilibrated (thermal) distribution function, a Maxwellian profile. This assumption works well for lighter elements that are pumped with soft X-rays, because their evolution is largely governed by collisional effects causing the electrons to rapidly assume a thermal distribution. It will break down for experiments done with hard X-rays of $\mathcal{O}(10\,\mathrm{keV})$, as these will produce more energetic electrons that need more time to equilibrate. My contribution enables our group to use the CCFLY code to model the evolution of higher-Z warm dense materials irradiated with hard multi-keV X-rays.

In the new CCFLY version, the electron distribution function can take on any arbitrary shape depending on the electron-electron and electron-ion interactions in the system. The evolution of the distribution function was tracked with the Fokker-Planck equation, an approximation of the Boltzmann collision integral. In addition to integrating the elastic Fokker-Planck operator into the atomic-kinetics code, this work also involved generalising the physics models for all the rate formulas of all atomic transitions into a cross-section integral form. The elastic Fokker-Planck equation and its conservative properties are discussed in Chapter 2. Inelastic electron-ion interactions and their contributions to the Fokker-Planck equation are discussed in Chapter 3.

The experimental part of my thesis focuses on measuring the rate of collisional ionisation and recombination in warm dense magnesium. In these collisional processes, the charge of an ion is either increased (ionisation) or reduced (recombination) due to a collisional interaction with the free electrons. For WDM studies, both processes heavily influence the time evolution of the degree of ionisation, as well as the equilibration behaviour of both the ion and electron populations. Furthermore, collisional rates are relevant to diffraction imaging applications on biological samples, as they relate to the rate of radiation damage formation [41].

In Chapter 4, an experimental dataset is presented from which the collisional ionisation rate for a solid-density, optically-thin magnesium plasma can be measured. The samples are created and probed with a single bright pulse of X-rays. This was the first direct measurement of such a kind and has been published in Physical Review

Letters [30]. Through some variation of the XFEL conditions, the collisional rates can be measured in a range of plasma conditions and degrees of continuum lowering, allowing for a more accurate measurement. The measurement is accompanied by some theoretical work: the data is presented together with a newly constructed parametric collisional cross-section model that is consistent with data obtained from dilute and dense plasma experiments[7]. The experiment itself was conducted by my other co-authors in the month before I started my DPhil.

1.3 Acknowledgements

The work presented here has received input from many people in research groups all over the world. I would like to acknowledge the value of their input and thank all collaborators for their contributions. Furthermore, I would like to gratefully acknowledge the financial support offered by grants from the Royal Society and the United Kingdom Engineering and Physical Sciences Research Council (EPSRC).

The experiment conducted at the SXR beamline of LCLS in California was proposed and carried out by the majority of the co-authors in the resulting publication [30]. At the time of the experiment, I had not yet started my DPhil degree. I want to express my thanks for the diligent way in which the experimental data has been collected and for valuable discussion during the analysis.

Extensive use was made of the collisional-radiative code SCFLY and later its successor CCFLY, originally written by R.W. Lee and H.-K. Chung and updated by O. Ciricosta. Nearly all previous experiments conducted in our Oxford research groups have added to our knowledge and expanded our atomic-kinetics suite. Dr. M. Kasim has been a key figure in recasting the SCFLY Fortran code into the object-oriented C++ code CCFLY. His knowledge on object-oriented programming was essential and he wrote the core architecture of the code that I connected my non-thermal electron module to. Dr. S. Ren also contributed to the technical implementation of the non-thermal electron module.

I also received theoretical support from within and outside the UK, most notably on the subjects of constructing and implementing collisional cross-section models. The implementation of these models has become one of the key components of the Fokker-Planck scheme to model non-equilibrium electron dynamics. I'm thankful for

[7]The electron density range examined here spans across 8 orders of magnitude, between ($10^{15} - 10^{23}\,\mathrm{cm}^{-3}$)

the fruitful discussions on atomic rate models with A.G. de la Varga, E.V. Fernandez-Tello, P. Velarde, S. Rose, G. Tallents, H.-K. Chung and A. Robinson.

Due to the computational nature of much of the work, extremely useful input also came from people in the Computer Science department. I want to express special thanks to T. Steeples for assisting in setting up the Catch2 unit- and system testing framework in our C++ code. These tests were used to verify the consistency between the thermal and non-thermal electron models for the special case of using a Maxwell-Boltzmann electron distribution. In addition to validating the non-thermal electron module within this framework, I also used it to generate a large fraction of the data and figures presented in Chapter 2 and 3. The insights I gained into systematic debugging and automated testing methods made the model implementations significantly more reliable, and will make it easier to maintain the code in the future.

Lastly, I want to thank my supervisors Dr. S.M. Vinko and Professor J.S. Wark for their guidance over my DPhil project. They played a key role in many areas, particularly in the experimental work that led up to our publication, and helped me get familiar with the concepts in a field that was still somewhat new to me at the start of my DPhil project.

Chapter 2

Elastic Electron Collisions in Atomic Kinetics

Contents

2.1 Introduction

Warm dense systems can be characterised by their high density of free electrons, in this thesis generally of order 10^{23} cm^{-3}. These free electrons act as an intermediary that can store thermal and electrostatic potential energy. In addition to the multitude of possible interactions between electrons and ions in a warm dense system, the electrons also interact with each other through elastic collisions.

The elastic collisions redistribute momentum and kinetic energy amongst the electrons and therefore play an important role in determining the overall state of the free electron population. Due to the elastic nature of these long-ranging Coulomb collisions, they conserve total vector momentum and kinetic energy. It is the subject of this chapter to describe the elastic collisional processes numerically, while imposing the proper conservation laws.

Although the physics describing the individual motion of charged particles under the influence of a potential is well-known, there are several practical complications that hamper the application of electromagnetic theory to describe electron behaviour in warm dense systems.

Firstly, the number of particles is intractably high, with electron densities being on the order of $\sim 10^{23}\,\mathrm{cm}^{-3}$ for hohlraum densities in Inertial Confinement Fusion (ICF) or X-ray Free Electron Laser (XFEL)-produced plasmas. A complete description of a system of electrons would be to track the position and velocity vectors over time for each electron. In order to capture all electrons in a cubic volume of a typical length scale of interest, for instance a Debye length[1], this would require tracking an impractically high number of electrons. Even the most powerful supercomputers are currently unable to perform such a task.

Secondly, in regimes with electron densities this high, the electrons can no longer be considered to be independently moving particles. A characteristic of Warm Dense Matter (WDM) is that the free electrons are strongly coupled to each other, thereby defining a quantum many-body physics problem. The picture of individual electrons moving in a pre-defined potential landscape should be replaced by a treatment in which the electrons undergo collective motion.

Thirdly, even if the above-mentioned complications could be overcome and one could compute a wave function for the total free electron population, the information

[1]The Debye length is ill-defined in this density regime, due to a Debye sphere not containing a significant number of electrons. The physical interpretation of screening is therefore not valid and in principle, one shouldn't make use of this classical plasma physics parameter for describing warm dense systems.

content would be so large that the results would need to be condensed down for further analysis and interpretation. The same would apply if one wanted to compute physical parameters of the warm dense system, e.g. atomic transition rates, transport properties or equilibration time scales.

What remains is the challenge to capture the behaviour of the free electron population in a way that can be practically implemented, while maintaining sufficient degrees of freedom to describe the relevant physics. An efficient method to do this stems from the kinetic theory of gases. Rather than attempting to track the motion of individual particles, this kinetic theory provides a statistical framework to describe particle populations in terms of their energy or velocity distribution function. The distribution function is the main parameter of interest in the discussion of the free electron description, and it can also be used to describe the inelastic collisional interactions of warm dense systems.

The subsequent sections provide an overview of the equations of motion for the electron distribution function and lay the foundation of the numerical schemes to study fast electron dynamics. A distinction will be made between an approach that assumes thermal equilibrium in the electron population, and a more generalised method that can describe non-equilibrium electron behaviour.

2.2 Distribution functions

2.2.1 Definitions

In this Subsection we will describe the mathematical description of the particle distribution function, and how it relates to the physical quantities in a WDM system. The distribution function, $f_v(\boldsymbol{x}, \boldsymbol{v}, t)$, is defined such that

$$f_v(\boldsymbol{x}, \boldsymbol{v}, t)\mathrm{d}\boldsymbol{x}\mathrm{d}\boldsymbol{v} \tag{2.1}$$

is the expectation value of the number of electrons[2], in an infinitesimal spatial volume $\mathrm{d}\boldsymbol{x}$, and velocity-space volume $\mathrm{d}\boldsymbol{v}$, at position $\boldsymbol{x}$ and velocity $\boldsymbol{v}$ at time t. The combination of position- and velocity-space that may be up to 6-dimensional[3] will be referred to as the phase space. The distribution function is effectively a particle density in phase space, and behaves in similar ways to a probability density function. It is

[2]In this thesis, the particles of interest will always be electrons, although this theory holds for any collection of identical fermions.

[3]6-D phase space would be made up of three spatial dimensions, and a further three dimensions in velocity-space.

a useful representation that can both capture physical quantities, as well as provide a computationally efficient framework for evaluating them. In the following sections we will review how the distribution function can be used to describe particle interactions, as well as how to extract physical quantities from this distribution function.

Physical parameters can be extracted from the distribution function by evaluating its moments, or if another perspective is preferred, by applying the relevant operator to the distribution function. In the context of operators, we apply an operator $\hat{A}(\boldsymbol{x}, \boldsymbol{v})$ to the distribution function and compute its expectation value by as:

$$\langle A(\boldsymbol{x}, t) \rangle = \int \mathrm{d}\boldsymbol{v} \hat{A}(\boldsymbol{x}, \boldsymbol{v}) f_v(\boldsymbol{x}, \boldsymbol{v}, t). \tag{2.2}$$

Choosing the operators such that they represent a physical quantity of interest, we can compute quantities such as the particle density. The density at a particular position $\boldsymbol{x}$ and time t can be computed by using the unit operator, which corresponds to the zeroth moment with respect to velocity as the number density is velocity-independent, as:

$$\begin{aligned} n_e(\boldsymbol{x}, t) &= \int f_v(\boldsymbol{x}, \boldsymbol{v}, t) \, \mathrm{d}\boldsymbol{v} \\ &= \int 4\pi v^2 f_v(\boldsymbol{x}, v, t) \, \mathrm{d}v, \end{aligned} \tag{2.3}$$

where in the second integral, the volume element $\mathrm{d}\boldsymbol{v}$ is computed as $4\pi v^2 \mathrm{d}v$, an integral over the magnitude of the velocity that makes use of spherical symmetry.

If required, the total number of particles can be computed by further integrating the density over space. Similarly to the electron density in Eq. 2.1, the momentum density of electrons with momentum $m_e \boldsymbol{v}_0$ can be expressed as $m_e \boldsymbol{v}_0 f_v(\boldsymbol{x}, \boldsymbol{v}, t)$. The expectation value of momentum $\boldsymbol{P}(\boldsymbol{x}, t)$ at a position $\boldsymbol{x}$ and time t therefore becomes

$$\int m_e \boldsymbol{v} f_v(\boldsymbol{x}, \boldsymbol{v}, t) \, \mathrm{d}\boldsymbol{v}. \tag{2.4}$$

In Eq. 2.4, the integration over velocity-space cannot be simplified by making use of spherical symmetry as the momentum is a vector quantity. It can be observed that the momentum density is proportional to the first moment of the distribution function. The energy density of electrons with kinetic energy $\frac{1}{2} m_e |\boldsymbol{v}_0|^2$ is $\frac{1}{2} m_e |\boldsymbol{v}_0|^2 f_v(\boldsymbol{x}, \boldsymbol{v}, t)$ and the concentration of kinetic energy $E_{kin}(\boldsymbol{x}, t)$, held by all the particles can be computed as:

$$\begin{aligned} E_{kin}(\boldsymbol{x}, t)/V &= \int \frac{1}{2} m_e v^2 f_v(\boldsymbol{x}, \boldsymbol{v}, t) \, \mathrm{d}\boldsymbol{v} \\ &= \int 2\pi m_e v^4 f_v(\boldsymbol{x}, v, t) \, \mathrm{d}v. \end{aligned} \tag{2.5}$$

This is the second moment of the distribution function, where v denotes the velocity magnitude $|\boldsymbol{v}|$. Even more physical quantities related to plasma physics (or alternatively, fluid dynamics) can be computed from the distribution function. For instance, the bulk flow velocity $\boldsymbol{V}$ can be computed by applying the operator $\hat{A}(\boldsymbol{x}) = n_e(\boldsymbol{x})^{-1}\boldsymbol{v}$. Defining the random particle velocity $\boldsymbol{v}_r$ as

$$\boldsymbol{v}_r = \boldsymbol{v} - \boldsymbol{V}, \tag{2.6}$$

we can compute the temperature by applying the operator $\hat{A} = \frac{1}{3}n_e^{-1}m_e v_r^2$, provided the particle system is in a state of local thermal equilibrium[4]. The relation for the particle temperature T is then given as:

$$k_B T(\boldsymbol{x}, t) = \frac{1}{3}m_e n_e^{-1}(\boldsymbol{x}, t) \int v_r(\boldsymbol{x}, \boldsymbol{v}, t)^2 f_v(\boldsymbol{x}, \boldsymbol{v}, t)\, \mathrm{d}\boldsymbol{v}, \tag{2.7}$$

where k_B denotes the Boltzmann constant. It is possible for different particle species to co-exist at different temperatures, even when they are in direct interaction with each other. This can only occur in non-equilibrium situations, as collisional interactions between particles would eventually eradicate any differences in energy concentrations. It should be noted that when the different particle species have very different masses, for instance in a proton-electron plasma, the equilibration time for species to equilibrate with each other can be far longer than for the species amongst themselves [42]. This observation justifies the omission of interactions between electrons and cold ions when considering the equilibration process of the electron distribution. The ion-electron scattering events are efficient at establishing isotropy, but the energy transfer is hampered by the large difference in particle mass. In gases, or in plasmas with a lower density such that they are not in the coupled regime, there are more fluid quantities that can be computed directly from the distribution function. However, in this thesis that concerns matter in the strongly coupled regime, the distribution function will be primarily used to compute atomic transition rates with the cross-section formalism.

In summary, the distribution function has a large informative capacity, being able to capture the bulk behaviour of a gas-like particle distribution in a concise form. This is due to the function having a 3-D spatial, 3-D velocity and temporal dependency; a total of seven independent parameters. The drawback to this approach is that in order to compute changes to the distribution, we need to consider these additional dependencies, leading to a great computational complexity. It can be more convenient to reduce the number of free parameters where possible at the expense of informative content, as we will explore in the next section.

[4]Having local thermal equilibrium is also the requirement for being able to define a temperature.

2.2.2 Transforming distribution functions

In the previous subsection we outlined the definition of the particle distribution and its uses in computing physical quantities such as a density, temperature and bulk flow velocity. We can consider the distribution function to be a density map that depends on seven parameters; three for space, three for velocity and one for time.

It is not convenient to work with the full seven-parameter dependencies in every situation, as it significantly increases the computational complexity of tracking the distribution over time. We will consider some physical regimes where the distribution can be described with fewer, and other parameters to make it more tractable. In the rest of this section we will explore the process of mapping the distribution function from one representation to another, for instance from velocity-space to energy-space.

In isotropic media, that is media with properties that are uniform in all directions, it is not always strictly necessary to separate the three velocity components. Rather, we can consider the velocity magnitude $v = \sqrt{\boldsymbol{v} \cdot \boldsymbol{v}}$ to drop two degrees of freedom. If in addition to being isotropic, the material can be estimated to be (locally) uniform, the space dependence can be dropped and what remains is a distribution with only a velocity magnitude and time dependency.

Particle interactions, such as elastic collisions, are often described in terms of their momentum rather than in terms of velocities. In this context, it is useful to be able to transform the velocity distribution to a momentum distribution, or more generally, be able to map one parameter space onto another. This can be done rather straightforwardly for any transformation where there exists a one-to-one mapping between the representations. For a transformation of a distribution function $f_X(x)$ in parameter space x, into another distribution $g_Y(y)$, through a known mapping $y(x)$, the density function $g(y)$ can be derived to satisfy the following relation:

$$g_Y(y) = f_X(x)\left|\frac{\mathrm{d}x}{\mathrm{d}y}\right|. \tag{2.8}$$

This ensures that the density of particles in some interval of parameter space, a physical quantity, is invariant under a transformation of the parameter space. For demonstration purposes, we can examine a case where distribution $f(x)$ is being transformed to the representation $g(y(x))$, illustrated in Fig. 2.1. Here, we consider the number of particles with an observable parameter x satisfying $a < x < b$, which is given by the integral

$$\int_a^b \mathrm{d}x\, f(x).$$

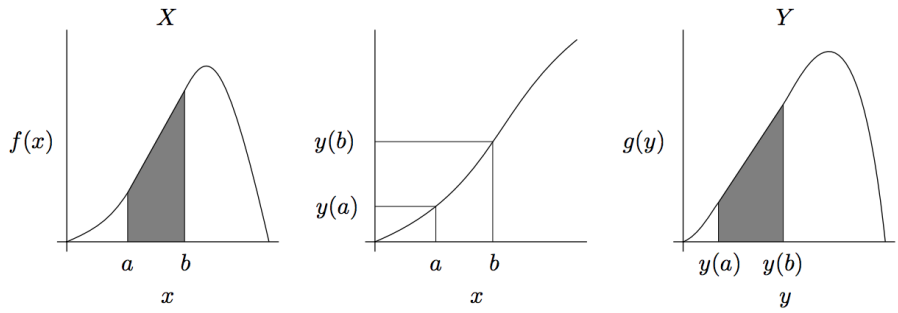

Figure 2.1: Transformation of a density function from parameter space x onto $y(x)$. The distribution functions change accordingly to preserve the density through the relation described in Eq. 2.8.

Under the transformation $x \to y(x)$, the particle number in this interval becomes

$$\int_{y(a)}^{y(b)} g(y)\,\mathrm{d}y.$$

Eq. (2.8) describes this transformation mathematically, allowing us to change the representation of distribution functions at will to whatever parameter space may be more convenient. Applying this to the specific case of electron distribution functions, we can make a transformation from a velocity-space to a momentum-space picture of the electron distribution. Noting again that the distribution relates to a particle density, this is the quantity to preserve under transformations. We denote f_v to be the velocity-space distribution and f_p to be the momentum-space distribution. Omitting possible spatial and temporal dependencies, and considering only the respective magnitudes of the velocity and density, a particle density of particles with velocity v is:

$$f_v(v_0)\mathrm{d}v = f_p(p_0)\mathrm{d}p, \tag{2.9}$$

where $p_0 = mv_0$ and $\mathrm{d}p = m\mathrm{d}v$ denotes a small momentum fluctuation around p_0. This is only valid for the non-relativistic case, although corrections can be made to apply the same approach to the relativistic regime. It becomes clear that in order to represent the same particle density, the distribution in momentum-space must abide the following relation:

$$\begin{aligned} f_p(p) &= f_v(v)\frac{\mathrm{d}v(p)}{\mathrm{d}p} \\ &= \frac{1}{m} f_v(v). \end{aligned} \tag{2.10}$$

Similarly, a velocity distribution can also be expressed in terms of energy. The energy-space representation is particularly useful for describing inelastic particle collisions,

or interactions with another particle species such as photons in isotropic media. In the spherically symmetric non-relativistic case,

$$\begin{aligned} f_E(E) &= 4\pi v^2 f_v(v) \frac{\mathrm{d}v(E)}{\mathrm{d}E} \\ &= \frac{4\pi\sqrt{2E}}{m^{3/2}} f_v(v) \\ &= \frac{4\pi v(E)}{m} f_v(v). \end{aligned} \tag{2.11}$$

There is no principle objection to constructing a relativistic energy-space representation of the particle distribution function, as is discussed in more detail in [43].

2.2.3 Maxwell-Boltzmann distribution

One of the most common distribution functions observed in nature and used in atomic kinetic theory is the Maxwell-Boltzmann (MB) distribution. Originally derived for weakly-interacting gases, this distribution describes the momentum distribution of a large particle collection in local thermodynamic equilibrium. Every classical particle distribution, provided there is conservation of kinetic energy and particles in a fixed volume, will eventually equilibrate into a MB distribution through inter-particle collisions that redistribute the kinetic energy. For this reason, the MB distribution is often also referred to as the thermal distribution. It should also be mentioned that the thermal distribution maximises the entropy, another indication that it is a state of equilibrium. In energy space, the MB distribution for a single particle species is given by:

$$f_{MB}(E) = 2n_e \sqrt{\frac{E}{\pi}} (k_B T)^{-3/2} \exp\left(-E/k_B T\right). \tag{2.12}$$

This distribution describes the probability of any one particle in the system to be found at a particular kinetic energy. For illustrative purposes, the distribution is plotted for various temperatures in Fig. 2.2 so we can examine the properties of this function in more detail. As is expected, the peak of the distribution shifts towards higher energies with increasing temperature. In hotter plasmas or gases, one is therefore more likely to find particles with a higher kinetic energy; the distribution is also broadened more. The energy with the highest likelihood can be found at the peak of the distribution where

$$\frac{\partial f_{MB}}{\partial E} = 0, \tag{2.13}$$

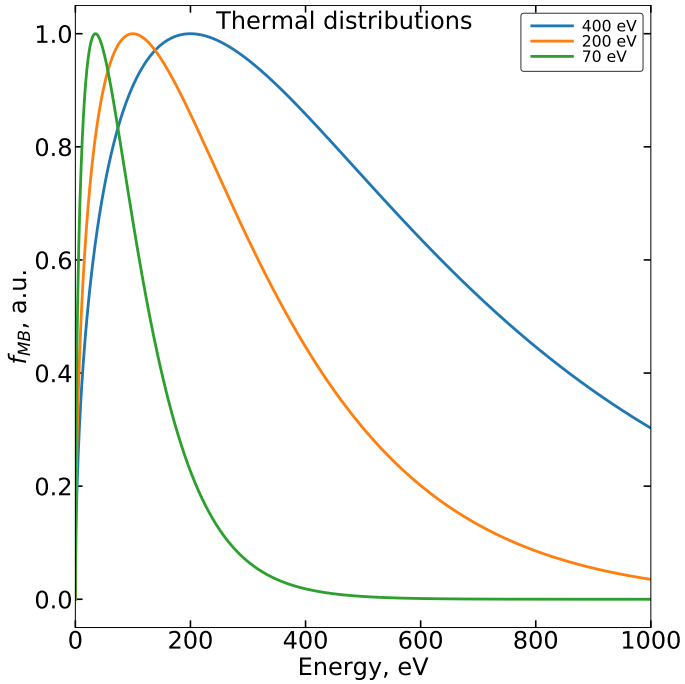

Figure 2.2: Maxwell-Boltzmann functions for a single particle distribution at different temperatures. All distributions are normalised by maximum to unity for visibility reasons.

and this condition is satisfied at $E = \frac{1}{2}k_BT$. The mean energy, however, is much higher and can be computed by averaging over the distribution through

$$\begin{aligned} \langle E \rangle &= \int_0^\infty E\, f_{MB}(E)\, \mathrm{d}E \\ &= \frac{3}{2}k_BT. \end{aligned} \tag{2.14}$$

The expectation value of the kinetic energy, also expressed as $\frac{1}{2}m\langle v^2 \rangle$, is equal to $\frac{3}{2}k_BT$. This result is consistent with the average energy obtained from applying the equipartition theorem to three degrees of translational motion.

The MB distribution is a useful approximation of the real distribution function when the time scale of inter-particle collisions is much smaller than any other process that adds or subtracts energy to the particle system.

The typical time scale required to reach a thermal distribution through the equilibration of a given particle distribution can vary across many orders of magnitude, depending on the conditions of the plasma system. The particle density plays a particularly important role in determining the equilibration time scale, as does the nature of the inter-particle collisions. For instance, there can be short-range interactions best described as head-on collisions or collisions mitigated by a force with a short

spatial range. Alternatively, collisions can be dominated by long-range interactions, such as Coulomb interactions. In this case, there can also be many-body interactions provided the particle density is sufficiently high and the description becomes more complicated.

In the next section, a framework will be discussed that describes the evolution of an arbitrary distribution function under the influence of both elastic inter-particle collisions. This will lead to a time-dependent description of the distribution function, rather than only having information about its final state in equilibrium.

The velocity- or energy distribution function provides a useful, concise way of describing the properties of a large collection of particles in warm dense systems. It eliminates the necessity to track individual particles, while still being able to describe macroscopic properties of the material. The distribution function can have any arbitrary shape, depending on how particles are added or removed to the system, how they are perturbed by external fields, and finally how they interact. An important distribution function is the MB distribution, a state that is attained after many inter-particle collisions that redistribute the kinetic energy in order to maximise the entropy.

2.3 Fokker-Planck Equation

This section will describe the equilibration process of an arbitrary distribution towards a MB distribution. The force that mitigates the interactions between particles is the long-ranging Coulomb force, a central force with $1/r^2$ behaviour. As the Coulomb potential scales with $1/r$, the strong coupling and large length scales cause the scattering processes to be dominated by small-angle collisions. Due to the nature of small-angle collisions, the Fokker-Planck framework is suitable for describing the electron-electron interactions in the system [44]. The equation itself is derived from the Boltzmann equation in Appendix A, and it is taken as a starting point for implementing a numerical framework that solves it.

2.3.1 Elastic collision operator

Provided that the electron distribution of an electron system is known at a certain point in time, its evolution can be described by the Fokker-Planck equation. The derivation and validity conditions of this equation are discussed in Appendix A. In

energy space[5], the evolution is described as

$$\frac{\partial f_E(E,t)}{\partial t}\Big|_{ee} = -\frac{\partial}{\partial E}\Big[a(E)f_E(E,t)\Big] + \frac{1}{2}\frac{\partial^2}{\partial E^2}\Big[D(E)f_E(E,t)\Big]. \tag{2.15}$$

Eq. 2.15 closely resembles a drift-diffusion equation with non-constant coefficients. The elastic collision terms can alter the shape of the distribution, while preserving particle density and total kinetic energy. It is a requirement that any numerical scheme used to solve this equation implicitly conserves these quantities. It is not possible to manually correct the distribution to conserve either of these quantities without violating the other conservation law. Additionally, the distribution function should equilibrate at the correct speed towards a MB distribution.

For the description of the conservative numerical scheme, it is more convenient to cast the Fokker-Planck equation into an operator form in which the operator is made to obey all relevant conservation laws. Adherence of the scheme to all conservation laws can be verified by computing the distribution moments directly from its theoretical form, as well as numerical experiments to test the operator. Following the lines of available literature on this topic, this collision operator will be given in its velocity-space representation.

In velocity-space, the Fokker-Planck equation is a fourth-order, three-dimensional, time-dependent and non-linear equation. There is, however, symmetry that can simplify the problem significantly. In this context, Rosenbluth rephrased the collision operators into potentials that are now referred to as the Rosenbluth potentials [45]. The potentials are constructed as a series expansion of spherical harmonics, and allow for the construction of a conservative numerical scheme.

First derived by Bobylev and Chuyanov [46], and cast into a non-relastivistic collision operator by Tzoufras *et al.* [47, 48], this formulation is given in integro-differential operator form by:

$$\left(\frac{\partial f_v(v)}{\partial t}\right)_{ee} = \frac{4\pi\Gamma_{ee}}{3}\frac{1}{v^2}\frac{\partial}{\partial v}\left[\frac{1}{v}\frac{\partial W(f_v(v),v)}{\partial v}\right], \tag{2.16a}$$

where the function $W(f_v(v),v)$ is given by:

$$W(f_v(v),v) = f_v\int_0^v f_u u^4 \mathrm{d}u + v^3 f_v\int_v^\infty f_u u \mathrm{d}u - 3\int_v^\infty f_u u \mathrm{d}u\int_0^v f_u u^2 \mathrm{d}u. \tag{2.16b}$$

The function $W(f_v(v),v,t)$ contains the time evolution of the electron distribution due to to electron-electron collisions that conserve particle number and kinetic energy.

[5]The distribution can always be transformed in a manner described in Subsection 2.2.2.

The pre-factor of Eq. 2.16a is defined as $(4\pi/3)\Gamma_{ee} = (4\pi/3)4\pi q_e^4 \ln\Lambda/m_e^2$, where q_e is the electron charge, and $\ln\Lambda$ denotes the Coulomb logarithm. For clarity, all velocity integrals in Eq. 2.16b are computed as integrals over spherical shells. It can be shown that when a thermal distribution is inserted into Eq. 2.16b, the time-derivatives are zero, reiterating the notion that the MB distribution is a stable solution. The fact that the effects of dynamical friction and energy diffusion as a result of Coulomb collisions can be captured into a single elastic collision operator implies that the friction and diffusion are related. It can be shown that indeed there is a direct relation between the Rosenbluth potentials associated with both quantities, therefore creating a direct link between the friction vector and diffusion tensor [49, 50].

The interpretation of the Coulomb logarithm in Eq. 2.16a is ill-defined for strongly coupled conditions, as a Debye sphere around an ion is only lowly populated with electrons, thus violating the assumptions used to construct the underlying plasma screening theory. The exact interpretation and numerical value of an appropriate Coulomb logarithm would be an interesting subject of research, but it is not being considered here. The Coulomb logarithm for electron-electron interactions in hot plasmas ($T > 36.2$ eV) is computed with a semi-empirical formula constructed by Huba [51]:

$$\ln\Lambda = 23.5 - \ln\left(n_e^{1/2} T^{-5/4}\right) - \left[10^{-5} + \left(\ln T - 2\right)^2/16\right]^{1/2}, \tag{2.17}$$

where the density and temperature have units cm^{-3} and eV, respectively.

The first paper by Tzoufras *et al.* [47] normalises the parameters in Eqs. 2.16a and 2.16b in a way that is more appropriate for electrons moving at relativistic velocities. Throughout this thesis, the electron velocities encountered are in the non-relativistic regime and this particular normalisation would result in parameters that become either intractably small, or so close to unity that the variation lies on the order of a floating point error. Therefore, the author adopted the normalisation introduced in a later paper by Tzoufras *et al.* [48]. This form uses dimensionless parameters defined as:

$$\begin{aligned} q &\longmapsto q/q_e \\ t &\longmapsto \left(\frac{4\sqrt{2\pi} n_e q_e^4 \ln\Lambda}{3\sqrt{m_e}(k_B T)^{3/2}}\right) t \\ v &\longmapsto v/v_t \\ m &\longmapsto m/m_e \\ f_v &\longmapsto \frac{\left(v_t\sqrt{2\pi}\right)^3}{n_e} f_v \end{aligned} \tag{2.18}$$

Eq. 2.18 is not limited to electrons and can be generalised to other identical particles. The velocity v_t is the thermal velocity $\sqrt{3k_BT/m_e}$ and the normalisation for time makes use of the e-e deflection time that will be introduced in Eq. 2.25. This normalisation simplifies the homogeneous Fokker-Planck equation into:

$$\left(\frac{\partial f_v(v)}{\partial t}\right)_{ee} = \frac{1}{v^2}\frac{\partial}{\partial v}\left[\frac{1}{v}\frac{\partial W(f_v(v),v)}{\partial v}\right], \tag{2.19}$$

where it must be taken into account that all parameters (and derived parameters) are made to be dimensionless; the velocity, time, charge, mass, and the distribution function itself. Eq. 2.19 is useful for propagating distribution function forward in time to model an equilibration process, as numerical stability is easier to achieve with normalised parameters. However, when computing any physical parameters for comparison with experiments or other calculations, the normalisation Eq. 2.18 must be reversed. Due to having to invert the normalisation, the specific choice of normalisation is in principle arbitrary.

The finite-difference form of Eq. 2.19 in normalised units is given as [47, 48]:

$$\frac{\Delta f_n}{\delta t} = \frac{1}{v_n^2}\frac{1}{\delta_n}\left[\frac{1}{v_{n+1/2}}\frac{W_{n+1}-W_n}{\delta_{n+1/2}} - \frac{1}{v_{n-1/2}}\frac{W_n - W_{n-1}}{\delta_{n-1/2}}\right], \tag{2.20}$$

with $v_{n+1/2} = \frac{1}{2}(v_n + v_{n+1})$, $\delta_n = \frac{1}{2}(v_{n+1} - v_{n-1})$, $\delta_{n+1/2} = v_{n+1} - v_n$, $f_n \equiv f_v(v_n)$ and $W_n \equiv W(v_n)$ defined by Eq. 2.16b. In order to be able to compute the derivatives, the definition $v_{-1} = 0$ is followed which leads to $W_{-1} = W(0) = 0$. The changes in density and energy as a result of in- or outflow of particles at the upper energy boundary are proportional to $\frac{W_{N-1}-W_{N-2}}{v_{(N-1)-1/2}\delta_{(N-1)-1/2}}$. To enforce energy and density conservation, it is required to set $W_{N-2} = W_{N-1}$. It should be noted that $(N-1)$ is the last grid point, as the indexing is zero-based.

For large velocities, Eq. 2.16b can be evaluated through standard discretisation techniques such as the chained trapezoid method. For velocities that are small compared with the characteristic velocity v_c of the distribution, the second and third term in Eq. 2.16b cancel up to $\mathcal{O}(v^5)$. It is necessary to modify the numerical scheme to capture this, in order for the distribution to equilibrate to a Maxwellian. This can be done by writing $W(v_n)$ as a Taylor series $f_n \approx f(0) + [f_1 - f(0)]\,(v_n^2/v_1^2)$ and

$f(0) = \left(f_0 - f_1 v_0^2/v_1^2\right) / \left(1 - v_0^2/v_1^2\right)$ [47]. This results in:

$$\begin{aligned} W(v_n < v_c) \equiv W_s(v) = f_n \times & \left[f(0)\frac{v_n^5}{5} + \left(f_1 - f(0)\right)\frac{v_n^7}{7v_1^2} \right] \\ & + \left[\left(f_n - f(0)\right) v_n^3 - \left(f_1 - f(0)\right)\frac{3v_n^5}{5v_1^2} \right] \\ & \times \sum_{k=n+1}^{N-1} \frac{1}{2}\left(f_k v_k + f_{k-1} v_{k-1}\right)\delta_{k-1/2}, \end{aligned} \tag{2.21}$$

$$\begin{aligned} W(v_n \geq v_c) \equiv W_l(v) = & f_n \sum_{k=0}^{n} \frac{1}{2}\left(f_k v_k^4 + f_{k-1} v_{k-1}^4\right)\delta_{k-1/2} \\ & + v_n^3 f_n \sum_{k=n+1}^{N-1} \frac{1}{2}\left(f_k v^k + f_{k-1} v_{k-1}\right)\delta_{k-1/2} \\ & - 3\left[\sum_{k=n+1}^{N-1} \frac{1}{2}\left(f_k v_k + f_{k-1} v_{k-1}\right)\delta_{k-1/2} \right] \\ & \times \left[\sum_{k=1}^{n} \frac{1}{2}\left(f_k v_k^2 + f_{k-1} v_{k-1}^2\right)\delta_{k-1/2} \right]. \end{aligned} \tag{2.22}$$

There are no dependencies on the shape of the distribution function in Eqs. 2.21 and 2.22, where the explicit dependence of W on $f_v(v)$ has been omitted from the notation. The method in which they are applied does not affect the density, momentum or energy conservation properties and Eq. 2.21 only contributes to being able to achieve a Maxwellian distribution after equilibration. The authors of Tzoufras *et al.* propose a recipe for selecting v_c as $\frac{3}{2}\Delta v < v_c < v_t$. In practice, where the first few velocities on the velocity grid are as low as possible, this amounts to allocating 2 grid points to resolve v_t and Eq. 2.21 will only be used on the first two nodes. This is also a requirement due to the number of degrees of freedom that Eq. 2.21 offers, as it only contains two free constants f_0 and f_1.

The numerical scheme described by Eqs. 2.20, 2.21 and 2.22 can be integrated with an implicit solver scheme. In this case, a backward Euler (first-order Runge-Kutta) method in the CVODE package is used [52]. The equations of the distribution are evaluated in their velocity-space representation for the elastic electron-electron interactions.

2.3.2 Conservation Laws

The elastic Fokker-Planck collision operator describes electron-electron collisions that redistribute kinetic energy and alter the distribution function over time. For an isolated system with a constant number of particles and energy, there is a unique solution

of the final distribution function, the MB distribution. This solution maximises the entropy and regardless of the initial state, any distribution will evolve towards an MB distribution.

The collisions that facilitate the thermalisation process preserve the number of electrons, their total vector momentum and total energy. In the spherically-symmetric velocity-space representation, the vector momentum cannot be computed and only the particle number and kinetic energy are conserved. This can be formulated by stating that the second, and fourth moment of the distribution function are constant, for any system without sources or sinks and a constant volume:

$$\frac{d}{dt}\left(n_e\right) = 4\pi \frac{d}{dt}\left(\int_0^\infty v^2 f_v(v,t)\,\mathrm{d}v\right) = 0 \;\forall t \tag{2.23}$$

$$\frac{d}{dt}\left(E_{kin}\right) = 2\pi m_e \frac{d}{dt}\left(\int_0^\infty v^4 f_v(v,t)\,\mathrm{d}v\right) = 0 \;\forall t \tag{2.24}$$

Note that the distribution moments are equal to the number density of electrons (Eq. 2.23) and total energy density (Eq.2.24), rather than the absolute values of aforementioned quantities. The absolute number of electrons, momentum and energy can be obtained by integrating these densities over space. In the isotropic systems discussed in this work, this amounts to simply multiplying by the volume.

Before adding inelastic collisional operators at a later stage, it should be verified that Eqs. 2.23 and 2.24 hold for a standalone calculation without ion-electron dynamics. Any possible deviation should fall within the range that can be expected of the numerical accuracy of the algorithm and grid parametrisation used to solve the homogeneous Fokker-Planck equation.

2.3.3 Collisional Time Scales

When we observe the time evolution of a non-equilibrium electron distribution towards its stationary Maxwellian solution, one of the key observables is the equilibration rate. Given the wide variety of possible initial value problems that can be posed, there are several relevant time scales that can be associated with the relaxation process. Each of them represents a physical process that can be defined in terms of a drag or diffusion coefficient in the Fokker-Planck equation, examples being the isotropisation time, the rate of momentum transfer (drag or dynamical friction), and the rate of energy diffusion. In benchmarking the collision operator, it would be ideal if each of these processes could be observed separately. This is not possible due to the inter-dependence of each process and as the functional form of the collision operator suggests, they all take place simultaneously.

This Subsection will list some of the collisional time scales that are relevant for the benchmarking. The main purpose is to obtain orders of magnitude estimates and scaling behaviour in order to better understand the behaviour of the collision operator, as well as to verify the results of time-dependent simulations. They are not exact equilibration rates and the most accurate estimates follow from the simulations themselves.

The elastic collision operator for an electron plasma introduces a natural time unit for the rate of change of the distribution function. This would be a characteristic duration that is needed before appreciable changes can be observed in a non-equilibrium distribution function as a result of elastic inter-particle collisions. Chandrasekhar and Spitzer proposed an approach for computing equilibration time scales using the concept of releasing test particles in a background field, and examining the collective effects of collisions on the test particles [42, 53]. A time scale that can be obtained directly by substituting a thermal distribution into the Fokker-Planck equation Eq. 2.16a is the electron-electron deflection time:

$$\tau_D = \frac{3\sqrt{m_e}(k_B T)^{3/2}}{4\sqrt{2\pi} n_e q_e^4 \ln \Lambda}. \tag{2.25}$$

This is the average time required to deflect a test particle off its original trajectory by 90 degrees as a result of interactions with its surrounding thermal background field [54]. The deflection time is the time scale at which anisotropy is removed from the system. Eq. 2.25 only considers the effect of electron-electron collisions. In systems that also contain ions, the deflection time is a factor $(Z + 1)$ shorter due to ion-electron interactions, where Z is the proton number.

Although the deflection time Eq. 2.25 is defined for a fully thermal distribution, it is a useful order of magnitude to consider for non-equilibrium problems because it is simple to compute and relates to other relevant time scales. Computing the deflection time for non-thermal distributions can be done by adopting an effective value for the temperature as $T \mapsto \frac{1}{n_e}\frac{2}{3}\int E f_E(E)\,\mathrm{d}E$ [55]. The effective temperature is the temperature of the thermal distribution that the system will have once equilibrium has been established. In strongly non-thermal systems, the deflection time can only be loosely associated with its physical interpretation.

For a warm dense system with a density $n_e = 1.0 \times 10^{23}$ cm^{-3} and an electron temperature $T = 50$ eV, the deflection time is approximately $1.2/\ln\Lambda$ fs. This indicates that the effects of electron-electron interactions on the distribution function should become noticeable within a few femtoseconds.

The two most noticeable effects that can be observed in time-dependent simulations of the distribution function are dynamical friction (energy exchange) and energy diffusion. Friction removes any differences between the average energy between particle groups, e.g. between a bulk of thermal electrons and a hot electron perturbation. Energy diffusion removes sharp distribution gradients in energy space by dispersing energy across an increased range, and acts as a smoothing effect. The two processes happen on similar time scales, but they have different proportionality relations with respect to the test particle energy. These relations can be retrieved directly from the Rosenbluth potentials from which the collision operator is derived [56].

The time scale associated with friction is the slowdown time τ_s, defined as the rate of momentum transfer between the two particle species. It depends on the bulk temperature and test particle's initial kinetic energy and is given by [42]:

$$\tau_s(E_i, n_e, k_B T) = \frac{\sqrt{\pi}}{6} \frac{1}{G(\sqrt{E_i/(k_B T)})} \left(\frac{E_i}{k_B T} \right)^{1/2} \tau_D, \tag{2.26}$$

where the function $G(x)$ is defined by Chandrasekhar as:

$$G(x) = \frac{\Phi(x) - x\Phi'(x)}{2x^2}, \tag{2.27}$$

with $\Phi(x)$ being the error function given by:

$$\Phi(x) = \frac{2}{\sqrt{\pi}} \int_0^x \exp(-y^2)\, \mathrm{d}y. \tag{2.28}$$

There exist two useful asymptotic forms that can be readily evaluated without the need for tabulated results for Eq. 2.27: one for an incoming particle with an energy $E_i \ll k_B T$ and the other for $E_i \gg k_B T$. The relation between the slowdown time and the deflection time can be made explicit by expressing their ratio as:

$$\tau_s(E_i, n_e, k_B T) = \begin{cases} \frac{1}{2}\tau_D, & \text{if } E_i \ll k_B T \\ \frac{\sqrt{\pi}}{3} \left(\frac{E_i}{k_B T} \right)^{3/2} \tau_D & \text{if} E_i \gg k_B T, \end{cases} \tag{2.29}$$

The slowdown time is the time constant with which the mean velocity of a test particles is reduced exponentially. In this context, Spitzer defined the "mean of a group of test particles" as the mean of repeated iterations with one test particle, and not as an ensemble average over multiple test particles simultaneously[6].

[6]If we had considered an ensemble of test particles decelerating as a group, the difference between $\langle v^2 \rangle$ and $\langle v \rangle^2$ would be the variance of the test particle velocity distribution. Naturally, the variance is zero for a single test particle.

Despite its simple functional form, the slowdown time only has a limited applicability, as in many cases it cannot be used without also considering the distortion of the test particle distribution as a result of energy diffusion. The proportionality behaviour is the most relevant content for a benchmark, as the intertwining of friction and diffusion makes it difficult to estimate precise relaxation times from the collision operator alone.

The effect of diffusion can be demonstrated by considering an initially mono-energetic test particle distribution. In order for this non-equilibrium distribution to relax to a Maxwellian, the energy needs to be diffused over the full energy range (while possibly eradicating mean energy differences through friction). Chandrasekhar has shown that a mono-energetic distribution is dispersed into a Gaussian in (vector) velocity-space [57]. For the special case of an isotropic, thermal distribution its corresponding width is described by a diffusion coefficient D that grows linearly with energy:

$$D(E_i) \propto E_i \frac{1}{\tau_D}, \tag{2.30}$$

where τ_D is the deflection time Eq. 2.25. Due to only considering one particle species, the time scales for isotropisation, momentum transfer and energy diffusion are related through the same time unit τ_D that will be used throughout the remainder of the Chapter. For test particles being introduced into a thermal field, the energy diffusion coefficient has useful asymptotic forms for energies far above and below the thermal energy:

$$D(E_i) = \begin{cases} \frac{16\sqrt{\pi}}{3\sqrt{2}} \frac{n_e q_e^4 \ln\Lambda}{m_e^{3/2}(k_B T)^{1/2}}, & \text{if } E_i \ll k_B T \\ \frac{2\pi n_e q_e^4 \ln\Lambda}{m_e^{3/2} E_i^{1/2}}, & \text{if} E_i \gg k_B T, \end{cases} \tag{2.31}$$

The asymptotic forms for high energies of both the slowdown and diffusion coefficients are an underestimate of the relaxation time for test particle velocities much higher than thermal, despite this being the range where the asymptotic forms can be constructed. Most importantly, the proportionality between energy diffusion and friction components Eqs. 2.29 and 2.31 is different. It is possible to vary the starting conditions of initial value problems in a way that demonstrates the mechanism of effect of each effect, while both are present at the same time.

2.3.4 Energy Discretisation

A thermal electron distribution can be uniquely described by its electron density and temperature, capturing all information in these two parameters alone. For an

arbitrary non-equilibrium distribution, the energy grid points need to be chosen such that they adequately capture the relevant degrees of freedom. The Fokker-Planck numerical scheme will be integrated into an atomic-kinetics code at a later stage, hence it is important that the energy grid is chosen such that it can be re-used to perform the inelastic ion-electron interactions that will be added to the description.

Firstly, the energy grid needs to be fine in the low-energy range up to $\sim$5 eV to be able to account for electrons ionised through pressure-ionisation. Having sufficient grid points in this range is also crucial for the stability of the elastic Fokker-Planck collision operator [47]. Secondly, the grid needs to reach high enough to capture the energetic electrons produced through photo-ionisation and Auger decay with energies of multiple keV. A rule of thumb is that the maximum grid energy should be twice the maximum energy that a free electron can obtain through an ion transition. In cases where electron-electron collisions achieve complete energy transfer, an outgoing electron can have the sum of the two incoming energies. It is not a likely event and truncating the grid at twice the maximum expected energy is a good approximation[7].

A natural choice of grid type that satisfies these criteria could be a logarithmic energy grid. Its properties would be desirable, having a fine grid spacing at the lower energies and a coarse spacing at larger energies in order to cover the range efficiently. However, the use of logarithmic energy or velocity grid spacings has shown to cause convergence problems in the Ordinary Differential Equation (ODE) solver. To overcome these challenges, a uniform, linear energy spacing has been used throughout this chapter. In the velocity-space representation in which Fokker-Planck equation is solved, the velocity grid is then non-uniform and its spacing grows as $\frac{1}{2\sqrt{v}}$. This demonstrates that the numerical scheme can still be used with a non-uniform velocity grid, allowing for the possibility to create more grid points at specific velocity ranges of interest.

2.4 Elastic Collisions Benchmarking

The isotropic Fokker-Planck equation that describes inter-particle collisional dynamics for small-angle collisions has been cast into a form proposed by Tzoufras *et al.* in Eq. 2.19 that conserves particle number and energy. The proposed elastic collision operator can be used to compute the time-evolution of any arbitrary electron distribution, provided it is known at some point in time.

[7]Truncating the grid at twice the maximum expected energy omits third-order processes and above.

The collision operator for a one-species plasma evolving due to elastic collisions alone has several general properties:

- Conservation of particle density
- Conservation of vector momentum (not of practical use here in the isotropic case)
- Conservation of total energy
- If the distribution function was positive at $t = 0$, it remains positive at all times: $f_E(E, t) > 0$, $\forall E$, $\forall t$)
- The Maxwell-Boltzmann distribution f_{MB} is stationary: $\frac{\partial f_{MB}}{\partial t} = 0$
- All solutions approach the thermal distribution: the Maxwell-Boltzmann distribution is the only stationary solution.

The last three properties follow from Boltzmann's H-theorem. A further criterion may be added, namely that the time evolution of an arbitrary distribution towards its Maxwellian solution takes place within the correct time range depending on its initial condition. No rigorous proofs for these statements will be provided in this thesis and instead it will be made plausible through some test cases that the elastic collision operator satisfies these conditions for the initial value problems and time-dependent simulations relevant to warm dense matter studies.

It is important to perform a benchmark on the elastic collision operator's conditions before adding inelastic ion-electron interactions that further complicate the time evolution as well as the conditions it should satisfy. To that end, the benchmark in this Chapter focuses exclusively on closed electron systems with a constant particle- and energy density. In this case, any density or energy fluctuations or drifts should fall within a range that can be expected of the accuracy of the numerical scheme, the ODE solver and the energy grid parametrisation used to compute the time-dependent distribution function. The inelastic interactions will be considered in Chapter 3.

In this section, a few test cases are presented where the distribution function is initialised to various non-equilibrium states before being left to evolve over time. Each of these cases serves to validate the requirements outlined above. The first case involves a thermal distribution that is perturbed by a comparatively small, mono-energetic population with a kinetic energy higher than the bulk thermal energy. This case has physical significance as it resembles the situation after a photo-ionisation

event in a warm dense system. Furthermore, it is suitable for a benchmark of the effects of dynamical friction that occur in Coulomb collisions. An added benefit is that the overall distribution function remains close to equilibrium, meaning that the system has a reasonably well-defined temperature and deflection time.

The other test cases introduce progressively larger perturbations to the distribution, up until the distribution becomes nearly mono-energetic. Under such circumstances, the energy diffusion term of the collision operator dominates over friction, allowing for a different type of benchmark. These cases are also useful to verify the conservation laws under a more significant exchange of energy amongst electrons, as well as a qualitative assessment on whether or not the final state is indeed the MB distribution. Another benefit of benchmarking the collision operator with large non-thermal populations is that it also adds non-linear effects to the interaction process. The non-thermal population is able to affect the mean kinetic energy of the thermal bulk population and vice versa, before the initial two populations equilibrate to a new temperature.

2.4.1 Lightly-perturbed thermal distribution

The first test case is an initial value problem where the distribution is initialised to a delta-perturbed thermal distribution of the form:

$$f_E(E, t = 0) = (1 - \alpha) f_{MB}(n_e, k_B T) + \alpha n_e \cdot \delta(E - E^*) \quad \text{with}\, 0 < \alpha < 1, \tag{2.32}$$

where $\delta(E - E^*)$ denotes the Dirac delta function with a perturbation strength $\alpha \in \mathbb{R}$. In this Subsection, $\alpha \ll 1$, but other benchmarks will use progressively stronger perturbations. The perturbation energy E^* is initially set to values above the thermal energy. This case corresponds to a small number of mono-energetic hot electrons being added to an electron plasma in Local Thermodynamic Equilibrium (LTE) with itself. In the computational scheme, the delta function is discretised in energy space and does have a finite width. The plasma conditions remain reasonably well-defined throughout the interaction because the mean kinetic energy is only changed by a few percent as a result of the perturbation.

The time-evolution of these initial value problems is computed through the elastic collision operator Eq. 2.20. In discretising the collision operator, the function $W(v, f(v))$ is computed with Eq. 2.21 for the first two grid points and Eq. 2.22 is applied to the remainder of the grid. The simulations are performed with the CCFLY radiative-collisional atomic-kinetics code that can be used to compute the XFEL-matter interaction. It can treat an ensemble of inelastic interactions between

light, electrons and ions, but it is used in a simplified form here that only considers electron-electron interactions. Throughout the evolution, the majority of the electron population is expected to remain in the MB distribution that it is initialised to, barring minor heating effects as a result of the energy contained in the perturbation. The total density and the total energy should remain constant up to the level of numerical accuracy.

The test scenario outlined above has physical significance, as it closely resembles an electron distribution in a warm dense system shortly after an ionisation event. Depending on the nature of the ionisation reaction, the free electrons can appear at near-zero kinetic energies (e.g. pressure-ionisation), or at energies far above the bulk temperature as is the case for Auger decay [34]. This situation will occur frequently in an atomic-kinetics code that considers interactions between ions, electrons and a radiation field.

The calculations presented in this Subsection are initialised with the parameters listed in Table 2.1. The Coulomb logarithm as computed from Eq. 2.17 is a slowly-

e-e calculation settings for a lightly-perturbed Maxwellian	
Parameter	Value
n_e	$2.0 \times 10^{23}\,\mathrm{cm}^{-3}$
T	40 eV
$\ln \Lambda$	≈ 0.84
# energy grid points	300
Minimum energy	0.01 eV
Maximum energy	500 eV
α	2.5×10^{-2}
E^*	$\{100, 300\}$ eV

Table 2.1: The simulation settings used to evaluate the elastic Fokker-Planck collision operator in this Subsection. The initial distribution is a lightly-perturbed thermal distribution. Inelastic interactions between ions and electrons are omitted.

varying function of the temperature and density. For the purpose of the test cases outlined here, it is treated as a constant.

2.4.1.1 Time Evolution

The first test case features a perturbed Maxwellian as defined in Eq. 2.32 with the parameters given in Table 2.1 and a perturbation strength $\alpha = 2.5 \times 10^{-2}$. This means that 97.5 % of the electron population is in local thermal equilibrium at a temperature of 40 eV. The perturbation that holds the remaining 2.5 % of the electrons is placed

at 300 eV, before the electron populations are left to equilibrate. As a consequence of the perturbation, the effective temperature is raised to 44 eV and this should be the temperature of the combined system once thermal equilibrium has been established through collisional interactions.

The distribution function is plotted in Fig. 2.3 for various points in time. The time is measured in units of the electron-electron deflection time Eq. 2.25 that is approximately equal to 6.0×10^{-16} s for these plasma conditions. The runtimes for the simulations in this Subsection are far longer than what would normally occur in the study of material states pumped by an XFEL where the interaction times of interest lie in the femtosecond regime [58]. This is done for demonstration purposes, as well as for gaining insight into the equilibration and conservative properties of the elastic collision operator. Most of the distribution remains nearly stationary over

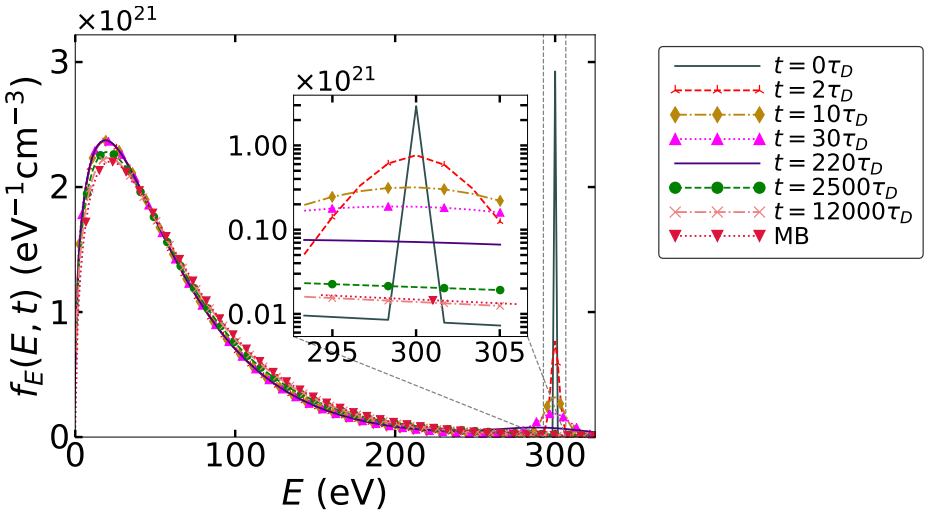

Figure 2.3: The time-dependent distribution function of a Maxwellian perturbed by a hot mono-energetic electron population represented as a delta-function centred around 300 eV. The bulk population absorbs the energy from the more energetic population. The time is measured in deflection time units $\tau_D \approx 6.0 \times 10^{-16}$ s as computed through Eq. 2.25. Other simulation parameters are listed in Table 2.1.

time and the region around the perturbation energy is brought into focus. For this particular case with $E^* \gg k_B T$, relaxation of the distribution to its thermal state can only be achieved by transferring kinetic energy from the perturbation to the bulk to cool down the perturbed electrons, and for the bulk to equilibrate at a temperature that is 4 eV higher than its initial value during or after the slowing down process. As can be seen in Fig. 2.3, the distribution of the non-thermal population is broadened towards higher and lower energies in the region of the perturbation energy within a few deflection times.

The perturbation is rapidly broadened (energy diffusion) at early times, as expected by examining the energy diffusion coefficient Eq. 2.30. Diffusion is driven by the large gradient of the distribution function around the perturbation energy, meaning it is faster at early times. The process of eradicating the energy difference between the thermal bulk and perturbation takes longer, and requires several dozens of deflection times before the non-thermal tail merges with the thermal bulk. This is more noticeable on a logarithmic scale.

In addition to the cooling of the hot electrons, part of the equilibration process involves heating the bulk population. Although this initial value problem is formulated as having a small perturbation around thermal equilibrium, it does involve a significant transfer in kinetic energy amongst the electron populations. The mono-energetic electrons with a kinetic energy of 300 eV represent only 2.5% of the total electron density, but they contain over 10% of the total energy in the system. Approximately $\frac{1}{12}$ of the energy in the system needs to be redistributed amongst the electrons in order to reach equilibrium.

The observations so far are in agreement with the asymptotic forms of the diffusion coefficient and the slowdown time. At energies far above thermal, the proportionality of the diffusion coefficient on energy causes it to dominate over dynamical friction. This finding can also be substantiated by Eq. 38 in Tzoufras *et al.* [47] and substituting Eq. 2.32 for the distribution function. The narrow distribution becomes wider and extends its range in both directions of energy-space, albeit with a slight bias towards smaller energies. This bias is caused by the friction component. The same behaviour can be observed in Fig. 2.4 by examining the time-derivatives that result from substituting Eq. 2.32 into the collision operator Eq. 2.16a at $t = 0$ with $\alpha = 2.5 \times 10^{-2}$.

The negative derivative directly on the perturbation energy shows that the peak is being reduced in magnitude, as would be expected. The energy is dispersed in the positive and negative direction, causing the initially narrow distribution to broaden. There is a slight bias towards lower energies caused by dynamical friction. Little energy leaves the region in energy-space $[E^* - \Delta E,\, E^* + \Delta E]$ around the perturbation energy $E^* = 300$ eV (for $\Delta E \sim 1$), a statement substantiated by the net outflow of electrons that can be computed as:

$$\int_{E^*-\Delta E}^{E^*+\Delta E} \frac{\partial f_E(E, t=0)}{\partial t}\, \mathrm{d}E. \tag{2.33}$$

Evaluating Eq. 2.33 for the value of $\Delta E = 10$ eV with the time-derivatives shown in Fig. 2.4, the resulting net outflow of electrons is approximately 2.0×10^{33} cm^{-3}s^{-1}

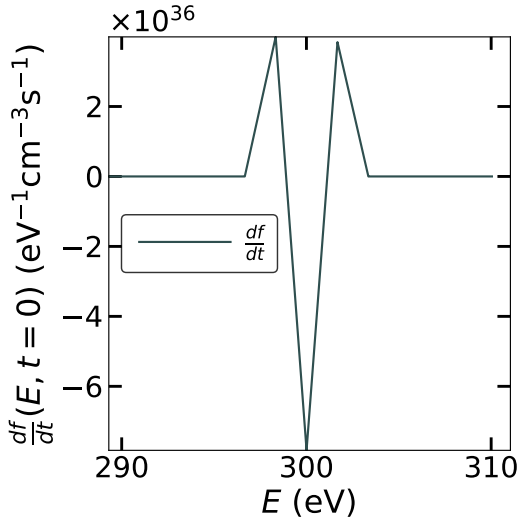

Figure 2.4: The time derivatives in the energy region around a delta-function perturbation to a thermal distribution function at $t = 0$. The derivatives immediately after initialisation show that the perturbation is being dispersed which will cause the distribution to broaden in both directions. This particular case was computed for a value of $\alpha = 2.5 \times 10^{-2}$, although the figure looks similar for other values of the perturbation strength of up to $\frac{1}{10}$.

which is much smaller than the magnitude of the time-derivative at the perturbation energy would suggest. Narrow perturbations with a higher mean kinetic energy than the background field are effectively dispersed by elastic e-e collisions within a few to several tens of deflection times, depending on the perturbation strength. Conversely, the elastic collisions are less efficient at transferring larger fractions of kinetic energy from a hot mono-energetic perturbation to a colder bulk population. This does not hamper the relaxation process of an ion-electron system, as there are in fact many other atomic transitions that can facilitate larger energy transfers and thereby complement the role of dynamical friction.

The presence of elastic collisional interactions between electrons can cause changes to a solid-density electron distribution on a time scale of several femtoseconds. This time scale is comparable to those associated with atomic state lifetimes and transitions that can occur in XFEL-irradiated plasmas [35]. Due to this similarity in collisional time scales, electron-electron collisions play an important role in smoothing out the distribution function and counteracting the formation of peaks in the energy-space electron density. This equilibrating effect can take place over the full electron energy range because there is no energy threshold for elastic e-e collisions to take effect, and it does not require the presence of any ion charge states.

After examining an initial value problem where the perturbation energy lies far above the bulk temperature, the next test case considers the situation in which the perturbation overlaps more with the thermal bulk distribution. When the perturbation is placed around an energy $E^* = 100$ eV, as shown in Fig. 2.5, the equilibration process is noticeably faster. The deflection time here is slightly different, with $\tau_D \approx 5.4 \times 10^{-16}$ s, as the equilibrium temperature of this initial value problem is lower. In order to restore equilibrium, it is not necessary to slow down the perturbing electrons as much as for the case of $E^* = 300$ eV and the perturbation has mostly vanished after 40 deflection times. This finding is consistent with the difference in slowdown time for electrons at an initial energy of 100 eV (when compared to 300 eV). The slowdown time is proportional to $(E^*)^{3/2}$, hence the slowdown time for the $E^* = 100$ eV case can be expected to be $\left(\frac{300}{100}\right)^{3/2} \approx 5.2$ times longer, neglecting the difference in diffusion rates due to the $\propto E^{1/2}$ proportionality on the diffusion rate.

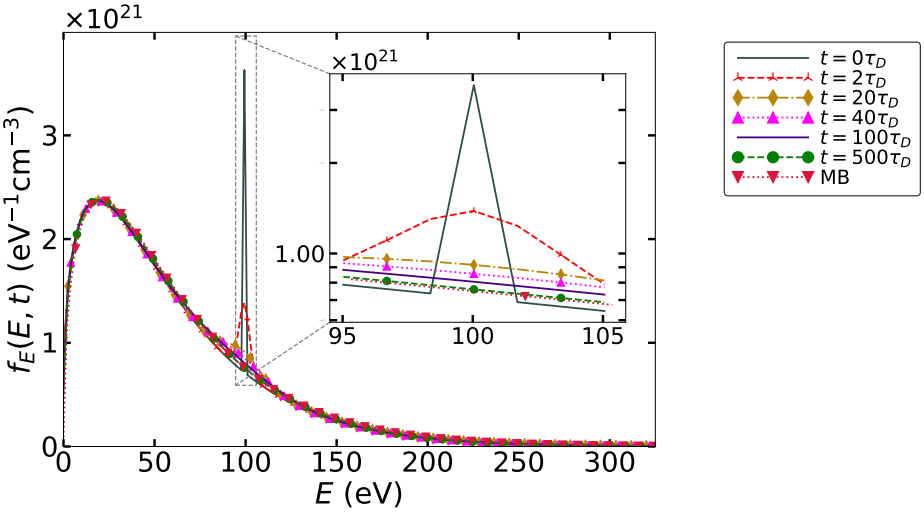

Figure 2.5: The time-dependent distribution function of a Maxwellian perturbed by a hot electron population represented as a delta-function centred around 100 eV. The distribution function equilibrates towards a single Maxwellian by absorbing the more energetic electrons into the bulk. The time is measured in deflection time units $\tau_D \approx 5.4 \times 10^{-16}$ s as given by Eq. 2.25. Other simulation parameters are listed in Table 2.1.

The perturbing population vanishes within several tens of deflection times, while thermal equilibrium is reached after several hundreds of deflection times. The energy difference between the perturbation energy and final temperature is smaller, hence it requires fewer collisional interactions to slow down the perturbing population and eradicate the energy difference. As the final temperature of the equilibrated system is also closer to its initial bulk temperature, the equilibration time is further reduced.

Based on the slowdown and diffusion coefficients Eq. 2.29 and 2.31, the time needed in order to reach equilibration can be expected to be shorter for the $E^* = 100$ eV case. The observations of the time-dependent distribution function do not contradict this expectation. Nevertheless, based on visual inspection of the distribution it is up to some level of interpretation where to define the precise point in time from which moment onwards the distribution can be considered to be in equilibrium.

2.4.1.2 Conservation Laws

It is crucial that the algorithm that propagates the distribution function forward in time implicitly preserves the particle density and energy. Due to the fact that these quantities are proportional to the second and fourth moment of the velocity-space distribution function, it is not possible to manually re-normalise the distribution at each time step to correct violations of conservation laws. From the time-dependent distribution function, it appears that the conservation laws are satisfied sufficiently much to not notice any visible deviations from particle- and energy conservation. It is therefore informative to quantify to what level of precision the collision operator can satisfy the conservation laws in numerical simulations.

Figs 2.6 display the computed free-electron density over time for the cases of $E^* = \{100, 300\}$ eV. The density is computed from the distribution moment Eq. 2.3. The

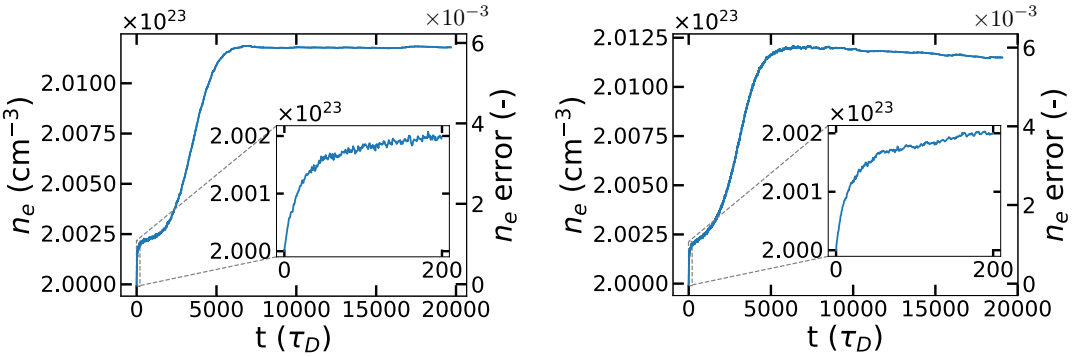

(a) Density for the case $E^* = 100$ eV. (b) Density for the case $E^* = 300$ eV.

Figure 2.6: The computed electron density as a function of time measured in units deflection time. In this system free of sinks and sources, the density is expected to be constant and any fluctuations and drifts are the result of inaccuracies in the numerical scheme or ODE solver. The deviations from perfect conservation are of order $\mathcal{O}(10^{-3})$ over the full time range.

relative error, computed as the fractional difference between the time-dependent value and its initial value, is plotted on the second (RHS) y-axis. There is little difference

between the density evolution when comparing the two perturbation energies. In both cases, the density is conserved up to an error that amounts to approximately 0.1% of the initial density.

There are some fluctuations in the density over time, but most of all an upward trend can be identified as the system moves closer to equilibrium. The time range is 20,000 deflection times which in this case is approximately equal to 10 ps for both systems. This is a long time scale when compared with the typical duration of the XFEL-plasma simulations encountered in this work that usually have run times up to $\sim$ 100 fs. At some point in time when the system has (nearly) equilibrated, the density ceases to fluctuate or drift.

The presence of an upward trend in the density may be a cause of concern when constructing density balances in more complex systems that also include ion-electron interactions. The largest increases in density appear to take place when the system is out of equilibrium, and this situation is ongoing when ion-electron transitions are taking place. Le *et al.* demonstrated that lower levels of fluctuations can be achieved by modelling the distribution function through more sophisticated basis function expansion, where the distribution at each discrete bin is written as a sum series [55]. The numerical accuracy that can be achieved with this approach appears to be bound primarily by floating point round-off errors. With the same discretisation approach and ODE solver as was used in this thesis, the authors achieve a similar numerical accuracy.

Similarly to the density, the closed system holds a fixed amount of energy from its initial time and this energy should be conserved. Figs 2.7 show the computed free-electron energy over time for the cases of $E^* = \{100, 300\}$ eV. The energy is computed from the distribution moment Eq. 2.5. In addition to fluctuations, the total kinetic energy held by the electrons has a downward trend over time. The fluctuations at early times are marginally larger for the $E^* = 100$ eV case which can be explained by the fact that this system equilibrates faster. Over the full evolution, the drift in kinetic energy is an order of magnitude lower when compared to the $E^* = 300$ eV case where there is more energy exchange.

The magnitude of the energy drift that amounts to approximately 0.01-0.1% depending on the perturbation energy, which is comparable to the variation of the density. Again, the duration of the simulation is longer than generally required for XFEL-plasma interactions where the XFEL acts as a pump. As the trends in the energy and density go in opposite directions, it can be deduced that (on average) the most significant errors in the numerical scheme are made at energies below the

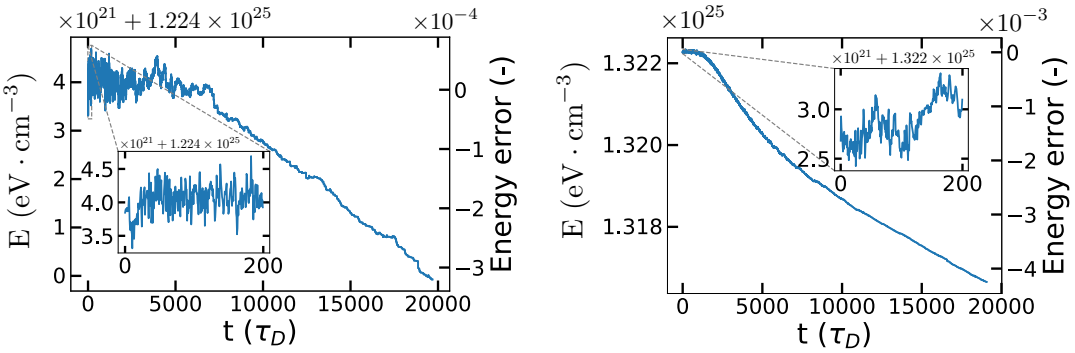

(a) Density for the case $E^* = 100$ eV.

(b) Density for the case $E^* = 300$ eV.

Figure 2.7: The computed electron kinetic energy as a function of time measured in units deflection time. In this closed system, the electron kinetic energy should remain constant. The deviations from perfect conservation are of order $\mathcal{O}(10^{-3})$ over the full time range.

thermal energy. On a net basis, the density increases while the total kinetic energy goes down and this indicates that too many electrons are created in the low-energy range.

Overall, the results concerning conservation laws are satisfactory for atomic-kinetics calculations with a runtime of up to a few hundred femtoseconds during which the distribution does not deviate much from equilibrium. When the distribution is far-removed from equilibrium, for instance as a result of sink or source terms, it should be re-verified that the drifts in energy and density remain at a similar order of magnitude as in the cases discussed here. If problems in the conservation laws occur, the discretisation scheme of the distribution function can be modified to use a different set of basis functions as proposed by Le *et al.* [55].

2.4.1.3 Relaxation Time Scale

After verifying the conservation laws, the last quantity that can be empirically verified is the time scale of the relaxation process. There are multiple physical processes that take place simultaneously, each of which could have its own time scale. For the cases discussed so far, Figs. 2.3 and 2.5 of the time-dependent distribution function show that the equilibration process of a thermalisation process involves several steps that take place simultaneously:

- Hot electrons are decelerated through dynamical friction (or more generally, energy differences between the bulk and the perturbation are removed through friction)

- The distribution of the perturbation is broadened through energy diffusion
- The combined system thermalises at its new equilibrium temperature (this had not yet happened until several hundreds of deflection times when the perturbation in Fig. 2.3 appeared to have vanished).

For a benchmark on the equilibration rate, it would be ideal if the dynamical friction and energy diffusion components could be studied independently. This is not the case, and they act simultaneously to bring a system closer to equilibrium. Through choosing various initial value problems, the role of each component can be demonstrated, but they cannot be completely isolated from each other. An empirical estimate of the relaxation rate is therefore not a direct estimate of either the slowdown or diffusion time scale, but rather of their combined effect.

The relaxation rate can be estimated by comparing the time-dependent distribution with the MB distribution of the same energy and density. The purpose of defining a quantitative measure for the amount of overlap between a distribution and its equilibrium is to avoid the need for retrieving a relaxation rate by visual inspection of the distribution function. Such figures can be useful for ranking the equilibration rate of different initial value problems, but are less suitable for obtaining quantitative estimates for relaxation times.

For a system with a fixed density of particles and energy, or more generally for a system in which the time-dependent density and total kinetic energy are known, the equilibrium distribution that will be reached after sufficient time has passed is known. It is therefore possible to compute the difference $\Delta f_{eq}(E,t)$ between a distribution at a time t and its equilibrium (MB) solution. This yields a construct that can be used to quantify the strength of a perturbation to the equilibrium, and estimate the minimum amount of energy exchange required to reach equilibrium. For these purposes, the non-thermal part of the distribution is defined as:

$$\Delta f_{eq}(E,t) = f_E(E,t) - \widetilde{f}_{MB}\left(n_e, k_B T = \frac{2}{3}\langle E\rangle\right), \tag{2.34}$$

where $\widetilde{f}_{MB}$ is the MB distribution that contains the same particle- and energy density as the current distribution $f_E(E,t)$. In equilibrium, there should be no difference and $\Delta f_{eq}(E,t) = 0$. Unlike the real distribution function, Δf_{eq} is not strictly non-negative.

The non-thermal part of the distribution Eq. 2.34 can be used to deduce physical quantities associated with the equilibration process through its modified distribution

moments. The fractional density of non-thermal particles $\beta_\rho(t)$ that has been introduced to the system can be retrieved up to some approximation by computing an integral that resembles the zeroth distribution moment:

$$\beta_\rho(t) = \frac{1}{2}\frac{1}{n_e}\int_0^\infty |\Delta f_{eq}(E,t)|\,\mathrm{d}E, \tag{2.35}$$

where the factor $\frac{1}{2}$ prevents double-counting. For an arbitrary time-dependent or initial value problem, β_ρ is an estimate of the number of electrons that does not live in equilibrium due to having been injected into the system or otherwise affected in a way that caused the distribution to go out of equilibrium (e.g. by adding external fields). The non-thermal density fraction $0 \leq \beta_\rho(t) \leq 1$ quantifies how far the equilibration process has progressed. When $\beta_\rho = 0$, the system is in equilibrium and $\beta_\rho = 1$ is a completely non-thermal distribution.

For larger perturbation strengths, $\beta_\rho(t=0) \neq \alpha$, because a large perturbation will also change the distribution of the thermal bulk. The necessity for the pre-factor $\frac{1}{2}$ in Eq. 2.35 stems from the observation that the non-thermal part of a distribution always has a zeroth moment of zero[8]:

$$\int_0^\infty \Delta f_{eq}(E,t)\,\mathrm{d}E = 0, \quad \forall t. \tag{2.36}$$

Eq. 2.36 holds because as a consequence of density- and energy conservation, any density excess at a particular energy (peak in the distribution function) leads to an equally large deficit elsewhere. When the electrons exchange energy, eventually these peaks and valleys in the distribution will cancel out. The perturbation strength has the appearance of a density, but it does not imply that only a fraction of the electron population is involved in the energy exchange process. On the contrary, the entire electron population interacts when restoring a non-equilibrium distribution of energy.

Quantities related to the energy exchange can be computed from the Δf_{eq} distribution. Each perturbation introduces an energy $\alpha n_e E^*$ to the system that needs to be (partially) redistributed amongst the electrons in order to establish equilibrium. For stronger perturbations, the energy that needs to be redistributed is smaller than $\alpha n_e E^*$ as a result of bulk heating. The time-dependent scalar quantity $\beta_E(t)$ specifies what fraction of the total energy in the system still needs to be redistributed between the electrons in order to reach equilibrium and is defined as:

$$\beta_E(t) \equiv \frac{1}{2}\frac{1}{\int_0^\infty E \cdot f_E(E,t)\,\mathrm{d}E}\int_0^\infty E \cdot |\Delta f_{eq}(E,t)|\,\mathrm{d}E, \tag{2.37}$$

[8]With the exception of inaccuracies in the conservation laws.

where the denominator is twice the total energy in the system in order to normalise the non-thermal energy fraction to $0 \leq \beta_E(t) \leq 1$. Eq. 2.37 assumes conservation of density and energy and needs a correction when electron sources or sinks are present. Eq. 2.37 is a lower bound of the actual energy exchange taking place, as it only accounts for reshaping the perturbed part of the distribution into a Maxwellian.

Similarly to the non-thermal density fraction Eq. 2.35, the case $\beta_E = 0$ implies that the distribution is thermal and $\beta_E = 1$ is a completely non-thermal distribution. The proportion of β_ρ to β_E can reveal in what energy range the most significant changes to the distribution are taking place.

Eqs. 2.35 and 2.37 are primarily intended to be used as a time tracker for the relaxation process. They should not be interpreted as the fraction of electrons that is still participating in the collisional interactions. On the contrary, the system remains strongly coupled and all electrons in the system are in constant interaction with each other.

Due to small drifts and fluctuations in the density and energy, the time range for which β_ρ and β_E are useful is restricted. Figures on the density and energy conservation (e.g. Fig. 2.7) show that the relative accuracies are capped at $\mathcal{O}(10^{-3})$ for the density and $\mathcal{O}(10^{-4})$ for the energy. Whenever a non-thermal fraction decays to approximately this level, it is unclear whether it is affected by the relaxation process or numerical errors. Despite requiring a more subtle interpretation due to density and energy fluctuations, the fractions will still be shown over larger time ranges.

Fig. 2.8 is produced by computing the non-thermal density fraction Eq. 2.35 for the initial value problems Eq. 2.32 with $E^* = \{100, 300\}$ eV and a perturbation strength $\alpha = 2.5 \times 10^{-2}$. The bulk temperature is 40 eV and the time is measured in deflection time units that are marginally different for the two cases due to a difference in the effective temperature (5.4×10^{-16} s and 6.0×10^{-16} s). The dotted lines are mean-squared error fits of the form

$$\beta = \widetilde{\beta_0} \exp\left(-t/\widetilde{t_r}\right), \tag{2.38}$$

for $0 \leq t \leq 3\tau_D$, where $\widetilde{\beta_0}$ (initial value) and $\widetilde{t_r}$ (decay time) are fit parameters. The fits to the decay times result in values of $\widetilde{t_r} \approx \{9.8 \pm 0.1, 97.4 \pm 0.4\} \cdot \tau_D$ for the cases $E^* = \{100, 300\}$ eV, respectively.

The non-thermal density fraction decays monotonically although this decay declines within several tens of deflection times for the case with the higher perturbation energy. This is due to the role of energy diffusion in the equilibration process. In this system, the mean kinetic energy of background particles is 60 eV, meaning that

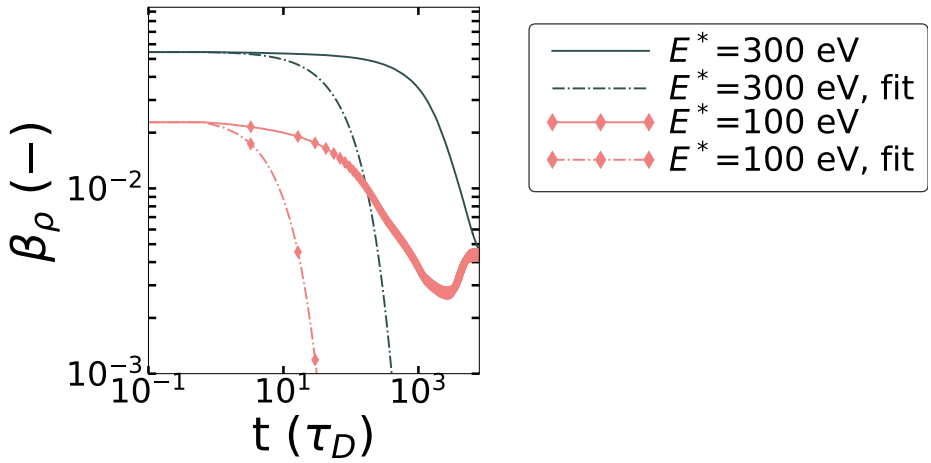

Figure 2.8: The fraction of non-thermal electrons in a lightly-perturbed Maxwellian plasma ($k_BT = 40\,\mathrm{eV}$, $n_e = 2.0 \times 10^{23}\,\mathrm{cm}^{-3}$) for two different perturbation energies E^* and a perturbation strength $\alpha = 2.5 \times 10^{-2}$. The time is measured in deflection time units and the dashed lines are exponential fits for $0 \leq t \leq 3\tau_D$. The perturbation strength decays exponentially at early times, before the decline flattens out.

the energy transfer required to reach equilibrium is relatively small for the case of $E^* = 100$ eV. At a higher perturbation energy $E^* = 300\,\mathrm{eV} = 5 \cdot \frac{3}{2}k_BT$, more energy transfer is needed during the relaxation process and it takes longer for the system to equilibrate.

If the relaxation process were primarily driven by dynamical friction, the difference in decay times would have been a factor $\left(\frac{300}{100}\right)^{3/2} \approx 5.2$ according to the slowdown time Eq. 2.29. That is not the case, and the relaxation time constant differs by a factor $97.4/9.8 \approx 10$. The increase in the relaxation time is larger than the asymptotic form of the slowdown time Eq. 2.29 would predict. This can either be caused by the effects of energy diffusion that are also energy-dependent, or the invalidity of the asymptotic formula in this energy range.

When using the non-thermal energy fraction $\beta_E(t)$, the findings (including fitted relaxation times) are the same and this test case does not lead to a particular preference of $\beta_\rho(t)$ over $\beta_E(t)$ or vice versa. For completeness, the decay of the energy fraction held by the non-thermal electrons is plotted in Fig. 2.9. Qualitatively, Figs. 2.8 and 2.9 are very similar.

2.4.2 Variable perturbation strength

Thus far, some initial value problems have been examined in which the initial distributions were only lightly perturbed from equilibrium ($\alpha \ll 1$). Even for small

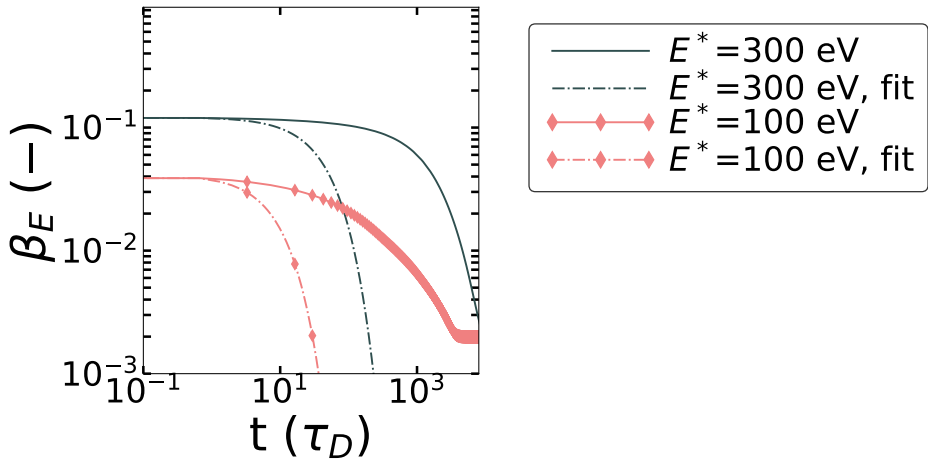

Figure 2.9: The energy fraction of the non-thermal electrons in a lightly-perturbed Maxwellian plasma ($k_BT = 40\,\mathrm{eV}$, $n_e = 2.0{\times}10^{23}\,\mathrm{cm}^{-3}$) for two different perturbation energies E^* and a perturbation strength $\alpha = 2.5 \times 10^{-2}$. The time is measured in deflection time units and the dashed lines are exponential fits for $0 \leq t \leq 3\tau_D$.

perturbations at energies above the bulk temperature, there can be a substantial transfer of energy between the thermal and non-thermal electron populations that is sufficient to slightly heat the bulk temperature of the system. Initially, the perturbation strength was set somewhat arbitrarily to the value of 2.5×10^{-2} in order to be large enough to notice, yet small enough to consider it a linearised perturbation problem. At this point it is unknown how the collision operator performs for initial value problems further removed from equilibrium (larger α), particularly with respect to the equilibration time.

In this Subsection, the perturbation strength α will be varied for the same initial value problem with the perturbed thermal distribution Eq. 2.32. The perturbation energy E^* will be fixed at 120 eV. Rather than choosing the same bulk temperature for all cases, the temperature is adjusted with the choice of α in order to keep the final temperature after equilibration fixed at 60 eV. This means that for a stronger perturbation (that contains more energy), the initial bulk temperature is lowered so that the equilibration temperature is the same for all cases. As a consequence, the effective temperature and derived parameters such as the Coulomb logarithm Eq. 2.17, deflection time Eq. 2.25 and slowdown time Eq. 2.26 are also fixed for all simulations in this Subsection. An overview of the simulation parameters is listed in Table 2.2. The amount of energy that is redistributed amongst the electrons grows with the perturbation strength, whereas the fraction of electrons that needs to be heated decreases with α. This creates a non-linearity that will shed light on the

Simulation parameters for variable α initial value problems	
Parameter	Value
n_e	$2.0 \times 10^{23}\,\mathrm{cm}^{-3}$
T_{eq}	60eV
$\ln \Lambda$	≈ 1.27
τ_D	$\approx 6.3 \times 10^{-16}$ s
# energy grid points	300
Minimum energy	0.01 eV
Maximum energy	500 eV
α	0.01 - 0.30
$k_B T$	56.5 - 59.9 eV
E^*	120 eV

Table 2.2: The simulation settings used in the scan over perturbation strength α to evaluate the non-linear effects of the elastic collision operator. α is varied between 0.01 and 0.30 and the initial bulk temperature $k_B T$ is chosen such that the final temperature of the equilibrated system is always 60 eV. Inelastic interactions between ions and electrons are omitted in this Subsection.

mechanics of the equilibration and conservative properties of collision operator. The time-dependent distribution function for each of these initial value problems is too similar to those of Figs. 2.3 and 2.5 to be able to infer more information than we already have.

A quantitative comparison can be made by computing the density- and energy conservation, as well as the relaxation times for cases with a perturbation strength in the range of $5.0 \times 10^{-3} \leq \alpha \leq 1.5 \times 10^{-1}$. In this range, the bulk temperature varies between 56.5-59.9 eV.

2.4.2.1 Conservation Laws

The cases with a stronger perturbation are more demanding on the collision operator with respect to the conservation laws, because they involve a larger transfer of energy between particles. Furthermore, there are fewer electrons in the system to transfer any excess energy to which introduces a non-linearity in the interaction process. Aside from a different redistribution of energy, there is no principal reason why the conservative properties of the collision operator should manifest themselves any differently.

Fig. 2.10 shows the density error computed for the solution of the time-dependent distribution function through Eq. 2.3 for all values of α. The initial density was $2.0 \times 10^{23}\,\mathrm{cm}^{-3}$ for all cases. The time range is sufficiently long for the system to

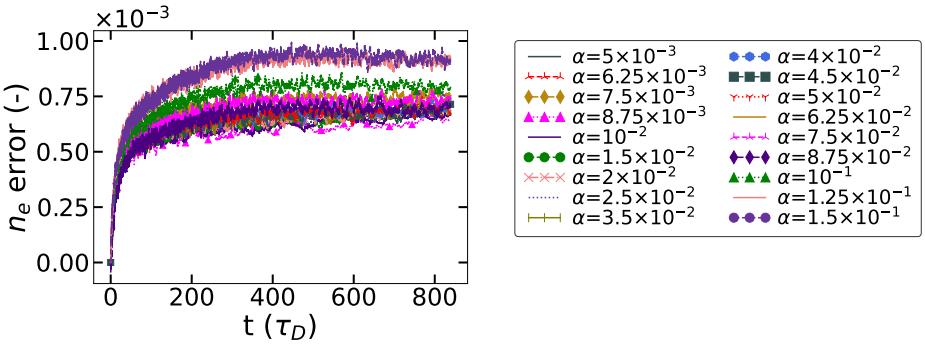

Figure 2.10: The density error as a function of time for a lightly-perturbed Maxwellian for various values of the perturbation strength α. The system is initialised at a density $n_e = 2.0 \times 10^{23}\,\mathrm{cm}^{-3}$ and has no sinks or sources. The largest drifts occur at early times when the distribution undergoes the largest changes as a result of choosing a non-equilibrium initial condition. Overall, the drifts and fluctuations remain within 0.1% of the initial density.

equilibrate and over the full time range, the density drifts and fluctuations remain below 0.1% of the initial density for all time steps and perturbation strengths. In the absence of sinks or sources, the initial density should have remained constant.

The conservation of energy is directly affected by variations in the density. An upward (artificial) drift in density would increase the total energy to the system creation and conversely, a downward drift would take energy out of the system.

Fig. 2.11 shows the energy error computed from the solution of the time-dependent distribution function through Eq. 2.5. The systems are initialised such that the total energy density equals $\frac{3}{2} n_e k_B T_{eq} = 1.8 \times 10^{25}\,\mathrm{eV \cdot cm}^{-3}$ with an equilibrium temperature $T_{eq} = 60$ eV. The energy error has the opposite trend when compared with the density error, as the numerical scheme produces a total energy below the value it should hold. The direction of the trend and the magnitude of the error, which is one order of magnitude smaller than that of the density, indicating that the energy error is being made in the low energy range.

2.4.2.2 Relaxation Time Scale

The non-thermal fraction $\beta_\rho(t)$ can also be computed for initial value problems (Eq. 2.32) with varying perturbation strengths α. The results thereof are plotted in Fig. 2.12. For lower perturbation strengths, the non-thermal fraction β_ρ is lower (as expected) and it decays faster. The thermal part of the distribution is barely affected by the hot electrons and the cooling process is linear.The dynamical friction is equally effective for all values of α as the energy difference compared with the bulk

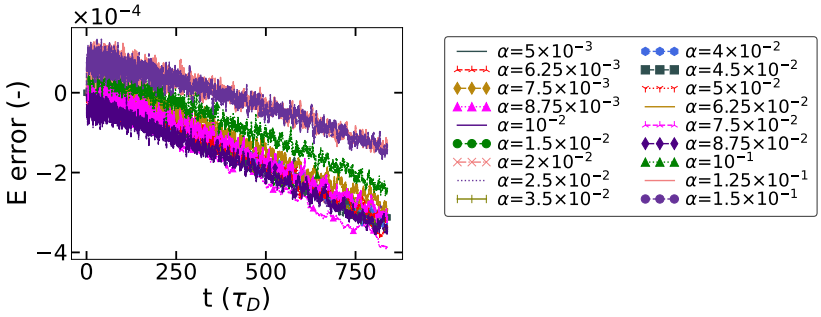

Figure 2.11: The energy error as a function of time for a lightly-perturbed Maxwellian for various values of the perturbation strength α. The sink- and source-free system is initialised at a total kinetic energy $E = 1.8 \times 10^{25}\,\mathrm{eV} \cdot \mathrm{cm}^{-3}$. The energy has a continuous downward trend that persists even after the distribution function stops evolving noticeably. Overall, the drifts and fluctuations remain below 0.01% of the initial energy.

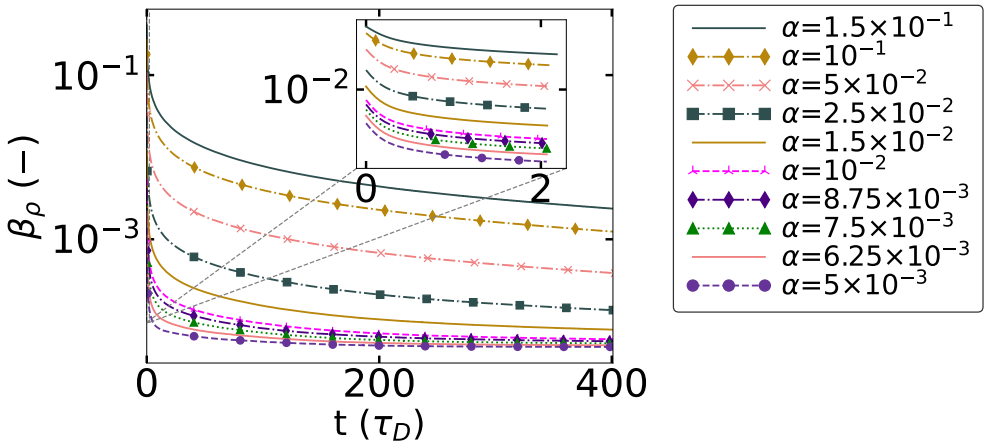

Figure 2.12: The non-thermal density fraction $\beta_\rho(t)$ as a function of time for a perturbed Maxwellian for various perturbation strengths α. The non-thermal score β_ρ decays with time for all cases, initially through an exponential relation before the decline slows down.

distribution is constant, so any differences in the decay rate arise due to the behaviour of the energy diffusion component. When α is large, so too is the gradient of the distribution around $E = E^*$, causing the diffusion contribution to increase. Exponential fits to the non-thermal fraction are shown in Fig. 2.13. The fit function for the non-thermal fraction is of the form $\beta = \widetilde{\beta}_0 \exp\left(-t/\widetilde{t}_r\right)$ in the range of $0 \leq t \leq \tau_D/2$, where $\widetilde{t}_r$ represents the relaxation time constant. The fitted relaxation times themselves are fitted with a linear function:

$$\widetilde{t}_r = p_0 + p_1 \cdot \alpha, \tag{2.39}$$

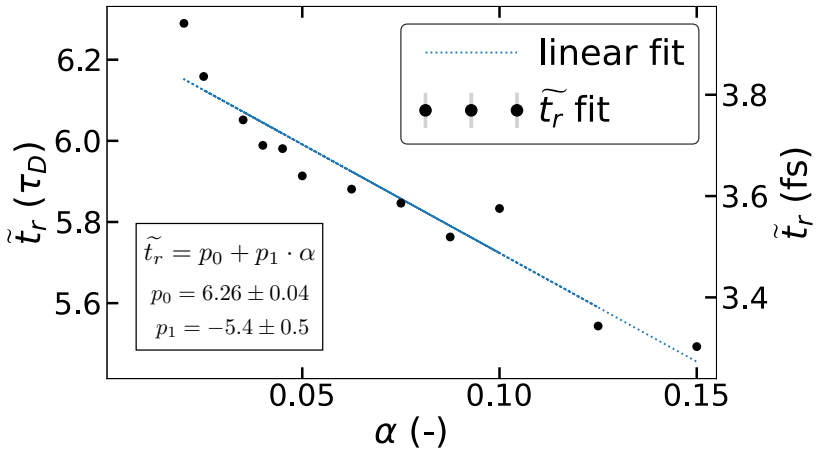

Figure 2.13: Fitted relaxation rates for a perturbed Maxwellian with various values of the perturbation strength α. The fitted function is of the form $\beta = \widetilde{\beta_0} \exp(-t/\widetilde{t_r})$ for $0 \leq t \leq \tau_D/2$, where $\widetilde{t_r}$ represents the relaxation time constant. The relaxation time grows (indicating slower equilibration) when the perturbation is stronger.

where p_0 captures the dynamical friction that is the same for all perturbation strengths, and p_1 is representative of the energy diffusion contribution. The fit constants are given as $\{p_0, p_1\} = \{6.26 \pm 0.04, -5.4 \pm 0.5\}$ where the uncertainties encompass 95% confidence intervals. The fitted relaxation time $\widetilde{t_r}$ decreases linearly with α. Larger perturbations introduce a stronger gradient $\frac{\partial f_E(E=E^*,t=0)}{\partial E}$ in the electron density. The decrease in in the decay time indicates that an increased contribution from the energy diffusion component accelerates the relaxation process in an exponential way. The scaling on the relaxation time is approximately linear, but the decay time is located in the exponent of the solution of a diffusion-broadened delta function [53].

The sign (negative trend) and proportionality of the fit coefficients are more significant than their numerical value. They show expected behaviour for the collision operator, as the linear scaling indicates the increased presence of energy diffusion. Dynamical friction is represented by the offset in Fig. 2.13 as it has the same contribution for all values of α because friction is driven by energy differences, a quantity that is the same for these initial value problems.

Traces of the non-thermal fractions β_ρ and β_E remain present even at times when the distribution appears to have become stationary. At this point, their magnitudes become close to the accuracy with which the conservation laws are adhered to. A non-zero contribution to the non-thermal part of the distribution may well be a numerical inaccuracy that has no physical meaning. The relevant time range to consider reaches up to several hundreds of deflection times during which the time-dependent solution of the distribution can still be seen to evolve.

2.4.3 Variable perturbation energy

The relaxation time of a non-equilibrium system depends on the energy where the perturbation is placed. A scan over the perturbation energy can reveal how the relaxation rate is impacted by the choice of perturbation energy E^*. The corresponding initial value problem of the delta-perturbed thermal distribution is still given by Eq. 2.32. The perturbation energy will be varied up to values of 350 eV while the initial thermal bulk temperature is such that the final system equilibrates at 60 eV for all cases with a total density $n_e = 2.0 \times 10^{23}\,\mathrm{cm}^{-3}$. Under these conditions, $\tau_D \approx 6.3 \times 10^{-16}$ s.

For the cases in this Subsection, the perturbation strength will be held constant at in the small perturbative range: $\alpha = 1.5 \times 10^{-2}$. Here, the non-linearities in the energy exchange process are absent and any variations in the relaxation behaviour can be attributed to the changes in perturbation energy. Particularly the energy domain $E^* > k_B T$ is useful as it can be related to the asymptotic limits of the slowdown time Eq. 2.29 and diffusion coefficient Eq. 2.31. Furthermore, superthermal perturbations can be tracked more easily as they leave a more distinct alteration in the distribution function.

The energy grid still has 300 points with a maximum energy of 500 eV. In order to avoid repeating similar results as before regarding the time evolution and conservation laws (that do not yield new findings for the aforementioned initial conditions), this Subsection focuses on the relaxation time scale.

2.4.3.1 Relaxation Time Scale

After initialising the distribution with a delta-perturbed Maxwellian and computing its time evolution, the non-thermal density fraction is retrieved from Eq. 2.35. For visibility reasons, only a subset of them is plotted in Fig. 2.14. For all energies, the density of the non-thermal population decays exponentially at early times. The perturbation is diffused and decelerated within a few tens of femtoseconds, after which the relaxation process slows down and continues at a lower rate until equilibrium is restored. The decay of the energy held by the non-thermal electrons can be computed through Eq. 2.37 and is shown in Fig. 2.15.

The decay of the non-thermal energy fraction energy β_E follows a pattern similar to that of β_ρ. By comparing Figs. 2.14 and 2.15, it can be seen that the ratio of the non-thermal density and energy decay speed is not constant. For lower perturbation energies and at early times, β_ρ decays faster than β_E. This can only be the case if the interactions that lead to equilibration primarily take place in the low-energy range.

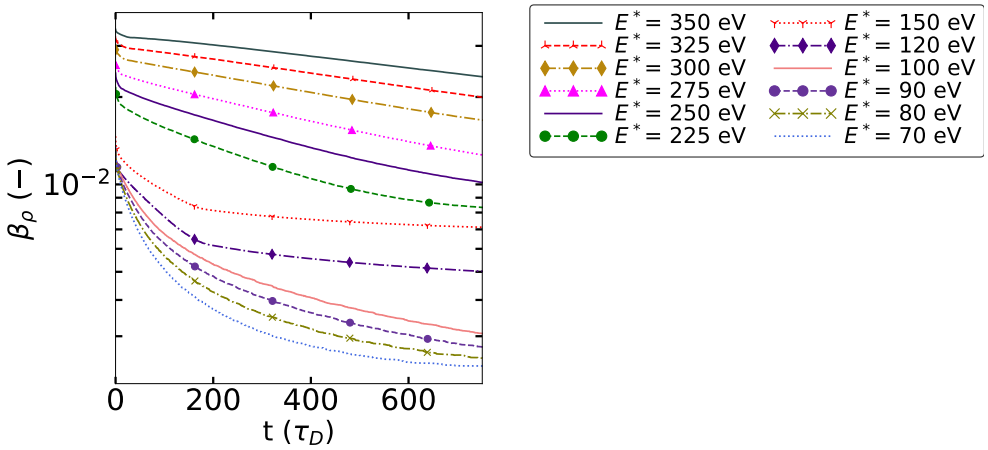

Figure 2.14: The non-thermal density fraction as a function of time for a perturbed Maxwellian for various values of the perturbation energy E^*. The non-thermal score β_ρ decays exponentially at early times, before the decay rate declines.

This is not surprising, considering this is where the perturbation was placed. For a larger E^*, the situation is the opposite and β_E decays faster than β_ρ, indicating the energy exchange process takes place at higher energies around the perturbation itself. After fitting a relaxation time $\widetilde{t_r}$ on the $\beta_\rho(t)$ slopes for the time range $0 \leq t \leq \tau_D$, it

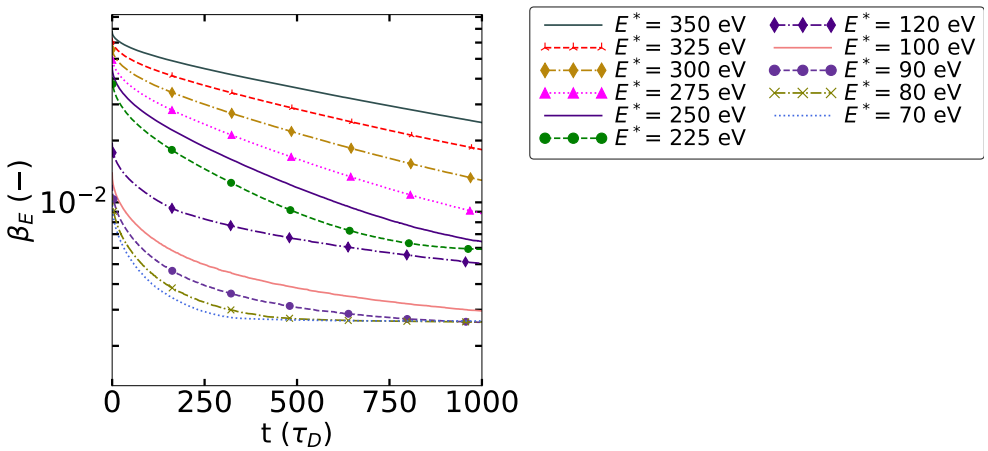

Figure 2.15: The non-thermal density fraction as a function of time for a perturbed Maxwellian for various values of the perturbation energy E^*. This parameter tracks the fraction of energy in the system that still needs to be exchanged before the distribution equilibrates. β_E shows exponential decay decays exponentially at early times, before the decay rate declines.

is informative to examine how the estimated relaxation time depends on E^*. To this end, the relaxation times are fitted with the function:

$$\widetilde{t_r} = p_0 + p_1 \cdot E^* + p_{3/2} \cdot (E^*)^{3/2}, \tag{2.40}$$

in the energy range $E^* > \frac{3}{2}k_BT$, where $\{p_0, p_1, p_{3/2}\}$ are fit coefficients labelled by the powers of the energy. Functionally, p_1 represents the contribution of energy diffusion and $p_{3/2}$ describes the dynamical friction (Eq. 2.29). The fits to the relaxation time at $t = 0$ are shown in Fig. 2.16 with 95% confidence fit coefficients $\{p_0, p_1, p_{3/2}\} = \{2.5 \pm 0.5, -5.8 \pm 1.5, 9.8 \pm 1.4\}$. For convenience, the perturbation energy is measured in units $k_BT = 60$ eV, the system's equilibrium temperature. As

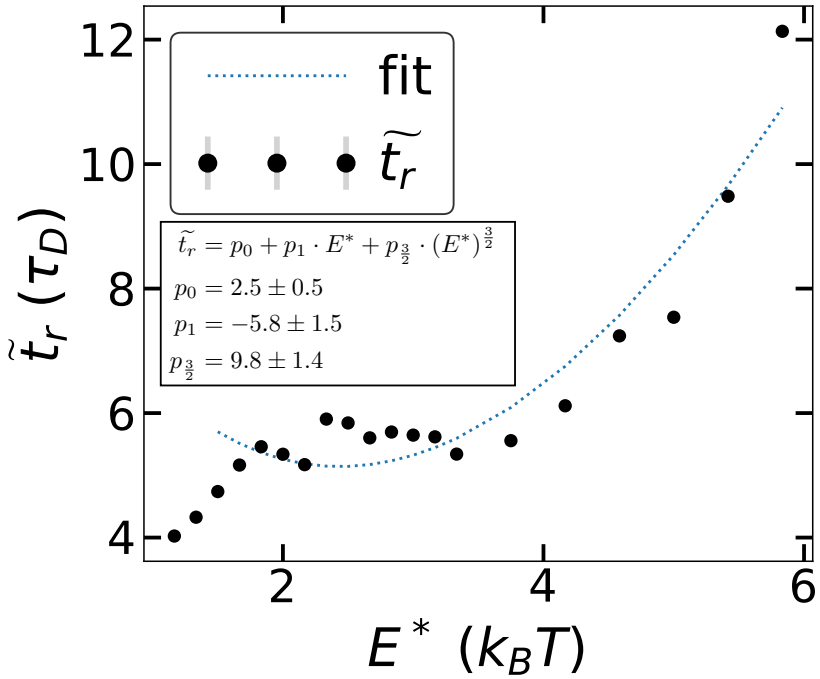

Figure 2.16: Fitted relaxation times for delta-perturbed Maxwellians as a function of perturbation energy. The relaxation time is affected by energy diffusion as well as dynamical friction.

indicated by the relatively large uncertainty in the fit parameters, the increase in relaxation time with energy is steeper than the proportionality $\widetilde{t_r} \propto (E^*)^{3/2}$ can describe. Contrary to the cases with a varying perturbation strength, the asymptotic limits of the slowdown and diffusion times Eqs. 2.29 and 2.31 result in an underestimate of the relaxation time. Spitzer notes that the energy exchange time approximations used in the benchmark are indeed an underestimate that omit contributions that grow in the range of $E^*/(k_BT) \gg 1$ [42]. Observing Fig. 2.16 yields a similar finding, as the estimated relaxation time is longer than the asymptotic limit formula would suggest. This does not impact the accuracy of the collision operator itself, and it merely shows that its features cannot always be replicated by a simple asymptotic formula.

There is another limiting factor to using the slowdown time expressions formulated by Spitzer. They were constructed for individual electrons, or species with such small

densities that they cannot interact with themselves. Even a perturbation of 1.5% of the particles in the system is already noticeable because they are concentrated in a small energy range. The perturbation strength cannot be set to much smaller values, because it would then fall in the range of the density fluctuations and become untraceable. The assumption of having a fully linearised perturbation problem is therefore not entirely satisfied.

In the atomic-kinetics simulations that CCFLY is designed to handle, hot electrons will be created at up to several tens of times the thermal energy. It should be noted that in this regime, elastic electron-electron collisions are not the only process to facilitate the energy transfer from the hot electrons to the bulk. There will be several inelastic ion-electron interactions that have similar or higher rates of energy transfer because the energy transfer per collisional event is larger. The most efficient processes are collisional ionisation and recombination and they will be discussed in the next two chapters.

2.4.4 Mono-energetic distribution

After exploring the perturbative regime, the next test case covers the opposite situation with a nearly fully non-thermal distribution. The chosen form for the initial value problems used in this Subsection is a delta-function in energy space that holds most of the electron density, and a small thermal background to avoid breaking the positivity criterion of the distribution function. The functional form of these initial value problems is still given by Eq. 2.32 for a perturbation strength $\alpha = 0.98$ and various initial energies E^*. E^* will be referred to as an initial energy for this Subsection because α is too large to speak of a perturbation. The symbol E^* will be retained by convention, as the functional form of the initial value problem Eq. 2.32 is still relevant here.

The cases of a mono-energetic initialisation are edge cases in which nearly all the energy in the system needs to be redistributed over energy space in order to re-establish equilibrium. The equilibration process is expected to be driven largely by energy diffusion, as there is no difference in mean kinetic energy between the small thermal background and the delta-peak. Dynamical friction does play an important role here as well, because the MB solution is not symmetric around E^* and this asymmetry can only be brought in through friction.

The final temperature T_{eq} after equilibration and the perturbation energy are related through $E^* = \frac{3}{2} k_B T_{eq}$. As a consequence, the deflection time τ_D is different for each case. All simulation settings are listed in Table 2.3. The runtime of the

calculations (when measured in deflection times) is also different, primarily because the relaxation rate depends on E^*.

Simulation parameters for delta-function initial value problems	
Parameter	Value
n_e	$1.0 \times 10^{23}\,\mathrm{cm}^{-3}$
α	0.98
E^*	$\{30, 45, 60, 120\}$ eV
# energy grid points	300
Minimum energy	0.01 eV
Maximum energy	$10 \cdot E^*$ for each case

Table 2.3: The simulation settings used in the strongly-perturbed time-dependent electron distribution calculations. The distribution is initialised to a delta-function with a small thermal background of the same mean energy. The deflection time depends on E^* and is different for each case.

The number of energy grid points had to be kept constant at 300 in order to maintain a reasonable computational time. The maximum grid energy is scaled such that it is ten times higher than the corresponding value of E^*, but may need to be increased further for higher energies.

2.4.4.1 Time Evolution

The time evolution of the distribution will be shown for the cases $E^* = \{30, 120\}$ eV, as they are the lowest and highest energies used in the simulations. When initialising a distribution to a tall narrow peak, the first expected change would be its broadening through energy diffusion. As can be seen in Fig. 2.17, this process is fast at early times and rapidly broadens the distribution to a width $\Delta E \approx E^*$ in fewer than 20 deflection times. This case is useful for testing the robustness of the numerical scheme's ODE solver as it produces the largest time-derivatives that can occur as a result of e-e collisions alone. Furthermore, these peaks in the time-derivatives are concentrated in a small region of the energy grid. After 410 deflection times, the asymmetry of a Maxwellian profile becomes visible and the broadening speed begins to stagnate. It then takes a further several thousands of deflection times before the distribution cannot be distinguished from a thermal profile. It is understandable that the relaxation rate decreases with time, as the time-derivatives that drive the equilibration process approach zero as the distribution becomes closer to thermal. The Fokker-Planck framework is being used far outside its intended range (near-thermal distributions with small perturbations), yet it still produces a sensible output.

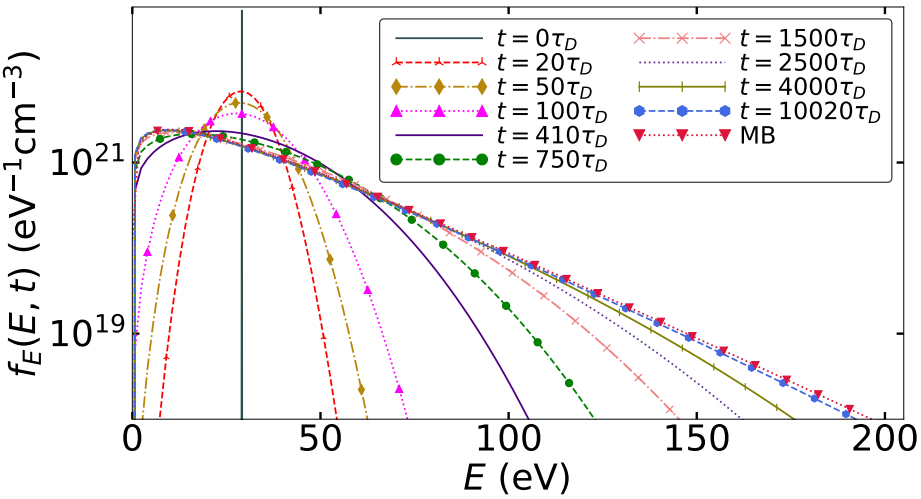

Figure 2.17: Time evolution of an electron distribution initialised to a delta-function around 30 eV, and a small (2%) thermal background of the same energy. Time is measured in deflection time units Eq. 2.25 computed with an effective $(T_{eq}, n_e) = (20\,\text{eV}, 1.0 \times 10^{23}\,\text{cm}^{-3})$.

At a higher initial energy of 120 eV, the time evolution of Fig. 2.18 looks similar. Within a few deflection times, the delta function has been broadened into a Gaussian profile of a width comparable to E^*. After around 100 deflection times, this width has doubled and the asymmetry of the MB distribution begins to surface. By this time, roughly half of the total energy in the system has been redistributed. When compared with the case of $E^* = 30$ eV, the relaxation process is approximately four times faster. The energy range over which energy needs to be diffused grows approximately linearly with E^*, so the increase in diffusivity itself increases at least quadratically based on these two observations.

2.4.4.2 Conservation Laws

For each choice of the perturbation energy, the system has a different energy density that is equal to $n_e \cdot E^*$. The number density is held constant at $n_e = 1.0 \times 10^{23}\,\text{cm}^{-3}$. The numerical accuracy made in the energy conservation is therefore more easily visualised by computing relative errors. This is also done for the number density. For this type of initial value problem, the collisional interactions are more localised in energy space. As opposed to having sharp gradients and differences in mean kinetic energies between two electron groups, the distribution function is broadened from a central energy through diffusion. For this reason, the level of agreement with energy and density conservation may well be different from the previous test cases that involve energetic perturbations.

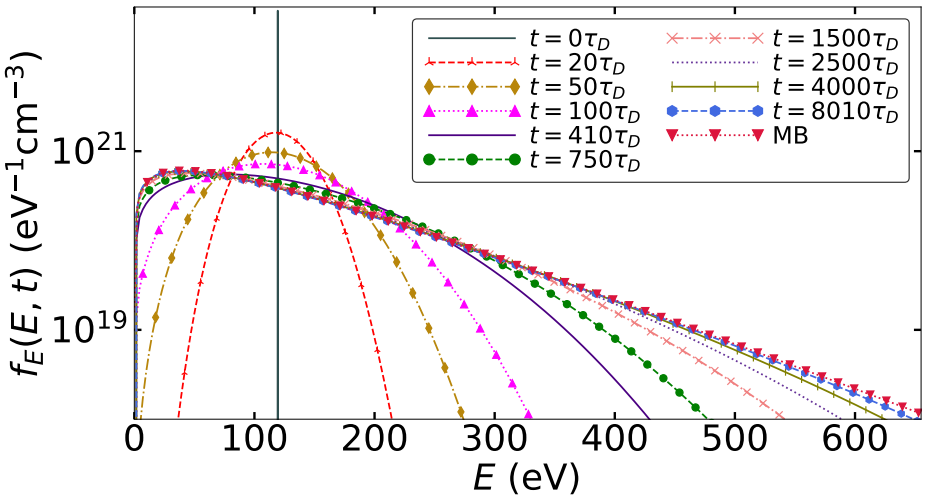

Figure 2.18: Time evolution of an electron distribution initialised to a delta-function around 120 eV, and a small (2%) thermal background of the same mean kinetic energy. Time is measured in deflection time units Eq. 2.25 computed with an effective $(T_{eq}, n_e) = (80\,\mathrm{eV}, 1.0 \times 10^{23}\,\mathrm{cm}^{-3})$.

The electron density for a few initial energies E^* between 30 and 120 eV is plotted in Fig. 2.19. The density is computed by applying Eq. 2.3 to the solution of the time-dependent distribution function. A logarithmic scale has been used for both axes

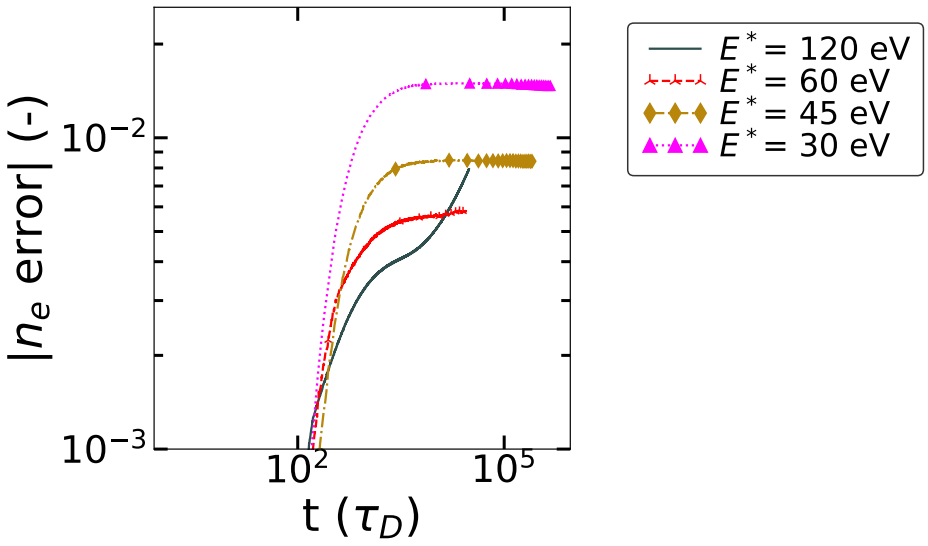

Figure 2.19: The density errors as a function of time for the distributions initialised to delta-functions of various central energies. The error is absolute, in order to fit both positive and negative fluctuations on a logarithmic grid.

because the time range when measured in deflection times is different for each simulation. The relative density error fluctuates between positive and negative numbers,

so the absolute values are taken to fit these errors on a logarithmic scale. Considering the significant exchange of energy within the system, the density conservation law is satisfied to a reasonably high degree. After equilibration, the highest error observed is under 2%. This is for the case of $E^* = 30$ eV, for which the energy grid choice may have been sub-optimal (the highest energy being too high). Overall, the results concerning density conservation are satisfactory for atomic-kinetics applications.

The relative error in the density is not a smooth function and even oscillates, although this is more desirable than recognising a distinct trend. The absolute value of the error is plotted in Fig. 2.20. The sign of the energy error is negative for all energies and times. The absolute value of the fluctuations is two orders of magnitude

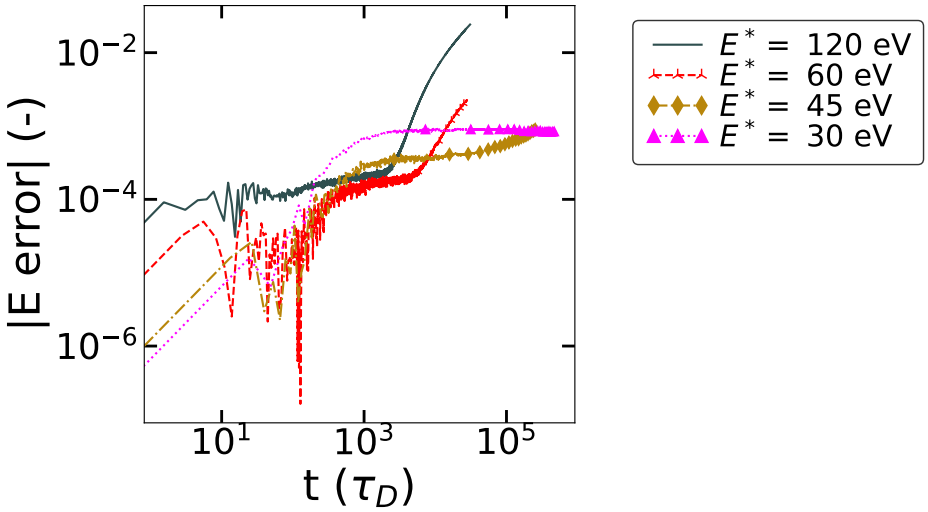

Figure 2.20: The energy errors as a function of time for the distributions initialised to delta-functions of various central energies. The error is plotted as its absolute value, although it is in fact negative in sign for all times and energies.

below those of the density errors. This finding reveals that the numerical inaccuracies occur at low energies. In all simulations discussed in this chapter, the energy grid has been linear in energy (quadratic in velocity). It has occurred that a higher degree of non-uniformity in the velocity grid led to larger numerical errors, so it may be useful to construct a grid that has a more steady increase in grid spacing.

Despite being an edge case not typically associated with a perturbative problem, the case of initialising a distribution to a mono-energetic peak has relevant similarities to the photo-ionisation process in XFEL-plasma interactions. When irradiating a plasma with X-rays, the free electrons at early times are primarily created through inner-shell photo-ionisation. The distribution of these free electrons would not be

mono-energetic, but can be approximated as a sum of delta peaks until they equilibrate towards a near-thermal distribution. With the intention to apply this simulation code to XFEL-plasma problems, it is useful to verify that the conservation laws are still satisfied in regimes with a larger energy exchange.

2.4.4.3 Relaxation Rate

As can be seen from the time evolution of the distribution function, the rates of energy diffusion at early times are sufficiently high to redistribute large fractions of the total energy within a few deflection times. This is when the largest changes to the distribution occur, before the rate of change reduces as a result of shrinking time-derivatives from the collision operator.

Due to the symmetry around the initial energy of the initial distribution, there is an alternative method to visualise when the relaxation process has completed. At early times, the distribution retains some degree of symmetry around its central energy until the stationary thermal distribution begins to take shape. The symmetry stems from the effect of energy diffusion. The time-dependent solution of a distribution initialised to a delta-function is a Gaussian that broadens over time [53, 56]. Without the effects of dynamical friction, the asymmetry of a thermal distribution could not be realised. The fraction of particles with energies below E^* (compared with the total density) can be used as a time tracker in a similar way to the non-thermal fractions β_ρ and β_E.

In a thermal distribution, the fraction of particles S with energies below the mean kinetic energy is equal to:

$$\begin{aligned} S &\equiv \int_0^{E^*=\frac{3}{2}k_BT} f_{MB}(E)\,\mathrm{d}E \\ &= \frac{2}{\sqrt{\pi}}\left[\Gamma\left(\frac{3}{2},0\right) - \Gamma\left(\frac{3}{2},\frac{3}{2}\right)\right] \\ &\approx 0.608, \end{aligned} \tag{2.41}$$

where $\Gamma(x,y) \equiv \int_y^\infty t^{x-1}\exp(-t)\,\mathrm{d}t$ is the incomplete Gamma function. At $t = 0$, the distribution is nearly symmetric and $S \approx \frac{1}{2}$. The speed with which the symmetry fraction moves from $\frac{1}{2}$ towards the value it would have in equilibrium can be used to quantify the relaxation rate. The symmetry fraction $S(t)$ is plotted in Fig. 2.21. All distributions decrease their symmetry until they reach a near-constant value given by Eq. 2.41. This shows that the symmetry can be used as a time tracker as well.

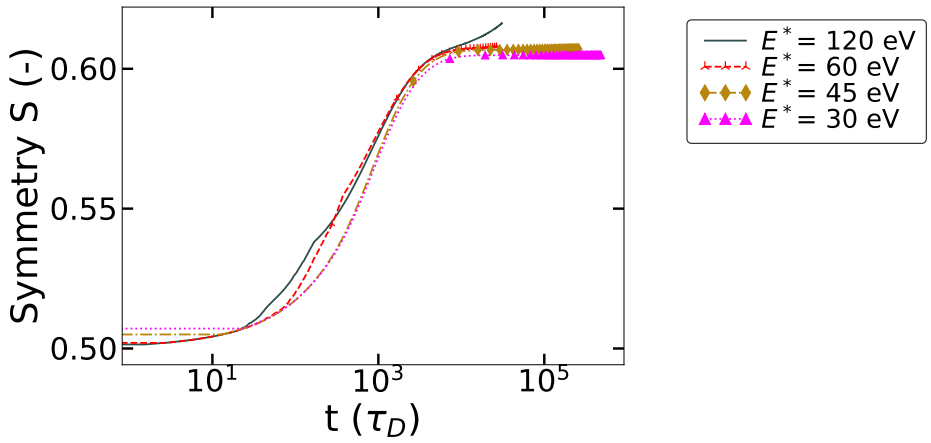

Figure 2.21: Symmetry of the delta-initialised distribution functions over time for various initial energies. All distributions take on the same symmetry factor after sufficient time passes, indicating equilibrium has been reached.

The cases with higher initial energies equilibrate faster. The time is plotted on a logarithmic scale, so the difference in relaxation speed is larger than it appears.

The maximum energy on the grid for the case $E^* = 120$ eV is not sufficiently high, which also caused a density drift in Fig. 2.19.

For a comparison with the other test cases, the non-thermal fractions β_ρ and βE used earlier are also computed for these initial value problems. They contain similar information about the relaxation rate, and their decay denotes equilibration. Fig. 2.22 shows the evolution of the non-thermal density fraction. The relaxation process takes

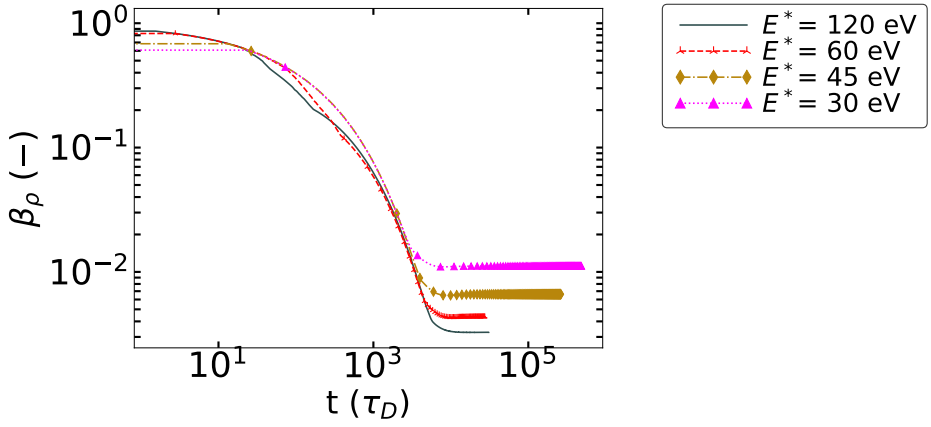

Figure 2.22: The decay of the non-thermal density fraction β_ρ for various initial energies. Contrary to before, $\beta_\rho(t = 0) \approx 1$.

a few thousand deflection times for all cases, and the relaxation rate increases with E^*. The time when the non-thermal fraction ceases to change coincides with the

moment after which no changes can be observed in the time-dependent distribution function. The decay of the non-thermal energy fraction confirms this observation in Fig. 2.23. The figures on the relaxation rate are consistent with each other and the

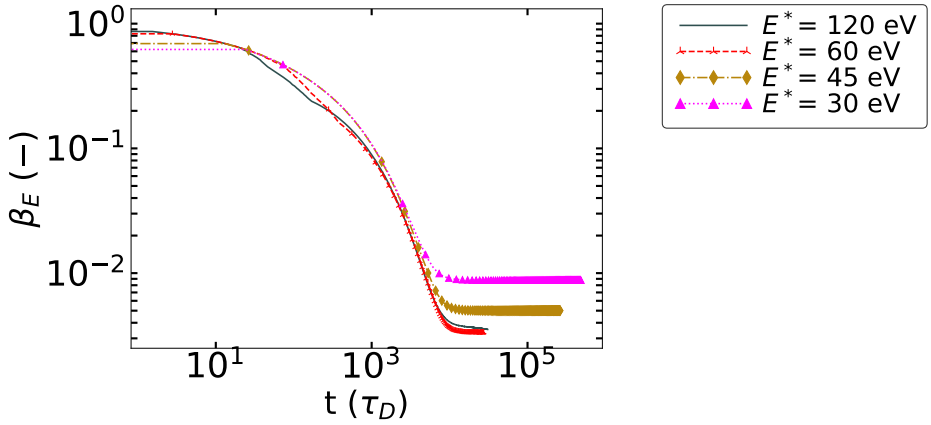

Figure 2.23: The decay of the non-thermal density fraction β_E for various initial energies. The decay is slower than for β_ρ, indicating the equilibration process at higher energies takes longer than in the low-energy range.

relaxation rate can be seen to increase with initial energy E^*. Figs. 2.23 shows that the decay of β_E is slightly slower than for β_ρ. This finding confirms that for initial value problems of this sort, the equilibration process takes longer at higher energies than in the low-energy regime. It can be understood by considering the energy range on which the distribution needs to be populated, which is $(0, E^*]$ for the low-energy range and $[E^*, \infty)$ for the upper range.

Finally, a fit of the relaxation times on β_ρ and β_E show that they contain similar information. Fig 2.24 shows the fitted relaxation times using the fit formula Eq. 2.38 for the time range $0 \leq t \leq 5\tau_D$, which results in nearly identical relaxation times. The relaxation time decreases with energy, indicating faster equilibrium. This is consistent with observations of the time-dependent distribution function, as well as graphs of the non-thermal density and energy fractions.

At larger energies, the MB solution is not only shifted but also broader. Despite this, the equilibration is still faster. The relaxation times obtained for early times are not necessarily representative of the entire equilibration process that can take several thousands of deflection times. However, they do contain sufficient information to rank the initial value problems in the order of the fastest relaxation time. The relaxation rates are consistent with figures shown by Le *et al.* [55].

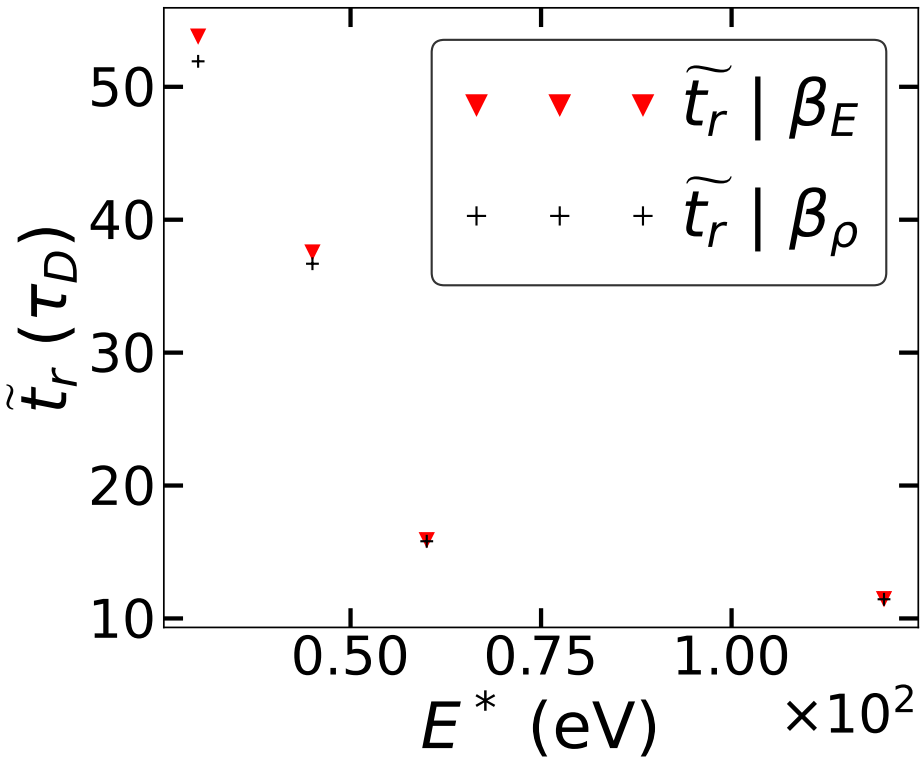

Figure 2.24: Fitted relaxation times for distributions initialised as delta-functions for various energies. The fits are obtained from the non-thermal density and energy fractions.

2.5 Conclusions

This Chapter introduces the concept of electron distribution functions, and the Fokker-Planck equation that governs their time evolution. Non-equilibrium distributions evolve towards the Maxwell-Boltzmann solution through successive Coulomb collisions that redistribute the energy amongst the electrons. Coulomb collisions homogenise the mean kinetic energy of different particle species or sub-distributions (dynamical friction), and diffuse particles in energy space to smoothen out sharp gradients in the distribution (energy diffusion). These effects are described by the elastic e-e collision operator that implicitly conserves the total density and energy.

The elastic collision operator has been implemented in the CCFLY atomic-kinetics code and applied to various initial value problems that only involve electron-electron interactions. The problems differ in the degree of non-equilibrium introduced into the system, ranging from the small to strong perturbative regime. Results on the time evolution, adherence to density- and energy conservation, and the relaxation time scales are discussed for each case. Three quantitative scores for defining the

degree of non-equilibrium in the electron system are also presented to supplement the discussion on the relaxation time scale.

The collision operator behaves as expected for all cases and computes the time evolution of arbitrary distributions towards their equilibrium solution. In the absence of ion-electron or radiation-electron interactions, the electron density and total energy should be conserved. Both conservation laws are satisfied up to relative errors in the range of $\mathcal{O}(10^{-4}) - \mathcal{O}(10^{-2})$ for the various cases with picosecond runtimes. This is sufficiently accurate to perform atomic-kinetics simulations that typically only run for several tens to hundreds of femtoseconds.

A time scale that estimates the order of magnitude during which changes to distribution function take place is the electron deflection time: the average time required to deflect an electron off its original trajectory by 90 degrees through successive Coulomb interactions. This natural time unit relates to the relaxation time through its relation to the rate of momentum and energy exchange, as well as energy diffusion. For solid-density systems of several tens of eV, this time is in the femtosecond range. The time-dependent simulations are in agreement with this finding.

For future work and experimental studies in which the CCFLY simulations will be used, the author would like to make a suggestion regarding the Coulomb logarithm. In the discussion throughout this Chapter, an empirical formula has been used for its numerical value without giving much attention to its validity or interpretation. When experimental data on the distribution function is available, the author believes it can be interesting to use the Coulomb logarithm as a fit parameter to verify how it compares with the empirical formula (Eq. 2.17).

Chapter 3

Inelastic Electron-Ion Interactions in the Strongly Coupled Regime

Contents

3.1 Introduction

In warm dense systems created through X-ray Free Electron Laser (XFEL) irradiation of a solid target there can be a wide variety of interactions between X-ray photons, free electrons and bound electrons. When an X-ray pulse hits a target, the X-ray photons are primarily absorbed through K-shell photo-ionisation, a process that produces energetic free electrons and excited ions with a hole in an inner shell. The majority of the excited ions, approximately 96% of them in magnesium, decay through Auger decay, thereby emitting another energetic electron [19]. The sequential occurrence of photo-ionisation and Auger decay acts as an efficient ionisation mechanism, and a pathway to couple energy from the radiation field into the free electrons.

The presence of an energetic free electron population and an intense X-ray radiation field opens up many reaction channels of spontaneous decay, collisionally- and radiation-induced atomic transitions. The atomic processes that follow mediate energy transfer between its various forms in the system: the radiation field, the electrostatic potential held by electrons to an ion, and the kinetic energy of the free electron populations. The system's state description, namely its time-dependent ion populations and electron distribution function, can be computed by tracking all the atomic transitions over time.

From the perspective of the electron distribution function, the ion-electron and radiation-electron interactions are inelastic by nature. Depending on the type of interaction, both electrons and energy can be added or subtracted from the free electron population. Previously, the radiative-collisional codes used in our research group were constructed on the assumption that the electron population always lives in equilibrium with itself, even when the ion populations do not. More precisely, the distribution was assumed to have a Maxwell-Boltzmann (MB) profile at a single temperature. This assumption significantly simplifies the computation of ion transition rates with the cross-section formalism, as well as the electron particle and energy balances.

The contents of this chapter will cover how to compute the evolution of the ion populations and electron distribution in a non-thermal system where both the ion- and electron populations can live in a state not described by Local Thermodynamic Equilibrium (LTE). This adds many degrees of freedom to the distribution function so that it can now describe non-thermal effects, such as having electrons much more energetic than the bulk of the distribution. As a result of this generalisation, the ion transition rates can now only be computed from their general cross-section integral forms without further simplification or semi-analytic expressions.

The electron distribution function itself still follows an evolution described by the Fokker-Planck equation introduced in Chapter 2. The Fokker-Planck equation there only contained the elastic collision operator that describes inter-electron collisional mechanics that bring the distribution towards equilibrium. When considering ion-electron interactions and a radiation field, the Fokker-Planck equation must be complemented with inelastic collision operators for each atomic transition. These inelastic operators describe the addition or subtraction of electrons and energy to and from the free population.

The chapter is written in a style such that the contents can be readily implemented into an atomic-kinetics code, as has been done with the Oxford-developed CCFLY code. In the underlying code-development project, the author generalised the zero-dimensional CCFLY code so that it can track arbitrary electron distribution functions during an atomic-kinetics calculation, and forego the need to impose a MB distribution. This involved modifying the ion transition rates, as well as the electron density and energy balances. The parts of the code that do not differ from the use case with thermalised electrons remained unchanged, and closely reflect the SCFLY radiative-collisional code [40, 59].

An overview will be given of the atomic processes that can occur in a warm dense XFEL-produced plasma, their associated transition rate model, and their inelastic collision operator. This also serves as a benchmark of the non-thermal CCFLY-extension and ensures that although it gives access to new non-equilibrium regimes, the results obtained are consistent with previous studies with imposed LTE assumptions. An introduction into the concepts of differential reaction cross-sections and detailed balance are required for the discussion of transition rates. Sections 1.1.2 and Appendix B provide a recapitulation on the concept of reaction cross-sections and detailed balance.

Finally, a demonstration of a full atomic-kinetics calculation for an X-ray irradiated magnesium sample will be discussed. This calculation cannot be benchmarked with results known from the thermal version of CCFLY, and serves to demonstrate the possibilities of a non-thermal electron module.

3.2 Warm Dense System Dynamics

Section 2.3 saw the introduction of the source-free Fokker-Planck equation applied to an isotropic medium. This equation describes the time-evolution of an electron distribution function as a result of inter-electron collisional interactions. Given an

initial condition, it can be used to compute the distribution for all future time steps through the formalism of the elastic collision operator and solved on a discrete energy grid through the numerical scheme described by Eq. 2.20.

In a warm dense system, the free-electron population does not live in isolation and the elastic interactions are only a subset of the true range of interactions that an electron can have with its surroundings. Free electrons in a warm dense system have sufficient kinetic energy to collisionally induce ion transitions, such as ionisation, recombination and excitation and de-excitation events. Additionally, the external radiation field supplied through the XFEL can trigger photon-induced ion transitions such as photo-ionisation, excitation, de-excitation or recombination events.

To complete the set of first-order interactions, free-free interactions such as Bremsstrahlung and inverse Bremsstrahlung should also be considered. They have been omitted in this thesis due to time constraints and will be implemented at a later stage. Finally, spontaneous decay reactions such Auger decay and its inverse, dielectronic recombination, contribute significantly to the heating process of XFEL-irradiated matter, as they add energetic electrons to the free-electron population.

An effective description for the time-evolution of a warm dense system subjected to an XFEL should include the ion transition rates, as well as a self-consistent method to describe the free-electron population.

3.2.1 Ion Transition Rates

The collisional and radiative interactions induce a range of ionic transitions whose rates can be computed through the cross-section formalism. Spontaneous rates that do not depend on the radiation field or free-electron population can be computed from atomic physics codes and treated as constants.

A description of the warm dense system can be composed by constructing a set of coupled rate equations, one for each charge state population. Charge states are defined as super-configurations in this work, a configuration whereby the atomic shell structure is defined only by the principal quantum number n of the bound electrons. For example, the configuration $K^x L^y M^z$ has a total of $(a + b + c)$ electrons, with a electrons in the K-shell ($n = 1$), b electrons in the L-shell ($n = 2$) and c electrons in the M-shell ($n = 3$). The super-configuration is a coarse description of the full state spectrum of an ion, but significantly reduces the number of states to several dozens or hundreds for atoms with atomic numbers $2 < Z < 20$.

Regardless of the profile of the electron distribution, a collisionally-induced ion transition rate $S^{-+}(t)/V$ that takes an ion from state $\mid -\rangle$ to state $\mid +\rangle$ can be computed with a cross-section integral of the form:

$$S^{-+}(t)/V = \int (2E/m_e)^{1/2} \sigma_{-+}(E) f_E(E,t) dE, \tag{3.1}$$

where $\sigma_{-+}(E)$ is the energy-dependent reaction cross-section, and the factor $(2E/m_e)^{1/2}$ is the electron's linear velocity. Photon-induced reaction rates have a similar form to Eq. 3.1, where the photon energy distribution is substituted for the electron distribution. For photon or electron distributions with an analytically expressible profile, such as a Gaussian or MB profile, the rate equation is generally simplified to semi-analytic expressions. When the electron distribution function can take on any arbitrary shape, Eq. 3.1 must be computed numerically on the discrete energy grid.

Computing the transition rates for all available ion states and transitions, a rate matrix $\underline{\underline{S}}$ can be constructed. For each available ion state N_j, the population is determined by the rate equations in the form of:

$$\frac{N_j(t+dt) - N_j(t)}{dt} = \sum_{j \neq k} S_{kj} N_j(t) - N_j(t) \sum_{j \neq k} S_{jk}, \tag{3.2}$$

which computes all the population rates S_{kj} that take other states N_k to state N_j, and subtracts the rates S_{jk} that depopulate state N_j. In isochoric conditions, the total ion density remains constant and populations can only be re-assigned to other states:

$$n_i = \sum_j N_j(t), \;\; \forall t. \tag{3.3}$$

The electron density can be calculated directly from the charge of the ion populations through the quasi-neutrality principle as:

$$n_e(t+dt) = \sum_j N_j(t+dt) z_j, \tag{3.4}$$

and the sum j runs over all possible ion configurations where z_j is the ionisation degree of each configuration. Through energy conservation, the total free-electron energy can also be computed from the ion transition rates. Transitions typically add energy to or draw energy from the free-electron population, a quantity that equals the reaction threshold. Knowing the rate of an ion transition, the effect it has on the free-electron energy can be computed by multiplying the rates by their respective

reaction thresholds. The energy being released into the free electron population is then given by:

$$\frac{dE_{kin}(t)}{dt} = \sum_j S_{jk} E_{jk} N_j(t). \tag{3.5}$$

Eq. 3.5 states that for every ion that undergoes a transition, the change in binding energy E_{jk} between the initial and final ion states is released into or drawn from the free electron population. This energy balance contains the effects of photo-absorption, Auger decay, as well as the collisional interactions between ions and electrons.

Eq. 3.5 omits free-free interactions which need to be summed separately. The method by which pressure-ionisation is implemented in atomic-kinetics codes often also leads to artificially created electron sources and sinks that need to be considered in the energy and density balance. This will be described in more detail in Section 3.4.

In a thermal system where the electron distribution function is always a MB distribution, the full distribution can be uniquely characterised by the electron density and temperature alone. For these systems, the temperature can be computed as:

$$\frac{3}{2} n_e(t) k_B T(t) = E_{kin}(t). \tag{3.6}$$

The time-evolution of the ions is coupled directly to the electron density and temperature, making Eqs. 3.2, 3.4, 3.5, and 3.6 a self-consistent set of equations. Energy conservation is directly imposed by treating the free-electron population simultaneously with the ions. This self-consistency is a feature implemented in the thermal version of the radiative-collisional non-LTE SCFLY and CCFLY codes [40].

A non-thermal system has an analogous description that is also self-consistent. The energy and density of the free-electron population remains directly coupled to the ion populations and their transition rates, with the additional degree of freedom that the distribution need not be Maxwellian. This causes additional complexities due to the fact that the electron density and mean kinetic energy alone are not sufficient to compute the full distribution function.

It requires a self-consistent calculation for each energy node on the discrete energy grid to correctly compute the ion transition rates, as well as the rates of change in the electron distribution function. This is the subject of the next Subsection.

3.2.2 Inhomogeneous Fokker-Planck Equation

While the system's ion populations undergo transitions through spontaneous, collisionally- or photon-driven reactions, the electron distribution function undergoes changes as well. Any energy or particles that are released or drawn from the distribution should

be considered in a self-consistent way, in a fashion similar to the treatment of a thermal system.

For this purpose, the Fokker-Planck equation Eq. 2.15 needs to be supplemented with inelastic collision operators that describe the source and sink terms of electrons and energy:

$$\begin{aligned}\frac{\partial f_E(E)}{\partial t}\Big|_{ee} = &-\frac{\partial}{\partial E}\Big[a(E)f_E(E)\Big] + \frac{1}{2}\frac{\partial^2}{\partial E^2}\Big[D(E)f_E(E)\Big] \\ &+I(f_E(E)) + S(E).\end{aligned} \tag{3.7}$$

Eq. 3.7 contains the elastic collision operator introduced earlier in Eq. 2.15, and adds a source $S(E)$ and inelastic term $I(f_E(E))$. The source term is a collection of interactions that do not depend on the electron distribution. Ion transitions that fall under this category are photo-ionisation and Auger decay. Both these processes release bound electrons to the free-electron population.

The collection of inelastic contributions $I(f_E(E))$ encompasses all ion-electron interactions whose rates depend on the electron distribution. This creates a circular dependence; the ion transition rates depend on the electron distribution, and the rates of change of the electron distribution depend on the ion transition rates. By capturing the effects on the electron distribution in an inelastic collision operator, a self-consistent treatment for the ion populations and electrons can be achieved.

The elastic collision operator is written for a distribution in velocity-space, whereas the inelastic operations are written as a function of energy-dependent cross-sections. It is therefore convenient to compute the elastic operator in velocity-space by transforming the energy-space distribution. The code architecture of the Fokker-Planck module integrated into CCFLY is shown in Fig. 3.1.

The distribution function itself is required to compute the time-derivatives as a result of elastic electron-electron interactions. For this purpose, the distribution is transformed from its energy-space representation to its velocity-space counterpart, before applying Eq. 2.20. The resulting time-derivatives are then transformed back to their energy-space representation. The ion-electron collision operators are computed in energy-space with the inelastic collision operators that are still to be described. Finally, source terms are added to the derivatives, which completes the set of derivatives. The current distribution function and its time-derivatives can then be fed into an Ordinary Differential Equation (ODE) solver.

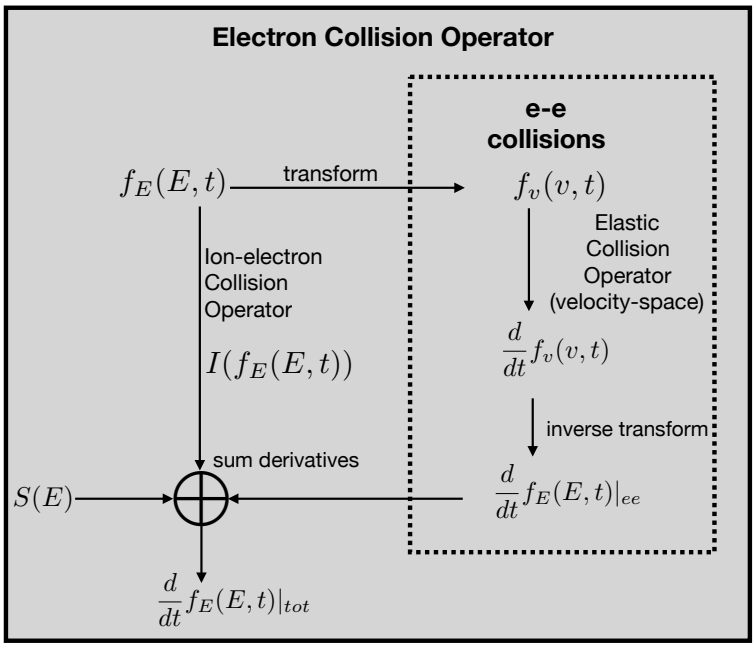

Figure 3.1: The time-derivatives of the electron distribution are computed as a sum of elastic inter-electron and inelastic electron-ion interactions, and source terms that do not depend on the distribution function. The elastic electron-electron collision operator is computed in velocity space.

3.3 Numerical Grid Operations

An equilibrated electron distribution, the MB distribution, lets itself be fully described by its electron density and temperature. The density can be determined by imposing quasi-neutrality of the combined ion and electron system, and the temperature can be derived from a self-consistent energy balance.

When the distribution function is allowed to take on any arbitrary shape, the distribution must be discretised in some way. In this work, the free-electron energy is discretised onto a grid. The choice of the energy grid has implications for the distribution functions that can be described, and the numerical errors of the transition rates and electron energy balances.

3.3.1 Discretisation Errors

There exist several guidelines when determining the energy grid for the free electrons. Firstly, the grid needs to be fine enough in the low-energy range up to $\sim$5 eV to be able to account for electrons ionised through pressure-ionisation. This energy domain also plays a role in the elastic collision operator scheme, and ensures that the distribution has the possibility to equilibrate to a Maxwellian [47].

Secondly, the grid needs to reach high enough to capture the high-energy electrons produced through photo-ionisation and Auger decay with energies of multiple keVs. A rule of thumb is that the maximum grid energy should be twice the maximum energy that a free electron can obtain through an ion transition. This is because elastic collisions between high-energy free electrons can produce electrons with even higher kinetic energies, although this is not a likely process[1].

In the mid-range, typical excitation and ionisation energy thresholds lie in the range of several tens to several hundreds of eV for materials with $10 < Z < 30$. In this energy range, the grid needs to be fine enough to be able to define the integration range of cross-section integrals. Close to the energy thresholds, the cross-sections can have more curved profiles and it is beneficial to have a grid fine enough to sample this curvature.

A natural choice of grid type that satisfies all these criteria is a logarithmic energy grid, possibly with some refinements in particular energy regions of interest, for instance for the study of resonant atomic transitions. For a range reaching from 0.01 eV to 10 keV, an energy grid with $\mathcal{O}(100)$ grid points can yield satisfactory results.

Whereas a MB distribution function often leads to semi-analytical expressions for the ion transition rates, the ion rates can generally only be calculated from numerical integration techniques for a non-equilibrium distribution. The accuracy of these integrals depends heavily on the grid-point density in the energy region where the reaction cross-section is strongly curved.

As shown in Fig. 3.2, the numerical errors arising from grid discretisation can be attributed largely to sampling errors of the reaction cross-sections. The distribution function itself is not represented so accurately in regions where it is strongly curved, for instance near its peak. Secondly, calculating the transition rates as a rate integral over a cross-section cannot be done as accurately when the cross-section varies rapidly in between grid points. Collisional ionisation- and excitation cross-sections are typically curved in the near-threshold region, and the ion transition rate can be miscalculated by undersampling.

The energy grid is also truncated at some finite value, leading to some numerical differences as compared with integrating the rate integral to infinity. This truncation error can be reduced by increasing the maximum energy that fits on the grid, although this will reduce the grid density if the same number of grid points is kept. The truncation and sampling errors can therefore not be optimised together, and the grid choice should be examined for each use case.

[1]Truncating the grid at twice the maximum expected energy omits any third-order processes.

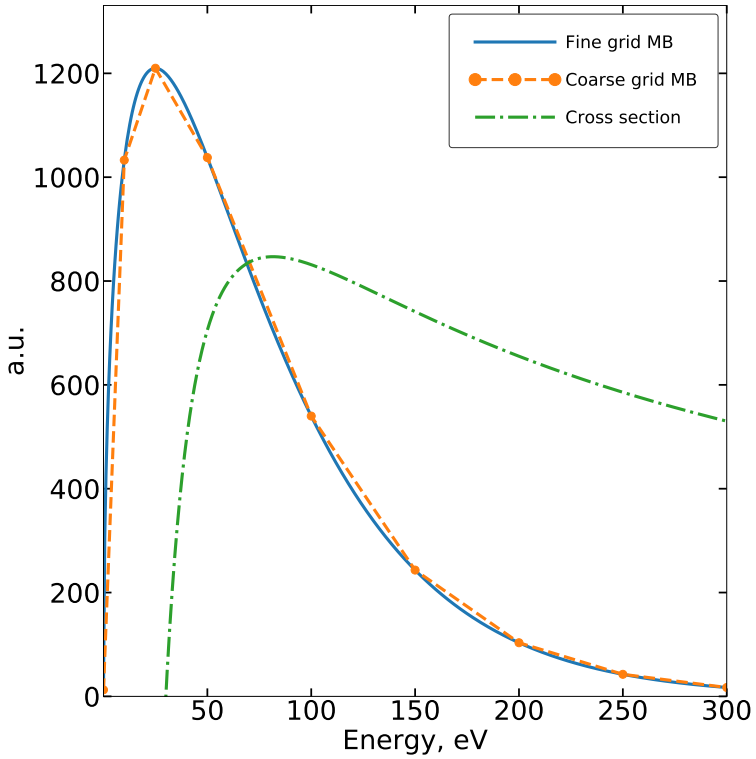

Figure 3.2: Maxwell-Boltzmann distributions on a coarse and fine energy grid, along with an exemplative reaction cross-section. Having a coarser grid leads to errors in representing the distribution function, and also in sampling the cross-section in transition rate integrals.

3.3.2 Interpolation Procedures

The numerical scheme for the elastic collision operator is written for the distribution function on the grid nodes. Executing this yields the time-derivatives directly on each grid point, allowing them to be processed further in an ODE solver. On the other hand, the inelastic collision operators yield operations on the distribution function at energy values that do not necessary lie exactly on the discrete grid.

An example where this occurs is pressure-ionisation. In the super-configuration mode of CCFLY, continuum lowering is treated as an instantaneous process whereby an ion species ceases to exist in a stepwise manner. This produces electrons that must be added to the distribution at an energy value that is prescribed by their binding energies. In principle, this energy value can take on any continuous value in the range up to a few eV. In order to maintain energy and density conservation simultaneously, it is necessary to interpolate a change in distribution function onto the discrete grid.

The same interpolation process occurs when computing time-derivatives due to inelastic ion-electron interactions. These processes can result in electrons being drawn

from or released into the free-electron population at any continuous energy allowed by the energy balance. It cannot be assumed that the energy grid is constructed such that these energies occur on the grid, and rounding off will lead to a violation in energy conservation.

The time-dependent density is computed from the electron distribution function through the composite trapezoid rule as:

$$\begin{aligned} n_e(t) &= \int_0^\infty f_E(E,t)\,\mathrm{d}E \\ &\approx \frac{1}{2}\sum_{i=0}^{N-2}\left(f_E(E_i,t)+f_E(E_{i+1},t)\right)\left(E_{i+1}-E_i\right) \\ &= \frac{1}{2}\sum_{i=0}^{N-2}\left(f_i(t)+f_{i+1}(t)\right)\left(E_{i+1}-E_i\right), \end{aligned} \tag{3.8}$$

where the substitution $f_i(t) \equiv f_E(E_i,t)$ has been used, with the reminder that the inelastic collision operators are all written for energy-space distribution functions in this thesis. The number of energy grid points is N, thereby setting the index of the highest energy equal to $N-1$. The distribution in Eq. 3.8 is normalised to the electron density by convention. No assumptions can be made about the step size in the integral, as the energy grid is typically non-uniform. Similarly, the total kinetic energy density held by the distribution is computed as:

$$\begin{aligned} E_{kin}(t) &= \int_0^\infty E f_E(E,t)\,\mathrm{d}E \\ &\approx \frac{1}{4}\sum_{i=0}^{N-2}\left(f_E(E_i,t)+f_E(E_{i+1},t)\right)\left(E_{i+1}+E_i\right)\left(E_{i+1}-E_i\right) \\ &= \frac{1}{4}\sum_{i=0}^{N-2}\left(f_i(t)+f_{i+1}(t)\right)\left(E_{i+1}^2-E_i^2\right), \end{aligned} \tag{3.9}$$

Eqs. 3.8 and 3.9 can be used to determine how to interpolate a change to the distribution function in case it takes place at an energy E^* that does not occur on the energy grid: $E^* \notin \{E_0,\ldots,E_{N-1}\}$. Given an energy grid $\{E_0,E_1,\ldots,E_{j-1},E_j,E_{j+1},\ldots,E_{N-1}\}$ on which the time-derivatives of the energy-space distribution is defined, electrons with energy $E_j < E^* < E_{j+1}$ for some $1 < j < N-1$ are released into the free-electron population at a production rate an amount of $\partial_t n$. The time-derivative notation is abbreviated to ∂_t. This situation is depicted in Fig. 3.3.

The rate of change in the number of electrons at this energy should then be distributed over the time-derivatives $\{\partial_t f_0,\ldots,\partial_t f_j,\ldots,\partial_t f_{N-1}\}$ such that they ac-

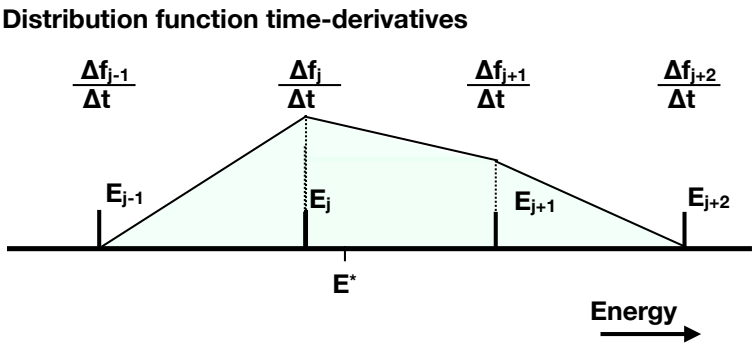

Figure 3.3: An inelastic atomic process causes the release of electrons with energy E^* into the free-electron population. The change is interpolated onto the time-derivative vector that is defined on the discrete energy grid.

curately represent the production of free electrons while conserving energy. For illustration purposes, the energy E^* is located between the grid points j and $j+1$: $E_j < E^* < E_{j+1}$. Assuming that E_{j-1} and E_{j+2} are defined on the grid, the production term is distributed between three energy bins: $E_{j-1} < E < E_j$, $E_j < E < E_{j+1}$, and $E_{j+1} < E < E_{j+2}$. The production rate of the number of electrons can be expressed as:

$$\partial_t n_e = \frac{1}{2} \sum_{i=j-1}^{j+1} \left(\partial_t f_i + \partial_t f_{i+1}\right) \left(E_{i+1} - E_i\right), \tag{3.10}$$

whereas the mean energy at which this density change occurs must obey the relation:

$$E^* = \left(\partial_t n_e\right)^{-1} \frac{1}{4} \sum_{i=j-1}^{j+1} \left(\partial_t f_i + \partial_t f_{i+1}\right) \left(E_{i+1}^2 - E_i^2\right). \tag{3.11}$$

As E^* and $\partial_t n_e t$ are given, the time-derivatives are to be chosen such that they simultaneously obey the relations Eqs. 3.10 and 3.11. Only the derivatives on the neighbouring grid points are allowed to undergo a change, and the change to the derivatives at grid points $j-1$ and $j+2$ are constrained to zero. Eqs. 3.10 and 3.11 can be written in a compact matrix-vector form:

$$\begin{pmatrix} (E_{j+1} - E_{j-1}) & (E_{j+2} - E_j) \\ (E_{j+1}^2 - E_{j-1}^2) & (E_{j+2}^2 - E_j^2) \end{pmatrix} \begin{pmatrix} \partial_t f_j \\ \partial_t f_{j+1} \end{pmatrix} = \begin{pmatrix} 2\partial_t n \\ 4E^* \partial_t n \end{pmatrix}. \tag{3.12}$$

The time-derivatives $\partial_t f_j$ and $\partial_t f_{j+1}$ can be determined from Eq. 3.12 by inverting the $2\times$ energy matrix. By handling time-derivatives through this scheme, the production or destruction rates of free electrons at any continuous value of energy can be captured in a discrete time-derivative vector while conserving density and energy. The same scheme can be used for instantaneous changes (e.g. pressure-ionisation), as well as for changes described through rates that need to be integrated over time.

For the boundary cases where $E^* < E_1$, Eq. 3.12 can be used by setting $E_{-1} = E_0$. This introduces an error in the energy conservation, but still conserves density. It is not possible to correct the energy balance if the energy grid does not allow it. If this scenario occurs often, the energy grid should be extended towards lower energies. Similarly, if $E^* > E_{N-2}$, the scheme can be modified by setting $E_{j+2} = E_{j+1}$. This too introduces a deviation in the energy conservation, but still preserves the total electron density.

It is possible to adopt a different scheme to account for changes to the distribution function. Eqs. 3.8 and 3.9 make use of the simplest possible integration method, which is computationally efficient. More sophisticated schemes such as variations of the Galerkin method can also be implemented [60]. Whichever method is used, it is important that the same scheme is adopted for both distribution function changes, as well as the computation of physical parameters.

3.4 Continuum lowering

,

Ionisation Potential Depression (IPD) is an effect that occurs only at high electron and ion densities, whereby the energy threshold between bound electrons and their free counterparts is lowered. It is caused by an overlap between the wave functions of the outer orbitals of ions, upon which an electron in that orbital can no longer be considered bound and is therefore pressure-ionised. This means that the energy required to ionise an ion is reduced as the density increases. Fig. 3.4 shows the effect of neighbouring atoms on the band structure of a magnesium atom and metal.

Whereas an isolated atom has a band structure without an upper limit on the principal quantum numbers of electrons, a magnesium metal has a distinct cut-off on the number of bound electrons. Above the M-shell, there are only conduction electrons and the continuum has been reduced. In a dense plasma, a similar effect occurs that grows stronger with an increasing electron density, pushing down the threshold to ionise an atom and further increasing the near-free (conduction) electron density. The difference between the ionisation potential of an isolated atom, and that of an atom in a dense plasma environment is the IPD.

The change in potential can be significant enough to alter the plasma dynamics, as transition rates often scale exponentially with energy thresholds. In addition to altering transition rates, IPD may even make certain ionic bound states unavailable.

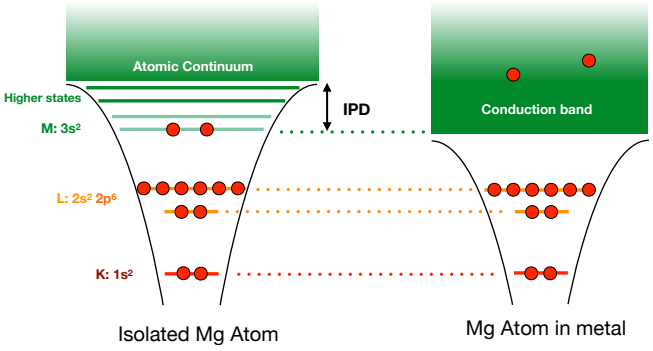

Figure 3.4: Effect of the ion surroundings on the ionisation potential. An atom in a metal or dense plasma environment has a cut-off on the maximum principal quantum number that a bound electron can have.

If an electron shell lies in the continuum and is pressure-ionised, no electronic configurations involving that shell can exist. This plays another role in the plasma dynamics as these states need no longer be considered.

3.4.1 Pressure-Ionisation Models

In a manner analogous to using parametric cross-section models, CCFLY and SCFLY require a parametric model for continuum lowering as well. Continuum lowering is an effect that must be accounted for and this work focuses on the implications of the IPD modelling on the treatment of the free-electron distribution.

At present, the large part of the atomic-kinetics that require a parametric IPD model make use of one of two models to describe continuum lowering in the solid-density regime. The first is a commonly-used model within the plasma physics and Inertial Confinement Fusion (ICF) community, and the second is the model used in the work of our own group. These models are inconsistent with each other and it should be noted that continuum lowering models are still an active area of research. Both models and their implications on spectroscopy diagnostics are discussed by Preston *et al.* in the context of High Energy Density (HED) science and listed here for convenience [61]. The first is a model by Stewart and Pyatt (SP):

$$\Delta P_{SP} = \frac{k_B T}{2(z^* + 1)} \left[\left(\frac{3(z^* + 1) z q_e^2}{4\pi\epsilon_0 \lambda_D k_B T} + 1 \right)^{2/3} - 1 \right], \tag{3.13}$$

where q_e is the electron charge, ϵ_0 the vacuum permittivity, and $z^* = \langle z^2 \rangle / \langle z \rangle$ is a measure of the ionisation levels in the system computed by the population weighted mean squared ionisation over the mean ionisation. It should be noted that generally, $z^* \neq \langle z \rangle$. The Debye length λ_D is computed for ions and electrons together, and the charge z is the charge after the ionisation event has taken place (z=1 for the neutral atom). The scaling behaviour is $\Delta P_{SP} \propto z^{2/3}$.

Another commonly used model has been proposed by Ecker and Kröll (EK), and is written as:

$$\Delta P_{EK} = \begin{cases} \frac{1}{4\pi\epsilon_0} \frac{z q_e^2}{\lambda_D}, & \text{if } n_i + n_e < n_{crit} \\ C_{EK} \frac{1}{4\pi\epsilon_0} \frac{z q_e^2}{r_{EK}} & \text{elsewhere,} \end{cases} \tag{3.14}$$

where the IPD function is two valued, depending on whether the sum of the ion and electron density is above or below a critical density. The EK radius in Eq. 3.14 is defined as the average inter-particle distance $r_{EK} = \left(\frac{3}{4\pi}\left[n_e + n_i\right]\right)^{1/3}$, counting both the ions and electrons. The IPD scales linearly with z on both sides of the critical density. The critical density is defined as:

$$n_{crit} = \frac{3}{4\pi} \left(\frac{4\pi\epsilon_0 k_B T}{Z^2 q_e^2} \right)^3, \tag{3.15}$$

with Z being the atomic number of the material. The critical density is, roughly speaking, the point where the plasma transitions from the weakly coupled into the strongly coupled regime. For all practical purposes, HED science takes place in the regime far above the critical density.

The constant C_{EK} in the EK model has been given a different value in work by Orlando Ciricosta *et al.* [38] than its original creators had in mind. Whereas originally, the constant was chosen such that the IPD was a continuous function between the two density regimes, Ciricosta set it to unity in order to match IPD measurements in dense plasmas created at Linac Coherent Light Source (LCLS). This model will be referred to as the Modified Ecker-Kröll (mEK) model as it largely preserves the parametric form. It is clear from the proportionality of the IPD models with respect to the ion charge ($\propto z^{2/3}$ compared with $\propto z$), that the mEK and SP models cannot be consistent across a broad range of charges.

The relevance of the model choice stems from the observation that with the SP-model, the M-shell remains bound for densities up to three times the solid density. This is ruled out by the EK model and creates a clear difference in the modelling of the ion populations. Both models are supported by experimental data, albeit with data from different laser facilities. K-β lines have been observed from laser-heated aluminium foils heated to inferred temperatures of 600 eV at electron densities around

3 times solid density [62]. On the other hand, direct measurements of the IPD on the LCLS facility by tuning the XFEL wavelength are more consistent with a modified EK model.

This thesis focuses on the implementation of the IPD models in the CCFLY code and the treatment of the pressure-ionised electrons that need to be considered in the description of the electron distribution function. It is not the goal of this work to address the questions surrounding the general modelling approach and model selection of continuum lowering.

In any application where the electron distribution has not thermalised yet, and the temperature thereby undefined, an effective temperature can be computed with the expectation value of the free electron kinetic energy $k_B T \approx 2/3\langle E_{kin}\rangle$. There is currently no framework to modify the analytic IPD models for arbitrary distribution functions and the adoption of an effective temperature circumvents this problem. Similarly, to the best of the author's knowledge it is currently not known how accurate the effective temperature description would be when a distribution deviates significantly from the equilibrium distributions.

3.4.2 Pressure-Ionisation Operator

In an atomic-kinetics calculation of an X-ray heated foil, the IPD is generally on the increase for all charge states due to the increase in electron density, until the point in time when the targets starts to expand and cool down. It will then occur that an ion state ceases to exist due to part of its upper shell now residing in the continuum. Any electrons that occupied this shell then join the free-electron population, implying that the distribution function needs to be accurately updated in order to conserve the bound and free electron density.

In the current atomic-kinetics simulations, it was opted to make pressure-ionisation an instantaneous process. For this purpose, the IPD is computed at each time step on a pre-determined grid and held constant until the next user-set time step is reached. The time grid that illustrates this is depicted in Fig. 3.5. Variables whose evolution is described by differential equations, such as the ion populations and electron distribution, are propagated forward in time with an ODE solver. The time steps selected by the solver are semi-stochastic and determined largely by the magnitude of the time-derivatives and numerical stability criteria. As a result, the number of time steps that the solver requires is not known a priori.

Considering an ion state i with population n_i that is pressure-ionised to a state j with fewer bound electrons at time $t = t_k$, the number of electrons ξ that is released

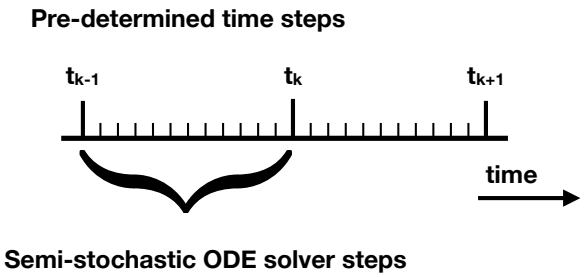

Figure 3.5: The time grids for instantaneously updated variables (IPD, XFEL radiation field) and continuously updated variables (free-electron distribution, ion populations). The user-defined time grid is the one the instantaneously updated variables are evaluated at. In between, the variables whose evolution is described by differential equations are propagated forward with an ODE solver. The solver chooses time steps according to numerical stability and accuracy criteria.

into the continuum can be computed from the charge of the initial and final ion states as $\xi = z_j - z_i$ electrons where z is the charge of the ions. The index k is used to denote the discrete time step. The energy released into the free-electron population can then be computed from the difference in the electrostatic potential held by the bound electrons as $dE = E_i - E_j$. This process is visualised in Fig. 3.6.

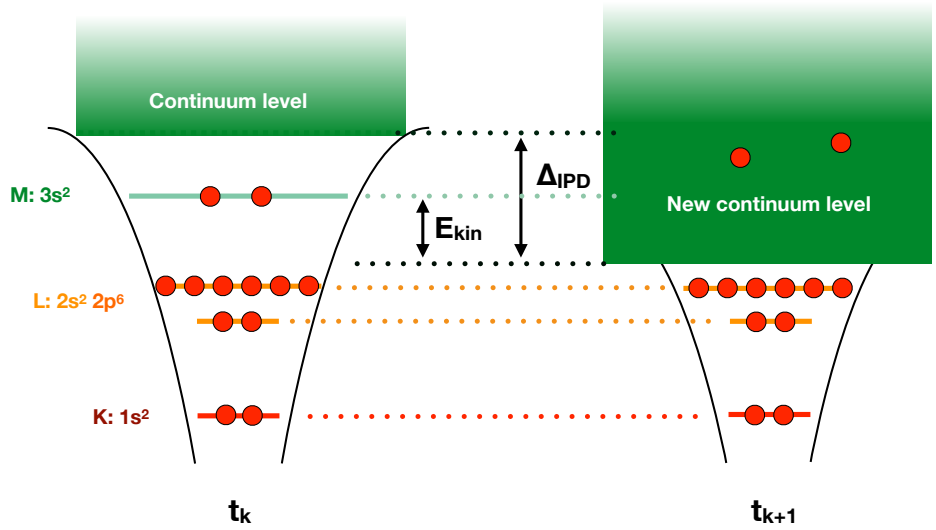

Figure 3.6: The effect of pressure ionisation of a bound shell in an ion in a simulation time step. The M-shell becomes pressure-ionised, and the two bound electrons join the free population. They obtain their binding energy as kinetic energy.

When the electron density increases in between time t_{k-1} and t_k to the point that it causes pressure-ionisation of a bound shell, the electrons in that shell are assigned to the free electron population. The initial state at time t_k is set to zero and the population is assigned to the newly created state. The electrons carry the difference

in binding energy so as to conserve the total energy; the energy contained in the ions and electrons does not change.

For this process, the corresponding Fokker-Planck operator can be written as:

$$\left(\frac{\partial f_E(E,t)}{\partial t}\right)_{IPD} = n_i \xi \delta(E - dE)\delta(t - t_k). \tag{3.16}$$

The operator Eq. 3.16 describes an instantaneous release of electrons into the continuum that preserves the total number of bound and free electrons, and their energy. The second delta-function represents the choice to make this an instantaneous process. Its physics is similar to the use case of the elastic Fokker-Planck operator examined in Section 2.4. Pressure-ionised electrons often have small kinetic energies for as long as the IPD varies gradually.

A CCFLY validation on IPD has been conducted with a near solid-density quasi-neutral Mg^{7+} system that is entirely in the $K^2L^0M^3$ super-configuration state. The density is such that continuum lowering given by the mEK model would pressure-ionise the entire M-shell, thereby adding three electrons per ion to the free-electron population. This process affects the ion population by depleting a state, the electron population by increasing its density and modifying the kinetic energy. Nevertheless, it is a process that should conserve the total number of bound and free electrons, as well as the energy retained by them. The parameters of this test scenario are listed in Table 3.1. With an M-shell ionisation threshold of 111.5 eV, the initial ion state can be pressure-ionised when the IPD exceeds this value. At the given electron density, this is the case and the continuum is lowered by ≈ 127 eV. This is sufficient to ionise one M-shell electron, which raises the free-electron density further and in turn increases the IPD. Through successive ionisations, the entire M-shell is depleted in one operation.

The case demonstrated here serves strictly to examine the conservative properties of the IPD operator. It is not realistic for any system to be entirely in one super-configuration state that is not the ground state, and particularly not with a depleted L-shell when the M-shell still holds three electrons. In a transient system, the M-shell electrons would typically be ionised before the L-shell electrons through collisional interactions. The artificial nature of this benchmark is the only reason that multiple pressure-ionised electrons can be produced for each ion with energies of $\mathcal{O}(100)$ eV. Typically, only one electron is pressure-ionised at a time and they are normally released with low kinetic energies which constitutes a less demanding numerical operation.

IPD CCFLY benchmark	
Parameter	Value
Material	Magnesium 7^+
Initial ion state	$K^2L^0M^3$
Final ion state	$K^2L^0M^0$
E_{-+}	760 eV
M-shell threshold	111.5 eV
n_i	4.0×10^{23} cm^{-3}
$n_e\|_{init}$	$\langle z \rangle \cdot n_i = 2.8 \times 10^{23}$ cm^{-3}
$T_e\|_{init}$	50 eV
# energy grid points	500
Minimum energy	0.01 eV
Maximum energy	1250.0 keV

Table 3.1: The simulation settings used to evaluate the pressure-ionisation Fokker-Planck operator for tracking the electron density and energy changes. The M-shell electrons of the initial ion state will be pressure-ionised when the mEK IPD is applied. The difference in binding energy between the initial and final ion state is E_{-+}.

Fig. 3.7 shows the density- and energy balance of the electrons held in the system. Given that the continuum lowering is strong enough to deplete the outer shell, pressure-ionisation reduces the density of bound electrons and transfers them to the free-electron population. The sum of bound and free electron densities represents the total number of electrons in the system, and this remains constant. The energy held by the bound and free electrons shows similar behaviour, as energy is transferred to the free-electron population. Importantly, the total density and energy are conserved during pressure-ionisation. The matter of reversibility is not addressed, as there is no need to implement a reverse operator in case the continuum is raised due to a decreasing electron density. The electron distribution function will be affected by pressure-ionisation at the distinct energies that correspond to the electrostatic potential held by the pressure-ionised electrons. For the process of ionising three M-shell electrons, Fig. 3.8 shows the change in the distribution. The distribution is initialised to a ($n_e = \langle z \rangle \cdot n_i = 2.8 \times 10^{23}\,\mathrm{cm}^{-3}$, $T = 50\,\mathrm{eV}$) thermal distribution. The complete ion population is put into the same state that is being pressure-ionised. Each of the three M-shell electrons leaves a distinct peak in the distribution function. The energies at which they appear are different due to two effects; after each ionisation, the binding energy of the remaining electrons increases as they become more strongly bound. Secondly, the change in electron density affects the degree of continuum lowering. As a result, continuum lowering can become a cascading effect that amplifies

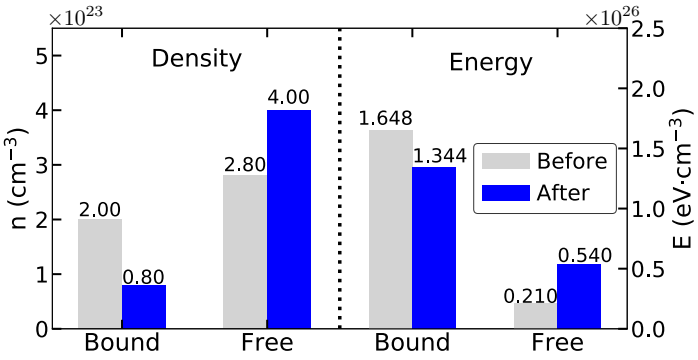

Figure 3.7: The density- and energy balance of the ion and electron system during pressure-ionisation. Both quantities are split between bound and free electrons. Pressure-ionisation transfers electrons and electrostatic potential energy to the free-electron population.

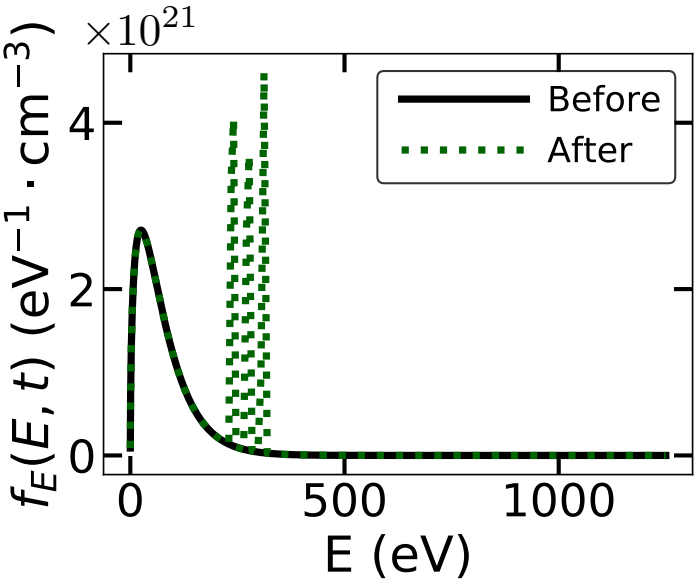

Figure 3.8: An electron distribution function before and after pressure-ionisation in the case detailed in Table 3.1. The distribution is initialised to a 50 eV thermal distribution, and sees the addition of three peaks for each of the pressure-ionised M-shell electrons.

itself. Depending on the mean kinetic energy in the distribution and the binding energy of the outer-shell electrons being ionised, pressure-ionisation can be either a heating or a cooling effect. There happens to be a difference in peak height and this carries no significance. The height of each peak is determined by its energy and how close or distant this energy may be from the nearest energy grid point. Therefore, the height can vary depending on its location while containing the same number of electrons.

The density is conserved exactly due to the conservative nature of the numerical schemes used to track the distribution function. Pressure-ionised electrons can appear at any continuous energy and need to be interpolated onto the discrete energy grid. The changes to the distribution are treated in the same way as the derivatives are interpolated in Eq. 3.12. There can be slight drift in the density of $\mathcal{O}(1\%)$ when pressure-ionising the entire ion population. This is caused by the cascade of ionisation events and the step-wise recalculation of the IPD in between each ionisation. The possible errors that arise are insignificant considering the fact that it will not normally occur that a significant fraction of the ions is pressure-ionised at once.

Sharp delta-function like modifications to the distribution function are not the ideal way to describe the physics of pressure-ionisation, as the electron shell structure is much more refined than the super-configuration model can represent. However, these peaks in the distribution are dispersed in a dense system in a similar way as the results presented in section 2.4. The numerical scheme can be modified to make pressure-ionisation a more gradual process in case numerical instabilities arise.

3.5 Benchmarking Rates and Conservation Laws

This section will assess the accuracy of the numerical schemes used by benchmarking the ion transition rates, and the conservation laws applied to the free electron distribution. The generalised numerical schemes should be consistent with results obtained from a thermal distribution, provided the numerical scheme operates on a discretised Maxwell-Boltzmann distribution. The cases will be outlined and applied to the following atomic transitions considered in ccfly; Collisional Excitation (CE), Collisional De-Excitation (CDE), Collisional Ionisation (CI), Three-Body Recombination (3BR), Photo-Ionisation (PI), Auger decay, Dielectronic Recombination (DR), and pressure ionisation. CCFLY also considers Radiative Excitation (RE) and Radiative De-Excitation (RDE) and Spontaneous Emission (SE), which will not be discussed in more detail as these process do not involve free electrons.

Despite imposing a thermal distribution in the free-electron population, it cannot be stated that the combined ion and electron system is in LTE. Throughout the benchmarks, the ion populations are frequently modified to values that differ from the Boltzmann or Saha distributions. In some cases, the electron density is also varied independently from the temperature. This is done purely to observe the effect on the ion transition rates and Fokker-Planck collision operators, but the conditions do not

necessarily reflect a static equilibrium. It is only the electron distribution that is thermal.

The full list of acronyms used for the atomic processes can be found after the Table of Contents. For clarity, the subscripts $-+$ and $+-$ are added to the cross-sections to indicate the direction of the atomic transition. By convention, $-+$ indicates a process whereby the ion gains energy and vice versa, $+-$ corresponds to a process whereby the ion loses energy. The residual energy of a free electron after a transition is denoted as P or E_{-+} throughout this section.

3.5.1 Maxwellian Test Case

For the non-thermal electron module to be consistent with results obtained in LTE conditions, the same ion rates should be recovered when the distribution is Maxwellian. Provided a parametric cross-section model $\sigma_{-+}(E)$ as a function of the impact energy, the volumetric rates S_{-+}/V of atomic transitions induced by electron collisions can be computed as:

$$S_{-+}/V = n_{-}(t) \int_0^\infty v(E)\sigma_{-+}(E) f_E(E)\,\mathrm{d}E, \tag{3.17}$$

where the velocity is computed from the energy as $v = \sqrt{2E/m_e}$ and n_- is the ion density of the charge state configuration undergoing a transition. For a MB distribution, Eq. 3.17 can be evaluated by using the analytic expression of the thermal distribution:

$$\begin{aligned} S_{-+}/V &= n_{-}(t) \int_0^\infty v(E)\sigma_{-+}(E) f_{MB}(E)\,\mathrm{d}E \\ &= n_{-}(t) \frac{2\sqrt{2}}{\sqrt{\pi m_e}} \left(k_B T\right)^{-3/2} \int_0^\infty \sqrt{E}\sigma_{-+}(E) \exp\left(-E/k_B T\right)\,\mathrm{d}E. \end{aligned} \tag{3.18}$$

Eq. 3.18 can often be evaluated through tabulated results for analytic cross-section expressions. This method of implementation is present in the SCFLY code, as well as in an earlier version of CCFLY that only considered thermal electron distributions. The non-thermal electron module computes the ion transition rate through composite trapezoidal integration, which should yield the same result. In the case where a

Maxwellian distribution is used for comparison, the ion rate can be computed as:

$$\begin{aligned} S_{-+}/V =\ & n_-(t) \int_0^\infty v(E)\sigma_{-+}(E) f_{MB}(E)\,\mathrm{d}E \\ \approx\ & n_-(t) \frac{2\sqrt{2}}{\sqrt{\pi m_e}} \left(k_B T\right)^{-3/2} \frac{1}{8} \sum_{i=0}^{N-2} \left(\sqrt{E_i} + \sqrt{_{i+1}}\right) \left(\sigma_{-+}(E_i) + \sigma_{-+}(E_{i+1})\right) \\ & \times \exp\left(-(E_i + E_{i+1})/k_B T\right)\ \left(E_{i+1} - E_i\right). \end{aligned} \tag{3.19}$$

Eq. 3.19 is subject to the truncation and sampling errors described in Subsection 3.3.1 that arise from the discrete energy grid. Accounting for these, Eq. 3.19 should yield the same ion transition rates as Eq. 3.18, provided the electron distribution and cross-section are the same. Any discrepancies should be linked to the energy grid selection for the non-thermal electron module to be considered consistent with equilibrium results.

Due to the coupled nature of the ion and free electrons, they evolve together and obey a density conservation law for the total number of bound and free electrons. Between the initial and final state of each atomic transition, a possible change in charge must be drawn from or released into the free electron population. For instance, a collisional excitation process should leave the free electron density intact. A collisional ionisation process, on the other hand, releases a bound electron into the free population. This is accounted for in the thermal mode by computing a density derivative for the free electrons as the product of the volumetric ion rate and the number of electrons liberated by each interaction as:

$$\frac{dn_e}{dt} = \zeta \cdot S_{-+}/V, \tag{3.20}$$

where ζ denotes the number of electrons added to the system per ion transition. Depending on the atomic process, ζ can take on integer values of $\{-1, 0, +1\}$. Applying Eq. 3.20 to each atomic transition, the principle of quasi-neutrality remains valid for all times of the interaction.

In the non-thermal mode, a similar relation must hold. The density change can now be computed as the expectation value of changes in the distribution function as:

$$\frac{dn_e}{dt} = \int_0^\infty \frac{df_E(E)}{dt}\,\mathrm{d}E \tag{3.21}$$

$$\approx \frac{1}{2} \sum_{i=0}^{N-2} \left(\frac{df_E(E_i)}{dt} + \frac{df_E(E_{i+1})}{dt}\right) \left(E_{i+1} - E_i\right). \tag{3.22}$$

Eq.3.22 reflects the fact that electrons can be displaced in energy-space through a multitude of pathways, and the total density change must be equal to that of the thermal electron mode if the distribution is Maxwellian. The time-derivatives of the electron energy and density are formulated as derivatives of the distribution function at each energy grid point. They cannot be compared for each energy grid point individually, but on the macroscopic scale however, the total changes in density and electron energy should match the thermal case. Eq. 3.20 and and 3.22 should yield the same result, regardless of the numerical value of the ion transition rate.

Any inelastic interaction can be associated with an energy transfer from the bound electrons to the free-electron population, or vice versa. The energy time-derivative for the free-electron population can be expressed as:

$$\frac{dE_{kin}}{dt} = E_{-+} \cdot S_{-+}/V, \tag{3.23}$$

where E_{-+} is the energy difference between the initial and final ion state. Eq. 3.23 gives the total amount of energy added to the free-electron population, with the convention that a positive change adds energy to the electrons. What is not revealed, is how this energy change is distributed over the electron distribution function. The energy change can be computed from the change in distribution as:

$$\frac{dE_{kin}}{dt} = \int_0^\infty \frac{df_E(E)}{dt}\,\mathrm{d}E \tag{3.24}$$

$$\approx \frac{1}{4}\sum_{i=1}^{N-2}\left(\frac{df_E(E_i)}{dt} + \frac{df_E(E_{i+1})}{dt}\right)\left(E_{i+1}^2 - E_i^2\right). \tag{3.25}$$

Similarly to the electron density, the energies obtained from Eqs. 3.23 and 3.25 should be equal, regardless of the value of the ion transition rate. This would ensure that the energy drawn from the electrostatic potential is conserved in the form of thermal energy, or vice-versa.

In the subsequent subsections, the validity of the energy and density conservation laws will be examined for each atomic transition. Additionally, the consistency in the ion rate will be verified for an imposed thermal electron distribution function. This acts as a benchmark for the numerical integration scheme used to compute the ion rates, and its coupling to the free-electron distribution function.

3.5.2 Collisional Excitation and De-Excitation

Collisional Excitation (CE) and its inverse, Collisional De-Excitation (CDE) are inelastic electron-ion interactions in which, as a result of free-electron collisions, a bound

electron can be raised (excitation) or lowered (de-excitation) into another bound shell. Both atomic transitions are depicted in Fig. 3.9.

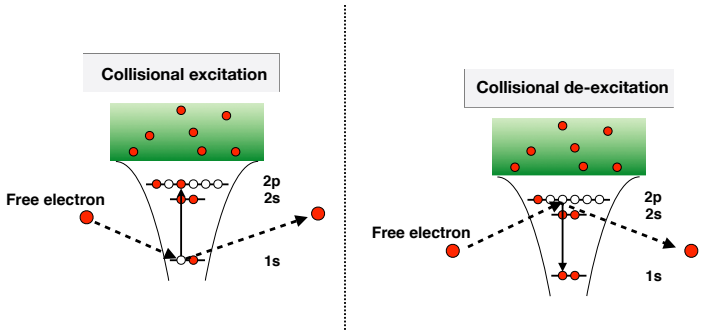

Figure 3.9: Collisional excitation and de-excitation in a magnesium ion. The ions undergo a bound-bound transition where an electron changes orbital as a consequence of a collision with a free electron. The free electron carries the residual energy to conserve energy.

3.5.2.1 Cross-section model

The excitation process depicted in Fig. 3.9 has a volumetric rate that can be computed with a single integral, provided the reaction cross-section $\sigma_{-+}(E)$ and the electron distribution function are known:

$$\begin{aligned} S^{CE}(t)/V &= n_-(t)\sqrt{2/m_e}\int_P^\infty \sqrt{E}\sigma_{-+}^{CE}(E)f_E(E,t)\mathrm{d}E \\ &\approx n_-(t)\frac{1}{2}\sqrt{2/m_e}\sum_{i=\arg\min_j(E_j-P>0)}^{N-2}\Big(\sqrt{E_{i+1}}\sigma_{-+}^{CE}(E_{i+1})f_E(E_{i+1},t) \\ &\quad -\sqrt{E_i}\sigma_{-+}^{CE}(E_i)f_E(E_i,t)\Big)(E_{i+1}-E_i)\,, \end{aligned} \tag{3.26}$$

where the integration starts at the excitation threshold P. The ion population is n_-, and scales linearly with the volumetric rate. The integral in Eq. 3.26 has been approximated through the trapezoid rule, where the summation starts at the first index j where the energy exceeds the reaction threshold: $E_j > P$. In both expressions for the rate, the probability is calculated that the electrons with a kinetic energy between (E_i, E_{i+1}) cause an excitation event. Below the energy threshold, this cannot take place. The cross-section for CDE can be obtained from the microscopic reversibility relation Eq. 1.10. This relation is only valid for bound-bound collisional processes, and will differ for the cross-sections of bound-free or radiative transitions. When the cross-section of the forward process is known, the cross-section for the inverse process

that de-excites the ion must obey the microscopic reversibility relation in order to model the correct behaviour in LTE. With this requirement, the CDE rate can be computed as:

$$\begin{aligned} S^{CDE}(t)/V =& n_+(t)\sqrt{2/m_e}\frac{g_-}{g_+}\int_0^\infty \sqrt{E}\sigma_{-+}^{CE}(E+P)f_E(E,t)\mathrm{d}E \\ \approx& n_+(t)\frac{1}{2}\sqrt{2/m_e}\frac{g_-}{g_+}\sum_{i=0}^{\arg\max_j(E_j+P<E_{N-1})}\Big(\sqrt{E_{i+1}}\sigma_{-+}^{CE}(E_{i+1})f_E(E_{i+1},t) \\ &-\sqrt{E_i}\sigma_{-+}(E_i)f_E(E_i,t)\Big)(E_{i+1}-E_i)\,, \end{aligned} \tag{3.27}$$

where $g_\pm$ denotes the state multiplicity of the ion super-configuration, and n_+ is the population of the excited ion undergoing a de-excitation transition. There is no reaction threshold for the free-electron impact, as the impact electron gains energy in this reaction. Nevertheless, the sum must be truncated at the index j such that the final free-electron energy $E_j + P$ is a value that fits on the energy grid. This truncation introduces an error that is proportional to $\int_{E_j}^\infty f_E(E)\,\mathrm{d}E$, the number of electrons with energies above the truncation point. If the error grows too large, the upper boundary of the energy grid must be increased.

The cross-section form for CE used in this work is given by the Van Regemorter model, a fitted form of Coulomb-Born calculations [63]. The cross-sections contain a correction factor to account for quantum effects, which is contained in the Gaunt factor [64]. The cross-section takes the form of:

$$\sigma_{-+}^{CE}(E) = \frac{8\pi^2 a_0^2}{\sqrt{3}}\frac{I_H^2}{P}\frac{F_{-+}G(E/P)}{E}, \tag{3.28}$$

where F_{-+} is the oscillator strength of the transition, and $G(E/P)$ is the Gaunt Factor (GF). For the GF, some different expressions exist in the form of power series. The one used in this work was originally proposed by Vainstein [65] (published in Russian) and is of the form:

$$G(E/P) = c_{-1}\ln(E/P) + \sum_{i=0}^{M} c_i\,(E/P)^{-i}\,, \tag{3.29}$$

for values of M up to 4 depending on the charge state configuration. Where fitted values were not available for Eq. 3.29, values from Mewe were used [66].

3.5.2.2 Inelastic Collision Operator

From the nature of the atomic transitions, it can be seen that the inelastic collision operator must conserve the total number of free electrons. The operator may merely act as a displacement operator, relocating electrons from a higher to a lower energy for CE and in the opposite direction for CDE. Whereas the electron density must be conserved, each excitation subtracts a constant amount of energy from the free-electron population. This should manifest itself as a cooling process. Conversely, a de-excitation event draws energy out of the ion electrostatic potential and therefore adds energy to the free-electron population. No such statement can be made for the momentum held by the free electrons. The ions are at room temperature in the regimes that occur in this work, and are capable of absorbing any amount of momentum required to maintain the energy balance.

To verify whether the inelastic collision operator acts as desired, similar methods can be used as in Section 2.3.1 where the elastic collision operator was benchmarked. Rates of change in the electron density and energy can be computed from the moments of the distribution function's time-derivatives:

$$\frac{d}{dt}\left(n_e\right) = \int_0^\infty \frac{df_E(E,t)}{dt}\,\mathrm{d}E = 0 \;\forall t, \tag{3.30}$$

$$\frac{d}{dt}\left(E_{kin}\right) = \int_0^\infty E\frac{df_E(E,t)}{dt}\,\mathrm{d}E = \mp E_{-+}S(t)^{\mp\pm}/V \;\forall t. \tag{3.31}$$

Eq. 3.30 computes the total density change in the free-electron population as the zeroth moment of the distribution's time-derivatives. Energy conservation is expressed through Eq. 3.31 which relates the ion transition rate and the excitation potential to the total change in energy in the free-electron population. For CE, the process in which an ion gains energy ($-+$ signs), this implies that energy is subtracted from the free electrons. The sign reversal for CDE ($+-$ signs) states that this energy is added to the free electrons for each de-excitation event. The ion transition rates scale linearly with the energy exchanged between the ion potential and free-electron kinetic energy.

The inelastic collision operator must obey the conservation laws Eqs. 3.30 and 3.31. In particular the energy conservation statement creates a direct coupling with the ion transition rate and population. The CE operator that does this is given as:

$$\begin{aligned}\left(\frac{\partial f_E(E,t)}{\partial t}\right)_{CE} = \; & n_-(t)\sqrt{2/m_e}\Big(-f_E(E,t)\sqrt{E}\,\sigma_{-+}^{CE}(E) \\ & + f_E(E+P,t)\sqrt{E+P}\,\sigma_{-+}^{CE}(E+P)\Big),\end{aligned} \tag{3.32}$$

where the inelastic operator $\left(\frac{\partial f_E(E,t)}{\partial t}\right)_{CE}$ is the CE contribution contained in the inelastic terms of the Fokker-Planck Eq. 3.7. The effect described in Eq. 3.32 is that of electrons being displaced from an energy E to an energy $E - P$ in the distribution function. This probability scales with the electron density at the kinetic energy being considered, the cross-section and the population of the ground-state ion species undergoing an upward transition.

For CDE, a similar operator can be formulated:

$$\left(\frac{\partial f_E(E,t)}{\partial t}\right)_{CDE} = n_+(t)\sqrt{2/m_e}\left(f_E(E+P,t)\sqrt{E+P}\,\sigma_{+-}^{CDE}(E+P) - f_E(E,t)\sqrt{E}\,\sigma_{+-}^{CDE}(E)\right). \tag{3.33}$$

Conversely for the CDE operator, the displacement operation adds the threshold energy P to each electron group inducing a de-excitation. The corresponding probability of this event scales with the electron density at the kinetic energy being considered, the cross-section and the population of the excited-state ion species undergoing a downward transition.

3.5.2.3 Benchmark

In line with the protocol outlined earlier, the rate calculations and inelastic collision operator for CE and CDE will be examined by using a discretised thermal distribution. The electrons are left to interact with a two-state ion system in a constrained CCFLY calculation. The calculation is initialised with thermal distributions at various temperatures, and allowed to run for a single time step.

The thermal version of CCFLY with semi-analytic expressions , which is based on SCFLY, is compared with a calculation done in the non-thermal mode with a discretised Maxwellian. Given an excitation transition between two ion states, the ion rates, and electron density- and energy change are computed at a range of temperatures. The results should be consistent between the thermal and non-thermal versions of CCFLY, as the same distribution has been imposed. The calculation parameters are listed in Table 3.2.

The transition between the lower and upper state listed in Table 3.2 is a synthetic test case that does not necessarily need to be realistic. Depending on the IPD model used, M-shell can be pressure-ionised and the upper state may exist at this electron density. For magnesium, a $K \rightarrow L$ collisional excitation requires temperatures on the order of 1 keV, a scenario that does not occur in the experimental work discussed in

CE and CDE CCFLY benchmark	
Parameter	Value
Material	Magnesium
Charge	6^+
Lower ion state	$K^2L^4M^0$
Upper ion state	$K^2L^3M^1$
E_{-+}	32.2 eV
n_-	1 cm^{-3}
n_+	1 cm^{-3}
n_i	4.31×10^{22} cm^{-3}
n_e	3.02×10^{23} cm^{-3}
T_e	10-250 eV
# energy grid points	250
Minimum energy	0.01 eV
Maximum energy	10.0 keV

Table 3.2: The simulation settings used to evaluate the inelastic Fokker-Planck collision operator for bound-bound collisional transitions. E_{-+} is the excitation potential between the lower and upper ion states, and $n_\pm$ are the target ion densities. Two modes of the CCFLY code will operate on these settings; one with a thermal distribution in the standard Maxwell-Boltzmann mode, the second with a discretised Maxwellian in the non-thermal mode. The consistency of the ion rates, electron density- and energy changes will be investigated.

this thesis. Regardless, the benchmarking calculation can demonstrate the accuracy of the ion rate calculations, as well as the electron distribution balance.

The ion densities of the upper and lower state (target states) are set to 1 cm^{-3}, as the rates of the ion transition rates, energy and density are linear in the ion density. The volumetric rates presented can therefore be interpreted as the rates per ion. The total ion density, composed of non-interacting ground-state ions of the same charge, is set to solid-density ($n_i = 4.31 \times 10^{23}\,\text{cm}^{-3}$) to obtain a representative degree of correct continuum lowering and quasi-neutrality in the system.

Ion Transition Rates

In the thermal electron distribution mode, the ion transition rates are computed with Eq. 3.18 and the CE and CDE cross-sections. For the specific choice of cross-sections in this Subsection, this results in semi-analytic expressions for the ion transition rates whose results are tabulated. In the non-thermal mode, the rates are calculated with Eq. 3.19. Provided the distribution is imposed to be Maxwellian, this should yield the same transition rate, omitting discretisation and truncation errors caused by the

discrete energy grid. The results of this comparison are plotted in Fig. 3.10. The

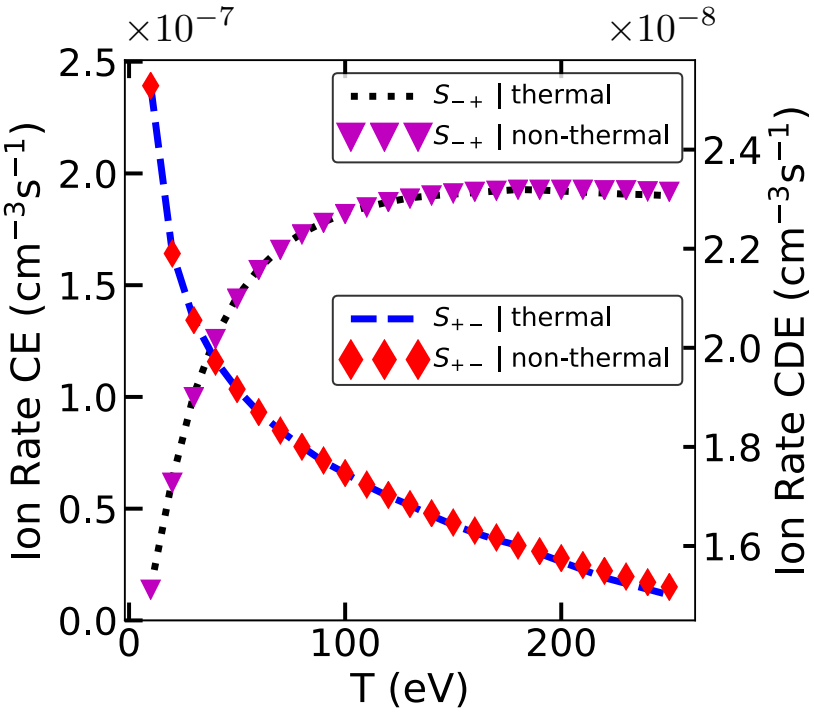

Figure 3.10: $L \to M$ collisional excitation (S_{-+}) and de-excitation (S_{+-}) rates in a 6^+ magnesium ion. The rates in the thermal version are calculated from semi-analytic cross-section expressions. Their counterparts in the non-thermal CCFLY version are computed for a discretised Maxwellian. Any differences can be traced back to grid discretisation errors.

density of data points is higher than the markers in Fig. 3.10 would suggest. Only every fifth data point is marked for visibility reasons, as the curves largely overlap. This style is retained for the figures in this subsection.

The ion rates have been computed with a target ion density of 1 cm^{-3}. Judging by the low rate[2], this makes bound-bound collisional transitions an unlikely process. It merely serves as a use case for demonstration and verification purposes here, but it may be of importance with heavier elements with populated states that contain at least three occupied atomic shells.

The excitation energy of 32.2 eV is small compared with the temperature change used in the benchmarking. From $T_e \sim 120\,\mathrm{eV}$ onwards, approximately 4 times the threshold, the excitation rate saturates. The de-excitation rate decreases with increasing temperature, as the energetic incentive to undergo a de-excitation is reduced.

[2]In subsequent sections, it will be demonstrated that other transition rates such as three-body recombination have rates on the inverse femtosecond time scale.

The energy grid was deliberately chosen to have a high grid density, so it can be seen that the ion rates match in the limiting case. The numerical scheme has the ability to retrieve the same transition rates in up to differences that are below 0.1% for all temperatures. Due to the large number of benchmarks required on all the atomic transitions, the effects of varying the grid density will be examined for other processes.

For verifying the density- and energy conservation of the collision operators Eqs. 3.32 and 3.33, it is relevant to depict their profile at various temperatures. From the same benchmarks, the time-derivatives as a result of CE and CDE were retrieved at $T_e = \{10, 50, 210\}$ eV, with the results plotted in Fig. 3.11. The results in Fig. 3.11 are computed with the non-thermal electron mode of CCFLY. The thermal version only requires a change in number density and total kinetic energy, a less detailed description than the full spectrum of the distribution function derivatives provided here.

As the distribution for this benchmarking case is thermal, and the cross-sections are smooth polynomials (Eq. 3.28), the collision operator would be expected to also have a smooth profile. Rather, it displays a spiked profile that has no intrinsic physical significance. It is a feature of the numerical scheme Eq. 3.12 together with the logarithmic energy-grid spacing, and would not occur if the grid spacing were uniform.

At higher energies, the spacing between grid points grows larger. This becomes visible in the collision operator for CE. Electrons that come from a higher energy bin are placed in a bin that lies $P = 32.2$ eV lower in energy, a bin that is much narrower than the bin of origin. This creates high peaks, as the density of electrons in a bin is proportional to the magnitude of the distribution function and its bin width, a width that will be lower than at the energy bin of origin. Due to the growth in bin size at higher energies, some closely-spaced bins at lower energies are not populated at all by this displacement operation.

The effect is less noticeable for CDE, as the displacement takes electrons up in energy space towards the wider energy bins. An averaging effect takes place, reducing the number of sharp peaks in the collision operator.

It may be more appropriate to distribute a change in the distribution to a larger collection of neighbouring energy groups when considering a single atomic transition. In a large-scale atomic-kinetics calculation, the problem is reduced by the number of transitions that can occur. The excitation threshold can take on a large range of continuous values, thereby distributing the electrons over more energy groups when considering the range of transitions. Should any artificial peak in the distribution

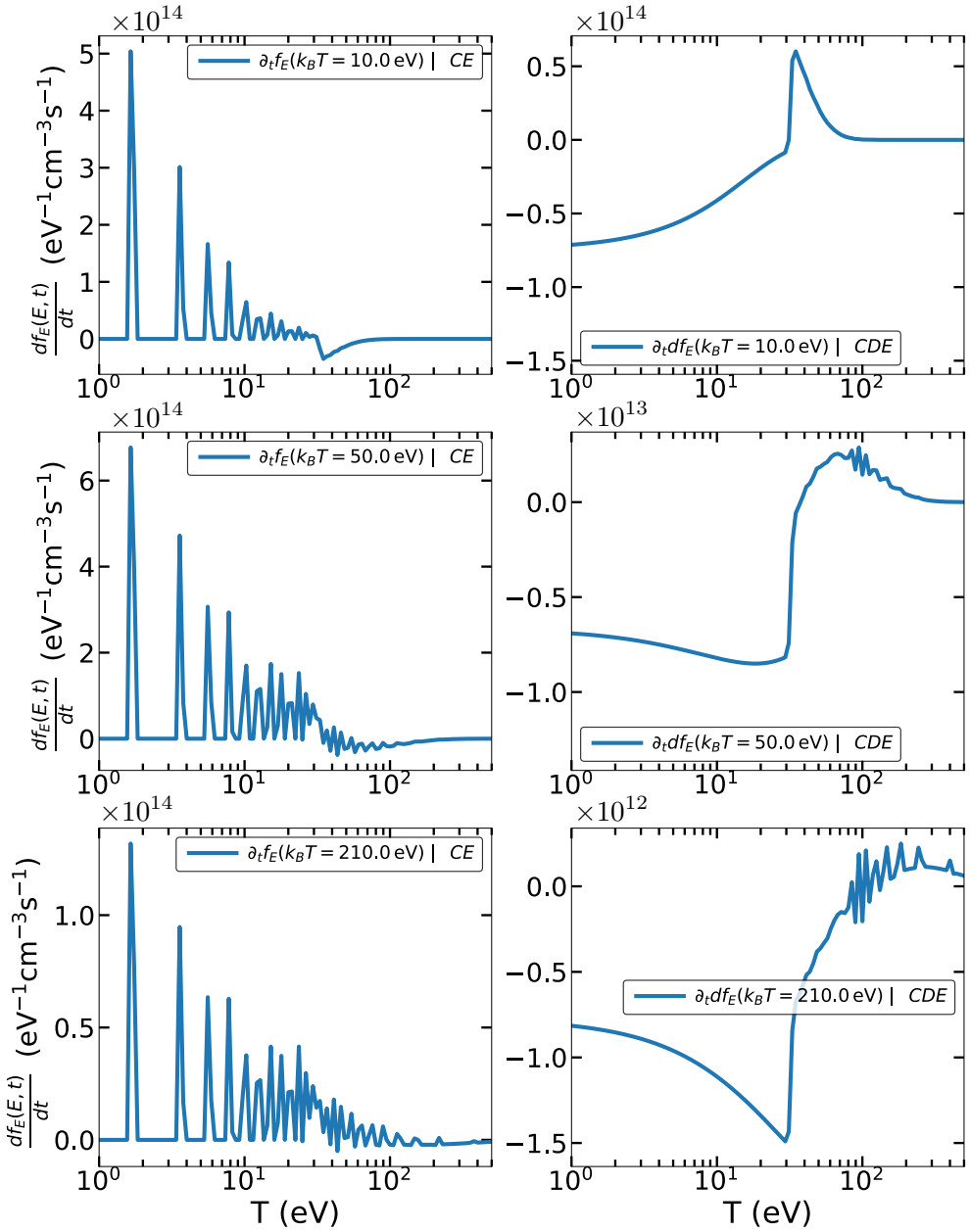

Figure 3.11: Inelastic collision operators for collisional excitation (left) and collisional de-excitation (right) in an Mg^{6+} $L \rightarrow M$ collisional transition. The collision operator should act as a displacement operator, relocating electrons from higher to lower energies (excitation) or vice-versa for de-excitation.

function still occur, it will blur out in subsequent time steps as any peak will produce large time-derivatives in the elastic collision operator.

Density Conservation

For the conservation of the electron density it is of importance that the collision operators plotted in Fig. 3.11 conserve the number of particles regardless of the ion transition rate, or the shape of distribution's time-derivatives. It is likely the case that a collision operator acting on a system with many possible transitions has a smoother profile. Nevertheless, for each number of transitions, conservation of density should hold.

This was examined by integrating the inelastic collision operator over energy, thereby obtaining the energy-independent time-derivative of the electron density Eq. 3.30. For both bound-bound processes, there should be no change in the electron density. Any deviations should be related to the electron grid parameters, integration methods or floating point errors. The findings are plotted in Fig. 3.12 The dotted

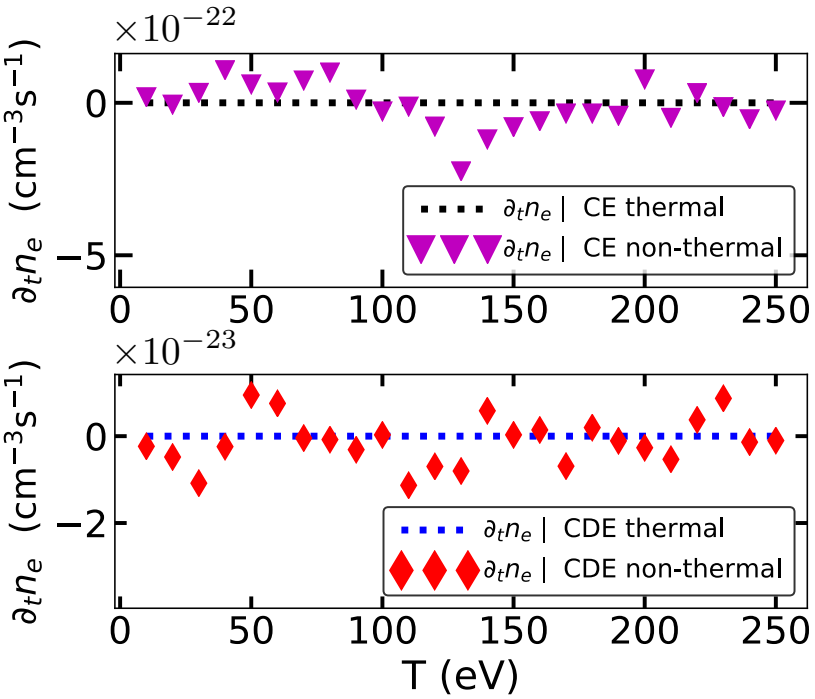

Figure 3.12: Electron density time-derivatives as a result of $L \to M$ collisional excitation (above) and de-excitation (below) in Mg^{6+}. Both processes should not affect the electron density and any deviations should be traceable to the numerical scheme or floating point errors.

lines in Fig. 3.12 mark the result obtained from the thermal CCFLY version; no density change is expected at any electron temperature. Results obtained from the non-thermal version fluctuate around density changes of $\mathcal{O}(10^{-23} - 10^{-22})$ cm^{-3} per ion transition. The target ion density is set to 1 cm^{-3}, with the total ion density

(of non-interacting ground-state ions of the same charge) set to $4.31 \times 10^{23}\,\mathrm{cm}^{-3}$. These fluctuations are insignificant when compared with the electron number density, even when considering the fluctuations of the full ion population. The numerical scheme therefore conserves electron energy, even when it has artefacts that manifest themselves in the form of sharp peaks in the collision operator.

Energy Conservation

Analogously to the verification of density conservation, there exists an energy conservation constraint that the collision operators must obey. Each bound-bound transition adds or subtracts a fixed amount of energy from the free-electron population, regardless of the ion transition rate. For a known transition rate, it is known how much energy is exchanged with the free-electron population.

This should be reflected in the collision operators, which reveal not only how much energy was added to or taken from the free-electron population, but also at which kinetic energies. The time-derivative of the total kinetic energy held by the free electrons can be computed with Eq. 3.31. The findings are plotted in Fig. 3.13 The time-derivatives of the free-electron total kinetic energy contain depend on the

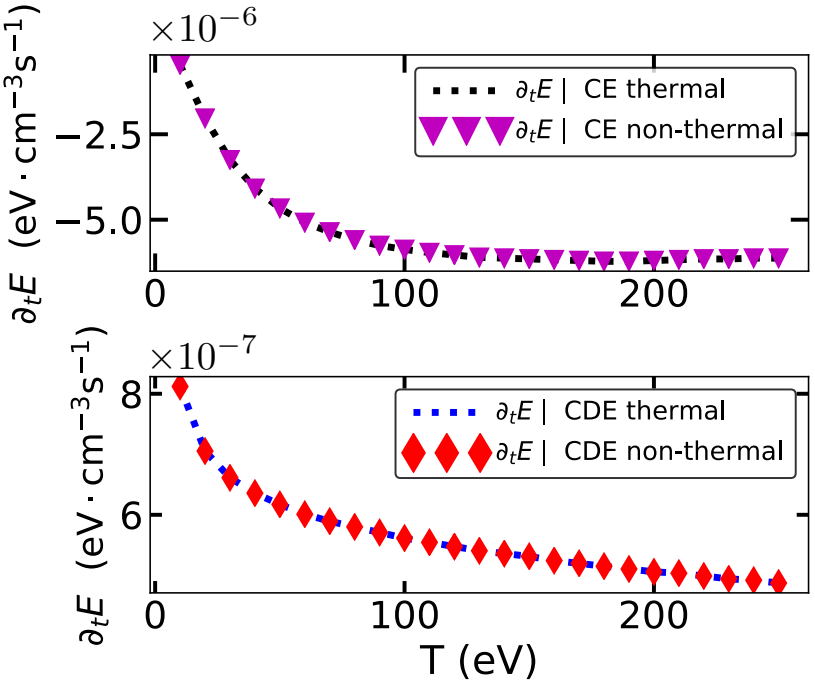

Figure 3.13: Electron energy time-derivatives as a result of $L \to M$ collisional excitation (above) and de-excitation (below) in Mg^{6+}. Excitation draws energy from the free electrons, de-excitation feeds energy into the free electrons. The energy per ion transition is fixed at the reaction threshold.

excitation potential, which is close to constant over all electron temperatures[3], and the ion transition rate. Excitation draws energy from the free population, resulting in a negative kinetic energy change for all temperatures. The energy derivative saturates in the same way that the ion transition rate does, as can be seen in Fig. 3.10.

The energy change for CDE also follows the same trend as the ion transition rate. In fact, it is a scaled version of its ion rate where the scaling factor is the excitation potential. The energy transfer to and from the free-electron population matches up to $< 0.1\%$ between the thermal and non-thermal CCFLY modes, a satisfactory result. The fluctuations are also distributed in the upward and downward direction, thereby partly cancelling out across the full temperature range.

The dotted lines in Fig. 3.12 mark the result obtained from the thermal CCFLY version; no density change is expected at any electron temperature. Results obtained from the non-thermal version fluctuate around density changes of $\mathcal{O}(10^{-23} - 10^{-22})$ cm^{-3} per ion transition. The numerical scheme therefore conserves electron energy, even when it has artefacts that manifest themselves in the form of sharp peaks in the collision operator.

The ion rates computed with the thermal and non-thermal version of CCFLY are in good agreement with each other, up to 0.1% discrepancies that are related to the energy grid discretisation. For various temperatures, the results obtained from an analytic thermal distribution and a discretised Maxwellian are consistent. The inelastic collision operator Eqs. 3.32 and 3.33 that has been implemented in CCFLY obeys the density and energy conservation laws for bound-bound collisional transitions.

Momentum does not occur in the discussion, as the total free-electron momentum is not a conserved quantity in inelastic ion-electron collisions.

3.5.3 Auger Decay and Dielectronic Recombination

Auger decay is one of the main heating processes in XFEL-heated solid-density plasmas. When a magnesium ion loses a core-electron, it has a probability of $\mathcal{O}(96\%)$ to decay through Auger decay for magnesium ions[4], with the remainder shedding their excess energy through radiative decay channels [19]. Auger recombination involves an electron dropping down into the core hole from a higher shell, while expelling another

[3]It can fluctuate up to second order with IPD, which is generally a function of the electron temperature and density.

[4]This probability is material-dependent. However, the fraction of ions that decays through Auger recombination is significant for low-Z elements.

electron that carries the residual energy P. Auger decay is named by the shells participating in the transition (vacancy-electron-electron), and in low-Z elements such as magnesium, as discussed in this thesis, the main contribution comes from KLL decay.

The Auger process produces highly energetic electrons that are added to the free population, and because of the high rate of Auger decay, this makes it possible to use X-ray heating to create warm dense plasmas in well-controlled conditions. Its inverse process is DR, a two-step reaction whereby a free electron is captured without the immediate emission of radiation. Instead, the residual energy of the electron capture is used to excite a bound-bound transition in the ion. In the second step, this excited state decays to a more stable ion state through the emission of a photon. Due to the discrete energy levels of the bound ion states, DR is a resonant process in which free electrons can be absorbed.

In the discussion of the DR transition rates and conservation laws, only the radiation-less capture of a free electron is considered. Only this step involves an interaction between the ion and the free-electron population and therefore only this part of the interaction model needs to be generalised to be able to deal with a non-thermal electron distribution. The subsequent decay process does not depend on the free-electron distribution function and is omitted from the discussion. Both processes are pictured in Fig. 3.14.

3.5.3.1 Cross-section Model

Auger decay has a rate that is, to first order, constant with respect to the plasma conditions. There are some slight density effects, where a high electron density ($> 10^{24}\,\mathrm{cm}^{-3}$ for a magnesium plasma) can alter the Auger rate by $\mathcal{O}(1\%)$, but these are negligible for our purposes [67]. The Auger rate can therefore be modelled as having a constant value for each charge state configuration. The Auger rates calculated for the purpose of this thesis are obtained from a Dirac-Hartree-Slater code and treated as being constant [68].

The ejected electron has a narrow spread in energy that is determined by the level structure of the ion. For computational purposes, it can be considered a delta-function source of electrons in energy-space. This can be done because for atoms with $Z \gtrsim 10$, any ejected Auger electron has an energy above 1 keV. In this range, the resolution of the free-electron energy grid is several tens of eV. In cases where the true energy spread does matter, the energy spread can be related to the excited state's lifetime to approximate a typical spread [69].

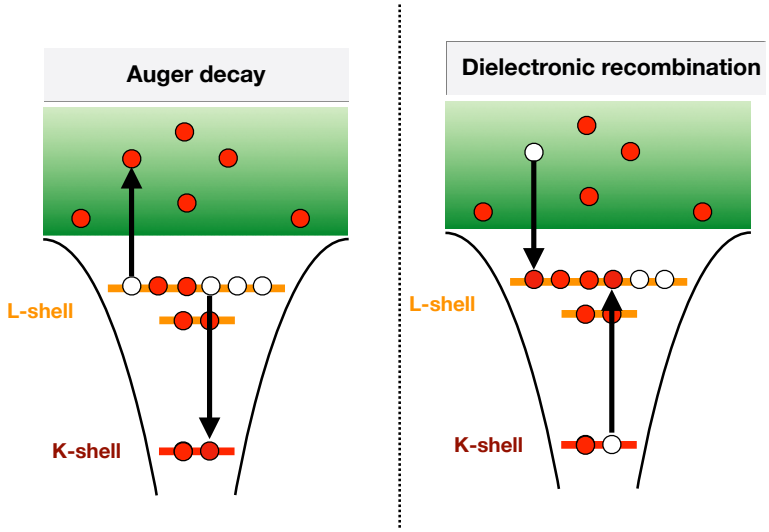

Figure 3.14: Auger recombination in a magnesium ion (left) and its inverse, dielectronic recombination (right). In Auger decay, a spontaneous process, an L-shell electron drops down to fill a K-shell vacancy. The excess energy is carried by another L-shell electron that is ionised as a result. The final charge of the ion is decreased, while its total binding energy has also decreased. The radiation-less capture of dielectronic recombination follows the same reaction pathway in reverse order, before the ion subsequently decays to a more stable state upon the emission of a photon.

The DR transition is a resonant process induced by a free electron. Assuming a delta-function energy spread in ejected electrons and a MB distribution, the DR rate can be directly related to the Auger rate through detailed balance without an explicit cross-section model formulation:

$$S^{DR}(t)/V = n_+(t) n_e \frac{1}{4\pi\sqrt{2\pi}} \frac{h^3}{m_e^{3/2}} \frac{g_-}{g_+} (k_B T)^{3/2} \exp\left(P/k_B T\right) S^{KLL}/V. \tag{3.34}$$

Eq. 3.34 is already present in SCFLY and the thermal-electron version of CCFLY, and acts as the benchmark for DR. The relation is fundamentally different from what would be expected at a resonant transition typically associated with radiationless capture. Also derived from microscopic reversibility is the DR cross-section that can be applied to a non-thermal electron distribution:

$$\sigma_{+-}^{DR}(E) = \frac{g_-}{g_+} \frac{2}{m_e^3} \frac{h^3}{16\pi} \frac{S^{KLL}/V}{E} \delta(E - P). \tag{3.35}$$

Due to the delta-function dependence, the DR cross section samples the distribution at the transition energy P. Provided an arbitrary distribution function, Eq. 3.35 can be related to the ion transition rate:

$$S^{DR}(t)/V = n_+(t) \frac{\sqrt{2}}{16\pi} \frac{g_-}{g_+} \frac{h^3}{m_e^3} v(E = P) \frac{S^{KLL}/V}{P} f_E(E = P). \tag{3.36}$$

Eq. 3.36 is the generalised counterpart of Eq. 3.34 that can be used for non-thermal distribution functions.

3.5.3.2 Inelastic Collision Operator

Auger decay and DR add and subtract electrons to and from a narrow energy range. This resonant behaviour also manifests itself in the simple form of the inelastic collision operator. Auger decay can be considered a source term collected in S in Eq. 3.7 as there is no coupling to the distribution function. For an Auger process with a known rate, the strictly non-negative source can be written as:

$$S_{KLL}(E,t) = S^{KLL}(t)/V \cdot \delta(E-P), \tag{3.37}$$

where the only time-dependence originates from the time-dependent ion population contained in the volumetric rate. The delta function ensures that electrons are ejected at the resonant energy, and one electron is ejected per transition. The collision operator for DR is formulated as:

$$\left(\frac{\partial f_E(E,t)}{\partial t}\right)_{DR} = -n_+(t)\sqrt{2/m_e} f_E(E,t)\sqrt{E}\,\sigma_{+-}^{DR}(E) \cdot \delta(E-P). \tag{3.38}$$

Eq. 3.38 indicates that electrons can only be drawn from the free-electron population in a narrow energy range. The operator is non-positive, and draws one electron per transition from the free population.

3.5.3.3 Benchmark

Due to the temperature- and density-independence of the Auger rate, there is no variation in the ion transition rate between the free-electron modelling approaches for this process. The DR collision operator behaves similarly to the operators of CE and CDE, and similar benchmark methods can be used here.

The benchmark will be based on the $K^2L^5M^0 + e^- \leftrightharpoons K^1L^6M^1$ transitions in magnesium, a reaction channel that connects the ground state of a 5+ ion and its core-hole excited state. The remainder of the parameter ranges to compare the results of a thermal and non-thermal electron calculation are listed in Table 3.3: With the amount of continuum lowering in a magnesium system at this density range, the upper ion state is partially pressure-ionised and the M-shell electron will not be bound (according to the mEK model). Pressure-ionisation is not of relevance in this benchmark and in the CCFLY code used for these calculations, it would be applied after the collision operators. Although the system is at solid density, the densities of

CE and CDE CCFLY benchmark	
Parameter	Value
Material	Magnesium
Charge	5^+
Lower ion state	$K^2L^5M^0$
Upper ion state	$K^1L^6M^1$
E_{-+}	1238 eV
n_-	1 cm^{-3}
n_+	1 cm^{-3}
n_i	4.31×10^{23} cm^{-3}
n_e	$10^{23} - 10^{24}$ cm^{-3}
T_e	10-1500 eV
# energy grid points	10-10^4
Minimum energy	0.01 eV
Maximum energy	10.0 keV

Table 3.3: The simulation settings used to evaluate the inelastic Fokker-Planck collision operator for auto-ionisation transitions (Auger decay and dielectronic recombination). The energy difference between the lower and upper ion states E_{-+} excludes IPD. The ion densities of the target states is 1 cm^{-3} so that the rates can be interpreted as per-ion rates. Two modes of the CCFLY code will operate on these settings; one with a thermal distribution in the standard Maxwell-Boltzmann mode, the second with a discretised Maxwellian in the non-thermal mode. The consistency of the ion rates, electron density- and energy changes will be investigated.

the target ions is set to 1 cm^{-3} so that the rates can be interpreted as per-ion rates. The remainder of the ion population is set to the Mg^{6+} ground state to bring the ion density up to solid density. In the benchmark, there is no significance as to what the total ion density is as the transition listed in Table 3.3 is being considered in isolation.

For the non-thermal electron calculation to work correctly, it should be consistent with results from the thermal electron CCFLY module when the distribution function is an imposed Maxwellian. This will be verified for a range of electron temperatures, densities, and the number of grid points on the discretised energy grid. This parameter that can be independently set plays a particularly important role for a resonant process. The results of this benchmark can be of use when determining the energy grid spacing.

Ion Transition Rates

The ion transition rates were computed in the thermal and non-thermal electron mode, for a fixed density $n_e = 3.0 \times 10^{23}$ cm^{-3} and an energy grid with 300 grid

points. The remainder of the parameters are listed in Table 3.3. Volumetric ion transition rates are linear in the electron density and ion density, and the variation with temperature is more relevant for this process. This is the case because the threshold energy (> 1 keV) of the resonant DR process is far above the typical electron temperature range. The Auger rate is condition-independent, regardless of the modelling method of the electron distribution. The ion transition rates are plotted in Fig. 3.15.

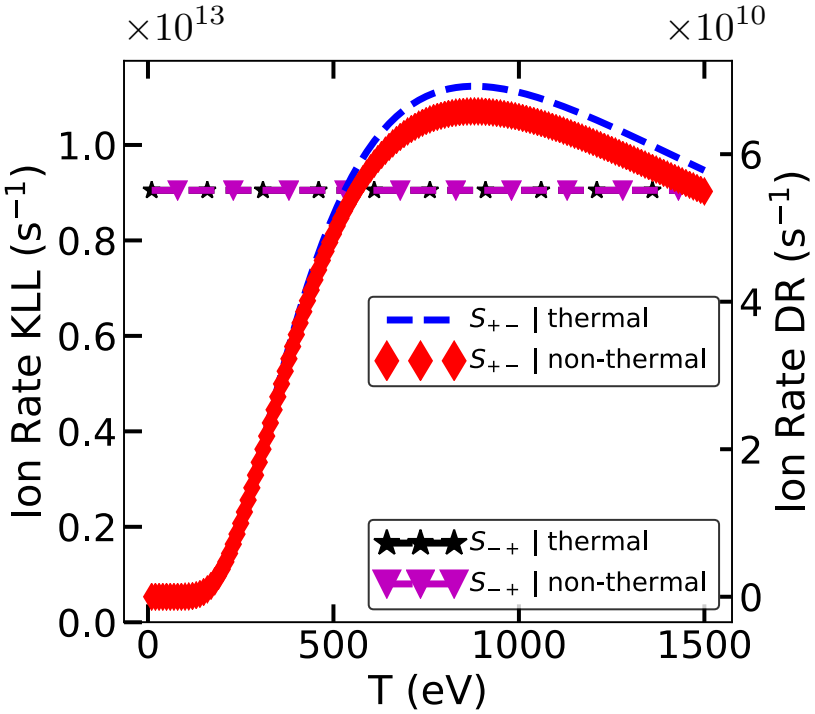

Figure 3.15: KLL Auger recombination (S_{-+}) and Dielectronic Recombination (DR) (S_{+-}) rates in Mg^{5+}. The Auger rates are constant. The DR rates in the thermal version are calculated from detailed balance, and from a cross-section expression in the non-thermal mode with a discretised Maxwellian. Any differences can be traced back to grid discretisation errors.

The Auger rate is treated as a constant in the CCFLY code, hence there is no difference between the thermal and non-thermal electron mode. In the temperature range accessible with XFEL-produced plasmas, typically a few hundred eV, there is no noticeable difference ($< 1\%$) for the DR rates. Differences arise in the temperature range $T \gtrsim 500$ eV, where the overlap between the distribution and cross-section grow larger. The delta-function DR cross-section is located at an energy where the energy grid has spacings of $\mathcal{O}(30)$ eV, a spacing that is not fine enough to resolve the cross-section. This is the cause of discrepancies of order 5% or below, a result that indicates

the energy spacing is sufficiently small.

The DR collision operator displays strongly resonant behaviour around the same energy as the residual energy of Auger-ionised electrons. The residual energy is the ionisation potential listed in Table 3.3 supplemented by the IPD computed with the mEK model Eq. 3.14. The Auger source and DR collision operator are plotted in Fig. 3.16 at $T = 160$ eV, a density $n_e = 3.0 \times 10^{23}\,\mathrm{cm}^{-3}$ and an energy grid with 300 points.

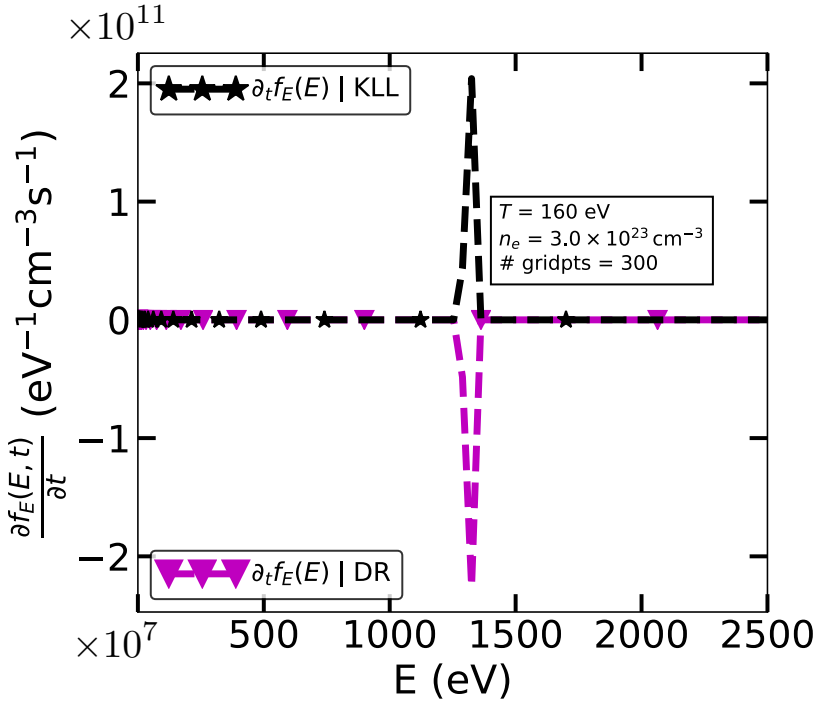

Figure 3.16: KLL Auger source and Dielectronic Recombination (DR) collision operator in Mg^{5+}. Both processes are resonant and only affect the free-electron population in a narrow energy range around the reaction threshold. The magnitude of the DR operator is much smaller than the strength of the Auger source, re-enforcing the stability of the lower K^2L^5 ion state.

Note that the scale on the negative axis (10^7) is different from the positive scale (10^{11}). In the full temperature range examined here, the transition rate of Auger decay is at least 4 orders of magnitude higher than the DR rate. The cause for this observation lies in the instability of the $K^1L^6M^1$ state that undergoes Auger decay, and the stability of the state it transitions into (K^2L^5). DR acts as a slight reduction in the Auger rates, as the electrons released by the same ion can then induce a DR event. Additionally, photo-electrons or Auger electrons from higher energies can do the same as they collisionally release energy. The benchmarking continues for DR only, as there is no variation in the Auger source with the plasma conditions.

Conservation Laws

Each DR event withdraws one electron from the free-electron population that becomes bound in a high energy shell, thereby producing an unstable ion state. The collision operator should reflect this through its negative density time-derivative, which should equal the ion transition rate in magnitude. Each electron that is withdrawn from the free-electron population originates from the narrow energy range around the reaction threshold. The collision operator should reflect this by having a negative energy time-derivative whose magnitude equals the product of the ion rate and the energy threshold. These requirements are formulated in Eqs. 3.39 and 3.40:

$$\frac{d}{dt}\left(n_e\right) = \int_0^\infty \frac{df_E(E,t}{dt}\,\mathrm{d}E = -S^{DR}(t)/V \;\forall t, \tag{3.39}$$

$$\frac{d}{dt}\left(E_{kin}\right) = \int_0^\infty E\frac{df_E(E,t)}{dt}\,\mathrm{d}E = -E_{-+}S^{DR}(t)/V \;\forall t. \tag{3.40}$$

It will be examined how well the conservation laws are abided by for variations in electron density, and the number of energy grid points. The scan over electron density will be done at a constant temperature $T = 100\,\mathrm{eV}$ and an energy grid containing 300 grid points. All other parameters remain as specified in Table 3.3. This use case will test the linearity of the electron density- and energy loss with respect to density, with the results plotted in Fig. 3.17.

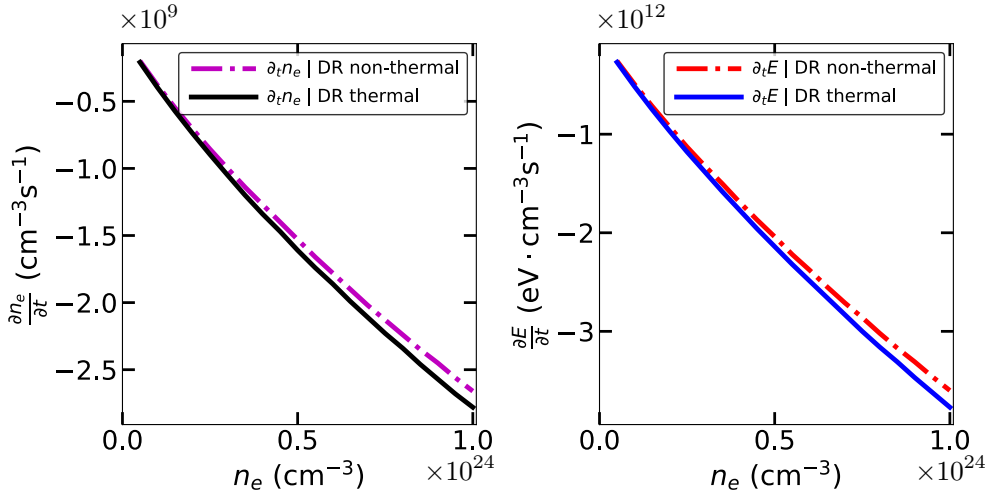

Figure 3.17: Dielectronic Recombination density- (above) and energy (below) loss rates due to the collisional operator Eq. 3.38 against density in Mg^{5+}. Both loss rates are linear in electron density for the thermal electron calculations. In the non-thermal mode, the discrepancies are caused by a slight mismatch in ion transition rate.

The loss rates of the density and energy density are linear in the thermal electron calculations. The discrepancies between the thermal and non-thermal case with an

imposed Maxwellian are directly proportional to the mismatch in ion transition rates. The observation indicates that the energy- and density balance is carried out as expected. More importantly, the evolution of the distribution function is computed self-consistently, with every modification to the distribution being traceable to the ion transition.

Finally, the last use case of the DR examines the accuracy of the collision operator while varying the number of energy grid points. The energy grid (logarithmic) spacing is a parameter that can be changed independently, and it is in line with intuition to choose the number of grid points as high as computationally practical. The cost and benefits of the number of grid points can be quantified by varying the number of grid points between 10 and 10,000 on a $10^{-2} - 10^{4}$ eV energy grid at a fixed temperature $T = 100\,\mathrm{eV}$ and density $n_e = 5.0 \times 10^{23}\,\mathrm{cm}^{-3}$.

The energy- and density conservation laws are the benchmarked quantity, as they can be computed from a thermal electron mode as a reference. For the non-thermal case, the density and energy time-derivatives are computed with the distribution integrals used in Eqs. 3.39 and 3.40, with the comparison plotted in Fig. 3.18.

Results obtained from the thermal electron module compute the density- and energy time-derivatives directly from the ion transition rates, and act as a benchmark once more. It requires at least $\mathcal{O}(100)$ energy grid points before these values can be approached in the non-thermal electron mode. The differences arise due to the differences in the ion transition rate, or rather, the inability to calculate it accurately with a coarse grid. Above ~ 200 grid points, there is no noticeable gain to refining the energy grid even further. DR, being a resonant process, places the highest requirement on the fineness of the energy grid, and the figure of 200 grid points can be taken as a reference for a full atomic-kinetics calculation.

3.5.4 Collisional Ionisation and Three-Body Recombination

Collisional bound-free transitions in warm dense plasma systems are critical to establish LTE during the short-lived time frames of laboratory-created plasmas. These transitions mitigate the transfer of energy, as well as electrons, from a bound state to the free-electron population. As such, they can drive a system towards equilibrium by altering the electron density and mean kinetic energy simultaneously. Due to their relevance in the equilibration process, this sub-set of bound-free transitions is of great importance to the overall description of warm dense matter.

Fig. 3.19 depicts the process of Collisional Ionisation (CI) and its inverse process, Three-Body Recombination (3BR), for a 7^{+} magnesium ion. The ionisation process

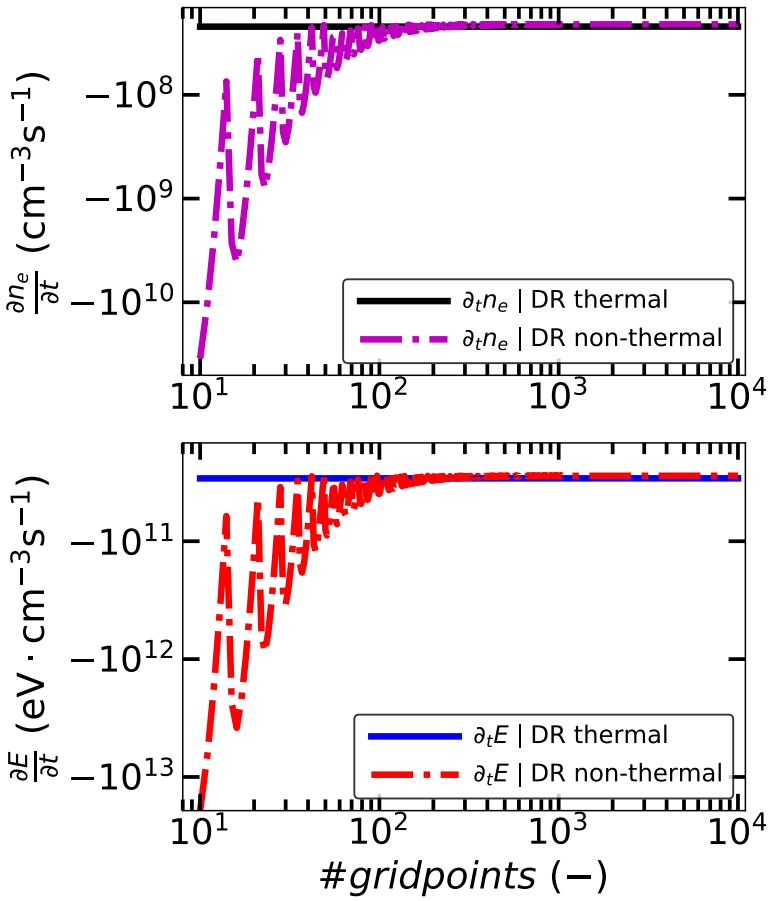

Figure 3.18: Dielectronic Recombination density- (above) and energy (below) loss rates due to the collisional operator Eq. 3.38 against the number of energy grid points. Both conservation laws can only be maintained with a minimum of $\mathcal{O}(100)$ energy grid points on a 10 keV energy range.

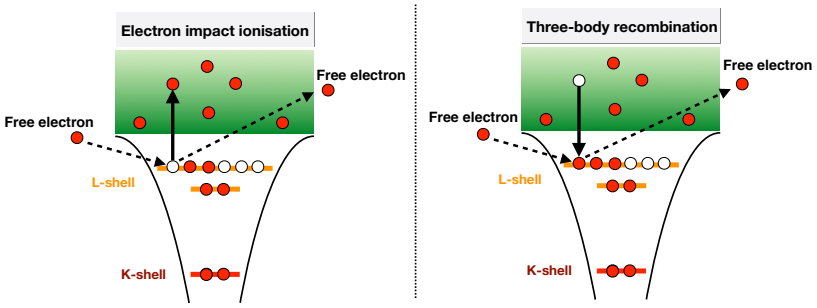

Figure 3.19: Collisional bound-free transitions in a magnesium ion. Collisions by free electrons induce an ionisation event (collisional ionisation), causing the ion to increase its charge. In the inverse process, three-body recombination, an electron collisionally recombines and the ion increases its charge. The residual energy is carried by the free electrons.

is induced by a free electron that collides with the ion, giving off its kinetic energy to ionise a bound L-shell electron. The electrons redistribute the residual energy and remain in the continuum. CI removes kinetic energy from the free-electron population while increasing its density and therefore acts as a cooling effect. In 3BR, a free electron becomes bound and the binding energy is carried away by another free electron. This process reduces the free-electron density while increasing its mean kinetic energy, and acts as a heating process. The temperature-density conditions of the warm dense system determine which of the two processes is more likely to happen, and they both aid in establishing LTE.

The description involving a distinct electron inducing an ionisation event is the binary picture that is consistent with a non-interacting free-electron population. The same applies to the situation where a single electron carries away the full excess energy after a recombination event. In a strongly coupled plasma, the binary picture is not accurate and collisions have a more collective nature [70]. It is therefore more precise to speak of a collisional event induced by a group of electrons that share in providing the threshold energy to cause an ionisation. Vice versa, the residual energy after a recombination transition is shared between a group of electrons.

3.5.4.1 Cross-section Model

Similar to the excitation and de-excitation transitions, CI and 3BR ion transition rates can be modelled with the cross-section formalism. The CI can be computed in the same method as a collisional excitation rate (Eq. 3.26), albeit with a different cross-section. For use in atomic-kinetics codes, where ion transition rates must be computed for a wide variety of atomic states and conditions, the cross-section models of interest are formulated in parametric form. The 3BR rate can be constructed from microscopic reversibility principles in order to link it directly to the CI cross-section.

There exist many forms of CI cross-sections, some of which will be discussed in more detail in Ch. 4. This extended chapter that is entirely focused on impact ionisation will also address the matter of parametrising density effects such as shielding and continuum lowering into the cross-section model.

The majority of parametric models contain at least a logarithmic term of the form $\log(E/P)$, where E is the impact energy and P the ionisation threshold. This term originates from the Bethe stopping power law that was formulated in 1930 for describing the attenuation of a charged particle flux traversing a medium [71]. In this application, the energy given off by a charge particle is absorbed by the medium through ionisation events. Many parametric models that have been proposed in

the decades that followed build on this logarithmic form, with refinements in the form of rescaling and the addition of extra terms that better describe near-threshold behaviour of the cross-section model [72–74]. In this benchmark, the cross-section model used to describe the probability of a CI event occurring in an atomic sub-shell containing ξ electrons was originally proposed by Lotz [72]:

$$\sigma_{-+}^{CI}(E) = C_{Lotz}\xi\frac{\ln(E/P)}{E\cdot P}, \quad E \geq P, \tag{3.41}$$

where P is the ionisation potential and C_{Lotz} is a material- and charge configuration-dependent constant.

Given a cross-section model $\sigma_{-+}^{CI}(E)$, the CI ion transition rate can be computed as:

$$\begin{aligned} S^{CI}(t)/V =& n_- \sqrt{2/m_e}\int_P^\infty \sqrt{E}\sigma_{-+}^{CI}(E) f_E(E,t)\mathrm{d}E \\ \approx& n_- \frac{1}{2}\sqrt{2/m_e}\sum_{i=\arg\min_j(E_j-P>0)}^{N-2}\Big(\sqrt{E_{i+1}}\sigma_{-+}^{CI}(E_{i+1}) f_E(E_{i+1},t) \\ &- \sqrt{E_i}\sigma_{-+}^{CI}(E_i) f_E(E_i,t)\Big)\left(E_{i+1}-E_i\right). \end{aligned} \tag{3.42}$$

In the binary picture, each ionisation event caused by an electron with energy E leaves a residual energy $(E-P)$ that is shared between the two outgoing electrons. This energy can be partitioned in many ways, some of which are more likely than others. With a constrained thermal electron distribution, any created electrons are implicitly allocated uniformly over the full energy range. In the cross-section formalism, this corresponds to having a uniform differential cross-section for all energies:

$$\frac{d\sigma^{CI}}{dW}|_u = \frac{1}{E-P}, \tag{3.43}$$

so that the normalisation $\int_P^E \frac{d\sigma^{CI}}{dW}|_u \mathrm{dW} = 1$ is recovered. W is defined as the energy transfer from the incoming electron to the lowest-energy outgoing electron. The atomic-kinetics codes SCFLY and CCFLY in its Maxwellian electron mode therefore both operate with a uniform differential cross-section, stated implicitly through the electron density- and energy balances Eqs. 3.4, 3.5 and microscopic reversibility relations for the ion transition rates.

Early scattering theory formulated by Thomson and Rutherford indicates that it is more likely for one of the electrons to carry the majority of the energy and the other to remain nearly static, rather than observing a near-even split [75]. Derived from classical mechanics for weakly-coupled systems, this differential cross-section

expresses the likelihood of observing a post-collision energy partitioning where one electron carries an energy $E - W$ [76]:

$$\frac{d\sigma^{CI}}{dW}|_R = \frac{\pi q_e^4}{E}\frac{1}{W^2}, \tag{3.44}$$

where the electron charge q_e is given in cgs units, and $P < W < E$ is the energy loss of the incident electron that initially had energy E. The energy loss must be at least the threshold potential, in which it retains all the energy and the ionised electron remains static. In the other extreme case, the incident electron loses all its energy (while remaining unbound) and the ionised electron carries the full residual energy. The cross-section of observing an ionisation event with an incident particle of energy E that scatters into two electrons with energies $(E - W, W - P)$ can be formulated as:

$$\sigma_{-+}^{CI}(E, W) = \sigma_{-+}^{CI}(E)\frac{d\sigma^{CI}}{dW}\left(\int_P^E \frac{d\sigma^{CI}}{dW}\,\mathrm{d}W\right)^{-1}, \tag{3.45}$$

where the differential cross-section (either uniform or Rutherford) has been normalised to account for unit conversions and the discretisation methods used to evaluate the cross-section integral Eq. 3.42. Despite its parametric form, normalising the differential cross-section analytically can create numerical inconsistencies between the ion transition rate and electron density time-derivative to evaluate, because the rate is still computed on a discretised energy grid. Self-consistency between the mean ion charge and electron density (effectively the enforcement of quasi-neutrality) can only be obtained when the differential cross-section is normalised through the same discretised integration method as in the rate calculation of Eq. 3.42.

The differential cross-section in a coupled electron system reflects the nature of the collisional interactions, and the energy distribution of the electron groups undergoing collective collisions. There is no a priori reason to believe that the differential cross-section takes on a profile derived for uncoupled systems, nor is there a reason to believe it it perfectly uniform across all energies. It is therefore a possible area of future research, and the numerical schemes presented here are flexible and can be easily modified to accommodate any arbitrary parametric single- and differential cross-section form.

The 3BR rate is a double integral over the energies of the two incoming electrons j and k. In order to relate the cross-sections of ionisation and recombination to each other, the pair of incoming electron energies is denoted as $(E_j = W - P, E_k = E - W)$,

which will result in a residual energy E being carried away by the single electron post-recombination. The 3BR transition rate becomes:

$$\begin{aligned} S^{3BR}(t)/V &= n_+(t)\frac{2}{m_e}\int_0^\infty\int_0^\infty \sqrt{E_jE_k}f_E(E_j,t)f_E(E_k,t)\sigma_{+-}^{3BR}(E_j,E_k)\,\mathrm{d}E_j\mathrm{d}E_k \\ &= n_+(t)\frac{2}{m_e}\int_P^\infty\int_P^{E-P} \sqrt{(E-W)(W-P)}f_E(E-W,t) \\ &\qquad \times f_E(W-P,t)\sigma_{+-}^{3BR}(E,W)\,\mathrm{d}W\mathrm{d}E \\ &\approx n_+(t)\frac{2}{m_e}\sum_{j=0}^{M_j}\sum_{k=0}^{M_k}\sqrt{E_jE_k}f_E(E_j,t)f_E(E_k,t)\sigma_{+-}^{3BR}(E_j,E_k)\,\Delta E_j\Delta E_k, \end{aligned} \tag{3.46}$$

with $M_j = \arg\max_j(E_j + P + E_0 \leq E_{N-1})$ and $M_k = \arg\max_k(E_j + P + E_k \leq E_{N-1})$. The double integral in Eq. 3.46 runs over both incident particle energies. In discrete form, the summation boundaries are such that the ejected electron has an energy that fits on the energy grid. Observing this criterion, the 3BR transition rate is computed from all possible electron energy pairs in the system.

In integral form, Eq. 3.46 is deliberately written in the energy-transfer formalism, making use of the same parameters as in Eq. 3.42 to reflect the fact that it is the inverse transition. The outgoing electron carries the energy of the two incident electrons and the ionisation potential, summed up as $(E-W)+(W-P)+P=E$. This energy has a lower bound of P, as both electron energies must be non-negative, and no upper boundary. The energy balance and parameterisation is depicted in Fig. 3.20. The differential cross-sections of CI and 3BR can be related to each other

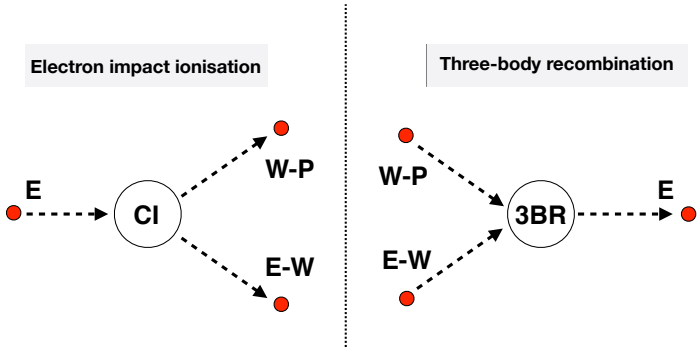

Figure 3.20: The energy balance of collisional ionisation (left) and recombination (right). For ionisation with impact energy E, the residual energy after ionisation is parametrised in terms of an energy transfer W. The ionisation threshold P is required to liberate the second electron. The inverse transition (recombination) is parametrised in the same manner to construct the transition rates.

through the microscopic reversibility principle. By constructing a two-level system

in LTE and forming the rate equations for the upward and downward transition, the cross-section relation is obtained:

$$\sigma_{+-}^{3BR}(E,W) = \frac{h^3}{16\pi m_e}\frac{g_-}{g_+}\frac{E}{(E-W)(W-P)}\sigma_{-+}^{CI}(E,W) \tag{3.47}$$

Eq. 3.47 is often referred to as the Fowler relation. Though derived for equilibrium conditions, it is valid in non-LTE systems as well due to the density- and temperature independence of the relation. It is a condition for any system that accurately describes equilibrium, that the CI and 3BR cross-sections satisfy Eq. 3.47. This symmetry translates to the energy partitioning between two incident electrons in the recombination process in the same way that it relates the outgoing electrons of ionisation.

With the Fowler relation, the 3BR rate Eq. 3.46 can be rewritten as:

$$\begin{aligned} S^{3BR}(t)/V =& n_+(t)\frac{h^3}{8\pi m_e^2}\frac{g_-}{g_+}\int_0^\infty\int_0^\infty f_E(E_j,t)f_E(E_k,t)\frac{E_j+E_k+P}{\sqrt{E_jE_k}} \\ &\times \sigma_{-+}^{CI}(E_j+E_k+P,W)\,\mathrm{d}E_j\mathrm{d}E_k \\ \approx& n_+(t)\frac{h^3}{8\pi m_e^2}\frac{g_-}{g_+}\sum_{j=0}^{M_j}\sum_{k=0}^{M_k}[f_E(E_j,t)\Delta E_j f_E(E_k,t)\Delta E_k] \\ &\times \frac{E_j+E_k+P}{E_jE_k}\,\sigma_{-+}^{CI}(E_j+E_k+P,W), \end{aligned} \tag{3.48}$$

with $M_j = \arg\max_j(E_j+P+E_0 \leq E_{N-1})$ and $M_k = \arg\max_k(E_j+P+E_k \leq E_{N-1})$. The recombination rate has been expressed as a function of the ionisation cross-section. The same differential cross-section should be used here as for the ionisation process, with $W = (E_j+E_k+P)-E_j = E_k+P$ being the energy transfer experienced by electron j by convention. It is equally valid to define W as the energy transfer of electron k. Between square brackets there is a density product of the electron population at energies (E_j, E_k) and for this reason, the recombination rate scales quadratically with the electron density.

3.5.4.2 Inelastic Collision Operator

Due to the differential cross-section and the increased number of particles involved, the collision operators for three-body processes are more elaborate than the operators presented thus far. For ionisation, there is one destruction operator that removes the incident electron from the distribution. Subsequently, two electrons are created at different energies as prescribed by the differential cross-section Eq. 3.45. The CI operator must reflect the creation of an additional electron per transition, at the

expense of the ionisation potential. Any residual energy must also be preserved in the creation of the ionised electrons.

The ionisation collision operator can be formulated as:

$$\begin{aligned}\left(\frac{\partial f_E(E,t)}{\partial t}\right)_{CI} = &- n_-(t)\sqrt{\frac{2}{m_e}} f_E(E,t)\sqrt{E}\sigma_{-+}^{CI}(E) \\ &+ 2n_-(t)\sqrt{\frac{2}{m_e}}\int_P^{E-P}\left(\int_P^{E-P}\frac{d\sigma}{dW}\,\mathrm{d}W\right)^{-1} \\ &\times\sqrt{E+W}\,\sigma_{-+}^{CI}(E+W)f_E(E+W,t)\left(\frac{d\sigma}{dW}\right)\mathrm{d}W.\end{aligned} \tag{3.49}$$

The collision operator for impact ionisation Eq. 3.49 contains a term that removes electrons that induce an ionisation event. In return, two electrons are created at energies $E_j - W$ and $W - P$ for each ionisation, where W is the energy transfer and E_j the impact energy. The operator lowers the total kinetic energy held by the free electrons while increasing the density. The differential cross-section distributes the outgoing electron energy across the electron pairs, giving additional weight to energy combinations that are more likely to occur. The differential cross-section is normalised by the inner integral.

Conversely, the operator for recombination contains an annihilation operator for two electrons that remove the incident electrons from the distribution. A creation operator must account for the outgoing electron. The recombination operator must add the ionisation potential to the free-electron population while lowering the density and can be written as:

$$\begin{aligned}\left(\frac{\partial f_E(E,t)}{\partial t}\right)_{3BR} = &- 2n_+(t)\frac{2}{m_e}\sqrt{E}f_E(E,t)\int_P^{E-P}\left(\int_P^{E-P}\frac{d\sigma}{dW}\left(\frac{d\sigma}{dW}\right)\mathrm{d}W\right)^{-1} \\ &\times\sqrt{W-P}f_E(W-P,t)\,\sigma_{+-}^{3BR}(E+W,W)\,\mathrm{d}W \\ = &\, n_+(t)\frac{2}{m_e}\int_P^{E-P}\left(\int_P^{E-P}\frac{d\sigma}{dW}\,\mathrm{d}W\right)^{-1}\sqrt{(E-W)(W-P)} \\ &\times f_E(E-W,t)f_E(W-P,t)\sigma_{+-}^{3BR}(E,W)\left(\frac{d\sigma}{dW}\right)\mathrm{d}W.\end{aligned} \tag{3.50}$$

The cross-section in Eq. 3.50 includes a normalised differential cross-section for both the creation and annihilation terms. At each recombination event, two electrons are removed at energies $E - W$ and $W - P$ and one electron is created at an energy $(E - W) + (W - P) + P = E$. The operator increases the mean kinetic energy in the free-electron distribution while lowering its density.

3.5.4.3 Benchmark

The bound-free collisional transitions will be benchmarked on a Mg^{7+} transition that is revisited in the experimental work discussed in Ch. 4. It works with core-hole ionised states that have a lower ionisation potential, enabling the test case to work across a broader range of temperatures. The transition of interest is $K^1L^4 \leftrightharpoons K^1L^3 + e^-$, two super-configurational states that differ by one electron in their L-shell occupation. The remainder of the benchmark parameters are summarised in Table 3.4. Relevant for this benchmark is the ionisation potential $E_{-+} = 277\,\text{eV}$, a

CI and 3BR CCFLY benchmark	
Parameter	Value
Material	Magnesium 7^+
Lower ion state	$K^1L^4M^0$
Upper ion state	$K^1L^3M^1$
E_{-+}	277 eV
n_-	1 cm^{-3}
n_+	1 cm^{-3}
n_e	$10^{23} - 10^{24}$ cm^{-3}
T_e	10-500 eV
Cross-section	Lotz
$\frac{d\sigma}{dW}$	Uniform, Rutherford
# energy grid points	250
Minimum energy	0.01 eV
Maximum energy	10.0 keV

Table 3.4: The simulation settings used to evaluate the inelastic Fokker-Planck collision operator for bound-free collisional transitions. Two modes of the CCFLY code will operate on these settings; one with a thermal distribution in the standard Maxwell-Boltzmann mode, the second with a discretised Maxwellian in the non-thermal mode. The consistency of the ion rates, electron density- and energy changes will be investigated.

value that will be strongly attenuated by continuum lowering in the density range of interest. The continuum lowering model used here is the modified Ecker-Kröll model given by Eq. 3.14. The consequences of this model choice stretch beyond the numerical value of the IPD. In this model, the M-shell of magnesium is pressure-ionised and the super-configuration states can be described solely by the K- and L-shell occupation numbers. There are no consequences of the IPD model choice for the benchmark with respect to bound-free transition rates. What is most relevant for this case, is that the ionisation potential is varied as an additional degree of freedom and that

is the primary motivation to include IPD in the benchmarking. It would be equally useful to repeat the analysis for a different bound-free transition.

Varying the density tests the reliability of the 3BR operator, as the recombination rate scales quadratically with the density as per Eq. 3.46. The number of grid points is kept constant at 250, a number that originates from the DR benchmark. The cross-section models for bound-free collisional transitions are non-resonant and generally smoother functions than the delta-function like cross-sections previously examined. It is expected that 250 grid points are sufficient over this density and temperature range. The model choice, Lotz in this case, is also arbitrary and it is only important that the cross-section is a continuous function for energy values above the ionisation threshold. It can be readily exchanged for any other parametric model, as will be done in Ch. 4.

Ion Transition Rates

The first comparison to be made is between the ion transition rates of the ionisation and recombination process. As before, these will be computed for the benchmark parameters with a thermal distribution as well as a discretised Maxwellian in the non-thermal numerical scheme. For the specific case of using a Lotz cross-section (Eq. 3.41) and a thermal distribution, the impact ionisation rate Eq. 3.42 can be simplified to:

$$\begin{aligned} S^{CI}(t)/V =& C_{Lotz} n_- n_e \sqrt{\frac{8}{\pi m_e}} \left(k_B T\right)^{-3/2} \xi \int_P^\infty \frac{\ln\left(E/P\right)}{P} \exp\left(-E/k_B T\right) \mathrm{d}E \\ =& n_- n_e \sqrt{\frac{8}{\pi m_e}} \left(k_B T\right)^{-1/2} C_{Lotz}\, \xi \frac{1}{P} E_1\left(P/k_B T\right), \end{aligned} \tag{3.51}$$

where E_1 denotes the exponential integral of the first kind, $\xi = 4$ for the upper ion state chosen in Table 3.4, and $C_{Lotz} \approx 4.5 \times 10^{-14}\,\mathrm{cm}^{-2}\mathrm{eV}^2$ for this material and charge state [77]. For all temperatures and densities, the results from Eq. 3.51 should be similar to the rate computed with a discrete Maxwellian and Eq. 3.42.

For the same transition, the recombination rate will be computed for the discrete Maxwellian distribution with Eq. 3.46. With a thermal distribution, the recombination rate is directly linked to the ionisation rate due to the detailed balance principle and does not require any integration procedures to be evaluated. The rate becomes:

$$\begin{aligned} S^{3BR}_{+-}(t)/V|_{MB} =& \frac{g_-}{2g_+} \lambda_e^3 n_e \int_0^\infty f_{MB}(E,t) v(E) \sigma^{CI}_{-+}(E)\, \mathrm{d}E \\ =& \frac{g_-}{2g_+} \lambda_e^3 n_e^2 \left(k_B T\right)^{-3/2} \exp\left(-P/k_B T\right) S^{CI}_{-+}(t)/V, \end{aligned} \tag{3.52}$$

where λ_E is the thermal De-Broglie wavelength. Contrary to most other collisional rates, the 3BR rate scales quadratically with the electron density. In solid-density plasmas, this makes it amongst the highest transition rates. The time dependence remains, as the temperature can still change over time despite the parametric form of the distribution being a Maxwellian.

Fig. 3.21 shows the ionisation and recombination rates for a variable temperature, at a constant electron density of $3.0 \times 10^{23}\,\mathrm{cm}^{-3}$. Due to the constant electron density, the IPD is constant and leads to an ionisation threshold $P = 146.7\,\mathrm{eV}$ as is marked in the dashed vertical line. The transition rates are computed for a target ion density of $1\ \mathrm{cm}^{-3}$, meaning the rates can be interpreted as a per-ion rate. The remainder of the ions are put in the K^2L^3 (7^+) state to maintain a solid ion density and obtain the correct continuum lowering. All results presented here scale linearly with the target ion density.

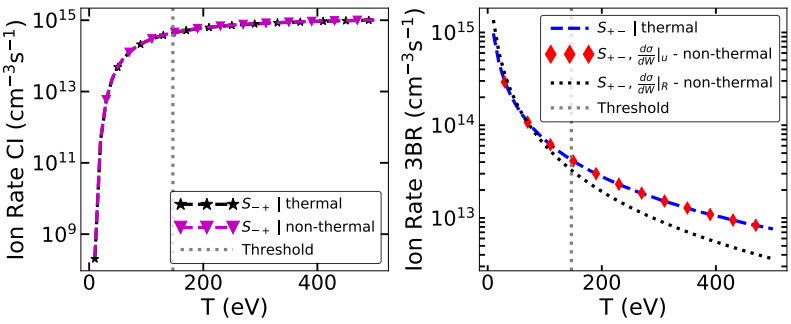

Figure 3.21: L-shell Collisional Ionisation (CI, S_{-+}) and Three-Body Recombination (3BR, S_{+-}) rates in Mg^{7+} computed in the thermal and non-thermal electron modes, for a uniform and Rutherford differential cross-section. The density $n_e = 3.0 \times 10^{23}\,\mathrm{cm}^{-3}$ is constant, as is the ionisation threshold at $P = 146.7\,\mathrm{eV}$.

Fig. 3.21 compares the ion rates computed with the thermal (Eq. 3.51) and non-thermal scheme (Eq. 3.42) for a Maxwellian distribution. Additionally, the differential cross-section that determines the pairing of the outgoing (ionisation) and incoming (recombination) electrons is varied between the uniform Eq. 3.43 and Rutherford functional form Eq. 3.44. Both differential cross-sections are normalised according to Eq. 3.45.

The ionisation rate flattens off to a frequency on the femtosecond time scale as soon as the temperature exceeds the ionisation threshold. Below the threshold, it is possible to observe ionisation due to the long tail of the Maxwellian that contains sufficiently energetic electrons. The rate observed for the thermal and non-thermal scheme differs no more than 1% over the full temperature range. These minor differences arise due

to the truncation error introduced by the finite sum of Eq. 3.42 as compared to an integral that runs to infinity, and the energy grid spacing. Between the differential cross-section models, there is no difference in the ionisation rate. The differential cross-section only influences the distribution of outgoing electron energies, and not the rate at which they are produced. The incoming electrons and their cross-section are in no way influenced for the ionisation process.

The recombination rate has the opposite trend and decreases with increasing temperature. As three-body recombination removes electrons from the free population while adding thermal energy, it is a heating effect that becomes increasingly unlikely as the system heats up. However, being a collisional process whose cross-section is linked to that of ionisation, it maintains a non-negligible rate even at temperatures above the ionisation threshold.

The recombination rate does depend on the differential cross-section, as it acts as a pairing mechanism to determine which pairs of electrons mitigate the energy transfer process. Results obtained from detailed balance with a thermal distribution (Eq. 3.52) match to the rates computed with the full non-thermal rate integral Eq. 3.46 only if a uniform differential cross-section is used. In thermal equilibrium, this implies that there is no energy-dependence on how electrons pair up to induce a recombination event. Applying the Rutherford differential cross-section Eq. 3.44 reduces the recombination rate at temperatures $T > 70\,\mathrm{eV}$ and increases the rates at temperatures below 70 eV, as compared to the thermal results. The Rutherford model loosely states that it is more likely to pair up an energetic electron with a near-static electron. This mechanism enhances the rate when there is a significant cold electron population, or possibly an energetic tail or spike in the distribution. For a bulk of electrons at a comparable energy to the threshold, the relative energy transfer after recombination is generally large, causing the ion transition rate to decrease.

In order for the atomic-kinetic models to obey equilibrium relations (detailed balance), it is a requirement that the differential cross-section used for the ionisation process are the same as for the recombination process. As the ionisation rate is computed from a single integral, the same ionisation rate can be recovered for any differential cross-section. This appears to be a contradiction with detailed balance, as the recombination rate can be seen to differ between the Rutherford and uniform energy pairing. The electron distribution could remain Maxwellian as long as the collision operators for ionisation and recombination sum to zero, but the ion populations would not remain in balance. Based on these observations, the conditions that a system in LTE obeys should be extended to having a uniform differential cross-section

for three-body interactions. This does not rule out having a strongly coupled system, as it still allows for uniform coupling.

The collision operators Eqs. 3.49 and 3.50 are plotted in Fig. 3.22 for three temperatures at a constant density. For visibility reasons, the energy grid is linear in the range of $0.01 - 1000$ eV with 1000 grid points. The operators are evaluated for the uniform and Rutherford differential cross-section, and they differ most in the lower energy range $T \lesssim 10$ eV. The effect of the Rutherford cross-section is an enhancement of the collision operator at low energies, as it makes it more likely for electrons to be scattered off (ionisation) or drawn from (recombination) at low energies. Over the remainder of the energy range, there is no significant change to the collison operator.

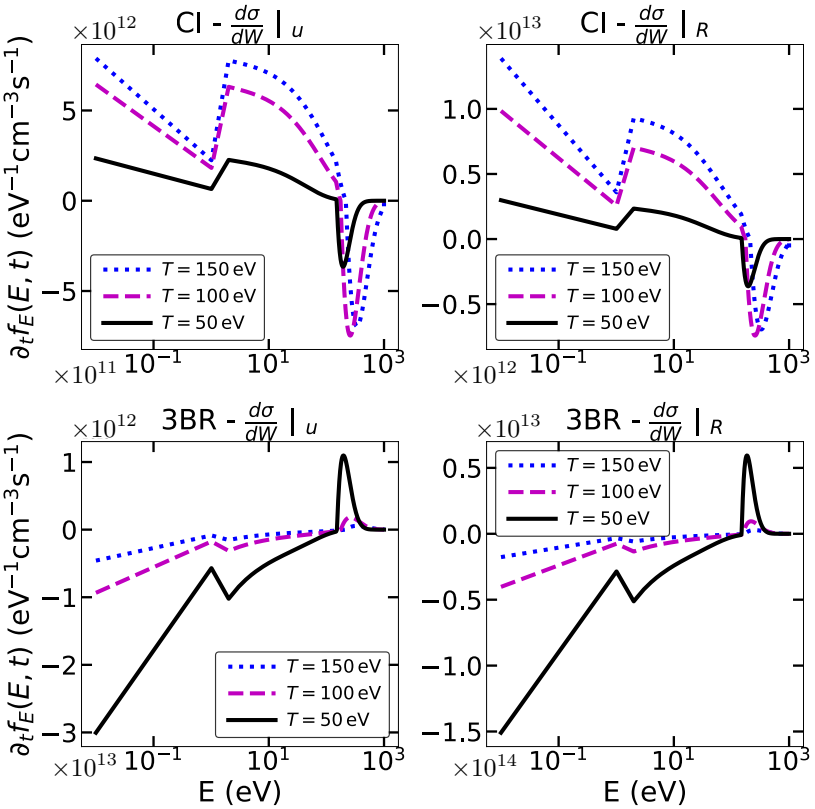

Figure 3.22: The collisional- ionisation (top) and recombination (bottom) collision operators for various temperatures of the core-hole ionised Mg^{7+} state. The density is held constant at $n_e = 3.0 \times 10^{23}\,\mathrm{cm}^{-3}$, for a uniform and Rutherford differential cross-section.

In addition to displacing electrons by the ionisation threshold, the ionisation and recombination operators also affect the number of free electrons. The trends displayed by the collision operators is similar to those of the ion transition rates. At higher temperatures, ionisation is a more likely process than recombination, and vice versa.

Most collisional transition rates scale linearly with the electron density in a similar way as to the ion density. CI and 3BR behave differently due to continuum lowering. Whereas excitation and de-excitation events are inner-shell transitions, the bound-free interactions discussed here involve the outermost electron shell that is strongly affected by the IPD. As a result, increasing the electron density will not only linearly increase the rates but also strongly decrease the ionisation threshold, causing further non-linear enhancement to the rate.

The effects on the ionisation rate of varying the electron density are visualised in Fig. 3.23. In the figures containing density scans, Fig. 3.23 and 3.24, the density is varied independently from the ion density that remains constant at $n_i = 4.31 \times 10^{22}\,\mathrm{cm}^{-3}$. The threshold potential is computed by subtracting the IPD as computed with the mEK model of Eq. 3.14 from the atomic potential, and plotted alongside the rate in the dashed yellow curve.

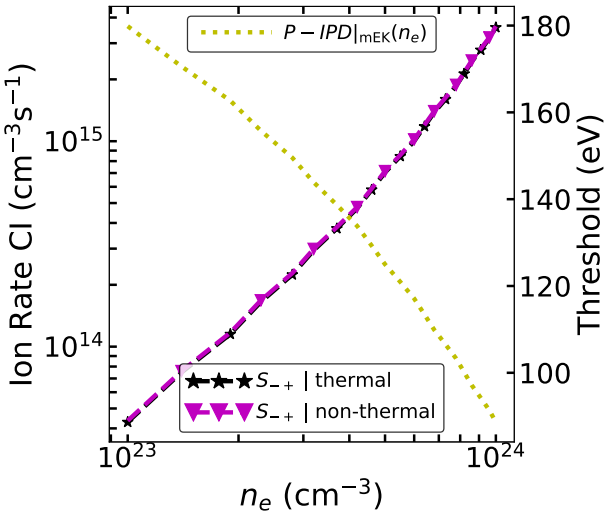

Figure 3.23: L-shell collisional Ionisation (CI, S_{-+}) rate of core-vacancy Mg^{7+} as a function of the electron density in the thermal and non-thermal electron modes. The temperature is held constant at 100 eV. The rate grows non-linearly, enhanced by continuum lowering.

Continuum lowering enhances the scaling of the ionisation rate by an order of magnitude over this density range. Varying the density thus effectively corresponds to varying the ionisation threshold, which increases the thoroughness of this benchmark. The thermal and non-thermal electron modes remain in good agreement for all density values. There is no difference between the differential cross-section models, hence they are omitted in this comparison.

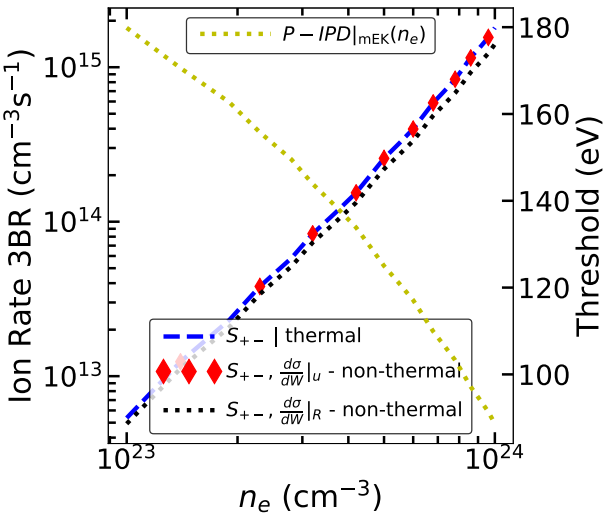

Figure 3.24: L-shell collisional recombination (3BR, S_{+-}) rate of core-vacancy Mg^{7+} as a function of the electron density in the thermal and non-thermal electron modes. The temperature is held constant at 100 eV. The rate grows non-linearly, enhanced by continuum lowering.

Eq. 3.46 and 3.52 reveal that the 3BR rate scales quadratically with the electron density. Over a density range of $10^{23} - 10^{24}\,\mathrm{cm}^{-3}$, there should be an increase in the transition rate of at least two orders of magnitude. This is expected to be further increased due to continuum lowering, as Eq 3.52. Continuum lowering weakens the exponential decay of the recombination rate, while enhancing the ionisation rate. The two effects combined cause the recombination rate to grow faster than the quadratic scaling for increasing density. Results obtained for the density scan of the recombination rate are plotted in Fig. 3.24.

The Rutherford differential cross-section lowers the ion transition rate by 10- 12% over the full density range. The trends are similar, with the recombination rate increasing by nearly three orders of magnitude for one order of magnitude density variation. Due to this behaviour, CI and 3BR processes are of great interest to warm dense matter studies, as they become amongst the highest transition rates in the system.

Density Conservation

The high bound-free collisional interaction rates have a profound effect on the free-electron population as they involve the simultaneous exchange of particles and energy between free-electron population and ion states. Each ionisation event releases one electron and a self-consistent energy balance can only be maintained if the collision

operator reflects this constraint. This self-consistency between density changes and the ion rates is even more important than the agreement between results obtained from the thermal and non-thermal electron mode. As shown earlier, it is possible that the 3BR rates differ depending on the differential cross-section. When there is no reason to assume a particular cross-section profile, the numerical scheme should be constructed such that it maintains overall density conservation for all cross-section models; the code should conserve the sum of ion and electron charge.

The time-derivatives of the electron density as a result of bound-free transitions can be computed with Eq. 3.22. They are the energy-integrated collision operators for ionisation and recombination and should obey:

$$\frac{dn_e}{dt} = \pm S_{\mp\pm}(t)/V, \tag{3.53}$$

meaning the free-electron density increases for ionisation $(-+)$ and decreases for recombination $(+-)$ with the same rate magnitude as the ion transition. Fig. 3.25 shows how the collision operator behaves over a range of temperatures and density, with one parameter being fixed. The density and temperatures are varied independently from each other while maintaining a Maxwellian profile. There is no LTE between the ion populations or electron shell occupation numbers as the system is not left to equilibrate before computing the transition rates. The transition rates for the ions and electron distribution function are computed from the static initialisation.

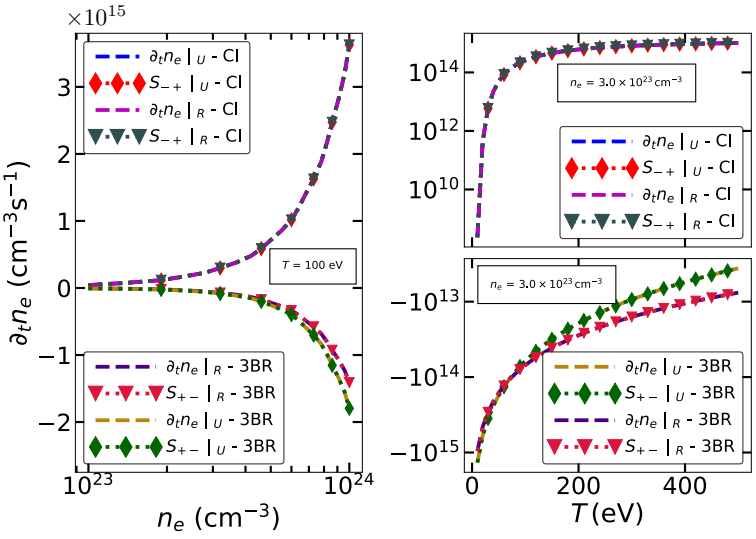

Figure 3.25: Density time-derivatives of the bound-free collisional operators in Mg^{7+} for various temperatures and densities in the non-thermal electron mode. The reference for all density rates is the ion rate and charge balance Eq. 3.53, whereas the non-thermal rates are obtained from their respective collision operator.

For all temperatures and densities, the impact ionisation rate is equal to the density time-derivative, the condition stated in Eq. 3.53. There match is exact due to the conservative nature of the aggregation methods used to interpolate time-derivatives onto the discrete energy grid, as described by Eq. 3.12. This is the non-thermal equivalent of a density calculation based on quasi-neutrality that has been implemented in the SCFLY collisional-radiative code [40]. For recombination, a similar relation holds and the ion transition rate is equal to the density rate in magnitude, but opposite in sign. The differences between the differential cross-sections arise solely due to differences in the ion rate.

Energy Conservation

Bound-free collisional transitions are a powerful mechanism to re-arrange the balance of kinetic energy held by the free electrons and electrostatic potential retained in the bound electrons. The exchange of each electron from the free to the bound population or vice versa is accompanied by an energy transfer of the ionisation potential. In order to conserve energy, the sum of electrostatic energy and thermal energy must be constant for a closed system. This translates to the requirement on the energy contained in the collision operators:

$$\frac{\partial E(t)}{\partial t} = \mp P \cdot S_{\mp\pm}(t)/V, \tag{3.54}$$

which states that ionisation subtracts an amount P from the free-electron energy and recombination adds it. The energy rates scale linearly with the ion transition rate and the energy is computed through the second moment of the collision operator as is done in Eq. 3.31. As long as Eq. 3.53 holds, the collision operators can be used in a self-consistent energy calculation. Fig. 3.26 shows the energy time-derivatives for a range of temperatures and density as a result of bound-free transitions occurring. When the density is varied, it reduces the ionisation potential through continuum lowering. This creates an extra degree of freedom that benefits the benchmark, as it omits the need to repeat the process for different atomic transitions with other ionisation thresholds.

Fig. 3.26 shows that energy conservation is indeed maintained, as the collision operators follow the product of the ion rate and ionisation potential exactly. There is no numerical difference at all as the method of aggregating the time-derivatives Eq. 3.12 is completely conservative. In an atomic-kinetics code, it could still not be ruled out that minute numerical differences arise when these time-derivatives are propagated forward in time through an ODE solver. This should be dealt with as it

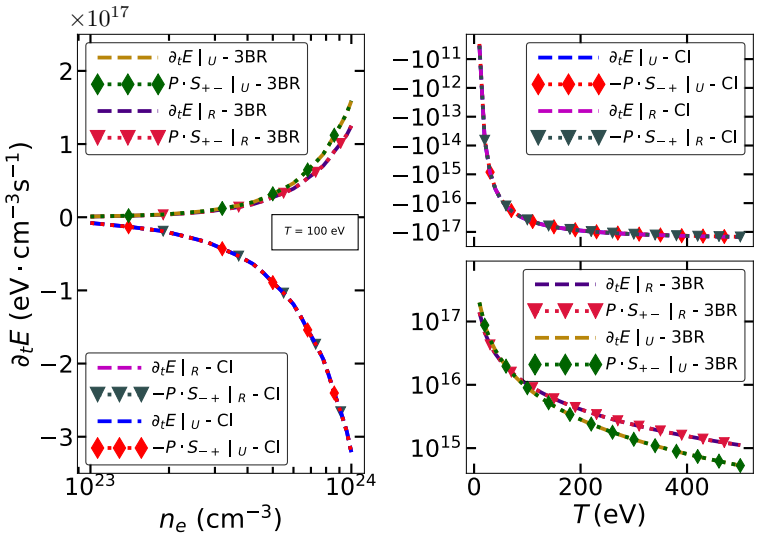

Figure 3.26: Free-electron total energy time-derivatives of the bound-free collisional operators in Mg^{7+} for various temperatures and densities in the non-thermal electron mode. The reference for all density rates is the ion rate and energy balance Eq. 3.54, whereas the non-thermal energy rates are obtained from their respective collision operator.

occurs and the numerical scheme can only be made to be conservative when evaluating the collision operators.

3.5.5 Photo-Ionisation and Radiative Recombination

Bound-free radiative transition processes are an essential component in the description of a non-equilibrium warm dense system. In the experimental creation of warm dense matter, inner-shell Photo-Ionisation (PI) acts as the primary absorption mechanism to couple energy from an X-ray field into the target. In addition, also middle and outer electron shells can also be photo-ionised albeit with a lower probability.

As its inverse process, Radiative Recombination (RR) involves the recombination of a free electron into a bound ionic state upon the emission of a photon. Being a reaction without an energy threshold, this process can occur spontaneously with a free electron of any energy. Due to the symmetry of the PI transition under time-reversal, a recombination process can also be induced by the X-ray field. The bound-free processes discussed here are depicted in Fig. 3.27. RR is significant but not due to its high transition rates; bound-free collisional transitions are more likely in solid-density systems. The diagnostic capabilities offered by the emitted photon are what generates the key interest in RR. The emitted photon's energy is the sum of the incident electron's kinetic energy and the ionisation threshold, and can reach

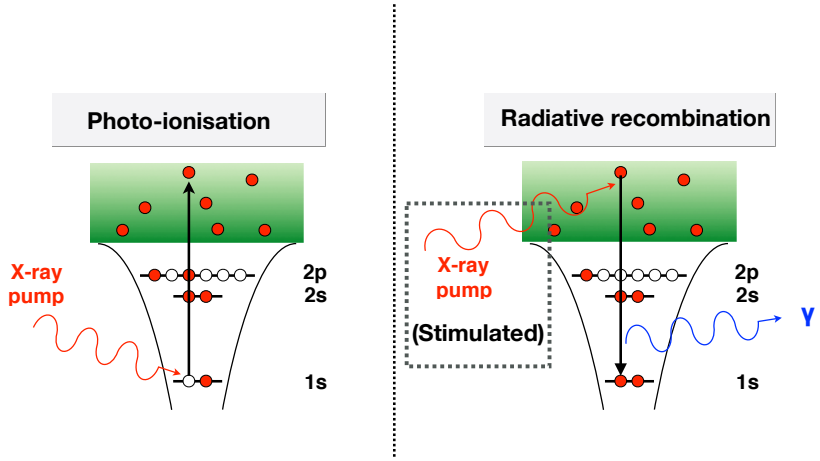

Figure 3.27: Photo-ionisation (left) and radiative recombination (right). Radiative recombination can happen spontaneously, or be induced by an incoming photon. The residual energy is emitted by another photon.

far higher energies than what would be observed in any bound-bound transition. This allows RR to be used as a diagnostic tool to detect the presence of high-energy electrons through spectroscopy.

3.5.5.1 Cross-section Model

Bound-free radiative rates can be induced by either a photon (ionisation or stimulated recombination), or an electron for spontaneous recombination. In essence, both the photon- and electron-induced reaction rates can be computed through the cross-section formalism in which a photon or electron can be used as the single incident particle.

In a zero-dimensional code, the radiation field $J_\nu(\nu, t)$ can be characterised as a frequency- and time-dependent intensity. In this thesis, the radiation field is approximated as a Gaussian function in both photon frequency ν and time as:

$$J_\nu(\nu, t) = I_0 \cdot \exp\left((\mu_t - t)^2/2\sigma_t^2\right) \cdot \exp\left((\mu_\nu - \nu)^2/2\sigma_\nu^2\right), \tag{3.55}$$

where the mean and spread of both quantities are denoted by μ and σ. The intensity maximum I_0 occurs at the central frequency and time. Given an incident X-ray field, the PI rate can be computed as:

$$S^{PI}(t)/V = 4\pi n_-(t) \int \frac{J_\nu(\nu, t)}{h\nu} \sigma_{-+}(\nu)\, \mathrm{d}(\nu), \tag{3.56}$$

where h is Planck's constant and $\sigma_{-+}(h\nu)$ is the energy-dependent ionisation cross-section. The fraction $\frac{J_\nu(h\nu,t)}{h\nu}$ represents the photon number density per unit area

and the factor 4π arises from integration over all solid angles. Each ionisation event produces one electron with an energy $E = h\nu - P$. The cross-section model used in this thesis is a series expansion by Veigele *et al.* [78] where available, and the Kramers cross-section [79] when not. The form proposed by Veigele is similar to those of Gaunt factors [64] with a set of experimentally obtained expansion coefficients $\{c_0, \ldots, c_M\}$:

$$\ln \sigma^{PI}(\nu) = \sum_{i=0}^{M} c_i \left(\ln \nu\right)^i, \quad h\nu > P. \tag{3.57}$$

Spontaneous RR occurs due to a vacancy in an electron shell and its rate can be computed as a collision integral:

$$S_{sp}^{RR}(t)/V = n_+(t)\sqrt{\frac{2}{m_e}}\int_0^\infty \sqrt{E}\,\sigma_{+-}^{RR}(E) f_E(E,t)\,\mathrm{d}E. \tag{3.58}$$

Eq. 3.58 describes a collisionally-induced recombination of the excited or ionised population n_+ that has no reaction threshold. In each recombination event, the incident electron is annihilated from the free-electron population upon the emission of a photon that carries away the residual energy. The recombination photon energy ensures energy conservation as the photon energy $h\nu = P + E$, where P is the ionisation threshold that separates the initial and final ion state, and E is the electron energy. More energetic electrons therefore generate more energetic photons and through this mechanism, the distribution function can be experimentally measured in the energy range that lies above the bound-bound recombination lines.

The recombination cross-section can be obtained by examining the transition rates in a static LTE system with a thermal electron distribution, Planckian radiation field and through use of the Boltzmann and Saha equations [5]. The result is a relation between the recombination- and ionisation cross-sections that was first derived by Milne:

$$\sigma_{+-}^{RR,sp}(E) = \sigma_{-+}^{PI}(\nu)\frac{g_-}{2g_+}\frac{(h\nu)^2}{m_e c^2 E}, \tag{3.59}$$

where E is the incident electron energy and the ion state multiplicities are $g_\pm$. Energy conservation is implicitly contained in Eq. 3.59 as the photon energy and electron energy must are directly related: $h\nu = E + P$. Finally, there is a contribution of the stimulated RR rate. The cross-sections for stimulated and spontaneous recombination can be related through microscopic reversibility relations, and the stimulated recombination cross-section can be written as [80]:

$$\sigma_{+-}^{RR,st}(E,\nu,t) = \frac{c^2}{2h\nu^3} J_\nu(\nu,t)\sigma_{+-}^{RR,sp}(E) \tag{3.60}$$

where there is a time-dependence through the radiation field. Eq. 3.60 can be considered to be a differential cross-section as it has a dependence on the electron distribution function and on the radiation field. Computing the total recombination rate that includes a radiation-induced contribution requires a double integral of the form:

$$S_{tot}^{RR}(t)/V = n_+(t)\sqrt{\frac{2}{m_e}}\int_0^\infty\int_0^\infty \sqrt{E}\,\sigma^{RR,tot}(E,\nu,t)f_E(E,t)\,\mathrm{d}\nu\,\mathrm{d}E. \tag{3.61}$$

There is no energy threshold to induce a recombination event as it is a reaction that releases electrostatic energy. When both stimulated and spontaneous recombination are to be calculated together, the total RR cross-section can be composed as:

$$\sigma_{+-}^{RR,tot}(E,\nu,t) = \left(1+\frac{c^2}{2h\nu^3}J_\nu(\nu,t)\right)\sigma_{+-}^{RR,sp}(E), \tag{3.62}$$

where the time-dependence only arises due to the radiation field.

3.5.5.2 Inelastic Collision Operator

When using XFELs, the spread in frequency of the incident X-ray field can be very narrow ($< 1\%$). Due to this small bandwidth, the X-ray field can be treated as near-monochromatic as far as the recombination electrons are concerned. The electrons will be created at energies where the energy bin size on a discrete grid is comparable to the frequency bandwidth of the radiation field. The photo-pump acts like a source term in a similar way to way Auger electrons are added to the free population. The PI rate does not depend on the distribution function itself. Its contribution to the Fokker-Planck equation for the electron balance can be written as:

$$S_{PI}(t) = S^{PI}(t)/V \cdot \delta(E-(h\nu-P)), \tag{3.63}$$

which states that one electron is produced per ionisation at an energy that remains after subtracting the ionisation potential from the photon energy. The effective rate including stimulated recombination is used, as the ionisation and stimulated recombination rate are both computed through an integral over the photon energy. Eq. 3.63 is a non-negative operator, even in a system where there are more excited-state ions than ground state populations.

Contrary to the ionisation process, both the stimulated and spontaneous recombination Fokker-Planck operators do depend on the electron distribution function. Accumulating their cross-sections into a total cross-section of the form in Eq. 3.62, the inelastic collision operator can be written as:

$$\left(\frac{\partial f_E(E,t)}{\partial t}\right)_{RR} = -n_+(t)\sqrt{2/m_e}f_E(E,t)\sqrt{E}\int_0^\infty \sigma_{+-}^{RR,tot}(E,\nu,t)\,\mathrm{d}\nu. \tag{3.64}$$

Eq. 3.64 is strinctly non-positive over the full energy range. In the absence of a radiation field, the operator only contains contributions from the spontaneous recombination component.

3.5.5.3 Benchmark

Due to the combination of having a spontaneous and induced recombination reaction channel, the benchmark must be split into a case with and one without an external radiation field. The primary focus will be recombination, as ionisation has a straightforward source term described by Eq. 3.63 that conserves density and energy exactly for all possible plasma conditions. Extending the electron model to include non-thermal behaviour does not affect the PI rate calculations in any way.

For recombination, the benchmark will be based on a transition that occurs in solid-density Mg^{9+}. This state is produced at the later stages of an XFEL-plasma interaction when a high energy density has been achieved. The system is kept at quasi-neutrality and therefore has an electron density $n_e = \langle z \rangle n_i = 3.88 \times 10^{23}\,\mathrm{cm}^{-3}$ and the ion target density of the excited state population is set to unity. The remainder of the ions reside in the 9^+ ground state. In line with previous benchmarks, the ion rates will be compared between the thermal and non-thermal electron models, followed by the energy- and density conservation laws. A full overview of the benchmark parameters is listed in Table 3.5. The temperature range is far higher than the normal operational mode of CCFLY. This is to verify the transition rates in the temperature region above the reaction threshold, and purely used to investigate the validity of the numerical schemes implemented here. One of the benchmarks requires a radiation field to validate the stimulated recombination model. The peak intensity is the most relevant parameter of the X-ray field and the rates, density- and energy time-derivatives are computed at peak intensity and there is no temporal variation. Additionally, the photon energy is set to 1950 eV with a 0.1% frequency bandwidth μ_ν. There is some significance to the narrow bandwidth, as it can allow for simplifications in the rate calculations of the stimulated recombination rate. Compared to the photon energy, ionisation threshold and the mean kinetic energy of free electrons, the spread in photon energy is small enough to consider the radiation field monochromatic.

Radiationless Benchmark

The first benchmark is a radiation-less setup where only spontaneous recombination can occur. An ion system is placed in its Mg^{9+} ground state with one 10^+ target ion in the core-hole ionised state. In a non-thermal electron treatment, the transition

RR CCFLY benchmark	
Parameter	Value
Material	Magnesium 9^+
Lower ion state	$K^2L^1M^0$
Upper ion state	$K^1L^1M^0$
E_{-+}	1715 eV
n_i	4.31×10^{22} cm^{-3}
n_e	3.88×10^{23} cm^{-3}
T_e	10-2500 eV
I_0	0-10^{18} W/cm^2
Cross-section	Veigele
# energy grid points	250
Minimum energy	0.01 eV
Maximum energy	10.0 keV

Table 3.5: The simulation settings used to evaluate the inelastic Fokker-Planck collision operator for bound-free radiative transitions. Two modes of the CCFLY code will operate on these settings; one with a thermal distribution in the standard Maxwell-Boltzmann mode, the second with a discretised Maxwellian in the non-thermal mode. The consistency of the ion rates, electron density- and energy changes will be investigated. The ionisation potential between the upper and lower states is E_{-+} and I_0 denotes the incident X-ray intensity.

rate is computed through a discretised form of Eq. 3.58. When adding a radiation field at a later stage, the contribution from Eq. 3.60 can be added.

In case the distribution is an analytical Maxwellian, the rate equation takes on a simpler form:

$$\begin{aligned} S_{tot}^{RR}(t)/V = & n_+(t)\frac{g_-}{2g_+}\lambda_e^3 n_e \exp(-P/k_BT)4\pi \\ & \times \int_0^\infty \sigma_{-+}^{PI}(\nu)\left(J_\nu(\nu,t)+\frac{2h\nu^3}{c^2}\right)\frac{1}{h\nu}\exp\left(-h\nu/k_BT\right)\,\mathrm{d}\nu, \end{aligned} \tag{3.65}$$

where λ_e^3 is the thermal De Broglie length, P the ionisation potential between the initial and final ion state, and $g_\pm$ the state multiplicities. The total recombination rate is only an integral over the photon energies. Contributions from the stimulated and spontaneous components of the RR rates can be split by setting the radiation field to zero in Eq. 3.65.

Comparing the spontaneous RR rates computed with Eqs. 3.65 (analytical Maxwellian) and 3.58 (discretised Maxwellian) for a range of temperatures and $J_\nu = 0$ yields the data presented in Fig. 3.28. Only one target ion is core-hole ionised and able to undergo recombination, with the rest of the 10^+ ions remaining in the ground state.

The ion rates are volumetric, but can be interpreted as per-ion rate due to the target density of unity. Despite the instability of this ion and its high ionisation potential,

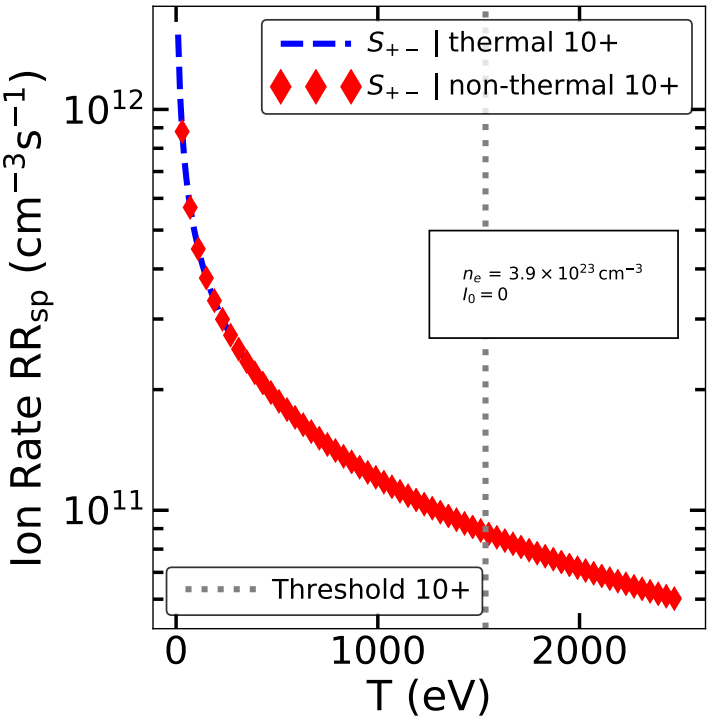

Figure 3.28: The radiative recombination rates for a core-hole ionised Mg^{10+} ion as a function of temperature. The density is held constant at $n_e = 3.88 \times 10^{23}\,\mathrm{cm}^{-3}$ and there is no radiation field present.

the recombination rate is 2-3 orders of magnitude smaller than the collisional bound-free transition rates. Even at temperatures above the ionisation threshold, there is no noticeable difference between the spontaneous recombination rates. As the temperature increases, the likelihood of recombination decreases. The temperature reaches so high that if the benchmark was not constrained, the excited ion state could become collisionally populated. However, this degree of freedom is not present in the benchmark.

The collision operators corresponding to this case are plotted in Fig. 3.29. For all temperatures, the operators are strictly non-positive and can only draw electrons from the free population. At lower temperatures, static electrons are the most likely ones to recombine and this is due to the ionisation cross-section peaking around its threshold energy. When the system gets hotter, the operator becomes more uniform across the energy range and the higher-energy electrons gain an increased likelihood of recombining as compared to their lower-energy counterparts.

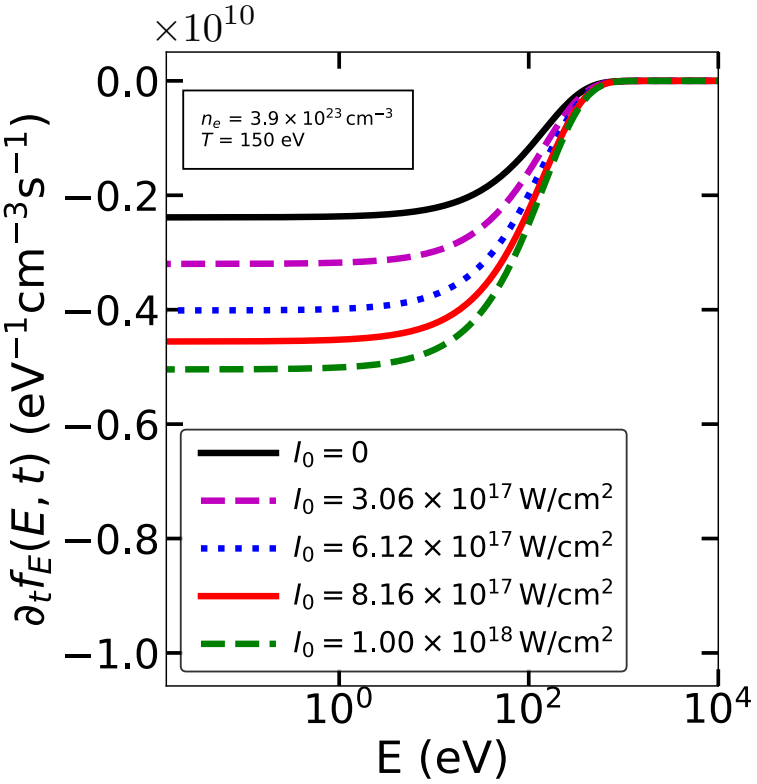

Figure 3.29: Spontaneous recombination collision operators for a core-hole ionised Mg^{10+} ion as a function of temperature. The operators are strictly non-positive for all temperatures.

Density conservation holds for the free-electron population during the recombination process. Each recombination absorbs one free electron and therefore the magnitude of the negative time-derivative of the electron number density must equal the ion transition rate:

$$\frac{dn_e}{dt} = -S_{RR}(t)/V, \tag{3.66}$$

where $S_{RR}(t)/V$ is the sum of the spontaneous and induced volumetric rates. In the non-thermal mode, this number density is computed from the zeroth moment of the distribution function's time-derivatives that are computed with the collision operator Eq. 3.64.

Energy conservation is not as straightforward to verify for bound-free radiative processes as they are for collisional interactions and cannot be formulated by observing only the ions and electrons in the system alone. The discussion on benchmarking the energy conservation laws is not relevant to computing the Fokker-Planck operator, as this is already known through Eq. 3.64. In addition to being able to validate the energy balance, the subsequent discussion also provides insight into the spectral

emission that is a signature of this type of recombination.

Each electron is drawn at a different energy in the distribution, does not couple any energy back into the free population and triggers the emission of a photon. The energy balance can only be formulated by including the emitted radiation.

Using the reference of a thermal electron system, the change in free-electron energy can be derived from observing the radiative losses emitted through the recombination photons and the change in electrostatic potential of the ion system. The energy carried away by the photons can be computed as:

$$\begin{aligned}\frac{dE}{dt}|_\gamma =& n_+(t)\frac{g_-}{2g_+}\lambda_e^3 n_e \exp(-P/k_BT)4\pi \\ &\times \int_0^\infty \sigma_{-+}^{PI}(\nu)(E+P)\left(J_\nu(\nu,t)+\frac{2h\nu^3}{c^2}\right)\frac{1}{h\nu}\exp\left(-h\nu/k_BT\right)\,\mathrm{d}\nu,\end{aligned} \tag{3.67}$$

where the integrands of the ion transition rate and energy time-derivative only differ by a factor $E+P$. This reflects the energy balance for each group of electron energies in the system, which is then accumulated through the integral.

Although the electrons lose all their energy to the radiation field, the majority of the energy in the radiation field typically comes from the change in electrostatic energy held by the ion populations in the system [5]. Defining the binding energy to be negative by convention, the electrostatic potential increases with each recombination event. The energy balance considering ions, electrons and photons reads:

$$\begin{aligned}\frac{dE}{dt}|_e =& \frac{dE}{dt}|_i - \frac{dE}{dt}|_\gamma \\ =& S_{+-}^{RR}(t)/V \cdot P - \frac{dE}{dt}|_\gamma,\end{aligned} \tag{3.68}$$

where the subscripts e, i and γ denote the electron, ion and photon populations, respectively. Eq. 3.68 has been simplified by observing that the change in electrostatic energy is P for each ion, regardless of the incident electron energy. The energy- and density balance of the radiation-less benchmark are plotted in Fig. 3.30. The energy balance in Fig. 3.30 is computed from the change in electrostatic potential in the ions, and the energy radiated away that is given by Eq. 3.67. The analytic thermal and generalised non-thermal electron models are consistent for both energy- and density conservation. Both time-derivatives saturate at a temperature where the ion transition rate becomes small. The energy derivative still retains a high absolute value because although it is unlikely for a very energetic electron to radiatively recombine, if it does happen it will give off all its energy.

[5] This is only true when the free-electron mean kinetic energy is below the ionisation threshold. In this benchmark, that is true when $T_e \leq 1.5\,\mathrm{keV}$.

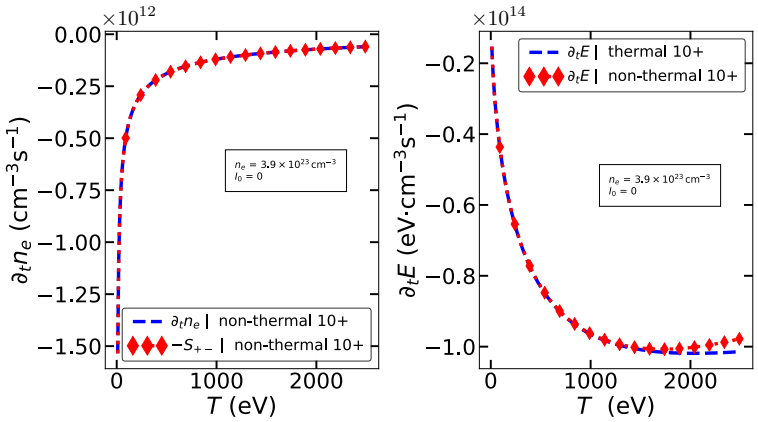

Figure 3.30: Density- and energy conservation during the spontaneous recombination process as a function of temperature. The density change in the free electrons is the negative ion transition rate. The energy change is computed from Eq. 3.68.

When using the generalised cross-section integral for an arbitrary distribution function, the energy contained in the outgoing radiation field can be computed as:

$$\frac{dE}{dt}|_{\gamma} = -n_{+}(t)\sqrt{\frac{2}{m_e}}\int_0^{\infty}\int_0^{\infty}\sqrt{E}\,\sigma^{RR,tot}(E,\nu,t)(E+P)f_E(E,t)\,\mathrm{d}\nu\,\mathrm{d}E. \quad (3.69)$$

Full Benchmark

Having verified the consistency in ion transition rates, density- and energy conservation of the spontaneous recombination process, an incident radiation field can be added to verify the same for the stimulated recombination process. When stimulated recombination occurs, it cannot be separated from spontaneous emission. In the remainder of the discussion, the recombination rates are the sum of both contributions. An optically-thin target is assumed so that the X-rays can penetrate the target without experiencing any opacity effects. The X-ray energy is chosen sufficiently high at 1950 eV to avoid resonant or near-threshold effects of the ionisation cross-section.

In order to visualise the effect of an external radiation field, the temperature is fixed for all calculations in which the radiation field is varied. The temperature and density of the electron distribution is marked in each figure.

When a radiation field is applied, it can induce ionisation as well as recombination events. The ionisation rate scales linearly with the peak XFEL intensity I_0 and is given by Eq. 3.56. This rate is computed for a single ground state Mg^{9+} ion and plotted in Fig. 3.31. It shows that the PI process happens on time scales of a few femtoseconds. The ionisation rate is independent from the electron energy or density insofar as they allow the X-rays to penetrate the target. The method to compute PI

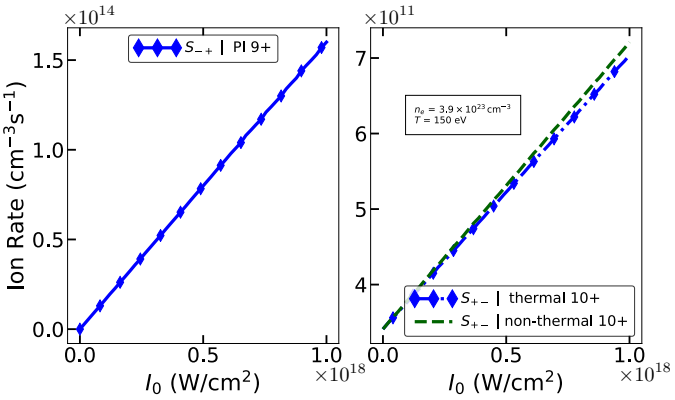

Figure 3.31: The photo-ionisation and total (spontaneous + stimulated) radiative recombination rates as a function of incident peak intensity in the $K^2L^1 \rightleftharpoons K^1L^1$ magnesium transition. The temperature and density are constrained to $n_e = 3.88 \times 10^{23}\,\mathrm{cm}^{-3}$ and $T = 150\,\mathrm{eV}$.

rates does not depend on the method in which the electron distribution is modelled, hence there is no comparison to be made. The total recombination rate is larger than it was in the case of spontaneous emission. With an electron temperature constrained to 150 eV, the data point at $I_0 = 0$ corresponds to the rate observed in Fig. 3.28. The recombination rates are calculated through Eq. 3.61 (discretised Maxwellian for non-thermal scheme) and 3.65 (analytical Maxwellian in thermal scheme). The rate magnitude of recombination is three orders of magnitude lower than that of ionisation, indicating it is an unlikely process to occur. Bound-free collisional recombination is much more prevalent in a solid-density system.

There is a slight difference between the results of the thermal- and non-thermal electron models. This arises due to the grid discretisation errors that become more significant as the recombination cross-section attains high numerical values at energies $E > 1\,\mathrm{keV}$. In this region, the step size between energy grid points is large.

An approximation that has been made to expedite the computational efforts when computing ion transition rates. In the double integral Eq. 3.61, the bandwidth of the radiation field is small for all XFEL applications. The scheme operates as if the radiation field were monochromatic, and the integral over the incident photon energies is computed first and held constant. This approximation has no consequences for the ion rates, but does aggregate photon energies and removes the bandwidth of the XFEL from the outgoing photons.

Comparing the ion transition rates of the spontaneous and total recombination rates, it can be seen that the induced component of RR is of a similar magnitude as the spontaneous contribution in this photon energy range. The photons only induce

the reaction but do not give off any energy that affects the energy balance. For this range of peak intensities, the collision operators Eq. 3.64 have been computed and plotted in Fig. 3.32. The collision operator for $I_0 = 0$ is the same as the operator at

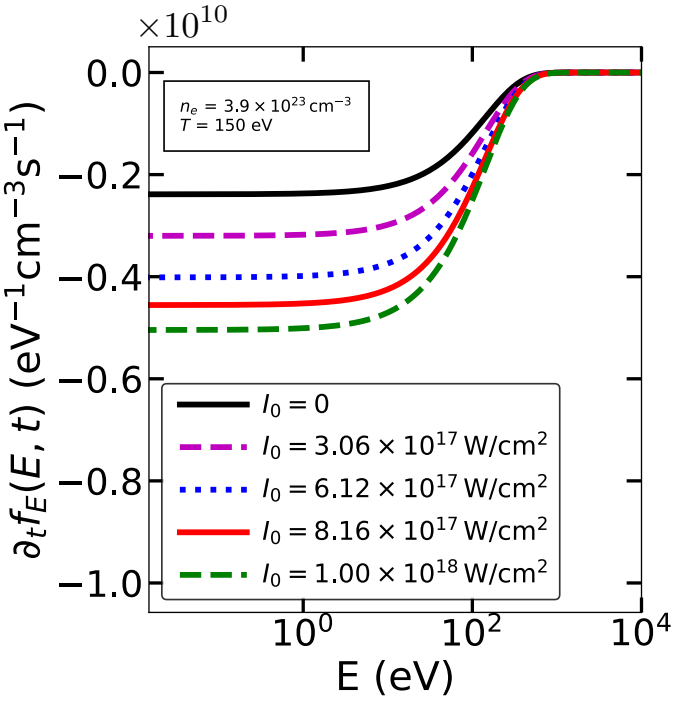

Figure 3.32: Total recombination collision operators for a core-hole ionised Mg^{10+} ion as a function of X-ray intensity. The operators are strictly non-positive for all temperatures and intensities.

$T = 150\,\mathrm{eV}$ in Fig. 3.29. By applying an increasingly strong incident X-ray field, the magnitude of the operator can be doubled while retaining the same qualitative form as a function of energy. The profile does not change because it is directly proportional to the PI cross-section for both stimulated and spontaneous recombination. Provided there is an excited-state population $n_+(t)$, the radiation field can only scale the total derivative by a constant value that depends on the beam parameters.

Integrating the collision operator over energy yields the change in density of the free-electron population. Rather than drawing the comparison between the two electron models, it is more relevant that each of them is self-consistent in its density calculation. Therefore, the density time-derivatives for the total RR rates are computed for the window of XFEL peak intensities. The results are plotted in Fig. 3.33. The numerical scheme conserves the sum of bound and free electrons exactly by drawing electrons from the free-electron population at the same rate as the ion transition occurs.

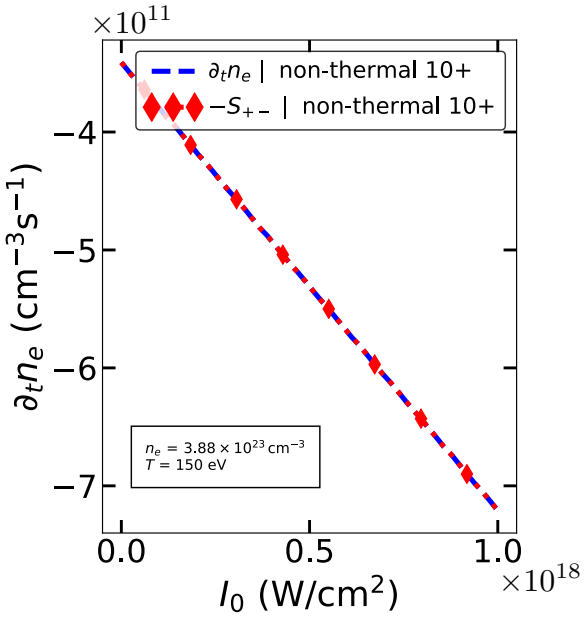

Figure 3.33: Total recombination collision operators for a core-hole ionised Mg^{10+} ion as a function of X-ray intensity. The operators are strictly non-positive for all temperatures.

The energy balance has a similar form as for the spontaneous recombination case. The incident X-rays only enhance the rate, but do not affect the energy balance. In this case, the emissivity will be calculated for future experimental use. It requires a photon field operator similar to the Fokker-Planck operator in order to calculate the energy-dependent radiation field. Given the reaction cross-section, the energy-dependent distribution $\varepsilon(\hbar\omega, t)$ of the recombination photons can be written as:

$$\begin{aligned}\varepsilon(\hbar\omega, t) = n_+(t)\sqrt{\frac{2}{m_e}}\int_0^\infty \sqrt{E = \hbar\omega - P} \\ \times \sigma^{RR,tot}(\hbar\omega - P, \nu, t)(\hbar\omega) f_E(E = \hbar\omega, t)\,\mathrm{d}\nu,\end{aligned} \tag{3.70}$$

provided $\hbar\omega - P \geq 0$. The outgoing photon energy has been written as $\hbar\omega$ to avoid confusion with the incoming X-ray photons. The photon operator Eq. 3.70 draws an energy E from the incident electron group, draws the ionisation potential P from the ion species and produces a photon with the residual energy $\hbar\omega = E+P$. The radiation production term $\varepsilon(\hbar\omega, t)$ can be considered the emissivity, the volumetric production of light at a specific emission wavelength. This quantity can in principle be measured through emission spectroscopy and is therefore of great interest. Due to the shifting operator whereby each photon is emitted at an energy P above the incident electron energy, the bound-free contribution to the total emissivity is separated in energy from the spectral region in which most bound-bound transitions occur.

The emissivity Eq. 3.70 is plotted in Fig. 3.34 for some incident X-ray intensities, together with the radiative losses and ion energy gains. From these quantities, the energy loss in the free-electron population can be computed. At a constant electron

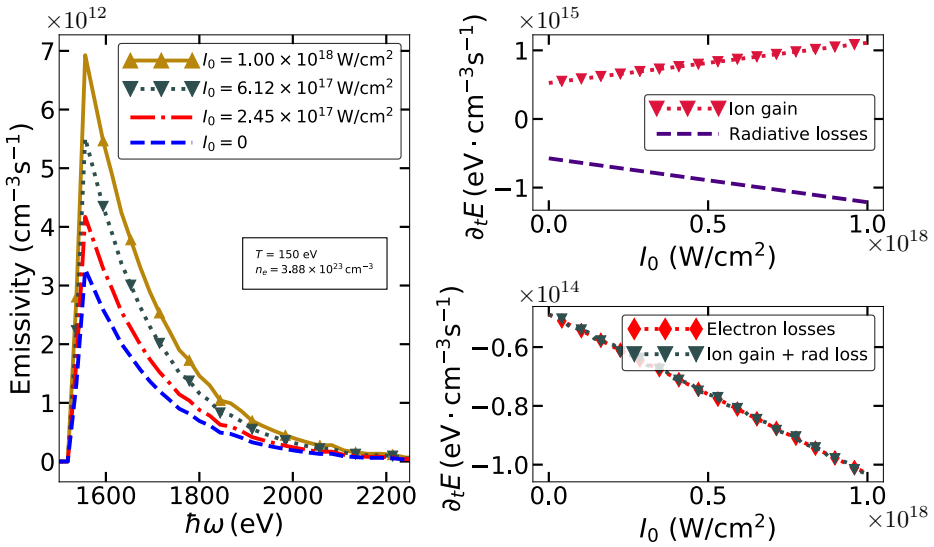

Figure 3.34: The emissivity and radiative energy loss rates of a Mg^{10+} ion that is photo-pumped by a 1950 eV X-ray field at various intensities. The X-rays enhance the stimulated recombination rate.

temperature and density of $(n_e, T) = (3.88 \times 10^{23}\,\mathrm{cm}^{-3}, 150\,\mathrm{eV})$ and a photon energy $h\nu = 1950\,\mathrm{eV}$, the X-ray field strongly enhances the RR rate of a core-hole Mg^{10+} ion. The target ion density is taken to be 1 cm^{-3}, with the remainder of the ions residing in a non-interacting ground state.

The emissivity, the volumetric production of light per frequency, has been computed with Eq. 3.70. Although it is not part of the self-consistent set of collision operators that governs the energy and particle transfer between free and bound electrons, this operator self-consistently couples the ion and electron energy to the photon field. Integrating the emissivity spectra over photon energy yields the total energy density contained by the photon field that originates from the target region.

The spectral region of the recombination process starts at the IPD-adjusted ionisation potential $P - \mathrm{IPD} = 1534$ eV. As will be discussed in more detail in Chapter 4, this constitutes a spectral gap of $\mathcal{O}(200)$ eV for magnesium with respect to the bound-bound emission lines. This statement is also valid for other materials, albeit with different spectral separations because the bound-bound transitions always have lower thresholds than their bound-free counterparts. Despite the relatively low intensity

that is a result of the low transition rate[6], a bound-free spectrum can be measured experimentally due to this spectral separation. Before drawing a comparison with experimental data, opacity effects need to be accounted for. Opacity effects do not influence the discussion in this section as it the energy balance only relates to the production term of light, and not to its transport properties.

The spectrum peaks approximately at the energy value corresponding to the sum of the bulk electron temperature and the ionisation potential. If there is a hotter non-thermal tail on the distribution, this will produce even more energetic photons. Measuring bound-free spectra provides a way to detect the presence of the high-energy tail of the electron distribution.

During the atomic transition, the ion state undergoes a change in electrostatic potential. The potential remains fixed and the energy exchange in the ion population can be computed as a product of this potential and the rate. The energy drawn from the ion population is nearly equal to the energy transmitted to the photon field. This implies that the emitted photons draw the majority of their energy from the ions, provided the electron system has a mean kinetic energy below the ionisation potential. When the energy changes in the ion population and radiation field are summed up, the statement of energy conservation Eq. 3.68 dictates that this should be the energy loss experienced by the free-electron population. Computing the first moment of the collision operator Eq. 3.64 shows that this indeed the case, as demonstrated by the electron losses shown in Fig. 3.34.

The Fokker-Planck numerical scheme has been extended such that the computation of the spontaneous and stimulated recombination transition rates and collision operators is consistent with equilibrium results. Additionally, RR can provide insight into the high-energy dynamics of the free-electron population as they have a characteristic spectral signature that is separated from the bound-bound transition lines.

3.6 Conclusions

The Fokker-Planck numerical framework proposed by Tzoufras *et al.* [47] that describes the evolution of the electron distribution function has been extended to include electron-ion interactions. In addition to the elastic electron-electron interactions, this equation now accounts for the electrons released or absorbed during inelastic

[6]The RR ion transition rate is several orders of magnitude lower than the bound-bound spontaneous emission rates.

electron-ion interactions. These processes are collisional excitation and de-excitation, Auger decay, dielectronic recombination, photo-ionisation, spontaneous and stimulated radiative recombination, collisional ionisation and three-body recombination. The model also contains radiative bound-bound transitions that have no interaction with the free-electron population. Each interaction has its own collision operator that describes how the ion transition affects the free-electron distribution function. Accumulating all collision operators discussed here into the Fokker-Planck equation, the full equation that includes electron-electron and electron-ion interactions reads:

$$\begin{aligned}\frac{df_E(E,t)}{dt} =& -\frac{\partial}{\partial E}\Big[a(E)f_E(E,t)\Big] + \frac{1}{2}\frac{\partial^2}{\partial E^2}\Big[D(E)f_E(E,t)\Big] \\ &+\sum_{\text{ions}}\Bigg[\left(\frac{\partial f_E(E,t)}{\partial t}\right)_{CE} + \left(\frac{\partial f_E(E,t)}{\partial t}\right)_{CDE} \\ &\quad + \left(\frac{\partial f_E(E,t)}{\partial t}\right)_{CI} + \left(\frac{\partial f_E(E,t)}{\partial t}\right)_{3BR} \\ &\quad + \left(\frac{\partial f_E(E,t)}{\partial t}\right)_{DR} + \left(\frac{\partial f_E(E,t)}{\partial t}\right)_{RR} \\ &\quad + S_{Auger}(t) + S_{PI}(t)\Bigg],\end{aligned} \tag{3.71}$$

where the sum aggregates the contributions of all the ion populations. The combination of an ion transition rate model coupled to the Fokker-Planck equation constitutes a self-consistent method to compute the density- and energy balance of the free-electron population together with the ion population dynamics in a warm dense system.

The ion transition rates, as well as the conservation laws for the electron density and total energy have been benchmarked for a thermal electron distribution. This was done by feeding a discrete thermal distribution into the numerical scheme and comparing these results to those obtained by computing the cross-section integrals with an analytical Maxwell-Boltzmann distribution. The transition rates and conservative properties are found to be in agreement in equilibrium after accounting for small numerical errors that can be expected when discretising the energy grid. After benchmarking the numerical scheme in known conditions, the scheme is now suitable to be used in non-equilibrium and time-dependent problems.

Chapter 4

Measuring Warm Dense Matter Collisional Ionisation Rates

Contents

4.1 Introduction

Collisional Ionisation (CI) is a collisional interaction between ions and electrons in which free electrons liberate bound electrons through impact. The incoming electrons need to overcome an ionisation potential, and the resulting electrons share any residual energy. Subsection 3.5.4 contains the theoretical background on the cross-section models and conservation laws relevant to bound-free collisional transitions. The reaction products of CI and its inverse, Three-Body Recombination (3BR) are given in Eq. 4.1.

$$\mathrm{e}^- + \mathrm{ion}_z \rightleftharpoons \mathrm{ion}_{z-1} + 2\mathrm{e}^-. \tag{4.1}$$

CI is a process that is not unique to Warm Dense Matter (WDM) physics, as it has been observed in the context of electric discharges in gases by Townsend [81], and later also in MOSFETS by McKay [82]. There, it is what is known as the avalanche effect of ionising radiation; after some form of radiation ionises an atom, the cascade of electron collisions that follows leads to the production of even more ionised electrons that can be detected. It is the operating mechanism of a Geiger counter that allows low fluxes of radiation to be measured with relatively simple electronics [83], and was used as the primary ionisation mechanism in the development of mass spectrometry [84].

CI is also related to the radiation stopping power of materials, defined as the loss rate of energy over the distance that the radiation travelled [85]. CI is one of the main mechanisms to slow down high-energy electrons in matter. As a result of this, the material gets damaged and this how radiation damage also relates to the frequency of CI events taking place.

In WDM physics, the ionisation balance, and directly through this, the charge state distribution of the ion populations, are determined by the rate of CI and its inverse process 3BR. The transition rates associated with these processes are amongst the highest in a hot dense system, and understanding them is critical in order to correctly model the ion population dynamics. Being a key factor in determining what state the material resides in, CI and 3BR influence all material properties through direct and indirect ways.

For example, the optical properties such as the opacity depend on the ion charge state configuration [27, 31]. In order to know the time-dependent opacity, the ionisation balance needs to be tracked over time.

Transport properties such as the thermal and electrical conductivity are even inversely proportional to the collisional rates [23–25]. For modelling these macroscopic

quantities, the collisional rates therefore also play an important role. This applies even more to non-equillibrium states of WDM.

The equillibration process itself is even described by collisions, because CI and 3BR are efficient processes to transfer kinetic energy from the free electron population into binding energy of the ions, and vice versa. Many plasmas created in a laboratory environment do not reside in the regime of Local Thermodynamic Equilibrium (LTE), because they are created through rapid heating or shock compression. Inherently, these methods produce an unstable system that evolves rapidly over time. Our success in modelling or interpreting experiments in the context of inertial confinement fusion [86] and in astrophysical plasmas [87] relies on our knowledge of collisional frequencies in the plasma [34]. Provided we leave a WDM for enough time, the collisional interactions will redistribute the energy between electrostatic potential energy and kinetic energy in such a way that LTE is eventually achieved.

Yet another consequence of high-frequency electron-ion collisions involving X-ray Free Electron Lasers (XFELs), but outside the field of plasma physics, can be found in diffractive imaging techniques [88]. In these imaging techniques, bright XFEL light sources are focussed onto single molecules for structural imaging. As a result of the high intensity of light, the evolution of a sample is similar as that of targets in WDM studies. The samples, often of interest to biology or chemistry studies, start off in room-temperature conditions and end up as a hot plasma. This time, the collisional processes taking place relate to the creation of electronic damage to the sample.

Many diffractive imaging techniques rely on the notion that we can obtain an image before the sample is destroyed by the intense irradiation process [89, 90]. Knowledge of the collisional ionisation frequencies, the main driver of electronic damage in bio-molecular imaging experiments, is critical to test this assumption. It also allows one to quantify the rate of damage formation, which places a fundamental limit on the highest attainable spatial resolution of the diffractive imaging technique.

With their roles in the population dynamics, transport properties, diffractive imaging and equillibration processes, it can be stated that the rates of CI and 3BR are fundamental state parameters. There are sufficient reasons to want to know the associated rates, but as the reader may have suspected, they are far from trivial to measure. It is experimentally challenging to create a hot dense system with tunable conditions, a requirement for any experiment to take place. Secondly, collisional processes are fast and take place on femtosecond time scales in a solid-density plasma system and any experimental effort used must be able to isolate the collisional rate from other competing atomic transitions [29]. To add to the challenge, collisions

in strongly coupled environments are no longer binary events, and instead have the characteristics of a many-body interaction. This many-body effect means that the reaction cross-section is radically different from the cross-sections found in isolated atoms.

This chapter will explore experimental work in plasma systems created before XFELs existed, with electron densities in the range of $10^{15} - 10^{17}\,\mathrm{cm}^{-3}$, as well as after the advent of XFELs when electron densities as high as multiple times solid density ($\sim 10^{23}\,\mathrm{cm}^{-3}$). The author will outline some LCLS experiments on CI rates in solid-density magnesium plasmas in various conditions, and infer a cross-section from the experimental data.

The material of choice will be magnesium, due to its simple atomic structure. At the densities of interest, only two superconfiguration shells are bound (K and L corresponding to $n = 1, 2$) so the interaction can be modelled with all its superconfiguration rather than having to truncate the number of accessible states.

The data analysis largely leans on the non-LTE collisional-radiative codes SCFLY (Fortran) and CCFLY (C++) introduced in Sections 1.1.4 and 3.2.1. For most purposes in this chapter, there is no difference in the outcomes of these codes. CCFLY completes any calculations significantly faster, but both codes work with the same rate models and atomic input data. The only difference lies in the treatment of the free electrons: it can be thermal (equillibrated to a Maxwell-Boltzmann (MB) distribution), or non-thermal and compute the distribution dynamics with a Fokker-Planck scheme outlined in Section 3.5.4. In the Fokker-Planck mode it is not yet possible to compute an emission spectrum at the time of writing. This is no problem for magnesium, as it turns out the distribution is close to thermal.

One of the main results from this chapter is the construction of a cross-section model for CI in magnesium. It is made to be consistent with previously known cross-section data obtained at electron densities in the range of $10^{15} - 10^{17}\,\mathrm{cm}^{-3}$, but scales correctly to account for density effects up to inferred electron densities exceeding $10^{23}\,\mathrm{cm}^{-3}$.

4.2 Cross-section models

Like all collisionally-induced transitions in atomic physics, the probability of an ionisation event occurring can be parametrised with the cross-section formalism. For a recapitulation, the cross-section concept is introduced in Appendix B. The cross-section for the inverse process 3BR is related to the CI cross-section through the

microscopic reversibility relation Eq. 3.47. Thus by correctly modelling the ionisation cross-section as a function of energy, the recombination rate is also implicitly obtained.

4.2.1 Theoretical models

A range of theoretical work has been done to compute cross-sections for low to mid-Z materials [91]. One such class of models is the suite of scaled hydrogenic approaches [33, 92]. The idea here is to obtain the cross-section for impact ionisation of a hydrogen-like atom either through calculations or measurements, before scaling the solution to that of the ion of interest with a different electron confguration. The benefit of this technique is that results can be obtained for complex charge state configurations for which direct calculations may not be feasible. A weakness is that the accuracy of the cross-section depends on knowledge of the scaling behaviour.

A second set of theoretical models includes the distorted wave model [93–96]. This approach requires a full quantum mechanical calculation to calculate the wave functions of an incoming electron and the ion system with which it interacts. Collisional cross-sections are then expressed in terms of the matrix elements connecting the initial electron population and initial ion, and the now increased number of electrons and the final state of the ion after the collision. The calculations is cumbersome to do and must be repeated for the many possible ion charge state configurations that can occur, as well as the many spatial arrangements in which the ions can be found.

Lastly, there are the binary encounter models [75, 97–99]. They are worth mentioning, despite having expressed concern over their applicability in the strongly coupled regime. These models capture CI cross-sections by describing them as inelastic Coulomb scattering effects from an incoming electron on a static atom. It is a semi-classical approach that is amongst the oldest of CI models. What the binary encounter, distorted wave and scaled hydrogenic models have in common is that they require calculations to be repeated for each particular set of electron and ion parameters. As a result they thus become computationally intense when used in atomic kinetics calculations when many ion states are present and the possible range of electron impact energies spans over many hundreds of eV.

This is the motivation to capture cross-sections in a parametric form as a function of some ion parameters and an incoming electron energy. The overarching goal of using this type of model is twofold. Firstly, the cross-section is a suitable way to quantify experimental data so that it can be used to compute rates for a wide range of electron temperature-density conditions. Secondly, parametric cross-sections can

be rapidly evaluated in atomic kinetics codes. When the cross-sections are derived from theory, a parametric fit is made to calculation results so the cross-sections can be evaluated or interpolated more easily without re-running the often computationally intense calculations.

4.2.2 Semi-empirical models

In addition to theoretical approaches, there are cross-section models drawn from experimental data. One of the oldest and simplest cross-section models was proposed by Lotz [72, 77]. It is a semi-empirical formula that was inspired by data on singly-ionised low-Z ions. For a sub-shell containing ξ electrons, the Lotz cross-section is given by:

$$\sigma_{Lotz}(E) = C_{Lotz} \sum_j \xi_j \frac{\ln\left(E/P_j\right)}{E \cdot P_j}, \;\; E \geq P_j, \tag{4.2}$$

where P_j denotes the ionisation potential, and $C_{Lotz} = 4.5 \times 10^{-14}\,\mathrm{cm^2eV^2}$ for magnesium. The summation runs across all occupied atomic sub-shells to add the contributions of different shells. In order to calculate the CI rate for a given ion, all its electrons must be considered and the total CI rate is obtained by summing up their respective contributions. The Lotz cross-section has the characteristic logarithmic tail also seen in the Bethe-Bloch stopping power formula [100].

As can be seen from Eq. 4.2, the cross-section rises steeply for the region around the threshold. Any measurement error of what the reaction threshold is can significantly alter the rate. In order to smoothen the transition around the threshold, Burgess and Chidichimo (BC) proposed a cross-section of the form [101, 102]:

$$\sigma_{BC}(E) = C_{BC}\pi a_0^2 \sum_j \xi_j \frac{I_H^2}{EP_j} \ln\left(E/P_j\right)^{1+\beta P_j/E}, \;\; E \geq P_j, \tag{4.3}$$

where I_H is the Rydberg constant, a_0 the Bohr radius, C_{BC} a material constant that is 2.3 for Mg, and β a smoothening parameter defined as:

$$\beta = \frac{1}{4}\left[\left(\frac{100z+91}{4z+3}\right)^{1/2} - 5\right], \tag{4.4}$$

where z is the ionisation degree of the ion before ionisation occurs. The smoothing effect is only appreciable for energies near the threshold, or for low charges, as $\lim_{z\to\infty}\beta(z) = 0$ and β rapidly decays for increasing charge. Interestingly, Burgess himself stated in the original paper that the model is deemed suitable for ionisation levels $2 \leq z \leq 5$, however, it is commonly used for higher ionisation states as well.

The BC cross-section can be seen as a generalisation of the Lotz case, as the Lotz cross-section is obtained (albeit with different constants) for the case $\beta = 0$. Due to their simplicity, both models have become popular over the last 50 years.

4.2.3 Density scaling

A major challenge for any cross-section model is to accurately describe ionisation probabilities for a wide range of electron densities. In dilute plasma systems ($\Gamma \ll 1$) where the kinetic energy of the electrons is much higher than their potential energy, e.g. a very hot system, or one at a low density, the mean free path length of the electrons is much larger than the charisteric macroscopic length scale of the plasma [54]. These systems can be approximated as being collisionless, indicating that collisions are not the dominant effect determining the plasma's dynamics. Other macroscopic effects alter the plasma in more significant ways in this case. If a collisional event does occur, it can be regarded as being a binary event without much loss of accuracy.

In contrast, in a dense system that is strongly coupled ($\Gamma \sim 1$), collisions occur in the form of many-body interactions. Some of the most significant density effects that occur are screening, Pauli blocking and the lowering of the ionisation potential. Two models for the Ionisation Potential Depression (IPD), from Modified Ecker-Kröll (mEK) and Stewart and Pyatt (SP) are given by Eqs. 3.13 and 3.14 and further described in Section 3.4. Both models return the IPD as a function of electron density, mean kinetic energy and the ion charge.

Zammit *et al.* showed that in strongly coupled plasmas, the cross-section rises significantly around the threshold energy [103]. The method they used is a convergent closely-coupled approach, an approach where the Schrödinger equation is expanded in order to calculate the cross-section as a sum of reaction channel probabilities [104,105]. What becomes clear in the qualitative sense is that the coupling in electrons increases the ionisation rate in a non-linear way. The physics behind this can be described by reformulating the one-particle electron distribution into a higher-order distribution that captures pair interactions or, alternatively, by modifying the cross-section so it scales with the density effect. In the latter case the distribution function can be left as it is, and the transition rates can still be computed with the same cross-section framework. The cross-section, however, then needs to be considered a function of the incoming energy and the surroundings of the ion.

Clark, Abdallah and Mann (CAM) constructed a cross-section from the distorted-wave model in a dense plasma environment in order to parametrise the increased cross-section in the near-threshold energy range. The many-body effects are entirely

contained in the IPD, so that the model can be applied at any electron density. The cross-section is written in parametric form so it can be readily evaluated at any desired value for the impact energy or IPD:

$$\sigma_{\mathrm{CAM}}(E) = \pi a_0^2 \sum_j \frac{\xi_j}{\left(P_j'/I_H\right)^2} \frac{P_j'}{E} \left\{ \left(c_1 + \frac{c_2 + c_3 \cdot l}{n} \right) \log\left(E/P_j'\right) \right. \tag{4.5}$$
$$+ \quad \left(c_4 + \frac{c_5 + c_6 \cdot l}{n} \right) \left(1 - \frac{P_j'}{E} \right)$$
$$\left. + \quad \left(c_7 + \frac{c_8 + c_9 \cdot l}{n} \right) \left(1 - \frac{P_j'}{E} \right)^2 \right\}.$$

The effective ionisation potential P_j' is the atomic potential corrected by the IPD. The weights $\{c_1, \ldots, c_9\}$ are material and charge-independent coefficients given by $\{1.5369, 0.99656, -0.61916, 2.4463, -2.4773, 3.2151, -1.4512, 1.7230, -0.47075\}$. Parameters n and l represent the principal and angular momentum quantum numbers of the electron undergoing ionisation. The logarithmic term is similar to the Lotz and BC models, and the linear and quadratic additions of the terms $\left(1 - \frac{P_j'}{E}\right)$ describe the screening that occurs at near-threshold energies. For super-configurations, the cross-section can be averaged over all angular momentum quantum numbers l with the substitution:

$$l \mapsto \frac{(4n+1)(n-1)}{6n} \tag{4.6}$$

into Eq. 4.5. This model, although it did not match our experimental data in its original form, was the starting point of constructing a description that scales cross-sections from the dilute into the solid-density regime. It turned out that the IPD scaling of the Lotz, BC and CAM models was still insufficient and that the cross-sections were in fact higher than any of these models predict.

For any cross-section model, it holds that once it is obtained from one either theory or experiments, the CI or 3BR transition rates can be computed from the rate integrals Eqs. 3.42 and 3.46.

4.3 Earlier experiments without X-ray FELs

Amongst earlier experimental efforts to measure impact ionisation rates were cross beam experiments [106–108]. Two beams of interacting particles with a known flux and beam shape would be directed through each other's path, after which the rate of ionisation can be inferred from the reaction products, as depicted in Fig. 4.1. If

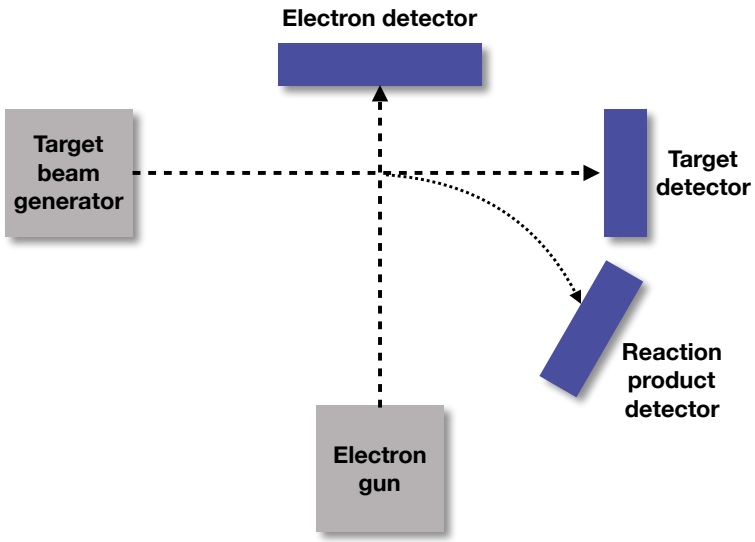

Figure 4.1: Schematic setup of a crossed beam experiment to measure collisional ionisation cross-sections. A beam of electrons is fired through a beam of target atoms. If an ionisation occurs, the ionised atom are deflected by an electric or magnetic field onto a detector.

an ionisation event occurs in a target atom, its charge will change and it can be deflected with an electric or magnetic field onto a detector. The detected current is then linearly proportional to the ionisation rate. Crossed beam methods have as a benefit that the impact energy can be tuned with a high resolution across a large range by accelerating the electrons, but their use is restricted to lowly-charged ionic charge states due to the cross-section decreasing with charge, and the difficulty of producing sufficiently large ion beam currents [109]. Crossed beam methods also rely on being able to collimate a beam in order to have a well-defined interaction volume. If the beam diverges too much or the volume is ill-defined, the inferred cross-section has a high measurement uncertainty.

An alternative group of methods that was developed around the same era are ion trap techniques [110–112]. In this approach, a plasma of a material of choice is first created and heated and compressed to the desired temperature and density, before introducing the ions of interest. The introduced ions then go through successive stages of ionisation until they equilibrate with the bulk plasma. As they advance through increasing levels of ionisation, the ions emit line emission which is then tracked over time. The collisional ionisation rate can be inferred by modeling the process with a rate equation model of coupled differential equations. Ion trap methods allow for measurements up to higher charge states, provided that the plasma conditions are well-defined, and that the atomic transition of interest can be isolated from other

competing processes [113]. Often that is not the case, as the contribution of multiple sub-shells needs to be considered, and neglecting inner-shell contributions can lead to errors of several tens of percents [110].

Though combining both methods can counter some of their shortcomings, what remains is that both methods are limited to electron densities $\lesssim 10^{17}\,\mathrm{cm}^{-3}$ [114]. The inability of creating a well-defined plasma at higher electron densities puts a cap on the range of conditions where CI rates can be studied. Until recently, collisional models could not be tested experimentally with either method in the WDM density conditions in which they are commonly deployed.

The cross beam and ion trap methods, combined with a range of other experimental setups, did lead to a vast collection of cross-section data in the electron density range up to $10^{17}\,\mathrm{cm}^{-3}$ [91]. This data is still useful to benchmark new cross-section models against by testing their scaling behaviour across a large density range.

4.4 Experiments at LCLS

Measuring CI rates in dense plasmas poses many experimental challenges related to the extremely short time scale on which they take place, and to the general difficulty of creating a well-characterised dense plasma at or near LTE [29]. With the advent of bright XFEL sources it is now possible to do just that due to their high peak brightness and femtosecond pulse duration [22]. The idea is to create a dense plasma in conditions where it is possible to isolate collisional processes from other competing processes, and measure their rates through emission spectroscopy.

Experiments on the Linac Coherent Light Source (LCLS) [2] facility at the Stanford Linear Accelerator Centre (SLAC) have shown that XFEL pulses are sufficiently intense to heat samples placed in the focus of the beam to temperatures approaching 200 eV within a few tens of femtoseconds [18, 40].

The short pulse length leads to a well defined mass density, as the ions in the plasma remain relatively cold and cannot move more than a lattice spacing during the pulse duration. The use of X-rays instead of optical wavelengths has the benefit that it allows isochoric heating, resulting in small temperature and density gradients in the direction of beam propagation. These factors together lay the foundation for creating a well-defined, solid-density plasma that can be used to study collisional rates.

4.4.1 Experimental setup

The experiments presented here to measure collisional ionisation rates in a solid-density magnesium plasma were conducted at the SXR beamline of LCLS. One of the setups, the most succesful one, is presented in Fig. 4.2. The targets are coated with a thin CH layer to prevent oxidation and target degradation. In order to create a stable target, the magnesium layer is mounted onto a silicon substrate that plays no further role in the experiment. A single shot of focussed X-rays heats the thin foil target and ionises the magnesium to ever increasing ionisation degrees. The peak intensity of the X-ray pulse is $\sim 10^{17}\,\mathrm{W\,cm^{-2}}$, sufficient to heat the sample to temperatures exceeding 100 eV. The photon energy is carefully tuned so that it lies below the K-edge for all

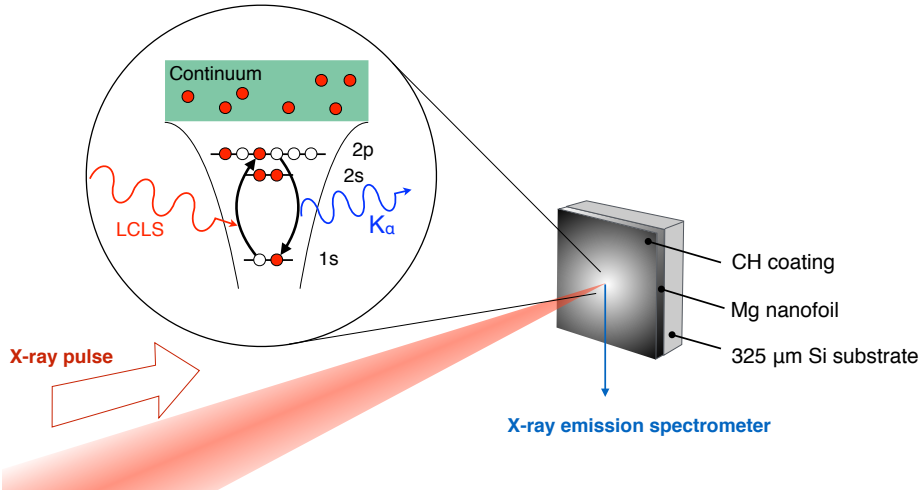

Figure 4.2: Experimental setup: a (54±2) nm thick Mg foil is irradiated by the focussed X-ray pulse [30]. The sample is ionised to ever increasing charge states, with an X-ray wavelength that is tuned to the bound-bound resonance in a 7^+ Mg ion. When the ground state 7^+ ion is created, the X-ray pump resonantly excites a $1s \rightarrow 2p$ transition, thereby creating a core-hole excited state. The excited state can then decay through Auger recombination or K_α emission. ©2018 American Physical Society.

but the 2^+ ground state of the ion states produced in this experiment and no direct K-shell photo-ionisation occurs in the charge states of interest. The primary source of ion states with a K-shell vacancy is the photo-induced K-to-L excitation in the ground state of Mg^{7+}. The resonant nature of the photo-pump is key to constrain the conditions in which a K-shell vacancy can be produced in the ion states.

At the start of the experiment, the pulse rapidly heats the target, and a combination of L-shell photoionisation and electron collisional L-shell ionisation burn through

the charge states until the 7^+ ion with super-configuration K^2L^3 is reached (2 electrons in K-shell, 3 in the L-shell). At this point, the X-ray pulse resonantly induces a 1s $\rightarrow$ 2p transition and produces a core-hole population, as illustrated in Fig. 4.2. In what follows we will index the charge state of the Mg ion via the K- and L-shell populations [32, 38].

The pulse emits approximately 10^{12} photons in a narrow bandwidth of photon energies that are carefully tuned to ionise the foil up to a chosen charge state, a state that will vary depending on the experiment. While the electrons are well into the strong-coupling WDM regime, the ions remain cold. The pulse has a Full Width at Half Maximum (FWHM) duration of 60 fs, too far below the electron-phonon coupling time to heat the ions, but sufficiently long to reach electron densities in the range of $10^{23} - 10^{24}\text{cm}^{-3}$.

Time-integrated emission spectroscopy records the K-α emission from the foil for each pulse. The emission spectrum records the presence of ion populations due to their characteristic emission wavelength. This technique can capture population dynamics even when it occurs on the femtosecond timescale. By tuning the XFEL photon energy, it is possible to pump a pre-selected charge state and produce a state analogous to population inversion. Selecting a particular charge state is the key to being able to isolate the CI process from competing processes so that it can be observed through emission spectroscopy. If we create a sizeable core-hole population with configuration K^1L^4, we can observe its characteristic emission line and that of its neighbours. When we create said charge state, it will have a lifetime that is primarily determined by the Auger lifetime (see Subsection 3.5.3). During this time, the ion may undergo an additional ionisation or recombination event before decaying as another charge state (K^1L^3 for ionisation, K^1L^5 for recombination). If this happens, it will be noticeable through the emission spectrum as the other charge state emit at different photon energies. Fig. 4.3 clarifies these reaction channels.

The condition for this experiment to be successful, is that only one core-hole state can be created through the X-ray pump. This is made possible by the narrow bandwidth of the photon energies, which is around 0.4 % at LCLS at a photon energy of 1304 eV. The K-α energies for each charge state are approximately 30 eV apart so the X-ray pump needs to be tuned carefully so as to not accidentally create an unwanted state. At a resonant transition, the efficiency of the pump also decreases drastically if the excitation energy is not matched exactly by the photon wavelength [37]. Provided the photon energy is tuned correctly, the intensity of the

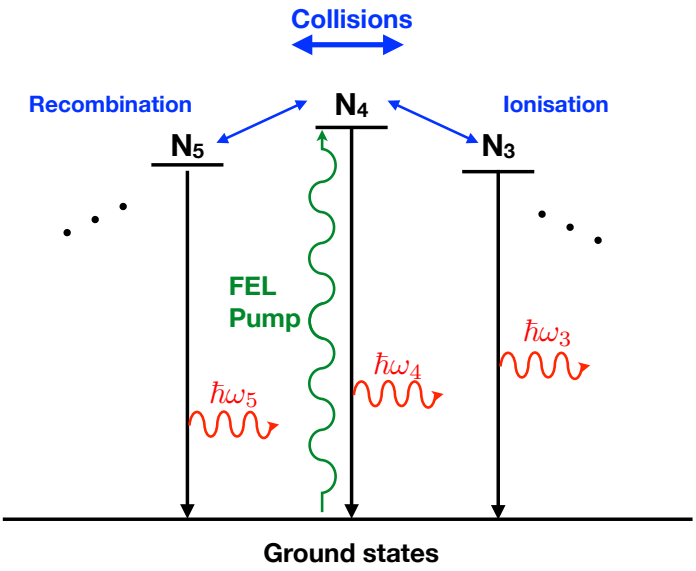

Figure 4.3: The X-ray pump resonantly excites a core-hole electron in Mg^{7+}. This creates the super-configuration K^1L^4 which can then decay through spontaneous emission or Auger decay. The subscripts on N denote the L-shell occupation. If the core-hole state undergoes a collisional transition, it can decay as a different charge state and be observed through spectroscopy.

emission lines surrounding the photo-pumped states contain information about the collisional frequencies with the L-shell electrons.

In the extreme case where there was no collisional interaction at all, the pumped state could only decay to its original ground state and no neighbouring emission lines would be observed. In the other extreme where the collisional frequencies were infinitely high, the core-hole states would be equipartitioned across all possible L-shell occupation levels. In this case, the emission spectrum of L to K photo-emission would be nearly uniform across all charge states[1]. The intensity ratio of neighbouring emission lines is therefore a measure of the collisional rates, for ionisation towards increasing charges, and recombination for lower charges. These principles of an Auger clock where the natural life-time of excited ion states states is used as an intrinsic clocking mechanism originate from femtochemistry [115].

The resonant X-ray pump is one method to isolate a charge state. It can be used for all choices of L-shell occupation, although it is most suitable for the middle states with occupation numbers between and including 3 and 6 so that there are neighbouring emission lines next to the pumped transition. It is also possible to create core-hole states with a non-resonant pump. In the non-resonant scheme, the X-ray pulse can be set to photo-ionise up to a certain charge state that can be controlled by

[1]The emissivity would only vary with emitted photon wavelength and the emission rate.

tuning the photon energy. This process is depicted in Fig. 4.4. With the non-resonant

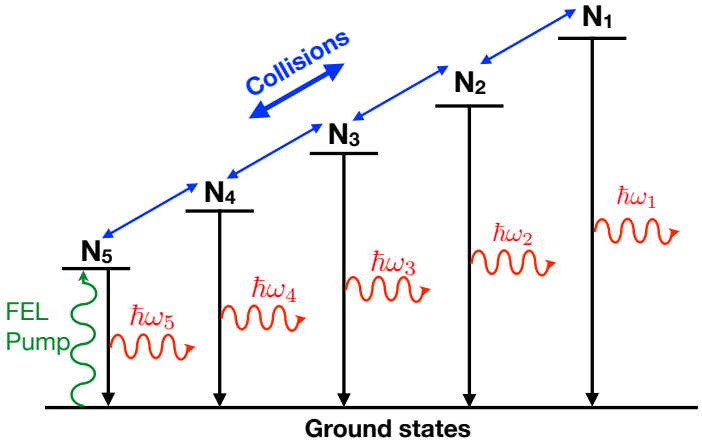

Figure 4.4: The multi-step reaction channel that produces core-hole states. The FEL pulse induces a core-hole excitation in the Mg^{5+} state. Before decaying through Auger or radiative decay, the core-hole state can undergo L-shell collisional ionisation or recombination. It then has a probability of decaying as another charge state.

X-ray pump, the charge state can be chosen by tuning the wavelength to its ionisation threshold while accounting for IPD. This is more challenging as it requires knowledge of the continuum lowering to be able to plan the experiment. When successful, this type of experiment only yields information about states above the pumped state.

With both the resonant and non-resonant setup, the same ion transition can be observed in different plasma conditions by changing the pumped state. For instance, if we want to observe the 7^+ to 8^+ transition, the pumped state can be set to be 6^+ (single collisional transition), or 5^+ (requires a two collisional events), or even 4^+ (requires three collisions). The higher the charge state, the higher the density it occurs at so this provides a method to measure the same transition rate in different conditions.

It is advantageous that the collisional frequencies are on the same order of magnitude as the Auger lifetimes. This makes the Auger lifetime a natural clocking mechanism for the collisional rates. Secondly, the short duration of the core-hole lifetime constrains the plasma conditions in which the collisional processes take place. We can identify a temperature and density range associated with the transition processes observed, making it easier to infer a cross-section from the data.

The target foils are chosen to be optically thin, in this case 54 ± 2 nm; they are much thinner than a typical absorption wavelength in the K-α energy range of interest. Due to this feature, any longitudinal gradients of the electron number or

energy density into the target are small. Furthermore, the intensity I_j of any K-α emission lines observed is linearly proportional to the population of the core-hole state:

$$\lim_{\kappa(\nu)L\to 0} I_j(\nu) = \int \varepsilon(\nu_j) L \, \mathrm{d}t \tag{4.7}$$

$$= h\nu_j S_j L \frac{\phi_i(\nu)}{4\pi} \int n_j(t) \, \mathrm{d}t, \tag{4.8}$$

for a foil of thickness L, where $\kappa(\nu)$ denotes the frequency-dependent opacity and $\varepsilon(\nu)$ the emissivity. The spontaneous emission rate (Einstein A coefficient) is given by S_j and the line profile, here taken to be a Voigt profile, is denoted by $\phi_i(\nu)$.

It is not possible to infer information about the cross-section if the emission line intensities saturate in an optically-thick target. In that case, it is unknown what the emitting ion populations have been. For a target in the intermediate optical thickness range, detailed knowledge of the opacity is required. Opacity effects are not sufficiently well understood at present to be modelled efficiently to take this approach. Furthermore, optical thinness also reduces the longitudinal temperature, density and population gradients in the direction of the X-ray pulse and leads to better-defined plasma conditions.

The next subsections will cover the experimental data for the resonant and non-resonant X-ray pump.

4.4.2 Above-edge X-ray pump

The experimentally recorded spectrum for a non-resonant X-ray pump are plotted in Fig. 4.5 for a pump photon energy of 1440 eV. This X-ray energy can produce core-hole states through photo-ionisation for Mg 7^+. Any emission lines above the pumped lines are the result of impact ionisation events that took place with the L-shell electrons of a core-hole excited state.

This spectrum provides evidence that CI events take place on a time scale that is of comparable magnitude as the lifetime of a core-hole ion, which is set by Auger decay. It is known that the Auger lifetimes are in the 1-10 fs range, so we can infer that the CI per-atom rates must be between $10^{14} - 10^{15}$ Hz.

The line intensity decays rapidly for subsequent charge states that lie above the pump, indicating this method is only suitable to detect up to two collisional transitions at once. While multiple collisional interactions are taking place, the system is still being heated further. Each subsequent ionisation event takes place at ever increasing temperatures and densities.

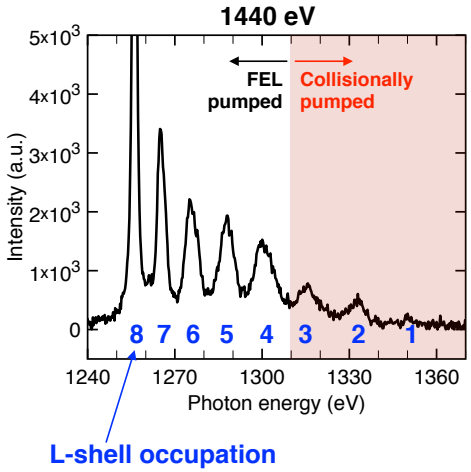

Figure 4.5: Non-resonantly pumped K-α emission spectrum for magnesium pumped at 1440 eV. The numerals below each emission line denote the L-shell electron occupation of the emitting ion state. The ion states with energies above the X-ray pump are created through collisional ionisation.

A target thickness of 54 nm led to finding an optimum between signal to noise ratio, and having a reasonably optically thin target. There was data available from 200nm and 500 nm thick foils, but unfortunately these targets are no longer optically thin. Opacity measurements presented by Preston *et al.* made this clear after the experiment discussed here had been conducted [28]. The same measurement, however, concluded that the maximum optical depth in the K-α spectral range is below 0.1, meaning the line intensities recorded here are linearly proportional to the ion populations. The thinnest targets available were 20 nm, clearly optically thin, but they had a poor signal to noise ratio. The emissivity scales linearly with the target thickness and there was too little signal to detect.

It requires a full atomic kinetics calculation to infer more detailed knowledge of the collisional processes and the conditions in which they take place. The conditions determine the degree of continuum lowering, and it is only possible to draw conclusions when the full time evolution of the sample is computed in a self-consistent way. This will follow, after the discussion on resonantly pumped data.

4.4.3 Resonant X-ray pump

The same experimental campaign also yielded a resonantly pumped dataset for a 54 nm thick magnesium target. The XFEL wavelength was tuned to 1304 eV with a ~ 5 eV bandwidth that overlaps the $K^2L^3 \rightarrow K^1L^4$ excitation. The emission spectrum

recorded for this experiment is plotted in in Fig. 4.6. The data shows that the K^1L^4

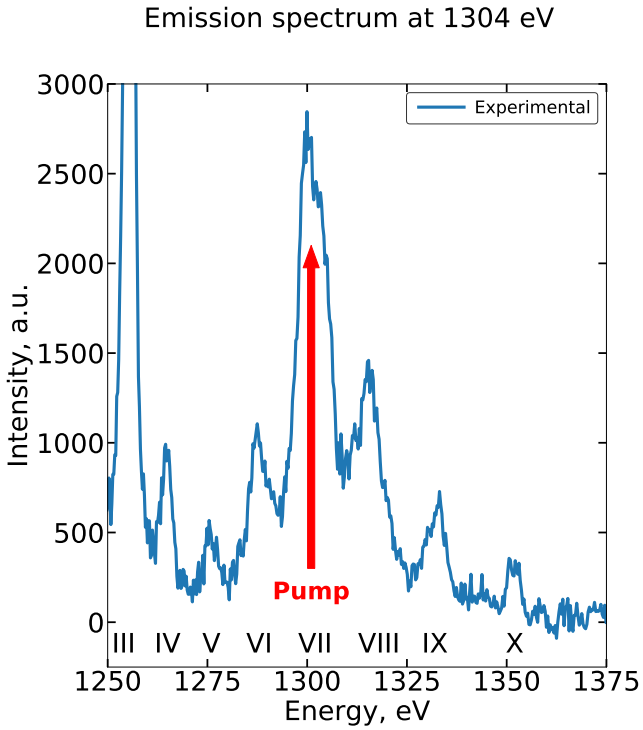

Figure 4.6: A resonantly pumped K-α emission spectrum of magnesium. Roman numerals denote the charge of the corresponding ion state. The X-ray creates a 7^+ excited state that can undergo collisional ionisation and recombination before it decays. The collisional interactions produce neighbouring charge states that are observed.

population was indeed the second-highest core-hole excited state in the system, beaten only by the cold K-α line marked with III, emited by the K^1L^8 super-configuration state. This is understandable, as the cold K-α line is emitted by a larger surface area of the target. The resonantly pumped transition can only be seen from target regions where the X-ray pump was at a sufficiently high intensity, whereas K^1L^8 can be produced with any stray X-ray photon outside the hottest target region as well. Due to slight jitter in the XFEL wavelength, the pump energy may have been high enough to directly ionise core-hole electrons from the Mg^{3+} state. It is not a concern, because the transition of interest lies 4 charge states away.

The spectrum also proves that radiative excitation is an efficient mechanism to create a population inversion of a chosen state. There is no other efficient mechanism to create K^1L^4 ions due to the XFEL photon energy being below the ionisation thresholds.

In addition to observing ionisation, a resonant pump also reveals the recombination dynamics towards lower charge states. Whereas the above-edge data is produced over transient plasma conditions, the resonant pump reduces the spread in plasma conditions. When the 7^+ core-hole excited state is created, the recombinations and ionisations start off in the same conditions. The second collisional and recombination interactions (line V and line IX) are still produced in a hotter and denser environment than the pumped line, but the transient spread is cut in half.

Despite having a strongly transient plasma, the resonant pump makes it possible to isolate a set of temperature-density conditions in which the measured collisional interactions take place. Having a narrower spread in plasma conditions benefits the data analysis, and improves the accuracy of the inferred cross-sections.

4.5 CCFLY atomic kinetics modelling

For the resonant and non-resonant datasets, a full atomic kinetics calculation is required to interpret the data beyond a simple order of magnitude estimate of the collisional rates. The emission spectrum is composed by ionic charge state configurations that evolve in transient plasma conditions, with varying degrees of continuum lowering. CCFLY, a collisional-radiative code designed for X-ray/plasma interactions, is our tool to model the plasma evolution.

Major ingredients to correctly model the WDM evolution are knowledge of the atomic level structure including continuum lowering, the energy density, encoding the XFEL beam parameters and finally, the collisional cross-sections. When we compute an emission spectrum with CCFLY, the cross-section can be used as an optimisation parameter to match the experimentally measured spectrum to calculations. The code can be used to compute an emission spectrum only in the thermal electron mode: with the distribution function constrained to a Maxwellian profile. This is a limitation in the code that will be addressed in the future, but at the time of writing it still exists. Secondly, the computational time of a calculation in the non-thermal mode is a few days, compared to a few seconds for the thermal mode.

Previous experimental work on creating solid-density plasmas [22], X-ray absorption measurements [17], continuum lowering [38], XFEL focal spot characterisation [116], resonant K-α spectroscopy [37] and K-shell opacities [28] all conglomerates into this project on collisional measurements. A reaction cross-section can only be inferred when the WDM sample is created in a reproducible, well-understood manner that can be modelled with the collisional cross-section as the only relevant unknown.

The work on absorption measurements is relevant for determining the energy density in the sample. Owing to the saturable absorption experiments presented by Rackstraw *et al.* the energy density in the focal region can be constrained [17]. The energy density is an input to simulations, and also puts a constraint on the accessible range of charge state distributions and plasma conditions. These conditions are subsequently the input for the IPD model that was benchmarked by Ciricosta *et al.* on LCLS-created solid-density plasmas [32]. Without addressing the questions about which IPD model is universally valid, there is IPD data available from samples in similar conditions. Having the correct IPD is essential, as the ionisation thresholds can be reduced by up to 50% for L-shell electrons in a dense environment.

Finally, the intensity profile of the XFEL in the focal region needs to be accounted for. The center of the focal spot sees a much higher intensity than the edges and will attain much higher temperatures and densities than other regions. CCFLY and SCFLY are both zero-dimensional codes that have no intrinsic way to account for target geometries. A method to overcome this problem is a focal-scan method, where the beam profile in focus is recorded with imprint targets [116]. This reveals the intensity distribution across the target surface. The target can then be divided in different intensity zones. The total emission spectrum is then a weighted sum of all intensity zones, the weights being given by the surface area S of each zone. A focal spot profile is depicted in Fig. 4.7. The intensity is plotted against the enclosed surface area in Fig. 4.7. For example, the enclosed area is zero in the center of the focal spot. On the outside perimeter of the focal area, the enclosed surface area is high but the intensity is low. The results of atomic-kinetics calculations are averaged through a weighted sum with weights given by the product of the intensity and enclosed surface area. This averaging process can be applied to any simulation output that has spatial variation due to the varying intensity: the spectra, populations, transition rates, temperature or density.

The spot profile is parameterised in the form of a super-Gaussian profile:

$$F(S) = F_1 \exp\left(-\left(\frac{S}{A_1}\right)^n\right) + F_2 \exp\left(-\left(\frac{S}{A_2}\right)^m\right), \tag{4.9}$$

with constants $\{F_1, F_2, A_1, A_2, n, m\}$ that are measured from spot imprints before the experiment. Eq. 4.9 describes the fluence scan plotted in Fig. 4.7. It can be sampled at any desired point and generally a set of 10-50 simulations is sufficient to obtain an accurate representation of the focal area of the XFEL. The calculations presented are a weighted sum of 20 simulations to represent the focal spot.

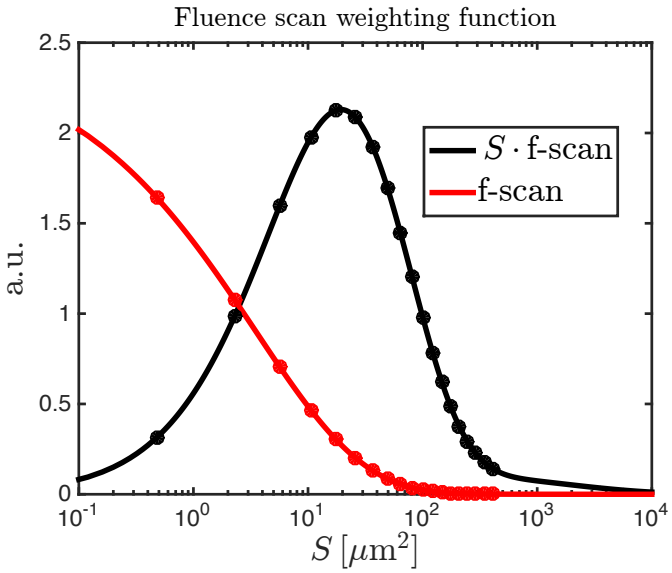

Figure 4.7: The measured intensity profile for an X-ray pulse from LCLS as a function of enclosed surface area S. In circular focal spots, the enclosed area is proportional to the squared distance from the focal spot center. The surface-weighted intensity has a distinct maximum away from the optical axis.

All the building blocks are present to model the experiments shown in Subsections 4.4.3 and 4.4.2. For the three collisional models described in Eqs. 4.2, 4.3 and 4.5, this results in emission spectra given in Fig. 4.8.

In the convention used here, the element symbols denote the number of electrons present in each ion state. It can be seen from the calculated emission spectra that the collisional rates predicted by the Lotz and BC models are far too low. When the core-hole excited ions with configuration K^1L^4 are created, the ionisation and recombination rates are insufficient to populate neighbouring charge states to levels observed experimentally. The line intensity ratios between the resonant transition line and its neighbours are so far off that they indicate we overlooked a strong density effect.

The CAM model performs better, but the experimental spectrum is only retrieved by manually scaling up the cross-section by 50%. This causes an inconsistency with data at low densities, but gives a good measure of what the collisional cross-section should be in the dense regime. The observations so far call for constructing a model with a stronger density scaling.

Retrieving the emission spectrum from simulations requires computing the correct evolution of the ion states and the conditions they live in, so the emission spectra

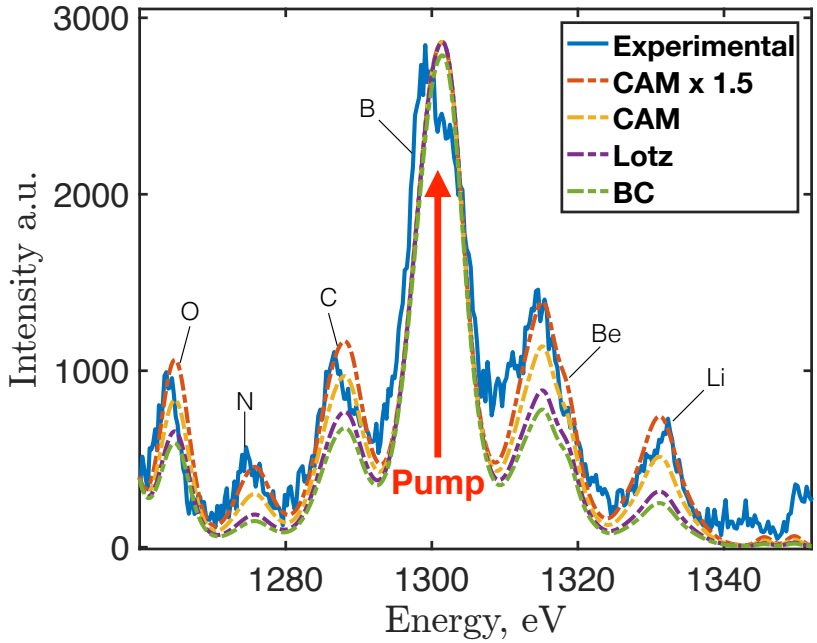

Figure 4.8: Calculated emission spectra compared to an experimental spectrum for resonantly-pumped magnesium. The pump energy is centered around 1304 eV. Collisional ionisation is modelled with the Lotz, Burgess-Chidichimo and Clark-Abdallah-Mann cross-sections..

can take the role of the cost function for testing each collisional model. If any aspect of the time evolution is modelled incorrectly, the spectra should show some level of disagreement. The only problem observed so far, seems to be that the collisional frequencies are not high enough. The shape of the calculated spectra is in good agreement with the data, giving confidence that the atomic models are are correct in the range of conditions they're being applied in.

4.6 Inferred cross-section model

Before discussing the temperature and density conditions of the measurements, as well as the non-resonantly pumped spectra, it is useful to formulate a more appropriate collisional cross-section model. It can already be seen from the spectra in Fig. 4.8 that continuing with the same cross-section models is futile as the line intensity ratios cannot be matched in the K-α emission spectrum. The spectra do give insight into the magnitude of the collisional frequencies. It is a reasonable estimate to state that the cross-sections are 50% larger than predicted by the CAM model and by estimating the temperature and density from prior knowledge, we can infer a cross-section. The

challenge that remains is to construct a model that produces this cross-section.

4.6.1 Cross-section formulation

The model introduced here, referred to as the Clark and Fontes (CF) cross-section in what follows, uses a functional form similar to the CAM model but applies the IPD scaling from the cross-section model introduced by Fontes, Sampson and Zhang [117]. This form also occured in a similar form in the BigBart code [118, 119], but did not have the correct coefficients to be in agreement with cross-sections both in the atomic limit and with the magnesium data presented here.

Both problems can be addressed at once, by making the cross-section consistent with impact ionisation data in the dilute limit first[2]. The correct scaling for high-density cross-sections then naturally follows and it can be shown that this cross-section does allow the spectra to be reproduced with CCFLY.

The cross-section form is given by:

$$\sigma_{\mathrm{CF}}(E) = \frac{\pi a_0^2}{(P_j/I_H)^2} \sum_j \frac{\zeta_j}{R_0^4} \frac{P_j^{'}}{E} \left[\left(c_1 + \frac{c_2 + c_3 \cdot l}{n} \right) \log\left(E/P_j^{'} \right) \right. \tag{4.10}$$
$$+ R_0 \left(c_4 + \frac{c_5 + c_6 \cdot l}{n} \right) \left(1 - \frac{P_j^{'}}{E} \right)$$
$$\left. + R_0^{r_n} \left(c_7 + \frac{c_8 + c_9 \cdot l}{n} \right) \left(1 - \frac{P_j^{'}}{E} \right)^2 \right].$$

As before, n and l denote the principal and azimuthal quantum number, respectively. The exponent $r_n = \{2.20, 1.90, 1.73, 1.65, 1.60, 1.56, 1.54, 1.52\}$ was determined by Fontes *et al.* for $n = \{1\text{-}7, \geq 8\}$ [117]. Special attention should be paid to the ionisation potential in Eq. 4.10. $P_j^{'}$ is the potential corrected by IPD and P_j is the potential for an isolated atom. The ratio of the IPD corrected- and atomic potential, R_0, equals $P_j^{'}/P_j$. In the atomic limit, $P_j^{'} = P_j$ and $R_0 = 1$. The coefficients $\{c_1, \ldots, c_9\}$ are to be determined with data in the dilute limit and this will be done now by examining the atomic cross-sections around the threshold potential.

In the limit $E/P_j^{'} \to 1$, where the kinetic energy of an incoming electron is only slightly above the ionisation threshold, it is desirable that all cross-section models give the same result for an isolated atom. Defining $E = 1 + x$ for $0 < x \ll 1$, the CF

[2]To within an uncertainty margin, as the atomic cross-sections differ by up to 50% amongst each other.

cross-section near threshold can be evaluated as:

$$\begin{aligned}\lim_{x\to 0}\sigma_{CF} = \lim_{x\to 0}\Big[&C_{1,2,3}\log(1+x)\\ &+ C_{4,5,6}\left(1-\frac{1}{1+x}\right)\\ &+ C_{7,8,9}\left(1-\frac{1}{1+x}\right)^2\Big]\\ &= C_{1,2,3}\left(\varepsilon-\frac{1}{2}x^2\right)+C_{4,5,6}\left(\varepsilon-x^2\right)+C_{7,8,9}\cdot x^2+\mathcal{O}\left(x^3\right),\end{aligned}$$

where the convention below has been used to compress the coefficients:

$$C_{i,i+1,i+2} = c_i + \frac{c_{i+1}+g\cdot c_{i+2}}{n}. \tag{4.11}$$

Doing the same for the BC cross-section, we obtain:

$$\begin{aligned}\lim_{x\to 0}\sigma_{BC} &= C_{BC}\lim_{x\to 0}\left(\log(1+x)^{\beta/(1+x)}\log(1+x)\right) \\ &= C_{BC}\left(x-\frac{1}{2}x^2\right)+\mathcal{O}\left(x^3\right)+\mathcal{O}\left(x\beta\right).\end{aligned} \tag{4.12}$$

Omitting the terms of $\mathcal{O}\left(x^3\right)$ and above, or mixed terms of $\mathcal{O}\left(x\beta\right)$, both cross-sections have a linear and quadratic contribution in the near-threshold regime.

By imposing that the CF and BC models are consistent near the threshold region for an isolated atom, the coefficients $\{c_1,\ldots,c_9\}$ can be determined by rescaling the groups $C_{i,i+1,i+2}$ by constants. This way, the relative scaling w.r.t. principal and azimuthal quantum number is preserved, but the overall magnitude is adjusted to the experimental data. With this scaling in mind, the coefficients can now be set to $\{c_1\cdots c_9\} = \{1.0633, 0.6895, -0.4284, 1.6925, -1.7140, 2.2244, -0.5020, 0.5961, -0.1629\}$. Once again, they are formulated as charge- and material-independent fitting constants. Any uncertainty present in the cross-section models at low densities translates into uncertainty in the CF cross-section.

4.6.2 Emission spectrum benchmark

Computing the emission spectrum with the CF model, the line intensity ratios are matched for all collisionally-populated states. This can be seen in Fig. 4.9 where all the tested cross-section models are plotted.

The agreement between the experimental and calculated spectrum with the CF cross-section indicates that this model correctly captures the ion population dynamics

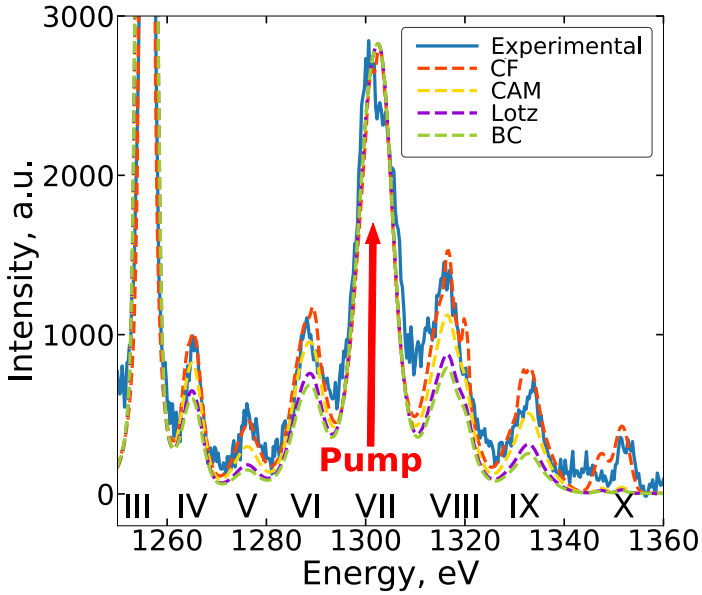

Figure 4.9: Experimental and simulated (with CF, CAM, Lotz and BC model) K_α emission spectrum resulting from resonantly driving the $K^2L^3 \rightarrow K^1L^4$ transition centered around 1304 eV [30]. After excitation the states relax through collisional ionisation (up in charge) and three-body recombination (down in charge). The numerals below each emission line denote the charge state of the emitting ion, III thus indicating the cold K_α line. ©2018 American Physical Society.

and electron conditions. The rates are also sufficiently high to populate neighbouring charge states. The cross-section itself can be inferred from the knowledge of the IPD, energy density and rate that has been obtained so far. The cross-sections are compared in Fig. 4.10.

Cross-sections in the atomic limit can differ by several tens of percents for Mg^{7+}, an uncertainty range that is not uncommon in WDM physics. The parametric models are on the upper part of the range, with the Lotz and CAM cross-sections being the furthest outliers. By construction, the CF model nearly overlaps with the BC cross-section.

When the density is increased, the ionisation threshold for the K^1L^4 state shifts is reduced by nearly 100 eV and the cross-section magnitude is increased by several factors. It is now when the differences between the parametric models are amplified. Although the CAM model scales up more quickly, it attains its maximum at a similar magnitude as the Lotz and BC cross-section. The CF model that was adjusted to match isolated-atom data naturally scales up to conditions in which the IPD changes the ionisation threshold by approximately 30%.

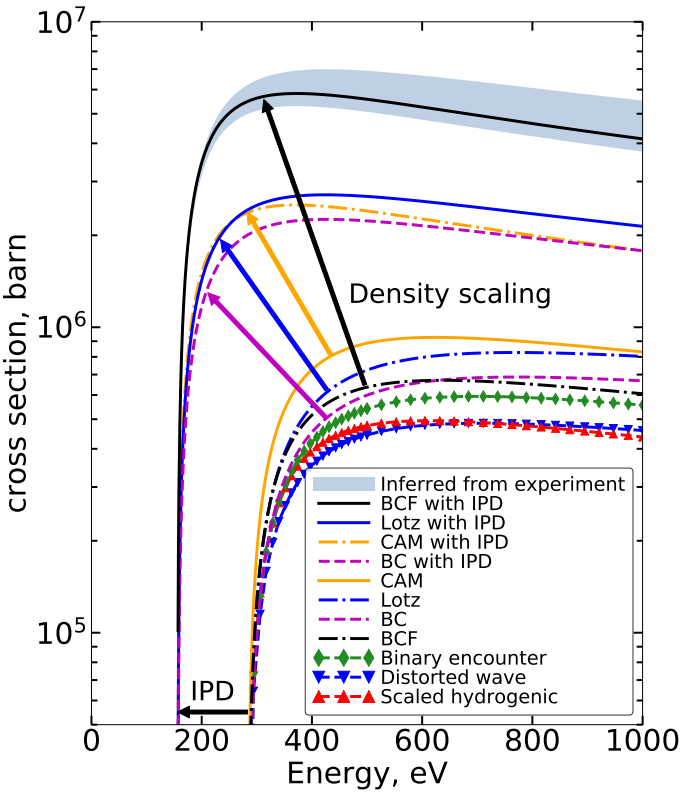

Figure 4.10: Collisional ionisation cross-section for the K^1L^4 (7^+) Mg ion [30]. Theoretical and semi-empirical models predict similar cross-sections in the atomic limit. Accounting for increasing density via IPD lowers the threshold and raises the cross-section; here the CF model differs significantly from the Lotz and BC models. The range of cross-sections consistent with our experimental results shown in Fig. 4.9 lies within the shaded band. ©2018 American Physical Society.

The IPD, temperature and density can all be modelled with CCFLY and it is important to do this correctly in order to reproduce an emission spectrum. The next Subsection will focus on the plasma conditions around the time of emission, as these play a vital role in interpreting the data.

4.6.3 Plasma conditions

The experiment with the non-resonant X-ray pump is designed to constrain the plasma conditions around the time of emission. This allows us to infer a cross-section for the CI rate, as the continuum lowering, conditions, and Auger lifetimes are all known and somewhat constant for the limited time window of interest. Note that the ionisation rate does not depend on these model choices and other inputs. If the choice for for instance the IPD model was different, the inferred cross-section would

need to be changed as well in a way that the same collisional rate is observed.

The non-LTE CCFLY calculations give insight into the temperature and density evolution so the initial hypothesis on well-constrained plasma conditions can be tested. Extracting the ion population of the emitting state K^1L^4 from the same calculations that produce the emission spectrum in Fig. 4.9 together with the electron temperature and density they occur in, we obtain the range of conditions in which the emission spectrum is produced.

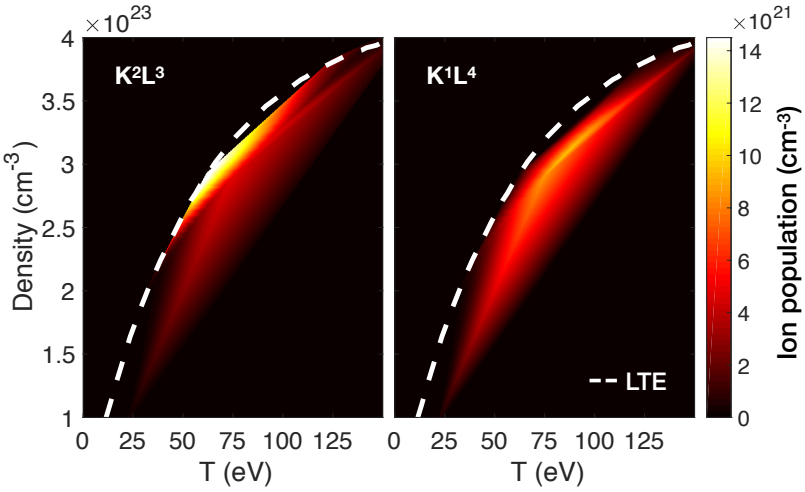

Figure 4.11: Simulated evolution of the pumped K^2L^3 (left) and K^1L^4 (right) populations in temperature-density space [30]. Charge state populations are obtained from CCFLY simulations using the CF model (Eq. 4.10) that match the experimental conditions and are binned in a 2D temperature-density histogram across all points in time and space. Both populations peak near the LTE conditions, represented by the white dotted curve. ©2018 American Physical Society.

The results of Fig. 4.11 are made for the resonantly-pumped dataset. The ground state of the pumped transition (K^2L^3) is seen to be present in conditions close to LTE, indicating that the ground state is well-equilibrated by collisional processes in the plasma. The core-excited state (K^1L^4) retains much of this characteristic but is shifted to slightly higher temperatures, as it takes some time to produce via photo-pumping the ground state, during which the system heats. The importance of this observation is that there exists a narrow temporal and spatial window of emission for each charge state. Equivalently, there is a narrow band of temperature-density conditions in which each charge state is found. The pumped state, 7^+ is present predominantly at temperatures at 75 eV and at electron densities around $3{\times}10^{23}$ cm^{-3}. Despite the rapid transient evolution of the plasma, the range of temperatures and densities associated with our measurement is small.

A comparison of the population magnitude shows that the resonant pump is efficient, exciting roughly half of the ground state ions. This explains the line intensity on-resonance, which is good for the signal to noise ratio.

4.7 Non-equilibrium electron behaviour

In the discussion about collisional rates and plasma conditions, the electron temperature plays a central role. Formally, it would be more appropriate to speak about a distribution until it has been demonstrated that the distribution is close to a Maxwellian. With the Fokker-Planck scheme discussed in Chapter 3, it can be investigated whether this is indeed the case.

With the newly constructed electron module, the author ran a CCFLY simulation with the following inputs summarised in Table 4.1. It is a calculation for magnesium that uses the cross-section model presented earlier in Section 4.6. All other parameters are similar to the simulations of the dataset of the resonantly-pumped target. Rather

CCFLY settings	
Parameter	Value
Material	magnesium
FWHM pulse length	60 fs
Central photon energy	1304 eV
Peak intensity	$8.6\times10^{16}\,\mathrm{Wcm}^{-2}$
Bandwidth	0.4%
Collisional model	Clark-Fontes
Initial condition	Room temperature solid density, temperature
Runtime	90 fs
# energy grid points	60

Table 4.1: The simulation settings used in the non-thermal electron calculation in CCFLY.

than averaging over 20 simulations to model the focal spot profile, a single calculation is examined here with the peak laser intensity set to 80% of the peak intensity in the experiment ($8.6 \times 10^{16}\,\mathrm{Wcm}^{-2}$). This is due to the runtime of approximately two weeks per simulation for a 150 fs runtime. The emitting target zone that is irradiated at 80% of the peak intensity is most representative for the emitted spectrum. The evolution of the sample is as expected; it heats up and undergoes atomic transitions. The distribution function of the electrons is plotted in Fig. 4.12 for times between 0

and 90 fs after the laser begins to irradiate the target. This Chapter has been written

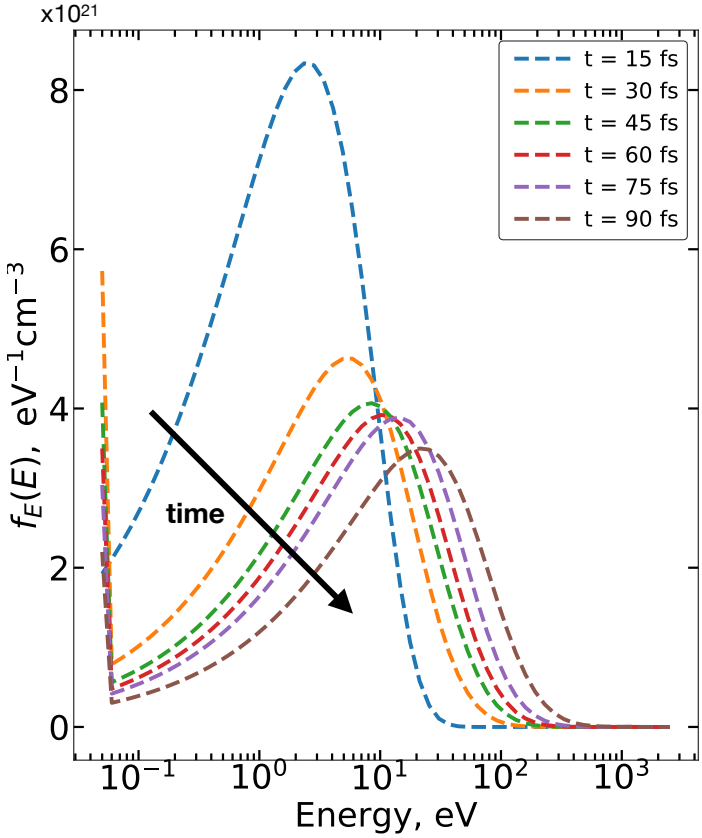

Figure 4.12: Simulated electron distributions of XFEL-irradiated magnesium. The sample heats up during irradiation, and the distribution maintains a near-Maxwellian profile.

before much of the work on the Fokker-Planck equation had been completed. The assumption of having a thermal electron distribution is relatively accurate and the author would like to include some preliminary work that was used to validate this assumption. The key result was that the distribution appears near-thermal at all times, and not much accuracy is lost by adopting its analytical form into the rate equations.

Despite some artefacts, Fig. 4.12 shows that there are no persisting high-energy electrons that distort the distribution into a non-Maxwellian profile. This finding is the key justification for using a Maxwellian-constrained distribution function in this chapter. Magnesium and other low-Z materials can be modelled well with a Maxwellian distribution function, a finding that is supported by calculations done with the BigBart code [34, 119]. The authors of the BigBart code also participated

in the data analysis published in the experiment with the resonant XFEL pump that was presented earlier.

Other benefits, though not a justification, for using an imposed Maxwellian profile are that the runtime of calculations is multiple orders of magnitude longer when the full Fokker-Planck calculation is used. Evaluating the collision operator Eq. 3.71 adds significantly to the run time and extends them from minutes to weeks. The code is currently also not yet equipped to compute emission spectra, which is the key part of matching calculations to the experiment. Also this will change in due course, when the code modules are being fully integrated with the spectral calculations.

4.8 Non-resonant benchmarks

Having obtained a cross-section model obtained from the resonantly-pumped emission spectra, it would be interesting to see how this model performs on other datasets. There is data available for non-resonantly pumped magnesium for a few different photon energies, and this section will demonstrate the spectra and conditions associated for two different a non-resonant pump energies that ionise up to different ionisation levels. The difference is that rather than exciting a K-shell electron to the L-shell, the pump ionises them into the continuum. The conditions during emission are more transient as there is less control over when an emitting charge state is produced, as we will see.

4.8.1 Photo-pump at 1364 eV

The first dataset was produced with an XFEL photon energy of 1364 eV. This is sufficient to photo-ionise magnesium atoms with charge states up to 5^+, which causes a bright emission spectrum up to line V. Any lines at higher energies have been populated by collisional events of the core-hole ionised states. The emission spectrum produced for this experiment, averaged over 100 laser shots, is plotted in Fig. 4.13.

Line III, the cold K-α line, is not given much importance as the majority of the emitting region remains cold and does not evolve. The peak is cropped out for visualisation reasons alone, and lies a factor of 10 above the intensity of line IV. The relative line ratios between line IV and V approximately match between simulation and experiment. The lack of height is compensated by a slight difference in line width, thereby reaching a comparable line intensity. The core-hole ionised populations are modelled in the same way as the experimental data shows.

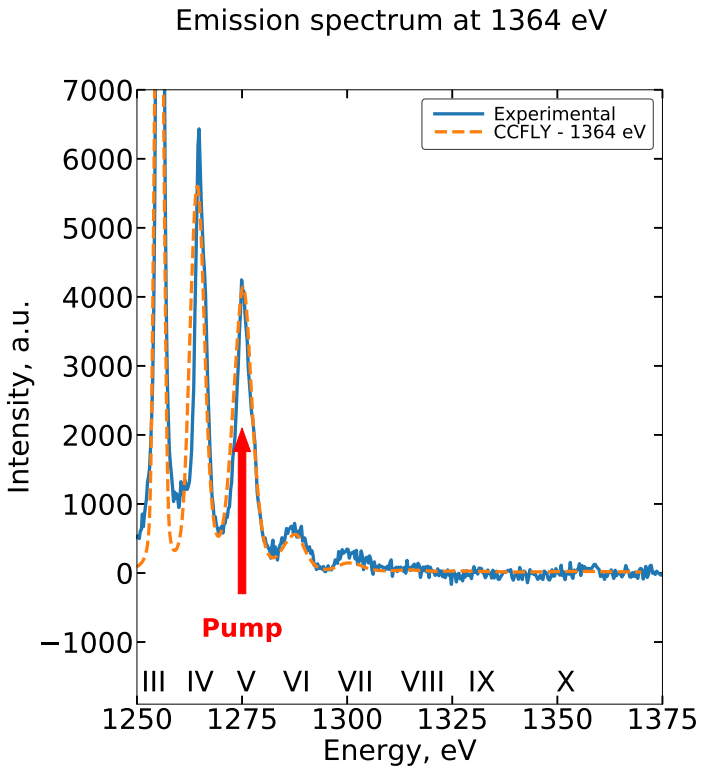

Figure 4.13: An emission spectrum of non-resonantly pumped magnesium at a photon energy of 1364 eV. This ionises up to a charge of 5, with any higher charge states created through collisional ionisation of the core-hole ionised states.

The collisional process that creates core-hole ionised Mg^{6+} with super-configuration K^1L^5 can be modelled with the same cross-section as the resonant case, Eq. 4.10. The magnitude of line VII is larger in the experiment, indicating that something has been overlooked in the simulations. This can be a drift in plasma conditions, as the system evolves over a broader range of conditions during the time of emission. To say more about the plasma conditions, let us examine what they are for the ground state and core-hole ionised populations of Mg^{5+} in Fig. 4.14.

Both states are formed earlier than desired at temperatures below the temperatures associated with LTE. This is the effect of the powerful X-ray pump early in the interaction process, as charge state 5^+ is a relatively low ionisation degree compared to what can be achieved with XFEL capabilities. The laser energy is deposited so quickly that for this state, the system has not had enough time to redistribute this energy through Auger decay and subsequent collisional processes to establish an LTE temperature and density.

Besides creating the ion states in conditions further removed from LTE, the spread

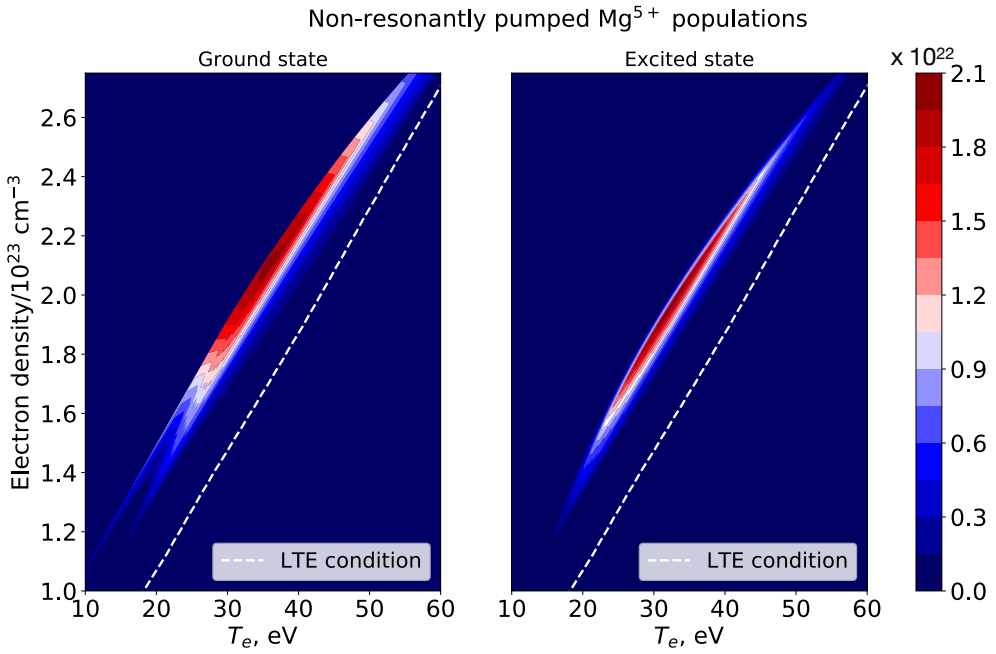

Figure 4.14: Plasma conditions associated at the time when Mg^{5+} states are created in photo-pumped magnesium. It can be seen that the creation of both the ground- and excited state are driven by the X-ray pump and not predominantly by collisions.

in conditions is also larger than for the resonant case. The typical density that both states are found in lies around $2.1\times10^{23}\,\mathrm{cm}^{-3}$ with 15% spread in both directions.

The spread in conditions can be explained by the observation that the creation of ions with super-configuration K^1L^6 can follow many pathways. There can be any combination of photo-induced and collisional ionisation on all charge states below the pump that leads up to the pumped charge state. Any expansion in the number of reaction channels increases the time window of emission, thereby leading to a wider window in temperature-density conditions.

4.8.2 Photo-pump at 1440 eV

A similar case as for 1364 eV can be examined for an X-ray pump energy centered around 1440 eV. This pump is tuned to photo-ionise magnesium ions up to charge state 7^+, the same state used for the resonant case and therefore the most interesting dataset to compare. Contrary to the resonant case, only ionisation effects can be detected. Any recombination events of the photo-pumped state blur in with the many reactions taking place in states that can be photo-pumped. This would appear to make a photo-pump above the ionisation edge to be a worse way of conducting an

experiment. Perhaps it is, when there is little prior knowledge of the cross-section, but it does provide a way to examine the IPD scaling of said cross-section across a range of plasma conditions. After all, the emitting state exists in a broader range of conditions.

The calculated and measured emission spectrum are plotted in Fig. 4.15.

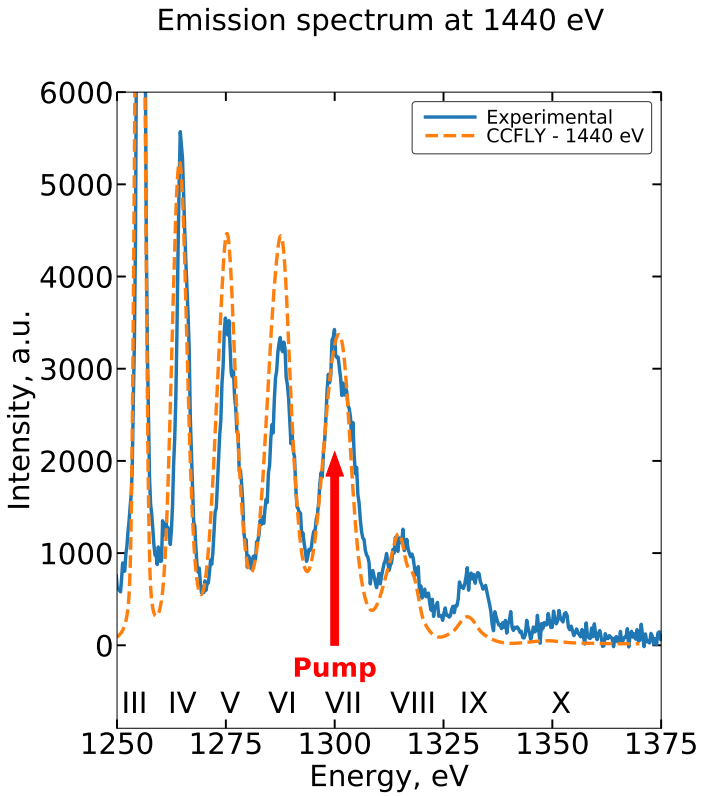

Figure 4.15: An emission spectrum of non-resonantly pumped magnesium at a photon energy of 1440 eV. This ionises up to a charge of 7, with any higher charge states created through collisional ionisation of the core-hole ionised states.

The spectra are scaled to match each other's intensity at line VII. There are $\sim 25\%$ discrepancies in the line intensities of line V and VI below the pump, indicating that the evolution of the system towards the pumped charge state is different from what the models would predict. This could be caused by collisional transitions between configuration K^1L^6, K^1L^5 and K^1L^4 happening at higher rates than expected. If this is true, then the IPD scaling reaches the correct magnitude eventually but does not scale up fast enough.

If the discrepancies cannot be explained by collisions, the differences must be caused by the photo-ionisation rates. For the resonant pump, the main criterion to be able to model the experiment is that there is an efficient pump of some kind, and

its magnitude can always be corrected for with a scalar factor. In the non-resonant case, detailed knowledge of the photo-ionisation process is required in combination with the collisional dynamics in order to model the emission lines below the ionisation edge. Furthermore, the full evolution of IPD must also be part of the calculations. If any of the three quantities is different in the experiment, it manifests itself in the intensity discrepancies observed here.

Above the ionisation edge, the emission lines are still exclusively caused by impact ionisation. The intensity ratio between lines VII and VIII are in agreement between simulation and experiment. The intensity of line IX line, the line caused by decay of charge state K^1L^2, is underestimated in simulations. This state is produced as a result of two ionisation events of the core-hole ionised state. It requires a hot, dense plasma to facilitate this process. It may be that in the simulations, the temperature-density evolution is not fast enough as compared with the experiment. Another possible cause for the discrepancy is the spatial profile of the emitting target zone. Only the hottest regions of the target can facilitate multiple collisional events in the core-hole ionised state. In this case, the method to model spot profile geometry is more prone to error as the emissivity of the target rapidly decays further away from the focal point of the X-ray pump.

Finally, the conditions around the time of emission are displayed in Fig. 4.16.

Compared to Mg^{5+}, the ground- and excited-state populations live in conditions much closer to LTE. The associated temperatures and densities are higher as expected. This state is created later in time than the previous case, and due to the ion populations living in conditions closer to LTE, the conclusion can be drawn that they are predominantly created by collisional events. The creation of these charge states is not driven by the laser as much as was the case for the Mg^{5+} populations.

The spread in temperature and density is still present, and larger than it was for the resonant case. It still holds that for the higher charge state examined here, the ion populations are closer to LTE.

4.9 Pump-probe proposal

The dataset of the resonantly-pumped target was produced with a single shot of X-rays. The XFEL acted simultaneously as the pump and probe, driving the heating process and producing a useful signal for the diagnostics. Provided there is a mechanism to heat a material, for instance an optical or another X-ray laser, an XFEL could in principle also act as a probe. This section will showcase some calculations as to

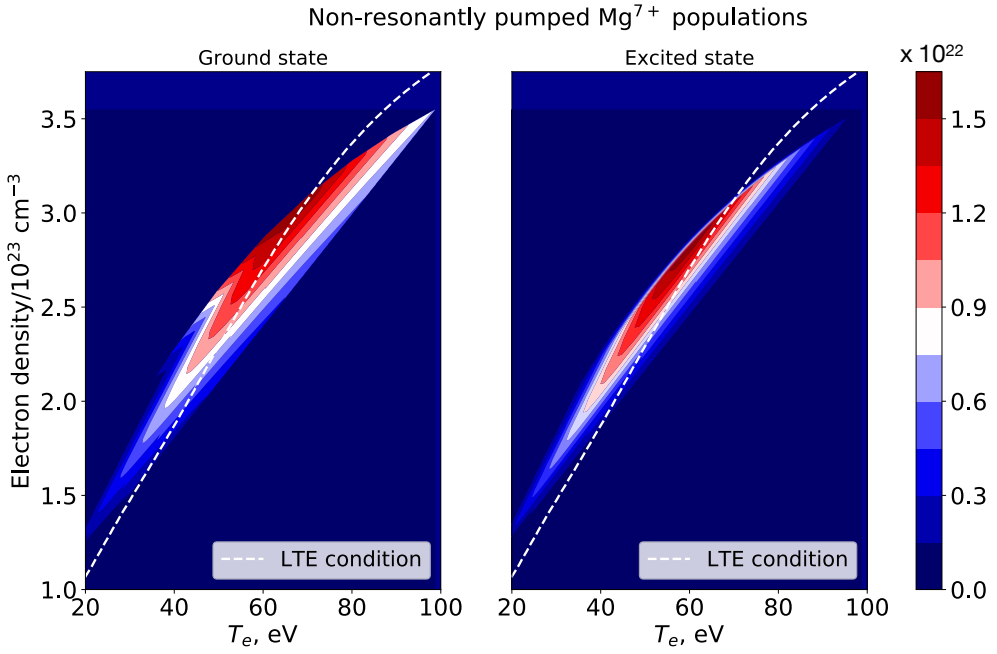

Figure 4.16: Plasma conditions associated at the time when Mg^{7+} states are created in photo-pumped magnesium. It can be seen that the creation of both the ground- and excited state are driven by the X-ray pump but reside closer to LTE conditions.

what the emission spectrum would be if a sample was brought to specific charge state at its LTE temperature, and then struck with a weak resonant probe that excites a K-shell electron to the L-shell. The ionisation level determines the electron density through the quasi-neutrality constraint, and the LTE temperature follows from the Saha equation Eq. 1.4.

The X-ray probe is set to 1% of the peak intensity, enough to produce a detectable signal but not strong enough to alter the temperature. The resulting spectra for these calculations are plotted in Fig. 4.17.

The spectra have some resemblance of the resonantly-pumped data in Fig. 4.9 as the brightest emission line is still centered on the probe energy. For each state, some emission lines around the probe can be observed and as before, lines at lower energies are caused by recombinaton and lines at higher energies follow from ionisation events in the excited state ions.

A resonant X-ray probe is so efficient in producing population inversion when an ion state is present, that it can be used to probe the existence of a population at a specific point in time by applying a variable pump-probe delay. Probing for a state with a variable time delay, the time- and spectrally integrated signal becomes a measure of the ion population at a point in time. It is therefore a possibility to measure

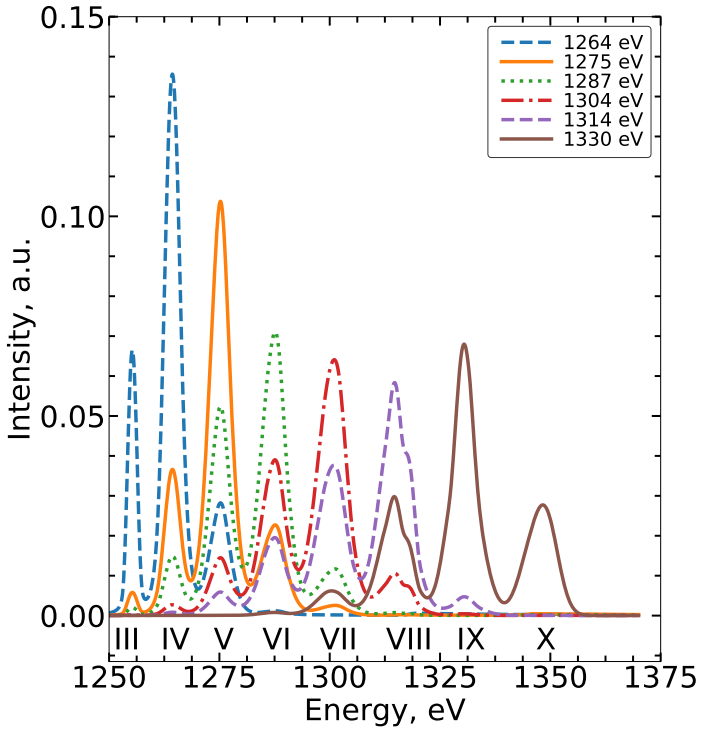

Figure 4.17: Simulated pump-probe experiments with a resonant probe on solid-density magnesium for charge states $3^+ - 9^+$. The material is brought to its LTE temperature with the density determined by the ionisation, before being probed with a resonantly-tuned XFEL.

the time-resolved charge state populations through time-integrated spectroscopy if a pump-probe system is available.

An interesting feature occurs in the spectrum probed at lines VI, VII and VIII, the cases that would be expected to match the experimental dataset. Rather than observing symmetric spectra, the emission lines created after recombination events (to the left) are brighter than the lines caused by ionisation. On closer inspection, it turned out that the electron temperature of these calculations was initialised slightly below the LTE temperature. This was not originally intended but reveals behaviour that adds diagnostic capabilities to this technique.

Because the temperature was too low to be in LTE, some way must be found to either increase the temperature or lower the density in order to re-establish LTE. Collisional recombination is the atomic process that achieves both these things simultaneously, so the system favoured recombination over ionisation, causing the emission spectrum to skew towards lower energies. This natural tendency towards equilibrium makes a pump-probe scheme a tool to obtain time-resolved measurements of the

Table 4.2: Simulation settings of the temperature scan in pump-probe Mg spectra.

Parameter	**value/unit**
Material	magnesium
FWHM pulse length	20 fs
Central photon energy	1304 eV
Peak intensity	$2.0\times10^{15}\,\mathrm{Wcm}^{-2}$
Bandwidth	0.4%
Collisional model	Clark-Fontes
Initial charge state	7^+, K^2L3
Electron density	$3.0\times10^{23}\,\mathrm{cm}^{-3}$
Runtime	150 fs
Temperature	50-105 eV
Focal scan # grid points	10

temperature and density, again through time-integrated spectroscopy.

If the population exists in LTE when it is probed, the spectrum should be symmetric after accounting for the emissivity of each excited state. The direction and degree of skewing are a measure of the temperature and density. This principle has been tested by running pump-probe CCFLY calculations with a short, weak X-ray pulse. The set of fixed parameters is summarised in Table 4.2, with a varying temperature. At a density determined by the charge state, the temperature dictates whether the ion populations live in LTE conditions or not and whether the system would favour ionisation or recombination in order to equilibrate. The X-ray pulse acts as a probe only, being bright enough to produce an emission spectrum but not containing enough energy to heat the target. For a range of electron temperatures between 50 and 105 eV, the emission spectrum was computed and plotted in Fig. 4.18 for temperature steps of 10 eV. All calculations are initialised for a magnesium system with a mean charge $\langle z\rangle = 7$ and an electron density $n_e = \langle z\rangle n_i = 3.0\times10^{23}\,\mathrm{cm}^{-3}$, for a range of temperatures. Depending on whether the temperature is below or above the corresponding LTE temperature at this density, the core-hole excited states experience a different ratio of ionisation and recombination events. A system that is too cold to be in LTE tends to favour recombination, as this lowers the density and increases the temperature. A system that is too hot can equilibrate itself with a positive ionisation balance, as this does the opposite.

As the system naturally equilibrates, the ratio of recombination-produced lines (below the probe energy) compared with ionisation-produced lines (above the probe energy) is a measure of the electron temperature. For a probe photon energy of $h\nu_p = 1304\,\mathrm{eV}$, the ratio $R(T)$ of integrated spectra below and above the probe

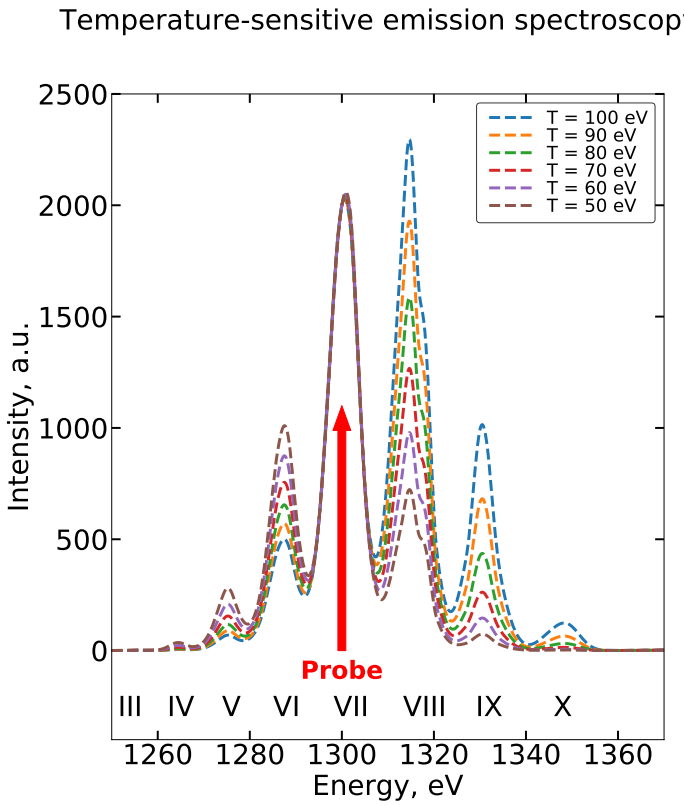

Figure 4.18: Simulated pump-probe spectra produced at different electron temperatures. A 7^+ Mg system is resonantly pumped at 1304 eV. Depending on whether the temperature is above or below its LTE temperature at fixed density, the system favours recombination over ionisation. This manifests itself as a skew in the spectra.

energy is defined as:

$$R(T) = \frac{\int_0^{h\nu_p} \frac{I(T,h\nu)}{h\nu}\,\mathrm{d}(h\nu)}{\int_{h\nu_p}^{\infty} \frac{I(T,h\nu)}{h\nu}\,\mathrm{d}(h\nu)}, \tag{4.13}$$

and this ratio is plotted in Fig. 4.19. This curve was computed with a temperature step size of 5 eV and appears to be almost linear across a temperature range of 50 eV. As long as the ratio of the Auger rate w.r.t. the radiative decay rate is approximately constant for all configurations that emit in the integration bounds, Eq. 4.13 describes how many probed ions underwent a recombination event as compared to an ionisation interaction. It is then irrelevant whether any, or multiple secondary collisions followed as ultimately, the state with a core-hole vacancy will decay and emit one photon. The factor $h\nu$ corrects for variations in the photon energy. The ratio of the integrated spectra above and below the resonant probe increases monotonically with electron temperature, making it a suitable probe. A calibration can be inferred from these calculations, or it can be used as a relative temperature measurement.

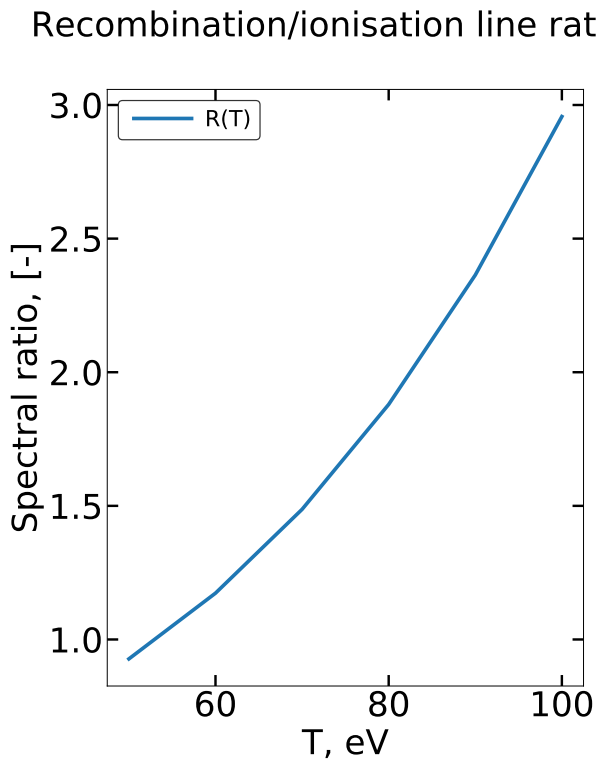

Figure 4.19: The ratio of recombination-produced against ionisation-produced spectral lines in calculated pump-probe spectra at different temperatures according to Eq. 4.13.

Calibrations can in principle also be derived by decomposing the emission spectra into a charge-resolved spectrum and correcting each line intensity for the core-hole lifetimes and photon energy, according to Eq. 4.8. This way, the time-integrated populations that produced each emission line can be computed. With knowledge of the populations, a temperature can be inferred by considering the detailed balance relations Eq. 3.52 between collisional ionisation and recombination. A derived calibration requires more knowledge about the state of the electron distribution and IPD.

Rather than fixing the density and varying the temperature, there is no objection to exchanging these variables and scanning over the density. The system will still attempt to equilibrate, leading to the same behaviour.

The experiment benefits from using a pulse length as short as possible, as it increases the temporal resolution of the temperature measurement. Furthermore, it is essential that there is uniquely identifiable bound-bound transition that can be associated with a same charge state across a range of conditions and does not overlap with any other spectral range of interest. This may not be as challenging for a two-

shell atom such as magnesium, but may pose more difficulty with heavier atoms that have 3 or 4 bound shells. Use of a resonant probe ensures more stability of the probe energy across a range of conditions. A bound-free probe would need to be adjusted for IPD, opening the door to an IPD measurement when the temperature and density are verified through a bound-bound probe.

Understanding the collisional interactions, we can infer a time-resolved temperature. Vice versa, if we know the temperature evolution, we can also conduct measurements on collisional rates at different temperatures without experiencing the drawbacks of heavily transient conditions.

Another possibility of this proposed setup, is to verify the IPD scaling of the cross-section introduced in Section 4.6. With single-shot data, the model can only be put to the test in conditions that the probed state lives in. The emitting charge state and the conditions it lives in cannot be tuned independently with a single shot in any trivial way. Data from the scaling across the density range that WDM evolves in could be used to refine the scaling dynamics further. The discrepancies between calculated and measured emision spectra for the non-resonantly pumped magnesium, with samples that emit during more transient conditions, indicate that it can be valuable to scan the scaling on a more refined density grid.

4.10 Conclusions

Collisional ionisation and recombination processes are some of the key processes that occur within dense plasmas. They are responsible for governing the charge state distribution, the redistribution of thermal and electrostatic potential energy in the plasma system and even influence transport and thermodynamic properties. This chapter discusses some early and more recent experimental methods to measure and parametrise collisional rates through cross-section models.

Collisional rates could be measured long before the advent of X-ray free-electron lasers, but only up to electron densities up to $10^{17}\,\mathrm{cm}^{-3}$. In this regime, the electrons are weakly interacting and collisions can be described as binary events. Cross-sections to model the probability of ionisation events occurring, can be simply inferred from the particle densities and ionisation rates.

In a hot dense system with electron densities beyond solid density, this behaviour changes fundamentally and the electrons are strongly coupled. The collisional rates in dense conditions are found to be higher than expected. The leading causes for this are density effects such as continuum lowering which lowers the ionisation threshold, and

plasma screening, which significantly enhances the cross-section near the ionisation threshold. It is the subject of this chapter to present a cross-section model that was validated on experimental data to describe the density-dependence of the collisional rates.

The experiments discussed here use a bright burst of near-monochromatic X-rays generated at the Linac Coherent Light Source to create a solid-density plasma. Ions in a hot dense system created through this method live in conditions close to local thermodynamic equillibrium, despite experiencing a rapid evolution on the femtosecond timescale. Furthermore, the sample is optically thin, meaning that the intensity of all observed spectral lines is directly proportional to the emitting charge state population.

The X-ray laser selectively excites (resonant process) or ionises (non-resonant) a K-shell electron of a predetermined charge state. The radiative decay process is observed through emission spectroscopy. Collisional interactions can alter the electronic configuration of the core-hole state ion before its decay, leading to the creation of spectral lines that cannot be produced through any other pathway. The intensity of these lines is proportional to the collisional rates and acts as a benchmark for the cross-section models.

The author compares experimental to simulated spectra for various rate models, and concludes that the popular rate models constructed by Lotz [72] and Burgess and Chidichimo [102] underestimate the rates by a factor 2-4 for a solid-density magnesium plasma. Continuum lowering is the primary cause of this discrepancy. The cross-section model proposed by the author in Ref. [30] is consistent with widely available experimental data at densities in the range of $10^{15} - 10^{17}\,\mathrm{cm}^{-3}$, as well as at up to three times solid density in the experiments presented.

For non-resonantly pumped magnesium, there are discrepancies between the simulated and experimental spectra on lines below the pumped transition. This indicates that the population dynamics could be more complex than the way they are modelled, which may be caused by the large number of reaction channels composed of radiative and collisional transitions that produce the below-edge core-hole ionised states. Alternatively, the recombination rate may be affected by a transient differential cross-section as the range of plasma conditions, and therefore the inter-electron coupling, change during the X-ray pulse. No solution has been found yet to resolve these discrepancies.

The temperature and density conditions are broader for the non-resonantly pumped data. Emitting ion states still reside in conditions reasonably close to LTE, and more

so for the higher charge states that are created later in time. The Mg^{5+} states that are created earlier during the irradiation show the effects of being photo-pumped, as they come into existence at a temperature lower than where they would normally be expected. This is evidence that they are in part produced through radiative transitions, rather than primarily through collisions. The Mg^{7+} states live in transient conditions more closely removed from LTE, indicating they are largely created through collisional interactions before the ground state is photo-ionised.

The observed faster rates of collisional ionisation are beneficial for attaining local thermodynamic equillibrium conditions in rapidly evolving, non-equilibrium plasma systems. The higher cross-sections at high electron densities can have consequences as transport properties such as the thermal and electric conductivity. The electron distribution function remains near-Maxwellian at all times.

More efficient collisional dynamics negatively affect the ability to use X-ray free-electron lasers for coherent diffraction imaging applications, as they can further limit the timescales before the onset of observable electron damage. This can restrict the spatial resolution in imaging applications used to study non-periodic nano-scale samples, such as viruses [120] or disordered crystals [121].

Chapter 5

Conclusions

I have presented the theoretical and computational background surrounding an expansion that I made to the capabilities of our collisional-radiative code CCFLY. With the newly implemented code module it can now describe non-equilibrium ion and electron behaviour in a solid-density plasma that is subjected to a high intensity of X-rays. The code simulates the evolution of a plasma by tracking its super-configuration ion populations over time and self-consistently computes the electron distribution function. It can be used to gain insight into the ion transition dynamics, plasma conditions and optical properties.

The experimental section of this thesis describes the measurement of the collisional ionisation rates in a solid-density magnesium plasma. The experiment makes use of a powerful X-ray free electron laser both to produce and probe the sample, and obtain a spectroscopic measurement of the rate and plasma conditions. This is the first direct measurement of the ionisation rate in the strongly-coupled regime where the rates are significantly enhanced by density effects such as ionisation potential depression.

Summary

Collisional-radiative models can be applied to compute the time-evolution of dense plasmas by solving a coupled system of multi-level atomic rate equations self-consistently with a radiation field. Our research group makes extensive use of the collisional-radiative code SCFLY (Fortran-77) and its successor CCFLY (C++) in modelling and analyse experimental data that relates to physical quantities in low-Z dense plasmas: ion transition rates, the degree of ionisation potential depression and radiative properties. The code is able to deal with non-LTE behaviour in the ion populations and historically assumed that the electron distribution function has a Maxwell-Boltzmann profile at all times.

In situations in which materials are subjected to hard X-rays that produced energetic photo-electrons, the assumption of having a thermal electron distribution breaks down. Such energetic electrons need time to give off their energy through collisional interactions with other electrons and ions before they equilibrate back into the thermal bulk of the free-electron population. This process happens sufficiently quickly in low-Z plasmas irradiated with soft X-rays, and can require too much time in the hard X-ray regime to assume an instantaneous thermalisation electron model.

The electron distribution function has been generalised so that it can take on any arbitrary form on a pre-defined electron energy grid. A generalised distribution function adds additional degrees of freedom to the system and replaces existing model

parameters such as the electron temperature and density. Its time-evolution has been modelled by using the Fokker-Planck equation. This integro-differential equation contains collisional operators for all types of elastic and inelastic interactions that can occur between the electrons, ions and photons in a warm dense system. The set of inelastic operators describes the transfer of electrons between the bound and free-electron population, as well as the energy transfer between ion electrostatic potential, the radiation field and the thermal energy held by the free-electron population.

Additionally, the elastic operators describe equilibration behaviour of the distribution function. In a closed system of a constant volume, the electron distribution of a warm dense system will equilibrate to a Maxwell-Boltzmann profile. Each operator adds, removes or displaces groups of electrons in energy-space as the time-evolution of the distribution is computed. They do so while intrinsically observing the same conservation laws on energy and density as the physical processes that they represent. By constructing a conservative numerical scheme for the electron distribution and fully integrating this with the atomic-kinetics code, it implicitly contains a self-consistent density and energy calculation that is analogous to the previously-used self-consistent collisional-radiative models that relied on the assumption of having a thermal electron distribution. All ion transition rate models and methods have been validated in known conditions by imposing an analytical and discrete thermal distribution to verify the accuracy of the transition rate calculations as well as the conservative properties.

The experimental section of this thesis describes a series of collisional ionisation frequency measurements in a solid-density magnesium plasma. These collisional rates are significantly enhanced in a solid-density system, primarily as a result of ionisation potential depression. The abundance of data available on collisional cross-sections was only valid for electron densities of up to $\lesssim 10^{17}$ cm^{-3}.

X-ray free electron lasers make it possible to perform spectroscopic ionisation rate measurements at solid-density. The presented experiments operate by photo-pumping a core-vacancy in a pre-selected charge state, and observing its radiative decay photons through emission spectroscopy. Whenever neighbouring excited charge states are populated through collisional interactions of the photo-pumped core-hole ion state, they manifest themselves in the form of emission lines. By observing the emission lines of states that an only be created through the sequence of photo-excitation or ionisation followed by a collisional interaction, the collisional frequencies can be measured from emission line intensity ratios.

The experiment leans on the use of an optically-thin yet solid-density plasma with a known energy density degree of continuum lowering. The data is accompanied by a newly-constructed parametric cross-section model that is consistent with the data presented in the electron density range of up to 3.0×10^{23} cm^{-3}, as well as with data observed in the lower density range through other experiments.

Future work

Much of the work presented in this thesis was built onto the results achieved by the work of researchers who came before me. I hope my modest contribution can assist in facilitating future research and I will give some suggestions on research questions, as well as shortcomings in the numerical schemes that can be addressed by the next round of researchers.

The plasmas discussed in this work are in the solid-density range and are therefore in the strongly-coupled regime. This gives rise to a variety of density effects and causes all collisional interactions to become a quantum many-body interaction. This is not yet represented in any of the ion transition rate calculations which are conducted as if each interaction is a binary effect. There is also experimental evidence that the transition rates of both bound-bound and bound-free rates are affected in a non-linear way that cannot be adequately described by continuum lowering alone.

To unite experimental data with the parametric cross-section formalism, the cross-sections themselves are scaled to obtain the correct rate. This viewpoint suggests that the ion is the primary object of change, when in fact it is the change in behaviour of the free-electron population that affects the rate. The Fokker-Planck scheme gives the opportunity to model how electrons of different energies interact with the ions in their proximity. Rather than scaling the cross-section as a function of Ionisation Potential Depression (IPD), it seems more appropriate to only account for the shift in energy and recover the scaling behaviour from the many-body nature of the collisional interactions. The Fokker-Planck scheme provides a framework that can be used to investigate how electrons of multiple energies can collectively induce collisional transitions. A first step has been made in this work by implementing a differential cross-section for, when adopting a classical viewpoint, the two incident electrons of a Three-Body Recombination (3BR) process. In a many-body interaction, there is no principal reason why only two incident particles should be considered. The Fokker-Planck numerical scheme can be modified to give insights into the nature of

many-body collisional processes, as well as the energy-dependent coupling between the electrons.

Another trait that the Fokker-Planck operator has inherited from classical plasma theory is the Coulomb logarithm. It appears in the elastic collision operator that describes elastic electron-electron interactions. In a strongly-coupled system, the numerical value and interpretation of the Coulomb logarithm is troublesome. It is worth clarifying how to interpret its physical meaning in plasma conditions where a Debye sphere is populated with fewer than one electron. In experimental studies, it may be of use to treat the Coulomb logarithm as a free model parameter rather than using empirical fit formulas to give it some value.

At the time of writing, the Fokker-Planck scheme can be used to compute the evolution of a super-configuration ion system and an arbitrary electron distribution. It it not yet possible to compute a time-integrated spectrum for the full set of ion populations. Particularly the bound-free emission is expected to be of interest, as it provides a mechanism to detect the presence of energetic non-thermal electrons. Section 3.5.5 lays out a method to compute the bound-free emissivity that has been implemented in CCFLY. Adding an opacity calculation, as well as bound-bound contributions to the spectrum would make the code a powerful research tool.

In addition to analysing experimental data where energetic electrons were directly injected, the code can then also be applied to materials that have been irradiated with hard X-rays. Having a spectral calculation allows for comparison with experimental data.

In the possible interactions between electrons, ions and photons and their coupled rate models, the free-free processes have been omitted for project planning reasons. Free-free processes such as bremsstrahlung and inverse bremsstrahlung do not have major effects on the electron distribution when compared to bound-free processes. However, they do emit photons in a spectral range that can be of interest when detecting energetic photons emitted through radiative recombination.

Amongst the more laborious tasks, but equally important for the accuracy of the Fokker-Planck scheme, would be to improve the interpolation methods (Eq. 3.12) through which changes in the distribution function are mapped onto a discrete grid. Whenever a change in the distribution is set to occur, for instance as a result of collisional excitation after which the incident electrons lose their energy, the distribution at a lower energy value needs to be updated. Currently, the full changes are split between only two neighbouring electron bins such that energy and density are conserved. This can lead to un-physical situations where the distribution function

becomes a heavily peaked profile, as seen in Fig. 3.11. Maintaining the same energy spread in the electron energy when it moves over the energy grid will make the code more robust when using non-uniform grids.

Finally, theoretical work on bound-bound emission spectra that have been probed with a weak resonant X-ray pulse indicate that it is possible to obtain temperature measurements by observing the line intensity ratios. This principle is inspired by the collisional ionisation rate measurements presented in Chapter 4. In that chapter and the accompanying publication, the collisional rates are inferred by constraining the plasma conditions. Conversely, when the collisional dynamics are well-understood, they can be used to infer the plasma conditions.

The operating principle described in Section 4.9 makes use of a resonantly $1s - 2p$ X-ray probe that creates a core-hole excitation. Collisional interactions during the life-time of the excited state can cause the state to decay as either a lower charge state (after recombination), or a higher charge state (after ionisation). Which process is more likely to occur depends on the plasma conditions with respect to Local Thermodynamic Equilibrium (LTE) conditions. As the system will naturally evolve towards LTE, the ratio of ionisation to recombination lines will indicate in which direction the equilibrium can be found. A more quantitative measurement can be obtained by repeating the process at different temperatures.

This set-up would be suitable to obtain pump-probe temperature measurements for various time delays. In the ideal case, it would make use of two different X-ray pulses so the warm dense system can be created with uniform conditions, before being probed with a second narrow-bandwidth probe.

Appendix A

Fokker-Planck Equation

The starting point of our description of a many-body system is the Hamiltonian for a system of N identical particles that interact through a pair-wise force. The Hamiltonian has the form of

$$\hat{H} = \frac{1}{2m}\sum_{i=1}^{N}|\vec{p_i}|^2 + \sum_{i=1}^{N}V(\vec{r_i}) + \sum_{i<j\leq N}U(\vec{r_i}-\vec{r_j}) \tag{A.1}$$

and sums up the kinetic energies, the influence of the external potential $V(\vec{r_i})$, and generally the most elaborate term, the result of particle interactions $U(\vec{r_i}-\vec{r_j})$. The number of particles N will typically be large, $N \sim \mathcal{O}(10^{23})$ as is often the case in statistical mechanics. The equations of motions for each particle are given by Hamilton's equations:

$$\frac{\partial\vec{p_i}}{\partial t} = -\frac{\partial H}{\partial\vec{r_i}} \qquad \text{and} \qquad \frac{\partial\vec{r_i}}{\partial t} = -\frac{\partial H}{\partial\vec{p_i}}. \tag{A.2}$$

Due to the interactions between particles, Eq.A.2 is a system of $6N$ coupled equations; three for momentum and three for position, for each particle. Despite not being practically useful for solving anything other than the most trivial systems, it does provide insight when applied to the continuity equation of a distribution function.

Rather than considering each individual particle in the collection of N identical particles, we will adopt the description of a probability density function $f(\vec{r_i},\vec{p_i};t)$ over the $6N$ dimensional phase space. There is an additional dependence of time as the distribution is generally time-dependent. The distribution function contains the same information as a list of positions and momenta for all N particles, but provides a different representation that we can transform into a useful framework later.

The distribution is normalised according to

$$\int \mathrm{d}^3 r_i \mathrm{d}^3 p_i \, f(\vec{r_i}, \vec{p_i}; t) = 1, \quad \forall t \tag{A.3}$$

As probability is conserved both locally and globally, it obeys the continuity equation; the probability distribution acts as an incompressible fluid in phase space. Any change in probability in one region of phase space must be compensated by a flow into neighbouring regions in order to preserve probability. The gradient operator in the phase space continuity equation is defined as $\bigtriangledown \equiv (\partial/\partial\vec{r_i}\, \partial/\partial\vec{p_i})$ and the flow vector is $(\dot{\vec{r_i}}, \dot{\vec{p_i}})$. The continuity equation reads

$$\frac{\partial f}{\partial t} + \sum_{i=1}^{N} \left(\frac{\partial}{\partial \vec{r_i}} \left(\dot{\vec{r_i}} f \right) + \frac{\partial}{\partial \vec{p_i}} \left(\dot{\vec{p_i}} f \right) \right) = 0 \tag{A.4}$$

Substituting Hamilton's equations from Eq. A.2 into Eq. A.4, his can be written as

$$\frac{\partial f}{\partial t} + \sum_{i=1}^{N} \left(\frac{\partial}{\partial \vec{r_i}} \left(\frac{\partial H}{\partial \vec{p_i}} f \right) - \frac{\partial}{\partial \vec{p_i}} \left(\frac{\partial H}{\partial \vec{r_i}} f \right) \right) = 0, \tag{A.5}$$

which in turn can be simplified to

$$\frac{\partial f}{\partial t} + \sum_{i=1}^{N} \left(\frac{\partial f}{\partial \vec{r_i}} \left(\frac{\partial H}{\partial \vec{p_i}} \right) - \frac{\partial f}{\partial \vec{p_i}} \left(\frac{\partial H}{\partial \vec{r_i}} \right) \right) = 0, \tag{A.6}$$

due to the independence of the partial derivatives. Eq. A.6 is Liouville's equation and it states that probability, or particle density in our context, cannot change as it moves along a trajectory in phase space. Any initial density is preserved, provided the evolution is described by a Hamiltonian that is not explicitly time-dependent[1].

Another commonly written, more concise, way of formulating Liouville's equation is through using the Poisson commutator brackets $\{A, B\} \equiv \frac{\partial A}{\partial \vec{r_i}} \cdot \frac{\partial B}{\partial \vec{p_i}} - \frac{\partial A}{\partial \vec{p_i}} \cdot \frac{\partial B}{\partial \vec{r_i}}$, thereby expressing the change in distribution function as

$$\frac{\partial f}{\partial t} = \{H, f\}. \tag{A.7}$$

From this result, we can see that any equillibrium distribution must Poisson commute with the Hamiltonian. Any distribution that is a function of the energy will satisfy this relation.

[1]For a cloud of electrons, this is valid as long as the electron-electron collisions are elastic. It will not be valid for an electron distribution function if there are also inelastic electron-ion collisions

Finally, we can use Liouville's equation to examine whether the expectation value of a physical quantity in phase space is preserved or not. Calculating the expectation value through Eq. A.7, its time dependence can be expressed as

$$\begin{aligned}\frac{d\langle A\rangle}{dt} &= \int d^3r_i d^3p_i\, A\frac{\partial f}{\partial t} \\ &= \int d^3r_i d^3p_i\, f\{A,H\} \\ &= \langle\{A,H\}\rangle.\end{aligned} \tag{A.8}$$

This can be obtained by using Hamilton's equations Eq. A.2 and using the fact that the distribution must asymptotically vanish to zero, which is the case as f is normalised.

Thusfar we have reformulated a computational framework to describe a many-particle system, without making it any more feasible to apply computational methods. We defined a distribution function that fully describes the particle system, but it still depends on $6N$ variables and will be untractably large. Noting that all particles are identical, it would be sufficient to know the one-particle distribution function and scaling it by N to obtain the correct density at a point $(\vec{r},\vec{p})$ in phase space:

$$f_1\left(\vec{r},\vec{p};t\right) = N\int\prod_{i=2}^{N} d^3r_i d^3p_i f\left(\vec{r},\vec{r_2},\ldots,\vec{r_N},\vec{p},\vec{p_2},\ldots,\vec{p_N};t\right), \tag{A.9}$$

with normalisation $\int d^3r d^3p f_1 = N$. For convenience, we considered the first particle with index $i=1$, although we could have picked any particle since they are identical. This distribution function in Eq. A.9 is often all we need to know about the system, as it can be used to compute macroscopic quantities such as the density, bulk momentum, kinetic energy density and other transport properties in Eqs. 2.3, 2.4, and 2.5.

The plan now is to derive a suitable expression for the one-particle distribution,and most importantly its evolution, so we can use it to analyse a realistic system of $\mathcal{O}\left(10^{23}\right)$ particles. Using Hamilton's equations from Eq. A.2 and the many-body Hamiltonian from Eq. A.1, we can compute the time derivative of f_1 to be

$$\begin{aligned}\frac{\partial f_1}{\partial t} &= N\int\prod_{i=2}^{N} d^3r_i d^3p_i\{H,f\} \\ &= N\int\prod_{i=2}^{N} d^3r_i d^3p_i \sum_{j=1}^{N}\left[-\frac{\vec{p_j}}{m}\cdot\frac{\partial f}{\partial\vec{r_j}} + \frac{\partial V}{\partial\vec{r_j}}\cdot\frac{\partial f}{\partial\vec{p_j}} + \sum_{k<l}\frac{\partial U\left(\vec{r_k}-\vec{r_l}\right)}{\partial\vec{r_j}}\cdot\frac{\partial f}{\partial\vec{p_j}}\right].\end{aligned} \tag{A.10}$$

In evaluating this expression, we obtain no contributions from the particles $j = 2, \cdots, N$ as can be seen by integrating by parts, and what remains are derivatives with respect to $\vec{r_1}$ and $\vec{p_1}$. Separating out the particle interactions, the evolution of the one-particle distribution can be written as

$$\begin{aligned} \frac{\partial f_1}{\partial t} &= \{H_1, f_1\} + N \sum_{k=2}^{N} \frac{\partial U\left(\vec{r_1} - \vec{r_k}\right)}{\partial \vec{r_1}} \cdot \frac{\partial f}{\partial \vec{p_1}} \\ &\equiv \{H_1, f_1\} + \left(\frac{\partial f_1}{\partial t}\right)_{coll} \end{aligned} \tag{A.11}$$

where the one-particle Hamiltonian is defined as $H_1 = \frac{p_1^2}{2m} + V(\vec{r_1})$. The one-particle distribution function is described by what looks like an inhomogeneous Liouville equation, where the first term describes the equation of motion for an independent particle unperturbed by collisions. The effects of particle interactions are contained in the second term of Eq. A.11, a contribution often referred to as the collision integral.

Unfortunately, the collision integral cannot be written as a function of the one-particle distribution, as indeed it captures all the interactions with particles $j = 2, \cdots, N$. It is not possible for a one-particle distribution to give any information about positional differences of two particles, making it fundamentally impossible to describe interactions. We will find that in order to calculate the one-particle distribution function, we need knowledge of the two-particle distribution. This, however, depends on corrections from the three-particle distribution, and so forth. In general, the n-particle distribution

$$f_n\left(\vec{r_1}, \ldots, \vec{r_n}, \vec{p_1}, \ldots, \vec{p_n}; t\right) = \frac{N!}{(N-n)!} \int \prod_{i=n+1}^{N} d^3 r_i d^3 p_i \, f\left(\vec{r_1}, \ldots, \vec{r_N}, \vec{p_1}, \ldots, \vec{p_N}; t\right) \tag{A.12}$$

obeys the relation

$$\frac{\partial f_n}{\partial t} = \{H_n, f_n\} + \sum_{i=1}^{N} \int d^3 r_{n+1} d^3 p_{n+1} \frac{\partial U\left(\vec{r_i} - \vec{r_{n+1}}\right)}{\partial \vec{r_i}} \cdot \frac{\partial f_{n+1}}{\partial \vec{p_i}}, \tag{A.13}$$

where the Hamiltonian H_n has been modified to a form similar in Eq. A.1 for $N = n$. Note that the total number of particles in the system has not changed, it is still N. However, interactions outside the sub-set of n particles are not considered in this form.

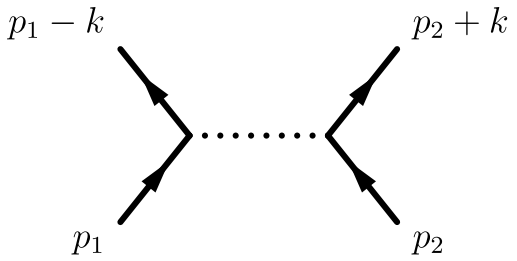

Figure A.1: Two identical particles with incoming momenta $\vec{p_1}$ and $\vec{p_2}$ scattering elastically at position $\vec{r}$. They exchange momentum $\vec{k}$, while preserving total momentum and kinetic energy. The interactive force is mitigated by a virtual photon.

Equations A.12, A.13, and the appropriate Hamiltonian define a set of equations for the one-particle distribution function. This theoretical result goes by the name of the BBGKY hierarchy, named after Bogoliubov, Born, Green, Kirkwood and Yvon [122–124].

The problem is, however, that this set of equations is not closed, which means that the n-particle distribution function always depends on successively higher orders of distribution functions. The consequence is that the time derivative of the one-particle distribuion cannot be written as a function of f_1 alone.

Although seemingly it doesn't help us any further, Eq. A.13 is a suitable form for constructing approximations. In order to proceed from here, we will do precisely that and build a series expansion that we can solve. The starting point of approximations is the Boltzmann equation, previously enountered in Eq. A.11. Though impossible to solve in its complete form, this equation is an exact description of the N-particle system. From the RHS of Eq. A.13, it can be seen that the rate of change of the one-particle distribution depends on two-particle scattering events.

We consider a scattering event as depicted in Fig. A.1 at a position $\vec{r}$. Two incoming particles with momenta $\vec{p_1}$ and $\vec{p_2}$ scatter into outgoing momenta $\vec{p_1'}$ and $\vec{p_2'}$. The sum of momentum and kinetic energy for these two particles is conserved, and the force is mitagated by a virtual photon.

The rate R at which this process will take place is proportional to the two-particle density, as well as on a coefficient α that in itself is proportional to the differential scattering cross section given.

$$R = \alpha(\vec{p_1}, \vec{p_2}|\vec{p_1}, \vec{p_2}) f_2(\vec{r}, \vec{r}, \vec{p_1}, \vec{p_2}) d^3p_2 d^3p_1' d^3p_2', \tag{A.14}$$

where momentum and energy conservation imposes constraints between incoming and outgoing momenta. An assumption that has been made here, is that the external

potential V as it appears in Eq. A.13 has a negligible effect on inter-particle scattering. This is generally true, as scattering occurs on extremely short length scales where external potentials do not vary enough to be of importance.

The rate constructed in Eq. A.14 is associated with depopulating the particle population with momentum $\vec{p_1}$. It is also possible for scattering processes to repopulate this momentum state. This rate has a similar form, subject to time reversal and the exchange of particles:

$$R = \alpha(\vec{p_1'}, \vec{p_2'}|\vec{p_2}, \vec{p_1}) f_2(\vec{r}, \vec{r}, \vec{p_1'}, \vec{p_2'}) d^3p_2 d^3p_1' d^3p_2'. \tag{A.15}$$

Any scattering process that is invariant under parity, spatial translation and time reversal is also invariant under the reversal of momenta:

$$\alpha(\vec{p_1}, \vec{p_2}|\vec{p_1}, \vec{p_2}) = \alpha(\vec{p_1'}, \vec{p_2'}|\vec{p_2}, \vec{p_1}) \tag{A.16}$$

This allows us to write the collision integral in a more concise form:

$$\left(\frac{\partial f_1}{\partial t}\right)_{coll} = \int d^3p_2 d^3p_1' d^3p_2' \, \alpha(\vec{p_1}, \vec{p_2}|\vec{p_1'}, \vec{p_2'}) \left[f_2(\vec{r}, \vec{r}, \vec{p_1'}, \vec{p_2'}) - f_2(\vec{r}, \vec{r}, \vec{p_1}, \vec{p_2})\right] \tag{A.17}$$

Finally, we need a way to express f_2 in f_1 which is where two assumptions come in. The first is that the typical timescale associated with a collision event, τ_c, is much smaller than the mean free time τ:

$$\tau_c \ll \tau$$

The one-particle distribution function then follows a Hamiltonian evolution for the majority of the time, perturbed by collisions in a time span τ_c during which the collision integral has a nonzero contribution. Motivated by this consideration, we can assume that the initial momenta of the two scattering particles are uncorrelated. After all, the momenta were the result of many previous scattering processes that took place with a large number of other particles. During the collision, however, the momenta are absolutely correlated, but then they have the mean free time to lose this correlation. The assumption that is also referred to as molecular chaos manifests itself in a separable distribution:

$$f_2(\vec{r}, \vec{r}, \vec{p_1}, \vec{p_2}) = f_1(\vec{r}, \vec{p_1}) f_1(\vec{r}, \vec{p_2}) \tag{A.18}$$

With this we can now obtain a form of the Boltzmann equation. This integro-differential equation is a closed form expression of the one-particle distribution function.

$$\left(\frac{\partial f_1}{\partial t}\right)_{coll} = \int d^3p_2 d^3p_1' d^3p_2' \, \alpha(\vec{p_1}, \vec{p_2}|\vec{p_1'}, \vec{p_2'}) \left[f_1(\vec{r}, \vec{p_1'}) f_1(\vec{r}, \vec{p_2'}) - f_1(\vec{r}, \vec{p_1}) f_1(\vec{r}, \vec{p_2})\right] \tag{A.19}$$

The assumption of molecular chaos has far-reaching consequences, as it introduces an arrow of time in the collision process. This is not entirely obvious from a seemingly innocent assumption, but has been proven rigorously in the H-theorem introduced by Ludwig Boltzmann [125].

Also of interest are the cases for which the collision integral vanishes. This criterion,

$$f_1^{eq}(\vec{r},\vec{p_1})f_1^{eq}(\vec{r},\vec{p_2}) = f_1^{eq}(\vec{r},\vec{p_1'})f_1^{eq}(\vec{r},\vec{p_2'}), \tag{A.20}$$

defines the detailed balance condition. This observation better defines the class of equillibrium distributions than the statement that they should Poisson commute with the Hamiltonian. As expected, the Maxwell-Boltzmann distribution Eq. 2.12 satisfies this criterion. Interestingly, this class of distributions allows for a drift velocity or streaming term and is not to be mistaken for system-wide stationary state. Hence, the Maxwell-Boltzmann distribution defines a state of local thermodynamic equillibrium with the particle density, drift velocity and kinetic energy density being allowed to vary over space.

Next, we will proceed with a method to solve or, more accurately stated, further approximate the Boltzmann equation in its current form with the Fokker-Planck formalism.

The electron systems of interest to us consist of a bulk that is largely at local thermodynamic equillibrium, with a relatively small fraction of the population brought out of equillibrium by a perturbation[2]. Furthermore, we note that in an electron gas, the scattering is generally dominated by small-angle collisions which carry small momentum changes. This assumption and observation allow us to linearise the Boltzmann Equation Eq. A.19 into a form that is much more computationally efficient.

Fast forwarding multiple decades from the work of Boltzmann in the 1870s, it was in the 1950s when the first successful attempts were made to linearise the Boltzmann equation and write it in a suitable form for effective computation. The key assumption relied on is that after collisions take place, the distribution is close to equillibrium, which is sufficient to linearise the Boltzmann equation [126–128].

Kramers and Moyal demonstrated that an integro-differential collision operator can be written as a series expansion that now bears their name [129, 130]:

$$\left(\frac{\partial f_1(\vec{p},t)}{\partial t}\right)_{coll} = \sum_{n=1}^{\infty} \frac{(-1)^n}{n!} \frac{\partial^n}{\partial \vec{p}^n} \left[A_n(\vec{p},t) f_n(\vec{p},t)\right], \tag{A.21}$$

[2]Even if the number of electrons that is perturbed becomes larger, this approach can still be valid as long as the equillibration process is fast and ensures that the out-of-equillibrium population at any point in time remains small.

where the expansion coefficients A_n depend on the momentum-transfer probabilities α from Eq. A.14 through the relation

$$A_n(\vec{p}) = \int d^3p' \, |\vec{p'} - \vec{p}|^n \alpha(\vec{p'}|\vec{p}. \tag{A.22}$$

For simplicity, we assumed isotropy by removing the directional dependence of the momentum transfer. What remains is to decide how many terms to consider. One may be inclined to think that this decision would depend on the required numerical accuracy, but this does not seem to be the case here. Pawula showed in 1962 that there can only be three answers to this question: one, two, or infinitely many terms, if we are to relate the solution to a probability distribution. If we consider the first two terms, we recover the homogeneous Fokker-Planck equation:

$$\left(\frac{\partial f_1(\vec{p},t)}{\partial t}\right)_{coll} = -\frac{\partial}{\partial \vec{p}}\left[a(\vec{p},t)f(\vec{p},t)\right] + \frac{1}{2}\frac{\partial^2}{\partial \vec{p}^2}\left[D(\vec{p},t)f(\vec{p},t)\right] \tag{A.23}$$

The Fokker-Planck equation Eq. A.23 is a versatile description that appears in many fields of research in Physics and Engineering, but also Finance and Sociology. The physical interpretation of the equation can therefore differ wildly. For us, the first derivative contains a drift coefficient a. This can be interpreted as a predictable force that is equivalent to friction. The second term, where the coefficient has been given the symbol D for diffusion, is a random term that describes diffusive behaviour. When a non-equillibrium distribution evolves towards equillibrium, it can be said that the energy transfer associated with the driving viscous force is dispersed through the diffusion term, as indicated by the opposite signs of each contribution.

The Fokker-Planck equation is linear in the distribution, but made to be non-linear by the dependence of the drift- and diffusion coefficients on both the momentum, and the distribution itself.

The same result can be derived in many ways, as has been done by Jenny *et al.* [131], and also for particles moving at relativistic velocities by Nayakshin *et al.* [43].

In preparation for an appropriate numerical scheme that can be implemented in a zero-dimensional atomic kinetics code, let us write Eq.A.23 for a distribution in energy space. We will drop the subscript for the one-particle distribution, and omit the explicit time dependence for brevity. For completeness, our description must also contain source- and inhomogeneous terms, which can add and remove particles from the distribution.

The energy-space distribution:

$$\frac{\partial f_E}{\partial t} = -\frac{\partial}{\partial E}\left[a(E)f_E(E)\right] + \frac{1}{2}\frac{\partial^2}{\partial E^2}\left[D(E)f_E(E)\right] + I(f) + S(E) \tag{A.24}$$

where the inelastic terms are contained in I and S represents an external source or sink.

Appendix B

Reaction cross section

Reaction cross sections is a fundamental description of the probability that a specific interaction will occur in a collision between two particles. This can be an ionisation or excitation event, or one of many other possible elastic or inelastic collisional interactions. The goal of this description, is to be able to compute transition rates for the population dynamics in Warm Dense Matter (WDM). The cross section formalism is broadly used in nuclear, particle and atomic physics to describe energy and momentum exchange between particles. It is also of importance in order to understand the atomic physics taking place in WDM, as most reaction rates that populate and depopulate ion charge states are described in the cross section formalism. The subsequent discussion was inspired by Section 1.6 from Oxenius [80].

The principles of this formalism are visualised in Fig. B.1 for a pair-wise interaction.

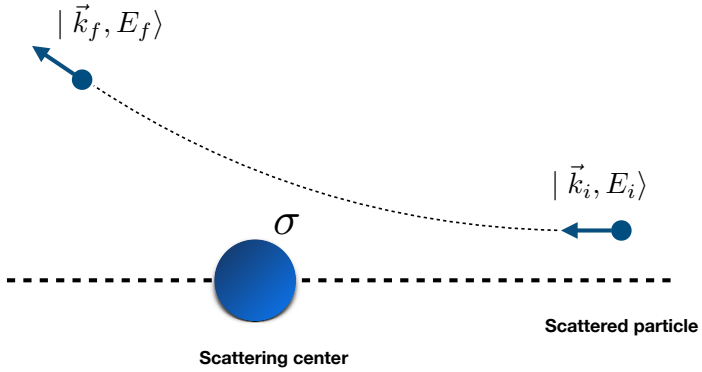

Figure B.1: A collisional event where an incoming particle scatters off a scattering center, under momentum exchange $\Delta\vec{k} = \vec{k_i} - \vec{k_f}$ and energy exchange $\Delta E = E_i - E_f$. The additional momentum and energy is absorbed by the scattering cross section, or any secondary particles that may have been created by the collision.

An incoming particle with momentum $\vec{k_i}$ and energy E_i approaches a scattering

center with a cross section σ. The scattering center is placed at rest in this observation frame. The cross section represents an effective target area that the incoming particle may or may not hit, depending on the magnitude of the cross section. It is analogous to an unskilled darts player throwing a dart at a darts board, where the probability for the dart to hit the board grows as the board becomes larger. A typical size for atomic cross sections is the surface area of a circle with the Bohr radius[1], $\pi a_0^2 \approx 8.79 \cdot 10^{-17}\,\mathrm{cm}^2$. Cross sections are often tabulated in units of barn, where 1 barn is equal to $10^{-24}\,\mathrm{cm}^2$.

After the interaction, the scattered particle has a different momentum and possibly a different kinetic energy. In general, both the scattering particle and scattering center will be moving as they can be of a comparable mass, with possible interaction pairs being electron-electron, photon-electron, photon-ion, or electron-ion. Occasionally, a third particle is involved only to mitigate momentum conservation. There are even situations, such as three-body recombination or many-body interactions in highly dense environments, where more than two particles interact with each other at once.

Elastic collisions preserve the total momentum and energy of the initial particle pair. Inelastic interactions generally involve the creation or destruction of particles, for instance through an ionisation event that 'produces' an extra free electron. The total energy between the initial and final states of all particles involved are then different, with energy having been absorbed or released by the ionisation threshold I_i.

A cross section for a two-particle interaction can be considered to be the transverse surface area. Its main use is to be able to compute a transition rate between two states for a scattering center being exposed to a flux of scattering particles. In this example, the scattering center is an ion and the scattered particle is an electron. For an isotropic system, we can describe this process in terms of an energy exchange and the momentum directions do not need to be considered. The scattering electrons have an energy distribution described by distribution function $f_E(E)$ which is normalised to the density according to

$$\rho_e = \int_0^\infty f_E(E)\mathrm{d}E. \tag{B.1}$$

When we want to compute the ion transition rate $S_{l,u}$ for a transition from state $\mid l\rangle$ to state $\mid u\rangle$, we compute a cross section integral

[1]This is the most probable distance between an electron and its nucleus in a hydrogen atom.

$$S_{l,u} = \int_0^\infty v(E) f_E(E) \sigma_{l,u}(E) \mathrm{d}E, \tag{B.2}$$

with the non-relativistic velocity being related to the energy by $v(E) = \sqrt{2E/m_e}$. Eq. B.2 represents as much as the flux of incident electrons ($v(E)f_E(E)$) multiplied by the probability of a transition for each incident electron ($\sigma_{l,u}$). Both quantities depend on the kinetic energy, so the transition rate is an integral over all possible incident energies. For inelastic collisions, the lower integration bound can be increased from zero to the reaction threshold as the cross section is zero below the threshold. The reaction threshold can be computed by considering the bound energy of the initial and final state of the scattering center. Eq. B.2 is the simplest form of a reaction cross section, where we are not concerned with the reaction products[2] of the ion transition, or their respective energy distributions.

In the common case when the incident particle distribution is thermal (Maxwell-Boltzmann), the rate integral becomes

$$S_{l,u} = \sqrt{\frac{8}{\pi m_e}} (k_B T)^{-3/2} \int_0^\infty E \sigma_{l,u}(E) \exp\left(-E/k_B T\right) \mathrm{d}E. \tag{B.3}$$

Both equations are implemented in the atomic-kinetics code, depending on the electron distribution being used. Eq. B.3 often reduces to a semi-analytic integral[3] and will generally be faster to evaluate than the full integration for an arbitrary electron distribution.

When a collisional interaction has only one incoming and one outgoing particle, the energy balance is straightforward. The outgoing particle's energy must equal the incoming energy, plus any changes in the binding energy of the ion. Whenever an interaction leads to the production or destruction of particles, the energy balance becomes non-trivial and we may be concerned by specifying the distribution of kinetic energy between reaction products. Here's where the differential cross section comes in. There are many definitions and use cases for differential cross sections even for a two-particle interaction[4] but here we use it to quantify the energy partitioning between particles.

For a collisional ionisation cross section[5], we have one incoming electron $\mid i\rangle$ and two outgoing electrons $\mid j\rangle$ and $\mid k\rangle$. The differential cross section would be defined

[2]There could be a production or destruction term of free electrons in an inelastic collision.

[3]These can be variations of the exponential integral for cross sections that vary logarithmically with incident energy.

[4]Most notably for specifying the incoming and outgoing propagation directions, or momentum exchange.

[5]The process whereby an ion is struck by an electron, resulting in a bound electron being ionised.

as the probability that the incoming electron causes an ionisation event where the outgoing electrons are scattered into an infinitesimal part of the phase space around energies E_j and E_k. Its dimensions are area, per incoming energy, per outgoing energy squared. The reaction rate can be computed from a differential cross section as

$$S_{l,u} \int_{\langle i \rangle} \int_{\langle j \rangle} \int_{\langle k \rangle} v(E_i) \frac{d\sigma_{l,u}}{dE_i dE_j dE_k} f_E(E_i) \cdot \delta(E_i - I_i - E_j - E_k) \mathrm{d}E_i \mathrm{d}E_j \mathrm{d}E_k \qquad \text{(B.4)}$$

where the integration domains run over the possible values of kinetic energies, subject to energy conservation as expressed by the delta function. Momentum is not conserved, as the heavy ion can absorb any momentum the electrons may have. In case this integration were to be done in velocity phase space for a non-isotropic system, Eq. B.4 would be a 6-fold integral: (3 for each velocity vector, for both outgoing particles). In practice, even doubly differential cross sections are not tabulated and the cross sections can only be derived from the detailed balance principle. For more details on the cross section formalism in the velocity-space representation, please refer to Oxenius [80].

References

[1] J. M. J. Madey. Stimulated emission of bremsstrahlung in a periodic magnetic field. *Journal of Applied Physics*, 42(5):1906–1913, 1971.

[2] P. Emma et al. First lasing and operation of an angstrom-wavelength free-electron laser. *Nat. Photon.*, 4(9):641–647, 2010.

[3] Alexander Fridman. *Plasma Chemistry*. Cambridge University Press, 2008.

[4] Meghnad N Saha and Alfred Fowler. On a physical theory of stellar spectra. *Proceedings of the Royal Society of London. Series A, Containing Papers of a Mathematical and Physical Character*, 99(697):135–153, 1921.

[5] J. Oxenius and E. Simonneau. Kinetic theory of spectral line formation. *Annals of Physics*, 234(1):60 – 101, 1994.

[6] J. Madey, M.O. Scully, and P. Sprangle. The free electron laser: conceptual history. *Physica Scripta*, 91(8):083003, jul 2016.

[7] C. Pellegrini. The history of x-ray free-electron lasers. *The European Physical Journal H*, 37(5):659–708, 2012.

[8] B. D. Patterson, R. Abela, H.-H. Braun, U. Flechsig, R. Ganter, Y. Kim, E. Kirk, A. Oppelt, M. Pedrozzi, S. Reiche, L. Rivkin, Th. Schmidt, B. Schmitt, V. N. Strocov, S. Tsujino, and A. F. Wrulich. Coherent science at the SwissFEL x-ray laser. *New Journal of Physics*, 12(3):035012, mar 2010.

[9] Á. Saá Hernández, E. Prat, and S. Reiche. Generation of two-color x-ray free-electron-laser pulses from a beam with a large energy chirp and a slotted foil. *Phys. Rev. Accel. Beams*, 22:030702, Mar 2019.

[10] M. Yabashi, H. Tanaka, T. Tanaka, H. Tomizawa, T. Togashi, M. Nagasono, T. Ishikawa, J. R. Harries, Y. Hikosaka, A. Hishikawa, K. Nagaya, N. Saito,

E. Shigemasa, K. Yamanouchi, and K. Ueda. Compact XFEL and AMO sciences: SACLA and SCSS. *Journal of Physics B: Atomic, Molecular and Optical Physics*, 46(16):164001, aug 2013.

[11] In Ko, Heung-Sik Kang, Hoon Heo, Changbum Kim, Gyujin Kim, Chang-Ki Min, Haeryong Yang, Soung Baek, Hyo-Jin Choi, Geonyeong Mun, and et al. Construction and commissioning of pal-xfel facility. *Applied Sciences*, 7(5):479, May 2017.

[12] M Nakatsutsumi, K Appel, C Baehtz, B Chen, T E Cowan, S Göde, Z Konopkova, A Pelka, G Priebe, A Schmidt, K Sukharnikov, I Thorpe, Th Tschentscher, and U Zastrau. Femtosecond laser-generated high-energy-density states studied by x-ray FELs. *Plasma Physics and Controlled Fusion*, 59(1):014028, nov 2016.

[13] C Pellegrini. X-ray free-electron lasers: from dreams to reality. *Physica Scripta*, T169:014004, dec 2016.

[14] H. Motz. Applications of the radiation from fast electron beams. *Journal of Applied Physics*, 22(5):527–535, 1951.

[15] R. Bonifacio, C. Pellegrini, and L.M. Narducci. Collective instabilities and high-gain regime in a free electron laser. *Optics Communications*, 50(6):373 – 378, 1984.

[16] C. Pellegrini, A. Marinelli, and S. Reiche. The physics of x-ray free-electron lasers. *Rev. Mod. Phys.*, 88:015006, Mar 2016.

[17] D. S. Rackstraw, O. Ciricosta, S. M. Vinko, B. Barbrel, T. Burian, Chalupský J., B. I. Cho, H.-K. Chung, G. L. Dakovski, K. Engelhorn, V. Hájková, P. Heimann, M. Holmes, L. Juha, J. Krzywinski, R. W. Lee, S. Toleikis, J. J. Turner, U. Zastrau, and J. S. Wark. Saturable absorption of an x-ray free-electron-laser heated solid-density aluminum plasma. *Phys. Rev. Lett.*, 114:015003, Jan 2015.

[18] Sam M. Vinko. X-ray free-electron laser studies of dense plasmas. *Journal of Plasma Physics*, 81(05):365810501, 2015.

[19] WALTER BAMBYNEK, BERND CRASEMANN, R. W. FINK, H. U. FREUND, HANS MARK, C. D. SWIFT, R. E. PRICE, and P. VENUGOPALA RAO. X-ray fluorescence yields, auger, and coster-kronig transition probabilities. *Rev. Mod. Phys.*, 44:716–813, Oct 1972.

[20] M. Dunne. X-ray free-electron lasers light up materials science. *Nature Reviews Materials*, 3(9):290–292, 2018.

[21] B. W. J. McNeil and N. R. Thompson. X-ray free-electron lasers. *Nature Photonics*, 4(12):814–821, 2010.

[22] S. M. Vinko et al. Creation and diagnosis of a solid-density plasma with an X-ray free-electron laser. *Nature*, 482(7383):59–62, 2012.

[23] O. Peyrusse. Atomic configuration averages and non-local thermodynamical equilibrium plasma spectroscopy calculations. *Journal of Physics B: Atomic, Molecular and Optical Physics*, 32(3):683, 1999.

[24] L. Spitzer and R. Härm. Transport phenomena in a completely ionized gas. *Phys. Rev.*, 89:977–981, Mar 1953.

[25] A. Ng, D. Parfeniuk, P. Celliers, L. DaSilva, R. M. More, and Y. T. Lee. Electrical conductivity of a dense plasma. *Phys. Rev. Lett.*, 57:1595–1598, Sep 1986.

[26] D.-K. Kim and I. Kim. Calculation of ionization balance and electrical conductivity in nonideal aluminum plasma. *Phys. Rev. E*, 68:056410, Nov 2003.

[27] G. Miloshevsky and A. Hassanein. Atomic and optical properties of warm dense copper. *Phys. Rev. E*, 92:033109, Sep 2015.

[28] T. R. Preston et al. Measurements of the k-shell opacity of a solid-density magnesium plasma heated by an x-ray free-electron laser. *Phys. Rev. Lett.*, 119:085001, 2017.

[29] S. M. Vinko et al. Investigation of femtosecond collisional ionization rates in a solid-density aluminium plasma. *Nat. Commun.*, 6:6397, 2015.

[30] Q. Y. van den Berg, E. V. Fernandez-Tello, T. Burian, J. Chalupský, H.-K Chung, O. Ciricosta, G. L. Dakovski, V. Hájková, P. Hollebon, L. Juha, J. Krzywinski, R. W. Lee, M. P. Minitti, T. R. Preston, A. G. de la Varga, V. Vozda, U. Zastrau, J. S. Wark, P. Velarde, and S. M. Vinko. Clocking femtosecond collisional dynamics via resonant x-ray spectroscopy. *Phys. Rev. Lett.*, 120:055002, Feb 2018.

[31] S. B. Hansen et al. Detailed analysis of hollow ions spectra from dense matter pumped by x-ray emission of relativistic laser plasma. *Physics of Plasmas*, 21(3):031213, 2014.

[32] O. Ciricosta et al. Measurements of continuum lowering in solid-density plasmas created from elements and compounds. *Nat. Commun.*, 7:11713, 05 2016.

[33] Richard M. More. Electronic energy-levels in dense plasmas. *J. of Quant. Spec. and Rad. Transfer*, 27(3):345 – 357, 1982.

[34] Alberto G. de la Varga, Pedro Velarde, François de Gaufridy, David Portillo, Manuel Cotelo, Alfonso Barbas, Agustín González, and Philippe Zeitoun. Non-maxwellian electron distributions in time-dependent simulations of low-z materials illuminated by a high-intensity x-ray laser. *High Energy Density Physics*, 9(3):542 – 547, 2013.

[35] L. Young, E. P. Kanter, B. Krässig, Y. Li, A. M. March, S. T. Pratt, R. Santra, S. H. Southworth, N. Rohringer, L. F. DiMauro, G. Doumy, C. A. Roedig, N. Berrah, L. Fang, M. Hoener, P. H. Bucksbaum, J. P. Cryan, S. Ghimire, J. M. Glownia, D. A. Reis, J. D. Bozek, C. Bostedt, and M. Messerschmidt. Femtosecond electronic response of atoms to ultra-intense x-rays. *Nature*, 466(7302):56–61, 2010.

[36] Orlando Ciricosta, Hyun-Kyung Chung, Richard Lee, and Justin S. Wark. Simulations of neon irradiated by intense x-ray laser radiation. *HEDP*, 7:111–116, 09 2011.

[37] B.I. Cho et al. Resonant k-alpha spectroscopy of solid-density aluminum plasmas. *Phys. Rev. Lett.*, 109:245003, 2012.

[38] O. Ciricosta et al. Direct measurements of the ionization potential depression in a dense plasma. *Phys. Rev. Lett.*, 109:065002, Aug 2012.

[39] B. I. Cho, M. S. Cho, M. Kim, H.-K. Chung, B. Barbrel, K. Engelhorn, T. Burian, J. Chalupský, O. Ciricosta, G. L. Dakovski, V. Hájková, M. Holmes, L. Juha, J. Krzywinski, R. W. Lee, Chang Hee Nam, D. S. Rackstraw, S. Toleikis, J. J. Turner, S. M. Vinko, J. S. Wark, U. Zastrau, and P. A. Heimann. Observation of reverse saturable absorption of an x-ray laser. *Phys. Rev. Lett.*, 119:075002, Aug 2017.

[40] O Ciricosta, S M Vinko, H Chung, C Jackson, R W Lee, T R Preston, D S Rackstraw, and J S Wark. Detailed model for hot-dense aluminum plasmas generated by an x-ray free electron laser. *Physics of Plasmas*, 23:022707, 2016.

[41] H. N. Chapman et al. Femtosecond diffractive imaging with a soft-x-ray free-electron laser. *Nat Phys*, 2(12):839–843, 12 2006.

[42] Lyman Spitzer. *Physics of fully ionized gases.* Interscience tracts on physics and astronomy.3. Interscience Publishers, New York, 1962.

[43] Sergei Nayakshin and Fulvio Melia. Self-consistent fokker-planck treatment of particle distributions in astrophysical plasmas. *The Astrophysical Journal Supplement Series*, 114(2):269–288, Feb 1998.

[44] A. D. Fokker. Die mittlere energie rotierender elektrischer dipole im strahlungsfeld. *Annalen der Physik*, 348(5):810–820, 1914.

[45] Marshall N. Rosenbluth, William M. MacDonald, and David L. Judd. Fokker-planck equation for an inverse-square force. *Phys. Rev.*, 107:1–6, Jul 1957.

[46] A.V. Bobylev and V.A. Chuyanov. On the numerical solution of landau's kinetic equation. *USSR Computational Mathematics and Mathematical Physics*, 16(2):121 – 130, 1976.

[47] M. Tzoufras, A.R. Bell, P.A. Norreys, and F.S. Tsung. A vlasov–fokker–planck code for high energy density physics. *Journal of Computational Physics*, 230(17):6475 – 6494, 2011.

[48] M. Tzoufras, A. Tableman, F. S. Tsung, W. B. Mori, and A. R. Bell. A multi-dimensional vlasov-fokker-planck code for arbitrarily anisotropic high-energy-density plasmas. *Physics of Plasmas*, 20(5):056303, 2013.

[49] D. A. Gurnett and A. Bhattacharjee. *Introduction to Plasma Physics: With Space and Laboratory Applications.* Cambridge University Press, 2005.

[50] William J. Longley, Meers M. Oppenheim, Alex C. Fletcher, and Yakov S. Dimant. Isr spectra simulations with electron-ion coulomb collisions. *Journal of Geophysical Research: Space Physics*, 123(4):2990–3004, 2018.

[51] J. D. Huba. NRL plasma formulary. *Naval Research Laboratory*, pages 34–35, 2013.

[52] Alan C. Hindmarsh, Peter N. Brown, Keith E. Grant, Steven L. Lee, Radu Serban, Dan E. Shumaker, and Carol S. Woodward. Sundials: Suite of nonlinear and differential/algebraic equation solvers. *ACM Trans. Math. Softw.*, 31(3):363–396, September 2005.

[53] S Chandrasekhar. Dynamical friction i. general considerations: The coefficient of dynamical friction. *Astrophys. J.*, 97:255, 1943.

[54] S.I. Braginskii. Transport processes in a plasma. *Reviews on plasma theory Vol.1*, 1963.

[55] Hai P. Le and Jean-Luc Cambier. Conservative algorithms for non-maxwellian plasma kinetics. *Physics of Plasmas*, 24(12):122105, 2017.

[56] Fred L. Hinton. Simulating coulomb collisions in a magnetized plasma. *Physics of Plasmas*, 15(4):042501, 2008.

[57] S. Chandrasekhar. Stochastic problems in physics and astronomy. *Rev. Mod. Phys.*, 15:1–89, Jan 1943.

[58] H. Wabnitz, L. Bittner, A. R. B. de Castro, R. Dohrmann, P. Gurtler, T. Laarmann, W. Laasch, J. Schulz, A. Swiderski, K. von Haeften, T. Moller, B. Faatz, A. Fateev, J. Feldhaus, C. Gerth, U. Hahn, E. Saldin, E. Schneidmiller, K. Sytchev, K. Tiedtke, R. Treusch, and M. Yurkov. Multiple ionization of atom clusters by intense soft x-rays from a free-electron laser. *Nature*, 420(6915):482–485, 12 2002.

[59] H.-K. Chung, M.H. Chen, and R.W. Lee. Extension of atomic configuration sets of the non-lte model in the application to the kî± diagnostics of hot dense matter. *High Energy Density Physics*, 3(1-2):57 – 64, 2007.

[60] Mehdi Dehghan and Vahid Mohammadi. The numerical solution of fokker–planck equation with radial basis functions (rbfs) based on the meshless technique of kansa-s approach and galerkin method. *Engineering Analysis with Boundary Elements*, 47:38 – 63, 2014.

[61] Thomas R. Preston, Sam M. Vinko, Orlando Ciricosta, Hyun-Kyung Chung, Richard W. Lee, and Justin S. Wark. The effects of ionization potential depression on the spectra emitted by hot dense aluminium plasmas. *High Energy Density Physics*, 9(2):258 – 263, 2013.

[62] D. J. Hoarty, P. Allan, S. F. James, C. R. D. Brown, L. M. R. Hobbs, M. P. Hill, J. W. O. Harris, J. Morton, M. G. Brookes, R. Shepherd, J. Dunn, H. Chen, E. Von Marley, P. Beiersdorfer, H. K. Chung, R. W. Lee, G. Brown, and J. Emig. Observations of the effect of ionization-potential depression in hot dense plasma. *Phys. Rev. Lett.*, 110:265003, Jun 2013.

[63] Henri van Regemorter. Rate of Collisional Excitation in Stellar Atmospheres. *Astr.Phys.J.*, 136:906, Nov 1962.

[64] J. A. Gaunt and Ralph Howard Fowler. Continuous absorption. *Philosophical Transactions of the Royal Society of London. Series A, Containing Papers of a Mathematical or Physical Character*, 229(670-680):163–204, 1930.

[65] L. A. Vainshtein. The Excitation of Atoms and Ions by Electron Impact. I. Calculation Ignoring Exchange. *Optics and Spectroscopy*, 11:163, Sep 1961.

[66] R. Mewe. Interpolation Formulae for the Electron Impact Excitation of Ions in the H-, He-, Li-, and Ne- Sequences. *Astr. and Astr. Phys.*, 20:215, Aug 1972.

[67] M. Belkhiri and C. J. Fontes. Influence of the plasma environment on auto-ionization. *Journal of Physics B: Atomic, Molecular and Optical Physics*, 49(17):175002, 2016.

[68] M. H. Chen, B. Crasemann, and H. Mark. Relativistic k-shell auger rates, level widths, and fluorescence yields. *Phys. Rev. A*, 21:436–441, 1980.

[69] Michael Pindzola, Donald Griffin, and Nigel Badnell. *Dielectronic Recombination*, pages 829–834. Springer New York, New York, NY, 2006.

[70] Th. Bornath, M. Schlanges, F. Morales, and R. Prenzel. Dynamical screening effects on rate coefficients for dense plasmas. *J. of Quant. Spec. and Rad. Transfer*, 58(4-6):501–508, 1997.

[71] H. Bethe. Zur theorie des durchgangs schneller korpuskularstrahlen durch materie. *Annalen der Physik*, 397(3):325–400, 1930.

[72] Wolfgang Lotz. An empirical formula for the electron-impact ionization cross-section. *Zeitschrift für Physik*, 206(2):205–211, April 1967.

[73] A. Burgess, H. P. Summers, Deirdre M. Cochrane, and R. W. P. McWhirter. Cross-sections for ionization of positive ions by electron impact. *Monthly Notices of the Royal Astronomical Society*, 179(2):275, 1977.

[74] R. E. H. Clark, J. Abdallah, Jr., and J. B. Mann. Integral and differential cross sections for electron impact ionization. *Astrophys. J.*, 381:597–600, 1991.

[75] J.J. Thomson. Xlii. ionization by moving electrified particles. *Philosophical Magazine Series 6*, 23(136):449–457, 1912.

[76] Xavier Llovet, Cedric J. Powell, Francesc Salvat, and Aleksander Jablonski. Cross sections for inner-shell ionization by electron impact. *Journal of Physical and Chemical Reference Data*, 43(1):013102, March 2014.

[77] Wolfgang Lotz. Electron-impact ionization cross-sections and ionization rate coefficients for atoms and ions from hydrogen to calcium. *Zeitschrift für Physik*, 216(3):241–247, 1968.

[78] Wm.J. Veigele. Photon cross sections from 0.1 kev to 1 mev for elements z = 1 to z = 94. *Atomic Data and Nuclear Data Tables*, 5(1):51 – 111, 1973.

[79] H. A. Kramers. Xciii. on the theory of x-ray absorption and of the continuous x-ray spectrum. *The London, Edinburgh, and Dublin Philosophical Magazine and Journal of Science*, 46(275):836–871, 1923.

[80] Joachim Oxenius. *Kinetic theory of particles and photons. Theoretical foundations of Non-LTE plasma spectroscopy.* 1986.

[81] J.S. Townsend. Electricity in gases. *Oxford University Press*, 1915.

[82] K. G. McKay. Avalanche breakdown in silicon. *Phys. Rev.*, 94:877–884, May 1954.

[83] H. Geiger and W. Müller. Elektronenzählrohr zur messung schwächster aktivitäten. *Naturwissenschaften*, 16(31):617–618, 1928.

[84] A. J. Dempster. A new method of positive ray analysis. *Phys. Rev.*, 11:316–325, Apr 1918.

[85] M.J. Berger, J.S. Coursey, M.A. Zucker, and J. Chang. Stopping-powers and range tables for electrons, protons, and helium ions, nist standard reference database 124, 1993.

[86] J. D. Lindl et al. The physics basis for ignition using indirect-drive targets on the national ignition facility. *Phys. Plasmas*, 11(2):339–491, 2004.

[87] F. J. Rogers and C. A. Iglesias. Astrophysical opacity. *Science*, 263(5143):50–55, 1994.

[88] R. Neutze, R. Wouts, D. van der Spoel, E. Weckert, and J. Hajdu. Potential for biomolecular imaging with femtosecond x-ray pulses. *Nature*, 406(6797):752–757, 08 2000.

[89] E. K. Curwood, H. M. Quiney, and K. A. Nugent. Determining electronic damage to biomolecular structures in x-ray free-electron-laser imaging experiments. *Phys. Rev. A*, 87:053407, 2013.

[90] C. Caleman et al. Simulations of radiation damage in biomolecular nanocrystals induced by femtosecond x-ray pulses. *J. Mod. Optics*, 58(16):1486–1497, 2011.

[91] M. A. Lennon, K. L. Bell, H. B. Gilbody, J. G. Hughes, A. E. Kingston, M. J. Murray, and F. J. Smith. Recommended data on the electron impact ionization of atoms and ions: Fluorine to nickel. *Journal of Physical and Chemical Reference Data*, 17(3):1285–1363, 1988.

[92] L B Golden and D H Sampson. Ionization of highly charged ions by electron impact. *Journal of Physics B: Atomic and Molecular Physics*, 10(11):2229, 1977.

[93] György Csanak, Howard S. Taylor, and Robert Yaris. Many-body methods applied to electron scattering from atoms and molecules. ii. inelastic processes. *Phys. Rev. A*, 3:1322–1328, Apr 1971.

[94] S. M. Younger. Electron-impact-ionization cross sections for highly ionized heliumlike atoms. *Phys. Rev. A*, 22:1425–1428, Oct 1980.

[95] Joseph B. Mann. Excitation collision strengths for iron ions calculated with a distorted wave method. *Atomic Data and Nuclear Data Tables*, 29(3):407 – 452, 1983.

[96] Douglas H. Sampson, Hong Lin Zhang, and Christopher J. Fontes. A fully relativistic approach for calculating atomic data for highly charged ions. *Physics Reports*, 477(4-6):111 – 214, 2009.

[97] Robert C. Stabler. Classical impulse approximation for inelastic electron-atom collisions. *Phys. Rev.*, 133:A1268–A1273, Mar 1964.

[98] Michal Gryziński. Classical theory of atomic collisions. i. theory of inelastic collisions. *Phys. Rev.*, 138:A336–A358, Apr 1965.

[99] A. Burgess and I. C. Percival. Classical theory of atomic scattering. *Advances in Atomic and Molecular Physics*, 4:109 – 141, 1968.

[100] H. Bethe and J. Ashkin. Experimental nuclear physics,. *J. Wiley, New York.*, 144:253, 1953.

[101] A. Burgess, H. P. Summers, Deirdre M. Cochrane, and R. W. P. McWhirter. Cross-sections for ionization of positive ions by electron impact. *Monthly Notices of the Royal Astronomical Society*, 179(2):275, 1977.

[102] Alan Burgess and Marita C. Chidichimo. Electron impact ionization of complex ions. *Monthly Notices of the Royal Astronomical Society*, 203(4):1269–1280, 1983.

[103] M C Zammit, D V Fursa, and I Bray. Convergent-close-coupling calculations for excitation and ionization processes of electron-hydrogen collisions in debye plasmas. *Phys. Rev. A*, 82:052705, 2010.

[104] Igor Bray and Andris T. Stelbovics. Explicit demonstration of the convergence of the close-coupling method for a coulomb three-body problem. *Phys. Rev. Lett.*, 69:53–56, Jul 1992.

[105] Igor Bray and Andris T. Stelbovics. The convergent close-coupling method for a coulomb three-body problem. *Computer Physics Communications*, 85(1):1 – 17, 1995.

[106] L. J. Kieffer and Gordon H. Dunn. Electron impact ionization cross-section data for atoms, atomic ions, and diatomic molecules: I. experimental data. *Rev. Mod. Phys.*, 38:1–35, Jan 1966.

[107] F. A.. Harrison. The determination of atomic collision cross sections using crossed electron and ion beams (and some sources of error in such experiments). *Br. J. Appl. Phys*, 17:371—382, 1966.

[108] B. Peart S. O. Martin and K. T. Dolder. Measurements of cross sections for the ionization of mg^{+} to mg^{2+} by electron impact. *Journal of Physics B: Atomic and Molecular Physics*, 1(4):537, 1968.

[109] D.H. Crandall, R.A. Phaneuf, B.E. Hasselquist, and D.C. Gregory. Measured cross sections for ionisation of c 3+ , n 4+ and o 5+ ions with contribution due to excitation-autoionisation. *Journal of Physics B: Atomic and Molecular Physics*, 12(7):L249, 1979.

[110] H. J. Kunze. Collisional ionization rates for lithium- and beryllium-like ions. *Phys. Rev. A*, 3:937–942, Mar 1971.

[111] E Kallne and L A Jones. Measurements of the ionisation rates of lithium-like ions. *Journal of Physics B: Atomic and Molecular Physics*, 10(18):3637, 1977.

[112] W. L. Rowan and J. R. Roberts. Electron-impact ionization-rate coefficients for lithiumlike nitrogen and oxygen. *Phys. Rev. A*, 19:90–98, Jan 1979.

[113] Hans R. Griem. Electron-ion collisional rate coefficients from time-dependent plasmas. *J. of Quant. Spec. and Rad. Transfer*, 40(3):403 – 420, 1988.

[114] E. Kallne L.A. Jones and D.B. Thomson. Measurement of the total collisional ionization rates of ne vi, vii and viii. *Journal of Physics B: Atomic and Molecular Physics*, 10(2):187, 1977.

[115] Ahmed H. Zewail. Femtochemistry:- atomic-scale dynamics of the chemical bond. *The Journal of Physical Chemistry A*, 104(24):5660–5694, 2000.

[116] J. Chalupský et al. Spot size characterization of focused non-Gaussian X-ray laser beams. *Opt. Express*, 18(26):27836–27845, dec 2010.

[117] Christopher J. Fontes, Douglas H. Sampson, and Hong Lin Zhang. Method for calculating the electron-impact ionization of ions of any complexity. *Phys. Rev. A*, 48:1975–1982, Sep 1993.

[118] A. G. de la Varga, P. Velarde, M. Cotelo, F. de Gaufridy, and P. Zeitoun. Radiative properties for warm and hot dense matter. *High Energy Density Physics*, 7(3):163 – 168, 2011.

[119] Alberto García de la Varga. Modelización de las propiedades radiativas e interacción de láseres ultraintensos con la materia, doctoral thesis etsii (upm). *Doctoral Thesis ETSII (UPM), http://oa.upm.es/32905/*, 2014.

[120] T. Ekeberg et al. Three-dimensional reconstruction of the giant mimivirus particle with an x-ray free-electron laser. *Phys. Rev. Lett.*, 114:098102, Mar 2015.

[121] K. Ayyer et al. Macromolecular diffractive imaging using imperfect crystals. *Nature*, 530(7589):202—206, 02 2016.

[122] John G. Kirkwood. The statistical mechanical theory of transport processes i. general theory. *The Journal of Chemical Physics*, 14(3):180–201, 1946.

[123] N.N. Bogolyubov. Kinetic equations. *Journal of Physics USSR*, 10:265–274, 1946.

[124] Max Born and H. S. Green. A general kinetic theory of liquids i. the molecular distribution functions. *Proceedings of the Royal Society of London. Series A. Mathematical and Physical Sciences*, 188(1012):10–18, 1946.

[125] Ludwig Boltzmann. *Further Studies on the Thermal Equilibrium of Gas Molecules*, pages 262–349. Sitzungsberichte Akademie der Wissenschaften, 1872.

[126] Z. Alterman, K. Frankowski, and C. L. Pekeris. Eigenvalues and Eigenfunctions of the Linearized Boltzmann Collision Operator for a Maxwell Gas and for a Gas of Rigid Spheres. *Astrophysical Journal, Supplement*, 7:291, November 1962.

[127] A.V. Bobylev and E. Mossberg. On some properties of linear and linearized boltzmann collision operators for hard spheres. *Kinetic and Related Models*, 1(1):521, 2008.

[128] B. J. Delarue and S. B. Pope. Application of pdf methods to compressible turbulent flows. *Physics of Fluids*, 9(9):2704–2715, 1997.

[129] H.A. Kramers. Brownian motion in a field of force and the diffusion model of chemical reactions. *Physica*, 7(4):284 – 304, 1940.

[130] J. E. Moyal. Stochastic processes and statistical physics. *Journal of the Royal Statistical Society. Series B (Methodological)*, 11(2):150–210, 1949.

[131] Patrick Jenny, Manuel Torrilhon, and Stefan Heinz. A solution algorithm for the fluid dynamic equations based on a stochastic model for molecular motion. *Journal of Computational Physics*, 229(4):1077 – 1098, 2010.